Role of $U(1)$ Gauge Symmetry in the Semiconductor Bloch Equations

Andrew Parks

Thesis submitted to the University of Ottawa
in partial fulfillment of the requirements for the degree of
Doctor of Philosophy in Physics

Department of Physics
Faculty of Science
University of Ottawa

Acknowledgements

First and foremost, I would like to thank my supervisor, Professor Thomas Brabec. His knowledge of light-matter interactions is truly impressive, and I have gained a wealth of new knowledge working with him. He has a kind and patient approach to both academic pursuits and life in general. I always came away from our discussions feeling more optimistic about my research.

I am grateful to the examiners for my thesis defence; Professors Pawel Hawrylak, Adina Luican-Mayer, Yue Zhang, and Miroslav Kolesik. Not only did they graciously accept the challenge of allowing me to defend my thesis within a very short timeframe, but they also asked insightful questions and provided valuable feedback. I would also like to thank Lorraine Houle in the graduate office, who was invaluable in facilitating the defence process. I would also like to thank the University of Ottawa and the Ontario Graduate Scholarship program for financial support.

I have lived in Ottawa for over a decade, and I have developed a wonderful network of friends here. I have greatly appreciated their support throughout my PhD, and the thought of moving away from here to pursue my next position fills me with mixed emotions.

Lastly, I would like to thank my parents, who have always loved and supported me. They have allowed me to become the person I am.

List of Publications

- A. M. Parks and T. Brabec, "Gauge invariant formulation of the semiconductor Bloch equations," in preparation
- A. M. Parks and T. Brabec, "Influence of interband mixture current for high harmonic generation in solids," in preparation
- A. Thorpe, N. Bouramand, A. M. Parks, E. Goulielmakis, and T. Brabec, "Mechanisms of high harmonic generation in solids," in peer review
- G. Ernotte, M. Taucer, P. B. Corkum, A. M. Parks, A. Thorpe, C. R. McDonald, and T. Brabec, "Strong field dynamics and spatial correlations in a maximally localized Wannier basis," in peer review
- J. L. Bégin, A. Jain, A. M. Parks, F. Hufnagel, P. B. Corkum, E. Karimi, T. Brabec, and R. Bhardwaj, "Scalable nonlinear helical dichroism in chiral and achiral molecules," accepted in Nature Photonics
- N. Boroumand, A. Thorpe, A. M. Parks, and T. Brabec, "Keldysh ionization theory of atoms: mathematical details," J. Phys. B: At. Mol. Opt. Phys. **55** 213001 (2022)
- A. M. Parks, G. Ernotte, A. Thorpe, C. R. McDonald, P. B. Corkum, M. Taucer, and T. Brabec, "Wannier Quasi-classical approach to high harmonic generation in semiconductors," Optica **7** (12), 1764-1772 (2020)
- G. Bart, I. Schubert, A. M. Parks, P. B. Corkum, and T. Brabec, "Coulomb blocking of sequential tunnel ionization in complex systems," Journal of Physics: Photonics **2**, 034007 (2020)
- S. Almalki, A. M. Parks, G. Bart, P. B. Corkum, T. Brabec, and C. R. McDonald, "High harmonic generation tomography of impurities in solids: Conceptual analysis," Phys. Rev. B **98**, 144307 (2018)
- S. Almalki, A. M. Parks, T. Brabec, and C. R. McDonald, "Nanoengineering of strong field processes in solids," J. Phys. B: At. Mol. Opt. Phys. **51** 084001 (2018)

Table of Contents

List of Figures

List of Appendices

List of Abbreviations

BZ Brillouin zone

DFT density functional theory

HHG high harmonic generation

MLWF maximally localized Wannier function

SBEs semiconductor Bloch equations

SFA strong field approximation

TB tight-binding

TDM transition dipole moment

WQC Wannier quasi-classical

Abstract

The semiconductor Bloch equations (SBEs) are an insightful and well-established formalism for studying light-matter interactions in solids. When Coulomb interactions between electrons are omitted, the SBEs are simplified to a single particle model. The SBEs in this single electron approximation have been used extensively to model strong-field interactions in condensed matter. The SBEs in the length gauge provide an intuitive and numerically efficient model of high harmonic generation (HHG) in solids. In this approach, the SBEs involve Berry connections and transition dipole moments, which are gauge dependent structural quantities. This thesis studies the role of gauge symmetry in the SBEs, and how it can be exploited to facilitate efficient numerical analysis of HHG in solids.

In the length gauge, the macroscopic current describing HHG can be decomposed into physically intuitive contributions. In particular, this leads to a contribution known as the "mixture" current, which has been overlooked by the HHG community until recently. We study the influence of this contribution using the analytic tight-binding model for gapped graphene. We derive an analytic gauge transformation that removes singular behaviour from the gapped graphene model, thus enabling efficient numerical integration of the SBEs.

We also present an alternative approach for simulating dynamics in tight-binding models. Instead of simulating the SBEs in the usual basis of Bloch functions, we transform to the basis in which the tight-binding Hamiltonian is represented. The dipole matrix elements necessarily vanish in this basis, and the SBEs can be integrated using only the Hamiltonian matrix elements. We first generalize the SBEs to accomodate a non-diagonal Hamiltonian matrix, and we demonstrate this formalism numerically using two different tight-binding models.

Finally, we derive a novel formulation of the SBEs which involve only gauge invariant matrix elements. Specifically, the Berry connections and transition dipole phases are replaced by a gauge invariant quantity known as the shift vector. This yields a fully gauge invariant description of HHG in solids, and the shift vector provides intuitive insight for HHG in systems with broken inversion symmetry. Further, the ability to describe HHG solely in terms of gauge invariant quantities raises new possibilities for tomographic reconstruction of crystal band structure, and this idea is discussed as a possible direction of future work.

Chapter 1
Introduction

The interaction of intense laser pulses with matter results in highly nonlinear dynamics, which lead to a variety of interesting phenomena. One of the most interesting of these processes is high harmonic generation (HHG), in which a system excited by a strong, coherent optical pulse emits harmonics many times greater than the frequency of the applied field. HHG in solids was first observed in a bulk semiconductor [1], and more recently has been explored in a wider variety of materials such as dielectrics [2, 3], two-dimensional semiconductors [4, 5], and nanostructures [6, 7]. Since HHG occurs on a sub-cycle timescale, its discovery has laid the foundation of attosecond science in condensed matter [8–12]. HHG in solids has also attracted attention as a potential source for generating ultrashort coherent XUV pulses [2], and has been used to reconstruct structural properties such as energy band structure [13] and Berry curvature [14, 15].

Several theoretical approaches have been developed to model HHG in solids, ranging from semiclassical analysis [16–18] to various quantum mechanical simulations; the latter including time-dependent density-functional theory [19, 20], as well as the semiconductor Bloch equations (SBEs) [21, 22]. The SBEs were originally derived [23] to include Coulomb interactions between charge carriers within the Hartree-Fock approximation. Omitting these Coulomb interactions leads to a significant simplification, resulting in a single-electron approximation of the SBEs. The SBEs within this single-electron approximation have been used extensively to model HHG in solids [13, 16–18, 24–36]. In particular, the single-electron SBEs in the length gauge [37, 38] provide an intuitive decompositon of the induced current into intraband and interband contributions [37, 39].

A disadvantage of the length gauge SBEs arises from the gauge freedom of certain structural quantities in a periodic solid. Physical observables are invariant with respect to phase rotations of the Bloch functions, which are eigenstates of a periodic crystal. Specifically, for the cell periodic functions $u_{m,\mathbf{k}}$ satisfying Bloch's theorem, invariance with respect to phase transformations

$$|u_{m,\mathbf{k}}\rangle \to |\tilde{u}_{m,\mathbf{k}}\rangle = e^{-i\chi_m(\mathbf{k})}|u_{m,\mathbf{k}}\rangle; \qquad \chi_m(\mathbf{k}) \in \mathbb{R}, \tag{1.1}$$

describes a gauge symmetry[1] of a periodic crystal. Although observables are independent of the phase χ_m, structural matrix elements such as the transition dipole moment (TDM) and the Berry connections are gauge dependent. While early theoretical studies of HHG in solids considered only the gauge invariant magnitude of the TDM [13, 16, 24], it was later determined that the TDM phase leads to the generation of even harmonics in crystals with broken inversion symmetry [27, 28]. A subsequent study showed that in such systems, both the complex TDMs and the Berry connections must be included in the SBEs to maintain gauge invariance of the overall theory [31]. These matrix elements involve $\mathbf{k}$-space gradients of the cell periodic functions, and are thus strongly dependent on the phase of $u_{m,\mathbf{k}}$. We refer to a specific choice of these $\mathbf{k}$-dependent phases as a Bloch gauge, and clearly a smooth and periodic gauge is essential for efficient numerical analysis of the SBEs.

The problem of obtaining a smooth Bloch gauge from numerical structural calculations has received considerable attention in recent years [32, 33, 36, 38]. If the Bloch functions are obtained from a numerical band structure calculation, the phase of $u_{m,\mathbf{k}}$ can exhibit discontinuous jumps throughout the Brillouin zone. As a result, the Bloch gauge must be smoothed before the TDM and Berry connection can be calculated numerically. Numerical approaches based on the parallel transport gauge transformation [41] have been demonstrated successfully [32], but the implementation is quite technical; especially for systems with degeneracies [33]. In this thesis we develop alternative approaches for simulating the SBEs that avoid the need for numerical gauge fixing.

The Hamiltonian matrix of a tight-binding model can be diagonalized analytically, which results in closed form expressions for the structural matrix elements entering the SBEs. Although tight-binding models are not as accurate as ab-initio band structure calculations, they are useful for developing understanding of HHG phenomena. Indeed, Jiang et al [28] used a tight-binding model for ZnO to perform simulations of the SBEs that revealed the mechanism generating even harmonics in prior experiments. Although tight-binding models avoid the issue of phase jumps arising from numerical diagonalization, in some models the matrix elements can exhibit non-smooth features at high symmetry points of the BZ. The two band tight-binding model for gapped graphene [42] has been used extensively as a prototype for modeling two-dimensional materials [27, 34, 43]. However, the Berry connections obtained from analytic diagonalization are typically singular at the minimum bandgap, while the TDM exhibits a discontinuous phase jump. We develop an analytic gauge smoothing function which eliminates the singular behaviour

[1]The gauge group for this symmetry is the one dimensional unitary group, since $e^{-i\chi_m(\mathbf{k})} \in U(1)$. The gauge symmetry of a periodic solid is thus analogous to, but distinct from, the $U(1)$ gauge symmetry of electromagnetism [40]. This will be discussed further in Chapter 2.

from the gapped graphene model. This allows efficient numerical integration of the SBEs including both the complex TDM and the Berry connections, which we apply to study the orientation dependence of HHG in gapped graphene.

One approach to circumvent the gauge smoothing issue in numerical band structure calculations is to transform the SBEs to a particular basis comprised of a linear combination of Bloch functions [30]. Specifically, the Wannier90 [44] software package has been developed to calculate maximally localized Wannier functions (MLWFs) [41, 45] from density functional theory (DFT) band structure calculations. The k-space gauge corresponding to the MLWFs is necessarily smooth and periodic, but the Bloch-like functions in this basis do not diagonalize the Hamiltonian. As a result, Wannier90 can be used to obtain smooth and periodic matrix elements in this non-diagonal basis, even though the initial Bloch gauge has non-smooth phases. Importantly, this approach shows that transforming the SBEs to a non-diagonal basis can be used to avoid the issues of a non-smooth Bloch gauge; the price paid is sacrificing the band picture. We develop an analogous approach for tight-binding models, in which the Hamiltonian matrix is represented in a basis of localized atomic orbitals. We show that simulating the SBEs in the orbital basis avoids any numerical complications arising from singular Berry connections in the Bloch basis.

Finally, we present a novel gauge invariant formulation of the SBEs, in which all gauge dependent phases are eliminated. Using a simple transformation of the density matrix elements, we show that the SBEs, together with the expressions for the current, can be evaluated using only gauge invariant structural quantities. Specifically, the Berry connections and TDM phase are replaced by a gauge invariant quantity known as the shift vector [46, 47]. This formalism is independent of the method used to obtain the band structure, and can be applied to both tight-binding and numerical band structure calculations. Importantly, this formalism eliminates the need for numerical gauge smoothing, since the required matrix elements are all gauge invariant. The role of the shift vector provides valuable insight for HHG phenomena, and also raises new possibilities for the reconstruction of structural quantities using HHG tomography.

This thesis is organized as follows. Chapter 2 reviews the derivation of the SBEs, as well as the expressions used to calculate the induced current. We pay particular attention to the interband mixture current [36], which has been overlooked by the HHG community until recently [39]. We also clarify the gauge transformation properties of the SBEs, as well as the matrix elements entering the mixture current. In chapter 3 we discuss the analytic tight-binding model of gapped graphene, and we develop a gauge transformation to remove singular behaviour from this model. We also derive expressions for the generalized derivatives [37] of the TDM, which are required to evaluate the mixture current. In chapter 4 we study the orientation dependence of HHG in

gapped graphene, with a particular focus on the contribution of the mixture current. Chapter 5 generalizes the SBEs to a non-diagonal basis, and we simulate HHG in the orbital basis for two different tight-binding models. In chapter 6 we present the gauge invariant formulation of the SBEs, which is then applied to study HHG in a model semiconductor with broken inversion symmetry. Finally, we conclude with chapter 7, which summarizes the important results and discusses possible avenues of future work.

Chapter 2
Semiconductor Bloch equations

In this chapter we review the dynamics of light-matter interactions in solids within the single electron approximation. Combining aspects of the approaches in Refs. [37] and [48], we formulate the SBEs in terms of the gauge covariant derivative for a periodic solid. Not only does this simplify the derivation, but it also reveals the gauge symmetry of the SBEs more clearly. In Sec. 2.2 we derive the expression for the induced current that ultimately generates HHG, and we pay close attention to the so-called mixture current [36, 39] that has been mostly overlooked in previous studies of HHG in solids. Finally, in Sec. 2.3 we discuss the $U(1)$ gauge symmetry of periodic solid, and the resulting gauge transformation relations that are relevant to light-matter interactions.

2.1 SBEs in static momentum frame

The Hamiltonian for a single electron in a periodic crystal is

$$H_0 = \frac{\mathbf{p}^2}{2} + U(\mathbf{x}), \tag{2.1}$$

where $\mathbf{p} = -i\nabla_{\mathbf{x}}$ is the momentum operator, $U(\mathbf{x})$ is the lattice potential, and the electron mass is $m_e = 1$ in atomic units. The periodic potential satisfies $U(\mathbf{x}) = U(\mathbf{x} + \mathbf{R})$ for any translation vector $\mathbf{R}$ of the crystal lattice. The Bloch functions $\Phi_{m,\mathbf{k}}$ are eigenstates of the crystal Hamiltonian, satisfying [49],

$$H_0|\Phi_{m,\mathbf{k}}\rangle = E_m(\mathbf{k})|\Phi_{m,\mathbf{k}}\rangle, \tag{2.2}$$

where $\mathbf{k}$ is a crystal momentum vector in the reciprocal lattice, and $E_m(\mathbf{k})$ is the energy dispersion of the band indexed by the integer m. The Bloch functions can be written as

$$|\Phi_{m,\mathbf{k}}\rangle = (1/\sqrt{Nv_c})e^{i\mathbf{k}\cdot\mathbf{x}}|u_{m,\mathbf{k}}\rangle$$

where N and v_c are the number and volume of primitive unit cells in the lattice. According to Bloch's theorem, the cell-periodic functions $u_{m,\mathbf{k}}(\mathbf{x}) = \langle \mathbf{x}|u_{m,\mathbf{k}}\rangle$ satisfy

$$u_{m,\mathbf{k}}(\mathbf{x}+\mathbf{R}) = u_{m,\mathbf{k}}(\mathbf{x}). \tag{2.3}$$

Further, the Bloch functions satisfy the orthogonality

$$\langle \Phi_{n,\mathbf{k}}|\Phi_{m,\mathbf{k}'}\rangle = \delta_{mn}\delta(\mathbf{k}-\mathbf{k}'), \tag{2.4}$$

while the cell-periodic functions are normalized according to $\langle u_m|u_m\rangle = v_c$.

In the semiclassical approximation, light-matter interactions are modeled by the minimal coupling Hamiltonian

$$H_A(t) = \left[\mathbf{p} - e\mathbf{A}(t)\right]^2/2 + U(\mathbf{x}), \tag{2.5}$$

where $\mathbf{A}(t)$ is the vector potential of the applied field, and $e = -1$ in atomic units. We work in the Coulomb gauge, where the scalar potential vanishes and the electric field is given by $\mathbf{F}(t) = -\partial_t \mathbf{A}(t)$. In the dipole approximation we assume the applied field to be spatially uniform, and we can obtain an equivalent interaction Hamiltonian using a gauge transformation [50] $H(t) = e^{\mathbf{A}(t)\cdot\mathbf{x}} H_A(t) e^{-\mathbf{A}(t)\cdot\mathbf{x}}$. The result of this transformation is

$$H(t) = H_0 - e\mathbf{F}(t)\cdot\mathbf{x}, \tag{2.6}$$

which is called the length gauge Hamiltonian [36–38]. Throughout this thesis we work in the length gauge, which requires a smaller number of bands for convergence [36], and also allows a decomposition of the induced current into physically intuitive contributions [36, 37, 39]. Although $H_A(t)$ satisfies the lattice periodicy, the position operator in $H(t)$ does not and it must be treated carefully.

To evaluate matrix elements of the position operator in the crystal momentum representation, we follow the prescription of Blount [49]. Details of this derivation can be found in Refs. [27, 36], and here we only highlight the essential features. We first observe that

$$i\nabla_{\mathbf{k}} e^{i\mathbf{k}\cdot\mathbf{x}} u_{m,\mathbf{k}}(\mathbf{x}) = e^{i\mathbf{k}\cdot\mathbf{x}} \left(i\nabla_{\mathbf{k}} - \mathbf{x}\right) u_{m,\mathbf{k}}(\mathbf{x}), \tag{2.7}$$

which allows the matrix elements between Bloch states to be written as

$$\begin{aligned}\langle\Phi_{n,\mathbf{k}'}|\mathbf{x}|\Phi_{m,\mathbf{k}}\rangle &= \int_V d\mathbf{x}\Phi^*_{n,\mathbf{k}'}(\mathbf{x})\mathbf{x}\Phi_{m,\mathbf{k}}(\mathbf{x}) \\ &= -i\nabla_{\mathbf{k}}\langle\Phi_{n,\mathbf{k}'}|\Phi_{m,\mathbf{k}}\rangle + \frac{i}{V}\int_V d\mathbf{x}e^{i(\mathbf{k}-\mathbf{k}')\cdot\mathbf{x}}u^*_{n,\mathbf{k}'}(\mathbf{x})\nabla_{\mathbf{k}}u_{m,\mathbf{k}}(\mathbf{x}),\end{aligned} \tag{2.8}$$

where $V = Nv_c$ is the crystal volume. Since $u_{m,\mathbf{k}}(\mathbf{x}) = u_{m,\mathbf{k}}(\mathbf{x}+\mathbf{R})$, the integral over the crystal volume can be converted to a sum of integrals over unit cells,

$$\langle\Phi_{n,\mathbf{k}'}|\mathbf{x}|\Phi_{m,\mathbf{k}}\rangle = -i\nabla_{\mathbf{k}}\langle\Phi_{n,\mathbf{k}'}|\Phi_{m,\mathbf{k}}\rangle + \frac{i}{V}\sum_{\mathbf{R}} e^{i(\mathbf{k}-\mathbf{k}')\cdot\mathbf{R}}\int_{v_c} d\mathbf{x}e^{i(\mathbf{k}-\mathbf{k}')\cdot\mathbf{x}}u^*_{n,\mathbf{k}'}(\mathbf{x})\nabla_{\mathbf{k}}u_{m,\mathbf{k}}(\mathbf{x}). \tag{2.9}$$

The remaining sum over lattice sites reduces to a delta function, leading to the familiar result [27, 36–38, 49]

$$\langle\Phi_{n,\mathbf{k}'}|\mathbf{x}|\Phi_{m,\mathbf{k}}\rangle = \left[-i\delta_{nm}\nabla_{\mathbf{k}} + \boldsymbol{\xi}_{nm}(\mathbf{k})\right]\delta(\mathbf{k}-\mathbf{k}'), \tag{2.10}$$

where

$$\boldsymbol{\xi}_{nm}(\mathbf{k}) = \langle u_{n,\mathbf{k}}|i\nabla_{\mathbf{k}}|u_{m,\mathbf{k}}\rangle \tag{2.11}$$

are the dipole matrix elements [36, 49]. Clearly the matrix elements (2.10) are diagonal in $\mathbf{k}$, which means the matrix elements of $H(t)$ are also diagonal in $\mathbf{k}$ as long as the field $\mathbf{F}(t)$ is independent of position. This last point is important; if the electric field depends on $\mathbf{x}$, the spatial integral arising from $\langle\Phi_{n,\mathbf{k}'}|\mathbf{F}(\mathbf{x},t)\cdot\mathbf{x}|\Phi_{m,\mathbf{k}}\rangle$ cannot be converted to a sum over equivalent unit cells since $\mathbf{F}(\mathbf{x},t)$ breaks translation symmetry.

When evaluating equations of motion in the crystal momentum representation, matrix elements of the position operator are always encountered in k-space integrals. To reveal the effect of the position operator on a k-dependent function $f(\mathbf{k})$, we consider

$$\begin{aligned}\sum_{\mathbf{k}'}\langle\Phi_{n,\mathbf{k}'}|\mathbf{x}|\Phi_{m,\mathbf{k}}\rangle f(\mathbf{k}') &= \sum_{\mathbf{k}'} f(\mathbf{k}')\left[-i\delta_{nm}\nabla_{\mathbf{k}} + \boldsymbol{\xi}_{nm}(\mathbf{k})\right]\delta(\mathbf{k}-\mathbf{k}') \\ &= \sum_{\mathbf{k}'}\delta(\mathbf{k}-\mathbf{k}')\left[i\delta_{nm}\nabla_{\mathbf{k}} + \boldsymbol{\xi}_{nm}(\mathbf{k})\right]f(\mathbf{k}'),\end{aligned} \tag{2.12}$$

where we have integrated by parts, noting that the surface term vanishes for an infinite periodic crystal [49]; provided f is itself a differentiable function. This motivates the replacement

$$\langle\Phi_{n,\mathbf{k}'}|\mathbf{x}|\Phi_{m,\mathbf{k}}\rangle f(\mathbf{k}) = \delta(\mathbf{k}-\mathbf{k}')\left[i\delta_{nm}\nabla_{\mathbf{k}} + \boldsymbol{\xi}_{nm}(\mathbf{k})\right]f(\mathbf{k}), \tag{2.13}$$

which has become a standard result used in the study of light-matter interactions in the length gauge [16, 18, 30, 37, 48]. We emphasize that this replacement only makes sense in the crystal momentum representation, where $\langle\Phi_{n,\mathbf{k}}|\mathbf{x}|\Phi_{m,\mathbf{k}}\rangle$ is interpreted as an operator acting on k-dependent functions.

We can define an operator $\mathbf{D}$ by writing the position operator as

$$\mathbf{x} = i\mathbf{D}. \tag{2.14}$$

The operator $\mathbf{D}$ is known as the gauge covariant derivative [48], and we label its matrix elements

$$\mathbf{D}_{nm,\mathbf{k}} \equiv \langle\Phi_{n,\mathbf{k}}|\mathbf{D}|\Phi_{m,\mathbf{k}}\rangle = -i\langle\Phi_{n,\mathbf{k}}|\mathbf{x}|\Phi_{m,\mathbf{k}}\rangle, \tag{2.15}$$

which are clearly diagonal in $\mathbf{k}$. Further, it is convenient to separate the matrix elements (2.11) into intraband Berry connections

$$\boldsymbol{\mathcal{A}}_n(\mathbf{k}) = \langle u_{n,\mathbf{k}}|i\nabla_{\mathbf{k}}|u_{n,\mathbf{k}}\rangle, \tag{2.16}$$

and interband transition dipole moments (TDMs)

$$\mathbf{d}_{nm}(\mathbf{k}) = (1-\delta_{nm})\langle u_{n,\mathbf{k}}|i\nabla_{\mathbf{k}}|u_{m,\mathbf{k}}\rangle. \tag{2.17}$$

As a result, we can also separate the covariant derivative into into intra- (ra) and interband (er) components

$$\mathbf{D} = \mathbf{D}^{\mathrm{ra}} + \mathbf{D}^{\mathrm{er}}, \tag{2.18}$$

which have matrix elements

$$\mathbf{D}^{\mathrm{ra}}_{nm,\mathbf{k}} = \delta_{nm}\left[\nabla_{\mathbf{k}} - i\boldsymbol{\mathcal{A}}_n(\mathbf{k})\right] \tag{2.19a}$$

$$\mathbf{D}^{\mathrm{er}}_{nm,\mathbf{k}} = -i\mathbf{d}_{nm}(\mathbf{k}). \tag{2.19b}$$

These decompositions will simplify the notation when evaluating commutators for equations of motion and observables.

Working in first quantization, the Bloch Ansatz for the time-dependent wavefunction is

$$|\psi(t)\rangle = \sum_{m,\mathbf{k}} a_m(\mathbf{k},t)|\Phi_{m,\mathbf{k}}\rangle, \tag{2.20}$$

where $a_m(\mathbf{k},t)$ is the time-dependent probability amplitude for Bloch state $\Phi_{m,\mathbf{k}}$. The density

matrix is

$$\rho(t) = |\psi(t)\rangle\langle\psi(t)|, \tag{2.21}$$

and its matrix elements in the Bloch basis are most generally given by

$$\rho_{nm}(\mathbf{k}, \mathbf{k}', t) = \langle\Phi_{n,\mathbf{k}}|\rho(t)|\Phi_{m,\mathbf{k}'}\rangle. \tag{2.22}$$

Since the electric field $\mathbf{F}(t)$ is independent of the position operator, both $H(t)$ and $\rho(t)$ are local operators with matrix elements diagonal in $\mathbf{k}$ [37, 49]. It is thus sufficient to consider the dynamics of the density matrix elements

$$\rho_{nm}(\mathbf{k}, t) = \langle\Phi_{n,\mathbf{k}}|\rho(t)|\Phi_{m,\mathbf{k}}\rangle = a_n(\mathbf{k}, t)a_m^*(\mathbf{k}, t), \tag{2.23}$$

within the single-electron and electric dipole approximations. In the Schrödinger representation, the equation of motion for the density matrix is

$$\partial_t\rho(t) = -i\left[H(t), \rho(t)\right]. \tag{2.24}$$

The commutator can be simplified according to

$$\begin{aligned}
\left[H(t), \rho(t)\right]_{nm} &= \left[H_0, \rho(t)\right]_{nm} - e\mathbf{F}(t)\cdot\left[\mathbf{x}, \rho(t)\right]_{nm} \\
&= \sum_{l,\mathbf{k}'}\left[\langle\Phi_{n,\mathbf{k}}|H_0|\Phi_{l,\mathbf{k}'}\rangle\langle\Phi_{l,\mathbf{k}'}|\rho(t)|\Phi_{n\mathbf{k}}\rangle - \langle\Phi_{n,\mathbf{k}}|\rho(t)|\Phi_{l,\mathbf{k}'}\rangle\langle\Phi_{l,\mathbf{k}'}|H_0|\Phi_{n\mathbf{k}}\rangle\right] \\
&\quad - ie\mathbf{F}(t)\cdot\left[\mathbf{D}, \rho(t)\right]_{nm} \\
&= \left[E_n(\mathbf{k}) - E_m(\mathbf{k})\right]\rho_{nm}(\mathbf{k}, t) - ie\mathbf{F}(t)\cdot\left[\mathbf{D}, \rho(t)\right]_{nm},
\end{aligned} \tag{2.25}$$

and from here onward we will not explicitly include summations over k-space, since we only consider local operators; i.e.

$$\langle\Phi_{n,\mathbf{k}}|\mathcal{O}|\Phi_{m,\mathbf{k}'}\rangle = \delta(\mathbf{k} - \mathbf{k}')\mathcal{O}_{nm}(\mathbf{k}). \tag{2.26}$$

Defining the energy difference between bands,

$$\varepsilon_{nm}(\mathbf{k}) \equiv E_n(\mathbf{k}) - E_m(\mathbf{k}), \tag{2.27}$$

we can write the density matrix equations succintly as

$$\left[\partial_t + i\varepsilon_{nm}(\mathbf{k})\right]\rho_{nm}(\mathbf{k},t) = e\mathbf{F}(t)\cdot\left[\mathbf{D},\rho(\mathbf{k},t)\right]_{nm}, \tag{2.28}$$

which differs from Eq. (55) of Ref. [48] by an overall sign, due to the different convention for the sign of the fundamental charge e. Using Eq. (2.19), the commutator is

$$\begin{aligned}\left[\mathbf{D},\rho(\mathbf{k},t)\right]_{nm} &= \sum_l \left[\mathbf{D}_{nl,\mathbf{k}}\rho_{lm}(\mathbf{k},t) - \rho_{nl}(\mathbf{k},t)\mathbf{D}_{lm,\mathbf{k}}\right] \\ &= \left[\nabla_{\mathbf{k}} - i\boldsymbol{\mathcal{A}}_{nm}(\mathbf{k})\right]\rho_{nm}(\mathbf{k},t) + \left[\mathbf{d}(\mathbf{k}),\rho(\mathbf{k},t)\right]_{nm},\end{aligned} \tag{2.29}$$

where

$$\boldsymbol{\mathcal{A}}_{nm}(\mathbf{k}) = \boldsymbol{\mathcal{A}}_n(\mathbf{k}) - \boldsymbol{\mathcal{A}}_m(\mathbf{k}) \tag{2.30}$$

is the difference of Berry connections between bands. Finally, defining the Rabi frequency [21]

$$\Omega_{nm}(\mathbf{k},t) = \mathbf{F}(t)\cdot\mathbf{d}_{nm}(\mathbf{k}), \tag{2.31}$$

we obtain the one-body semiconductor Bloch equations (SBEs)

$$\begin{aligned}\partial_t\rho_{nm}(\mathbf{k},t) =& -i\left[\varepsilon_{nm}(\mathbf{k}) - e\mathbf{F}(t)\cdot\boldsymbol{\mathcal{A}}_{nm}(\mathbf{k})\right]\rho_{nm}(\mathbf{k},t) \\ &+ ie\left[\Omega(\mathbf{k},t),\rho(\mathbf{k},t)\right]_{nm} - e\mathbf{F}(t)\cdot\nabla_{\mathbf{k}}\rho_{nm}(\mathbf{k},t).\end{aligned} \tag{2.32}$$

Although this form of the SBEs is used frequently in the literature [28, 30, 36, 39, 48], the gradient term can pose difficulty for numerical integration. In the next section, we will reformulate the SBEs by transforming to a non-inertial frame.

2.1.1 SBEs in comoving momentum frame

For Bloch electrons driven by a uniform electric field, the time-dependent crystal momentum is

$$\mathbf{k}(t) = \mathbf{k}(0) - e\mathbf{A}(t), \tag{2.33}$$

where $\mathbf{A}(t)$ is the vector potential. Since $\dot{\mathbf{k}}(t) = -e\dot{\mathbf{A}}(t) = e\mathbf{F}(t)$ in the Coulomb gauge, the total time-derivative of the density matrix is

$$\begin{aligned}\frac{d}{dt}\rho_{nm}(\mathbf{k},t) &= \frac{\partial}{\partial t}\rho_{nm}(\mathbf{k},t) + \dot{\mathbf{k}}(t)\cdot\nabla_{\mathbf{k}}\rho_{nm}(\mathbf{k},t) \\ &= \frac{\partial}{\partial t}\rho_{nm}(\mathbf{k},t) + e\mathbf{F}(t)\cdot\nabla_{\mathbf{k}}\rho_{nm}(\mathbf{k},t). \end{aligned} \tag{2.34}$$

This motivates the idea of eliminating the gradient term by transforming to a frame comoving with the vector potential [16]. The transformation can be formulated explicitly using the boost operator [39]

$$\mathcal{B}(t) = \mathcal{T}e^{\int_{-\infty}^{t} dt' \dot{\mathbf{k}}\cdot\nabla_{\mathbf{k}}}, \tag{2.35}$$

where $\mathcal{T}$ is the time-ordering operator along the k-space trajectory. Labeling the initial momenta $\mathbf{k}(0) = \mathbf{K}$, and defining

$$\mathbf{K}_t \equiv \mathbf{K} - e\mathbf{A}(t), \tag{2.36}$$

it can be shown [39] that the boost operator transforms k-space functions according to

$$\mathcal{B}(t)f(\mathbf{k}) = f(\mathbf{K}_t), \tag{2.37}$$

and we note that the action on Bloch states is given by

$$\mathcal{B}(t)|\Phi_{m,\mathbf{k}}\rangle = |\Phi_{m,\mathbf{K}_t}\rangle. \tag{2.38}$$

For matrix elements of on operator $\mathcal{O}(\mathbf{k})$, we have

$$\begin{aligned}\mathcal{B}(t)\mathcal{O}_{nm}(\mathbf{k}) &= \mathcal{B}(t)\langle\Phi_{m,\mathbf{k}}|\mathcal{O}(\mathbf{k})|\Phi_{n,\mathbf{k}}\rangle \\ &= \langle\Phi_{m,\mathbf{K}_t}|\mathcal{B}(t)\mathcal{O}(\mathbf{k})|\Phi_{n,\mathbf{k}}\rangle \\ &= \langle\Phi_{m,\mathbf{K}_t}|\mathcal{B}(t)\mathcal{O}(\mathbf{k})\mathcal{B}^{-1}(t)\mathcal{B}(t)|\Phi_{n,\mathbf{k}}\rangle \\ &= \langle\Phi_{m,\mathbf{K}_t}|\mathcal{B}(t)\mathcal{O}(\mathbf{k})\mathcal{B}^{-1}(t)|\Phi_{n,\mathbf{K}_t}\rangle \\ &= \langle\Phi_{m,\mathbf{K}_t}|\mathcal{O}(\mathbf{K}_t)|\Phi_{n,\mathbf{K}_t}\rangle \\ &= \mathcal{O}_{nm}(\mathbf{K}_t), \end{aligned} \tag{2.39}$$

where it is important to realize that the boost operator acts on all quantities appearing to its right, and inserting $\mathcal{B}^{-1}$ prevents the ket from being boosted twice. From this result we deduce the tranformation of operators,

$$\mathcal{B}(t)\mathcal{O}(\mathbf{k})\mathcal{B}^{-1}(t) = \mathcal{O}(\mathbf{K}_t). \tag{2.40}$$

In order to transform the SBEs, we first note that the derivative of the boost operator is[1]

$$\dot{\mathcal{B}}(t) = e\mathcal{B}(t)\mathbf{F}(t)\cdot\nabla_{\mathbf{k}}, \tag{2.41}$$

and thus

$$\begin{aligned}\partial_t\rho_{nm}(\mathbf{K},t) &= \partial_t\mathcal{B}(t)\rho_{nm}(\mathbf{k},t)\\ &= \mathcal{B}(t)\partial_t\rho_{nm}(\mathbf{k},t) + e\mathcal{B}(t)\mathbf{F}(t)\cdot\nabla_{\mathbf{k}}\rho_{nm}(\mathbf{k},t).\end{aligned} \tag{2.42}$$

Inserting the RHS of Eq. (2.32), we have (suppressing explicit time-dependence of $\mathcal{B}$)

$$\begin{aligned}\partial_t\rho_{nm}(\mathbf{K},t) =& -i\mathcal{B}\left[\varepsilon_{nm}(\mathbf{k}) - e\mathbf{F}(t)\cdot\boldsymbol{\mathcal{A}}_{nm}(\mathbf{k})\right]\rho_{nm}(\mathbf{k},t)\\ &+ ie\mathcal{B}\left[\Omega(\mathbf{k},t),\rho(\mathbf{k},t)\right]_{nm}\\ =& -i\left[\varepsilon_{nm}(\mathbf{K}_t) - e\mathbf{F}(t)\cdot\boldsymbol{\mathcal{A}}_{nm}(\mathbf{K}_t)\right]\mathcal{B}\rho_{nm}(\mathbf{k},t)\\ &+ ie\sum_{\mu}\left[\Omega_{n\mu}(\mathbf{K}_t,t)\mathcal{B}\rho_{\mu m}(\mathbf{k},t) - \Omega_{\mu n}(\mathbf{K}_t,t)\mathcal{B}\rho_{\mu m}(\mathbf{k},t)\right].\end{aligned} \tag{2.43}$$

Recognizing that $\mathcal{B}\rho_{nm}(\mathbf{k},t) = \rho_{nm}(\mathbf{K},t)$ simply transforms the density matrix elements to the comoving frame, we obtain

$$\begin{aligned}\partial_t\rho_{nm}(\mathbf{K},t) =& -i\left[\varepsilon_{nm}(\mathbf{K}_t) - e\mathbf{F}(t)\cdot\boldsymbol{\mathcal{A}}_{nm}(\mathbf{K}_t)\right]\rho_{nm}(\mathbf{K},t)\\ &+ ie\left[\Omega(\mathbf{K}_t,t),\rho(\mathbf{K},t)\right]_{nm}.\end{aligned} \tag{2.44}$$

By removing the gradient term, the frame transformation yields SBEs that are decoupled for all $\mathbf{K}$-points. The price paid is that the structural quantities on the RHS of Eq. (2.44) must be evaluated at the time-dependent momenta. If the band structure is known analytically this poses no difficulty; however, numerically calculated band structure must be interpolated from an initial calculation on a static k-mesh. Despite this complication, we prefer to work in the comoving frame as it generally leads to superior convergence of numerical simulations.

2.2 Calculating observables

The SBEs can be integrated numerically to calculate the time-dependent density matrix in response to an exciting optical pulse. We can then calculate observables such as the band occupations and the induced current, which are required to study the HHG spectrum.

[1]Note that $[\mathcal{B},\nabla_{\mathbf{k}}] = 0$ since $\dot{\mathbf{k}} = e\mathbf{F}$ is independent of $\mathbf{k}$ in the dipole approximation.

The macroscopic current is given by [30, 37, 48]

$$\mathbf{j}(t) = \int d\mathbf{k} \mathrm{Tr}\left[\mathbf{j}\rho(\mathbf{k},t)\right], \tag{2.45}$$

where $\mathbf{j}$ is the current operator and the trace is over the full set of Bloch states. In atomic units the current operator is $\mathbf{j} = e\mathbf{p}$, and the total current can be evaluated in terms of the momentum matrix elements as

$$\begin{aligned}\mathbf{j}(t) &= \sum_n \int d\mathbf{k} \langle \Phi_{n,\mathbf{k}} | \mathbf{p}\rho(\mathbf{k},t) | \Phi_{n,\mathbf{k}} \rangle \\ &= \sum_{m,n} \int d\mathbf{k} \mathbf{p}_{nm}(\mathbf{k}) \rho_{mn}(\mathbf{k},t).\end{aligned} \tag{2.46}$$

Further, using the relation [51]

$$\mathbf{p}_{nm}(\mathbf{k}) = i\varepsilon_{nm}(\mathbf{k})\mathbf{d}_{nm}(\mathbf{k}), \tag{2.47}$$

between dipole and momentum matrix elements, we obtain

$$\mathbf{j}(t) = \sum_n \int d\mathbf{k} \mathbf{p}_{nn}(\mathbf{k}) \rho_{nn}(\mathbf{k},t) + i \sum_{n \neq m} \int d\mathbf{k} \varepsilon_{nm}(\mathbf{k}) \mathbf{d}_{nm} \rho_{mn}(\mathbf{k},t). \tag{2.48}$$

While this expression is correct, we can gain more physical insight by evaluating the current using the position operator.

Noting that $\hbar = 1$ and $\mathbf{p} = \dot{\mathbf{x}}$ in atomic units, we can write the current operator as

$$\mathbf{j} = e\dot{\mathbf{x}} = -ie\left[\mathbf{x}, H(t)\right] = e\left[\mathbf{D}, H(t)\right], \tag{2.49}$$

and the macroscopic current is thus

$$\begin{aligned}\mathbf{j}(t) &= e \int d\mathbf{k} \mathrm{Tr}\left\{\left[\mathbf{D}, H(t)\right] \rho(\mathbf{k},t)\right\} \\ &= e \int d\mathbf{k} \mathrm{Tr}\left\{\left[\mathbf{D}^{\mathrm{ra}}, H(t)\right] \rho(\mathbf{k},t)\right\} + e \int d\mathbf{k} \mathrm{Tr}\left\{\left[\mathbf{D}^{\mathrm{er}}, H(t)\right] \rho(\mathbf{k},t)\right\}.\end{aligned} \tag{2.50}$$

Replacing $H(t)$ in the first term with

$$\begin{aligned} H(t) &= H_0 - e\mathbf{F}(t)\cdot\mathbf{x} \\ &= H_0 - ie\mathbf{F}(t)\cdot\mathbf{D}^{\mathrm{ra}} - ie\mathbf{F}(t)\cdot\mathbf{D}^{\mathrm{er}}, \end{aligned} \tag{2.51}$$

we can separate the current into four distinct contributions,

$$\mathbf{j}(t) = \mathbf{j}_{\mathrm{ra}}(t) + \mathbf{j}_{\mathrm{an}}(t) + \mathbf{j}_{\mathrm{mix}}(t) + \mathbf{j}_{\mathrm{pol}}(t), \tag{2.52}$$

where

$$\mathbf{j}_{\mathrm{ra}}(t) = e\int d\mathbf{k}\mathrm{Tr}\left\{\left[\mathbf{D}^{\mathrm{ra}}, H_0\right]\rho(\mathbf{k},t)\right\} \tag{2.53a}$$

$$\mathbf{j}_{\mathrm{an}}(t) = -ie^2\int d\mathbf{k}\mathrm{Tr}\left\{\left[\mathbf{D}^{\mathrm{ra}}, \mathbf{F}(t)\cdot\mathbf{D}^{\mathrm{ra}}\right]\rho(\mathbf{k},t)\right\} \tag{2.53b}$$

$$\mathbf{j}_{\mathrm{mix}}(t) = -ie^2\int d\mathbf{k}\mathrm{Tr}\left\{\left[\mathbf{D}^{\mathrm{ra}}, \mathbf{F}(t)\cdot\mathbf{D}^{\mathrm{er}}\right]\rho(\mathbf{k},t)\right\} \tag{2.53c}$$

$$\mathbf{j}_{\mathrm{pol}}(t) = e\int d\mathbf{k}\mathrm{Tr}\left\{\left[\mathbf{D}^{\mathrm{er}}, H(t)\right]\rho(\mathbf{k},t)\right\}, \tag{2.53d}$$

and the significance of the subscripts will be clarified as we evaluate each commutator.

The intraband current is simply

$$\mathbf{j}_{\mathrm{ra}}(t) = e\sum_n\int d\mathbf{k}\mathbf{v}_n(\mathbf{k})\rho_{nn}(\mathbf{k},t), \tag{2.54}$$

where $\mathbf{v}_n(\mathbf{k}) = \nabla_{\mathbf{k}}E_n(\mathbf{k})$ is the band velocity. Eq. (2.53b) gives an additional band-diagonal contribution, known as the anomalous current [36, 52]; given by

$$\begin{aligned} \mathbf{j}_{\mathrm{an}}(t) &= -i\int d\mathbf{k}\mathrm{Tr}\left\{\left[\mathbf{D}^{\mathrm{ra}}, \mathbf{F}(t)\cdot\mathbf{D}^{\mathrm{ra}}\right]\rho(\mathbf{k},t)\right\} \\ &= -i\sum_{n,a,b}\int d\mathbf{k}\left\{\mathbf{D}^{\mathrm{ra}}_{na,\mathbf{k}}\left[\mathbf{F}(t)\cdot\mathbf{D}^{\mathrm{ra}}_{ab,\mathbf{k}}\right] - \left[\mathbf{F}(t)\cdot\mathbf{D}^{\mathrm{ra}}_{na,\mathbf{k}}\right]\mathbf{D}^{\mathrm{ra}}_{ab,\mathbf{k}}\right\}\rho_{bn}(\mathbf{k},t) \\ &= -i\sum_{n}\int d\mathbf{k}\left\{\mathbf{D}^{\mathrm{ra}}_{nn,\mathbf{k}}\left[\mathbf{F}(t)\cdot\mathbf{D}^{\mathrm{ra}}_{nn,\mathbf{k}}\right] - \left[\mathbf{F}(t)\cdot\mathbf{D}^{\mathrm{ra}}_{nn,\mathbf{k}}\right]\mathbf{D}^{\mathrm{ra}}_{nn,\mathbf{k}}\right\}\rho_{nn}(\mathbf{k},t) \\ &= -i\sum_{n}\int d\mathbf{k}\left[\left(\nabla_{\mathbf{k}} - i\boldsymbol{\mathcal{A}}_n\right)\left(\mathbf{F}\cdot\nabla_{\mathbf{k}} - i\mathbf{F}\cdot\boldsymbol{\mathcal{A}}_n\right) - \left(\mathbf{F}\cdot\nabla_{\mathbf{k}} - i\mathbf{F}\cdot\boldsymbol{\mathcal{A}}_n\right)\left(\nabla_{\mathbf{k}} - i\boldsymbol{\mathcal{A}}_n\right)\right]\rho_{nn}(\mathbf{k},t), \end{aligned}$$

where we have suppressed explicit (k,t) dependence of terms in the square brackets. Since

$\partial_k \mathbf{F}(t) = 0$, there are only two non-vanishing terms

$$\begin{aligned}\mathbf{j}_{\mathrm{an}}(t) &= -\sum_n \int d\mathbf{k} \left[\nabla_{\mathbf{k}} \left(\mathbf{F}(t) \cdot \boldsymbol{\mathcal{A}}_n(\mathbf{k})\right) - \left(\mathbf{F}(t) \cdot \nabla_{\mathbf{k}}\right) \boldsymbol{\mathcal{A}}_n(\mathbf{k})\right] \rho_{nn}(\mathbf{k}, t) \\ &= -\sum_n \int d\mathbf{k} \left[\mathbf{F}(t) \times \boldsymbol{\Omega}_n(\mathbf{k})\right] \rho_{nn}(\mathbf{k}, t), \end{aligned} \tag{2.55}$$

where

$$\boldsymbol{\Omega}_n(\mathbf{k}) = \nabla_{\mathbf{k}} \times \boldsymbol{\mathcal{A}}_n(\mathbf{k}) \tag{2.56}$$

is the Berry curvature, which vanishes in centro-symmetric systems [52, 53]. Defining the matrix element

$$\mathbf{v}_n^a(\mathbf{k}, t) = \mathbf{F}(t) \cdot \boldsymbol{\Omega}_n(\mathbf{k}), \tag{2.57}$$

known as the anomalous velocity [52], the corresponding contribution to the current is

$$\mathbf{j}_{\mathrm{an}}(t) = -\sum_n \int d\mathbf{k} \mathbf{v}_n^a(\mathbf{k}, t) \rho_{nn}(\mathbf{k}, t). \tag{2.58}$$

The two remaining contributions to the total current; namely, $\mathbf{j}_{\mathrm{mix}}$ and $\mathbf{j}_{\mathrm{pol}}$, are interband currents. We first consider the polarization current

$$\begin{aligned}\mathbf{j}_{\mathrm{pol}}(t) &= e \int d\mathbf{k} \mathrm{Tr} \left\{\mathbf{D}^{\mathrm{er}} \left[H(t), \rho(\mathbf{k}, t)\right]\right\} \\ &= ie \int d\mathbf{k} \mathrm{Tr} \left[\mathbf{D}^{\mathrm{er}} \partial_t \rho(\mathbf{k}, t)\right] \\ &= ie \frac{d}{dt} \int d\mathbf{k} \mathrm{Tr} \left[\mathbf{D}^{\mathrm{er}} \rho(\mathbf{k}, t)\right], \end{aligned} \tag{2.59}$$

where we have used the cyclic invariance of the trace, as well as the equation of motion (2.24). We thus have

$$\begin{aligned}\mathbf{j}_{\mathrm{pol}}(t) &= ie \frac{d}{dt} \sum_{n \neq m} \int d\mathbf{k} \mathbf{D}^{\mathrm{er}}_{nm,\mathbf{k}} \rho_{mn}(\mathbf{k}, t) \\ &= \frac{d}{dt} \mathbf{p}_{er}(t), \end{aligned} \tag{2.60}$$

where

$$\mathbf{p}_{er}(t) = e \sum_{n \neq m} \int d\mathbf{k} \mathbf{d}_{nm}(\mathbf{k}) \rho_{mn}(\mathbf{k}, t) \tag{2.61}$$

is the interband polarization [21]. For the remaining interband contribution $\mathbf{j}_{\mathrm{mix}}$, the commutator

$[\mathbf{D}^{\mathrm{ra}}, \mathbf{F}(t)\cdot\mathbf{D}^{\mathrm{er}}]$ mixes the inter and intraband components of the covariant derivative. This interband "mixture" current [36] is evaluated as

$$\begin{aligned}\mathbf{j}_{\mathrm{mix}}(t) &= -i\int d\mathbf{k}\mathrm{Tr}\left\{[\mathbf{D}^{\mathrm{ra}}, \mathbf{F}(t)\cdot\mathbf{D}^{\mathrm{er}}]\,\rho(\mathbf{k},t)\right\}\\ &= -i\sum_{n,m}\int d\mathbf{k}\,[\mathbf{D}^{\mathrm{ra}}, \mathbf{F}(t)\cdot\mathbf{D}^{\mathrm{er}}]_{nm}\,\rho_{mn}(\mathbf{k},t)\\ &= -\sum_{n,m}\int d\mathbf{k}\,[\mathbf{D}^{\mathrm{ra}}, \Omega(\mathbf{k},t)]_{nm}\,\rho_{mn}(\mathbf{k},t),\end{aligned} \tag{2.62}$$

where we recall that $\Omega_{nm}(\mathbf{k},t) = \mathbf{F}(t)\cdot\mathbf{d}_{nm}(\mathbf{k})$ is the Rabi frequency [2]. Defining the matrix element

$$\begin{aligned}\mathbf{W}_{nm}(\mathbf{k},t) &= [\mathbf{D}^{\mathrm{ra}}, \Omega(\mathbf{k},t)]_{nm}\\ &= [\nabla_{\mathbf{k}} - i\boldsymbol{\mathcal{A}}_{nm}(\mathbf{k})]\,\Omega_{nm}(\mathbf{k},t)\\ &\equiv \boldsymbol{\mathcal{D}}_{\mathbf{k}}\Omega_{nm}(\mathbf{k},t),\end{aligned} \tag{2.63}$$

which is known as the generalized derivative [37, 46] of the Rabi frequency, the mixture current is

$$\mathbf{j}_{\mathrm{mix}}(t) = -\sum_{n,m}\int d\mathbf{k}\mathbf{W}_{nm}(\mathbf{k},t)\rho_{mn}(\mathbf{k},t). \tag{2.64}$$

The intraband current (2.54) and the interband polarization current (2.60) have been used extensively in the study of HHG in solids [11–13, 16, 24, 30, 34, 54]. In contrast, the mixture current (2.64) has only been explored recently in the context of HHG [36, 39], even though it had been identified in prior work [37, 46]. In a sense, $\mathbf{j}_{\mathrm{mix}}$ can be interpreted as the interband counterpart of the anomalous intraband current, as both contributions arise from the coupling of Bloch states with time-dependent crystal momentum driven by an external field [36]. In fact, it is clear from Eqs. (2.53b) and (2.53c) that the matrix elements $\mathbf{v}_n^a$ and $\mathbf{W}_{nm}$ vanish entirely in the absence of a driving field; in contrast to $\mathbf{v}_n$ and $\mathbf{d}_{nm}$, which enter the "non-anomalous" currents. Further, since the mixture current is directly proportional to the field strength via the Rabi frequency in Eq. (2.63), the overall magnitude of $\mathbf{j}_{\mathrm{mix}}(t)$ is likely to be smaller than the polarization current, unless $\mathbf{W}_{nm}$ achieves very large values. However, high harmonics are typically orders of magnitude weaker than the fundemental, and the influence of the mixture current on the HHG spectrum is not as obvious. Finally, we note that $\mathbf{W}_{nm}$ is non-vanishing

[2] Note that the Berry curvature $\boldsymbol{\Omega}_n = \nabla_{\mathbf{k}}\times\boldsymbol{\mathcal{A}}_n$ is a vector field involving a single band, while the Rabi frequency $\Omega_{nm}(\mathbf{k},t) = \mathbf{F}(t)\cdot\mathbf{d}_{nm}(\mathbf{k})$ is a scalar field involving two band indices.

even in centrosymmetric crystals, in contrast to the anomalous velocity.

2.2.1 Observables in comoving frame

To obtain expressions for the total current in the comoving frame, we start from the microscopic current

$$\mathrm{Tr}\left[\mathbf{j}\rho(t)\right] = \sum_n \langle \Phi_{n,\mathbf{k}} | \mathbf{j}\rho(t) | \Phi_{n,\mathbf{k}} \rangle, \tag{2.65}$$

and insert the boost operator to get

$$\begin{aligned}
\mathrm{Tr}\left[\mathbf{j}\rho(t)\right] &= \mathcal{B}\sum_n \langle \Phi_{n,\mathbf{k}} | \mathbf{j}\rho(t) | \Phi_{n,\mathbf{k}} \rangle \\
&= \sum_n \langle \Phi_{n,\mathbf{K}_t} | \left(\mathcal{B}\mathbf{j}\mathcal{B}^{-1}\right)\left(\mathcal{B}\rho(t)\mathcal{B}^{-1}\right) | \Phi_{n,\mathbf{K}_t} \rangle \\
&= \sum_{m,n} \mathbf{j}_{nm}(\mathbf{K}_t)\rho_{mn}(\mathbf{K},t),
\end{aligned} \tag{2.66}$$

where we have used the transformation (2.40). The macroscopic current is then given by

$$\mathbf{j}(t) = \sum_{m,n} \int_{\overline{BZ}} d\mathbf{K} \mathbf{j}_{nm}(\mathbf{K}_t)\rho_{mn}(\mathbf{K},t), \tag{2.67}$$

where $\overline{BZ}$ denotes the Brillouin zone in the comoving frame. Clearly, the end result of boosting to the comoving frame is to replace

$$\begin{aligned}
\int_{BZ} d\mathbf{k} &\to \int_{\overline{BZ}} d\mathbf{K} \\
\rho(\mathbf{k},t) &\to \rho(\mathbf{K},t),
\end{aligned}$$

while structural matrix elements are evaluated at the time-dependent momentum; i.e.

$$\mathcal{O}_{nm}(\mathbf{k}) \to \mathcal{O}_{nm}(\mathbf{K}_t).$$

The contributions to the current in the comoving frame are thus

$$\mathbf{j}_{\mathrm{ra}}(t) = e\sum_n \int_{\overline{BZ}} d\mathbf{K}\mathbf{v}_n(\mathbf{K}_t)\rho_{nn}(\mathbf{K},t) \tag{2.68a}$$

$$\mathbf{j}_{\mathrm{an}}(t) = -\sum_n \int_{\overline{BZ}} d\mathbf{K}\mathbf{v}^a_n(\mathbf{K}_t,t)\rho_{nn}(\mathbf{K},t) \tag{2.68b}$$

$$\mathbf{j}_{\mathrm{mix}}(t) = -\sum_{n,m} \int_{\overline{BZ}} d\mathbf{K}\mathbf{W}_{nm}(\mathbf{K}_t,t)\rho_{mn}(\mathbf{K},t) \tag{2.68c}$$

$$\mathbf{j}_{\mathrm{pol}}(t) = e\frac{d}{dt}\sum_{n\neq m} \int_{\overline{BZ}} d\mathbf{K}\mathbf{d}_{nm}(\mathbf{K}_t)\rho_{mn}(\mathbf{K},t). \tag{2.68d}$$

2.3 $U(1)$ gauge symmetry in a periodic solid

Quite generally, a gauge theory [40] is described by a gauge group G, and the property that observables are invariant under gauge transformations $\psi \to g\psi$, for any $g \in G$. Further, an operator $\mathcal{O}$ is described as gauge covariant if it transforms as $\mathcal{O} \to g\mathcal{O}g^{-1}$. In a periodic solid, observables are invariant under phase transformations of the Bloch states [31, 41, 49]

$$|u_{m,\mathbf{k}}\rangle \to |\tilde{u}_{m,\mathbf{k}}\rangle = e^{-i\chi_m(\mathbf{k})}|u_{m,\mathbf{k}}\rangle, \tag{2.69}$$

where $\chi_m(\mathbf{k}) \in \mathbb{R}$ satisfies the lattice periodicity, and is referred to as a gauge function. This transformation belongs to the gauge group $U(1)$ of phase rotations, and the theory is termed "local" in k-space since $\nabla_{\mathbf{k}}\chi_m(\mathbf{k}) \neq 0$. Although the transformation 2.69 is applied to the cell-periodic functions, the transformation of Bloch functions is equivalent; i.e. $|\tilde{\Phi}_{m,\mathbf{k}}\rangle = e^{-i\chi_m(\mathbf{k})}|\Phi_{m,\mathbf{k}}\rangle$. Next we examine the transformation properties of the various quantities appearing in the SBEs and the observables.

The band energies are clearly gauge invariant, since

$$\langle\tilde{\Phi}_{n,\mathbf{k}}|H_0|\tilde{\Phi}_{m,\mathbf{k}}\rangle = E_n(\mathbf{k})e^{i\chi_{nm}(\mathbf{k})}\langle\Phi_{n,\mathbf{k}}|\Phi_{m,\mathbf{k}}\rangle = E_n(\mathbf{k})\delta_{nm}, \tag{2.70}$$

where we have defined the difference of gauge functions

$$\chi_{nm}(\mathbf{k}) \equiv \chi_n(\mathbf{k}) - \chi_m(\mathbf{k}). \tag{2.71}$$

In contrast, the density matrix elements are covariant since they transform as

$$\begin{aligned}\tilde{\rho}_{nm}(\mathbf{k},t) &= \langle\tilde{\Phi}_{n,\mathbf{k}}|\rho(t)|\tilde{\Phi}_{m,\mathbf{k}}\rangle \\ &= e^{i\chi_{nm}(\mathbf{k})}\rho_{nm}(\mathbf{k},t),\end{aligned} \tag{2.72}$$

and we remark that the diagonal elements (band occupations) are gauge invariant. The TDM transforms as

$$\begin{aligned}\tilde{\mathbf{d}}_{nm}(\mathbf{k}) &= (1-\delta_{nm})\langle\tilde{u}_{n,\mathbf{k}}|i\nabla_{\mathbf{k}}|\tilde{u}_{m,\mathbf{k}}\rangle \\ &= (1-\delta_{nm})e^{i\chi_n(\mathbf{k})}\langle u_{n,\mathbf{k}}|i\nabla_{\mathbf{k}}|e^{-i\chi_m(\mathbf{k})}u_{m,\mathbf{k}}\rangle \\ &= e^{i\chi_{nm}(\mathbf{k})}\mathbf{d}_{nm}(\mathbf{k}),\end{aligned} \tag{2.73}$$

which is identical to the transformation of the density matrix. In contrast, the Berry connections transform as

$$\begin{aligned}\tilde{\boldsymbol{\mathcal{A}}}_n(\mathbf{k}) &= \langle\tilde{u}_{n,\mathbf{k}}|i\nabla_{\mathbf{k}}|\tilde{u}_{n,\mathbf{k}}\rangle \\ &= e^{i\chi_n(\mathbf{k})}\langle u_{n,\mathbf{k}}|i\nabla_{\mathbf{k}}e^{-i\chi_n(\mathbf{k})}|u_{n,\mathbf{k}}\rangle \\ &= \boldsymbol{\mathcal{A}}_n(\mathbf{k}) + \nabla_{\mathbf{k}}\chi_n(\mathbf{k}),\end{aligned} \tag{2.74}$$

which is not covariant due to the gradient term. This result also shows that the Berry curvature $\boldsymbol{\Omega}_n(\mathbf{k}) = \nabla_{\mathbf{k}} \times \boldsymbol{\mathcal{A}}_n(\mathbf{k})$ is gauge invariant, since the curl of a gradient is always zero.

It is also interesting to consider a gauge transformation of the covariant derivative,

$$\begin{aligned}e^{i\chi_m}\mathbf{D}_{mn,\mathbf{k}}e^{-i\chi_n} &= e^{i\chi_m}\left(\nabla_{\mathbf{k}}\delta_{mn} - i\boldsymbol{\xi}_{mn}\right)e^{-i\chi_n} \\ &= e^{i\chi_m}\left[\left(\nabla_{\mathbf{k}} - \boldsymbol{\mathcal{A}}_n\right)\delta_{mn} - i\mathbf{d}_{mn}\right]e^{-i\chi_n} \\ &= \left\{\left[\nabla_{\mathbf{k}} - i\left(\boldsymbol{\mathcal{A}}_n + \nabla_{\mathbf{k}}\right)\chi_n\right]\delta_{mn} - ie^{i\chi_m}\mathbf{d}_{mn}e^{-i\chi_n}\right\} \\ &= \left(\nabla_{\mathbf{k}} - i\tilde{\boldsymbol{\mathcal{A}}}_n\chi_n\right)\delta_{mn} - i\tilde{\mathbf{d}}_{mn} \\ &= \nabla_{\mathbf{k}}\delta_{mn} - i\tilde{\boldsymbol{\xi}}_{mn} \\ &= \tilde{\mathbf{D}}_{mn,\mathbf{k}},\end{aligned} \tag{2.75}$$

which is indeed a covariant transformation, as expected. Clearly the covariant derivative has the same form in any gauge, which is ensured by the non-trivial transformation of the Berry connections. That is, the Berry connection acts as a gauge field whose transformation (2.74) cancels the gauge-dependence of the gradient operator; making the overall transformation

(2.75) covariant. This is directly analogous to the role of the vector potential in quantum electrodynamics, which is a $U(1)$ gauge theory in real space [40]. In that case, the covariant derivative is $D_\mu = \partial_\mu - iA_\mu(\mathbf{x},t)$, with $A_\mu(\mathbf{x},t)$ a component of the electromagnetic vector potential. Even though the gauge fields $\boldsymbol{\mathcal{A}}_n$ and and $\mathbf{A}$ are not physical fields, their curls are gauge invariant. Indeed, the Berry curvature in a periodic solid is analogous to the magnetic field $\mathbf{B} = \nabla \times \mathbf{A}$ [52, 53].

In addition to simplifying derivations, formulating the SBEs in terms of the covariant derivative also helps to clarify the gauge structure of the SBEs. To demonstrate that the SBEs are gauge covariant, we simply transform both sides of Eq. (2.28) according to

$$\begin{aligned}
\left[\partial_t + i\varepsilon_{nm}(\mathbf{k})\right] e^{i\chi_n}\rho_{nm}(\mathbf{k},t)e^{-i\chi_m} =& e\mathbf{F}(t)\cdot e^{i\chi_n}\left[\mathbf{D},\rho(\mathbf{k},t)\right]_{nm} e^{-i\chi_m} \\
=& e\mathbf{F}(t)\cdot e^{i\chi_n}\sum_\mu \left[\mathbf{D}_{n\mu,\mathbf{k}}\rho_{\mu m}(\mathbf{k},t) - \rho_{n\mu}(\mathbf{k},t)\mathbf{D}_{\mu m,\mathbf{k}}\right] e^{-i\chi_m} \\
=& e\mathbf{F}(t)\cdot \sum_\mu \Big[e^{i\chi_n}\mathbf{D}_{n\mu,\mathbf{k}}e^{-i\chi_\mu}e^{i\chi_\mu}\rho_{\mu m}(\mathbf{k},t) \\
& -e^{i\chi_n}\rho_{n\mu}(\mathbf{k},t)e^{-i\chi_\mu}e^{i\chi_\mu}\mathbf{D}_{\mu m,\mathbf{k}}e^{-i\chi_m}\Big] . \qquad (2.76)
\end{aligned}$$

Using the transformation (2.75) for the covariant derivative and (2.72) for the density matrix, this simplifies to

$$\left[\partial_t + i\varepsilon_{nm}(\mathbf{k})\right]\tilde{\rho}_{nm}(\mathbf{k},t) = e\mathbf{F}(t)\cdot\sum_\mu\left[\tilde{\mathbf{D}},\tilde{\rho}(\mathbf{k},t)\right]_{nm} . \qquad (2.77)$$

This shows that the SBEs have the same form in the transformed gauge, with ρ_{nm} and $\mathbf{D}_{nm}$ replaced by their respective transformations. A similar result was derived in Ref. [31] by explicitly transforming the density matrix elements, TDM, and Berry connections appearing in Eq. (2.32). Here we observe that the gauge symmetry can be derived more succintly when the SBEs are formulated in terms of the covariant derivative. We emphasize that the gauge-dependent phases do not cancel when the SBEs are transformed; rather, they are absorbed by the transformation of the covariant quantities ρ and $\mathbf{D}$. We interpret this result to mean the SBEs are themselves gauge covariant, since both sides of Eqs. (2.28) and (2.77) differ by a phase factor $e^{i\chi_{nm}(\mathbf{k})}$. By contrast, we will see that observable quantities such as the current are gauge invariant, since gauge dependent phases cancel identically.

The intraband contributions to the current (2.54) and (2.58) involve only gauge invariant quantities, so their transformations are trivial. The interband currents are more interesting since they contain gauge dependent matrix elements. Using Eqs. (2.72) and (2.73) in (2.48), we can

transform the total interband current

$$\begin{aligned}\mathbf{j}_{\mathrm{er}}(t) &\to i\sum_{m\neq n}\int d\mathbf{k}\varepsilon_{nm}(\mathbf{k})\tilde{\mathbf{d}}_{nm}(\mathbf{k})\tilde{\rho}_{mn}(\mathbf{k},t)\\ &= i\sum_{m\neq n}\int d\mathbf{k}\varepsilon_{nm}(\mathbf{k})\left[e^{i\chi_{nm}}\mathbf{d}_{nm}(\mathbf{k})\right]\left[e^{i\chi_{mn}}\rho_{mn}(\mathbf{k},t)\right]\\ &= \mathbf{j}_{\mathrm{er}}(t),\end{aligned} \tag{2.78}$$

which is clearly gauge invariant since the phase factors cancel. Indeed, this result shows that the gauge covariance of the TDM and density matrix ensure the gauge invariance of the total current.

The transformation of the polarization current (2.60) is similar; however, the interband mixture current is more subtle. By inspection of Eqs. (2.72) and (2.64), we can immediately surmise that $\mathbf{W}_{nm}$ must be covariant in order to cancel the gauge dependence of the density matrix; otherwise the mixture current would not be gauge invariant. However, it is worthwhile to clarify the gauge dependence of the matrix elements $\mathbf{W}_{nm}$, and therewith the gauge dependence of the generalized derivative. Explicitly, for a gauge transformation (2.69) we calculate

$$\begin{aligned}\boldsymbol{\mathcal{D}}_{\mathbf{k}}\mathcal{O}_{nm} \to&\langle\tilde{\Phi}_{n,\mathbf{k}}|\left[\mathbf{D}^{\mathrm{ra}},\mathcal{O}\right]|\tilde{\Phi}_{m,\mathbf{k}}\rangle\\ \to&e^{i\chi_n}\langle\Phi_{n,\mathbf{k}}|\left[\mathbf{D}^{\mathrm{ra}},\mathcal{O}\right]e^{-i\chi_m}|\Phi_{m,\mathbf{k}}\rangle\\ \to&ie^{i\chi_n}\sum_{\lambda}\langle\Phi_{n,\mathbf{k}}|\mathbf{D}^{\mathrm{ra}}|\Phi_{\lambda,\mathbf{k}}\rangle\langle\Phi_{\lambda,\mathbf{k}}|\mathcal{O}|\Phi_m\rangle e^{-i\chi_m}\\ &-e^{i\chi_n}\sum_{\lambda}\langle\Phi_{n,\mathbf{k}}|\mathcal{O}|\Phi_{\lambda,\mathbf{k}}\rangle\langle\Phi_{\lambda,\mathbf{k}}|\mathbf{D}^{\mathrm{ra}}|\Phi_m\rangle e^{-i\chi_m}\\ \to&-ie^{i\chi_{nm}}\left[i\nabla_{\mathbf{k}}+\boldsymbol{\mathcal{A}}_n-i\left(\nabla_{\mathbf{k}}\chi_m\right)\right]\mathcal{O}_{nm}\\ &+ie^{i\chi_{nm}}\mathcal{O}_{nm}\left(\boldsymbol{\mathcal{A}}_m-i\nabla_{\mathbf{k}}\chi_m\right),\end{aligned} \tag{2.79}$$

where we have assumed $[\mathcal{O}_{nm}(\mathbf{k}),\chi_m(\mathbf{k})]=0$; i.e. that $\mathcal{O}(\mathbf{k})$ does not contain derivatives, and is thus covariant [3]. The gradients of the gauge function cancel, leaving

$$\boldsymbol{\mathcal{D}}_{\mathbf{k}}\mathcal{O}_{nm}(\mathbf{k})\to e^{i\chi_{nm}(\mathbf{k})}\boldsymbol{\mathcal{D}}_{\mathbf{k}}\mathcal{O}_{nm}(\mathbf{k}), \tag{2.80}$$

as expected. Not only does this general result verify the gauge invariance of the overall theory, but it also instructs us how to perform gauge transformations of the matrix elements $\mathbf{W}_{nm}$

[3] another approach for transforming the generalized derivative is to assume $\mathcal{O}(\mathbf{k})$ is covariant, and apply the relevant transformations to $\boldsymbol{\mathcal{A}}_{nm}(\mathbf{k})$ and $\mathcal{O}(\mathbf{k})$ in the RHS of $\boldsymbol{\mathcal{D}}_{\mathbf{k}}\mathcal{O}_{nm}(\mathbf{k})=(\nabla_{\mathbf{k}}-i\boldsymbol{\mathcal{A}}_{nm})$.

directly. This will be helpful when we consider gauge transformations of band structure, since the transformation (2.80) makes it unnecessary to recalculate the generalized derivatives of the TDM explicitly in the transformed gauge.

2.3.1 Gauge transformations in comoving frame

While gauge transformations are typically considered in the static momentum frame, it is worthwhile to clarify the gauge dependence of matrix elements in the comoving frame. The correct forms of the various gauge transformations might be intuitively obvious, but they can be derived explicitly using the boost operator. For example, applying the boost operator to Eq. (2.72) gives

$$\begin{aligned}\tilde{\rho}_{nm}(\mathbf{K},t) &= \mathcal{B}(t)\tilde{\rho}_{nm}(\mathbf{k},t)\\ &= \mathcal{B}(t)e^{i\chi_{nm}(\mathbf{k})}\rho_{nm}(\mathbf{k},t)\\ &= e^{i\chi_{nm}(\mathbf{K}_t)}\rho_{nm}(\mathbf{K},t),\end{aligned} \tag{2.81}$$

while the Berry connection transforms as

$$\begin{aligned}\tilde{\boldsymbol{\mathcal{A}}}_n(\mathbf{K}_t) &= \mathcal{B}(t)\tilde{\boldsymbol{\mathcal{A}}}_n(\mathbf{k})\\ &= \mathcal{B}(t)\left[\boldsymbol{\mathcal{A}}_n(\mathbf{k}) + \nabla_{\mathbf{k}}\chi_n(\mathbf{k})\right]\\ &= \boldsymbol{\mathcal{A}}_n(\mathbf{K}_t) + \nabla_{\mathbf{k}}\chi_n(\mathbf{k})|_{\mathbf{k}=\mathbf{K}_t}\,.\end{aligned} \tag{2.82}$$

Overall, we observe that in order to obtain the correct gauge transformation relations in the comoving frame, one simply replaces $\mathbf{k} \to \mathbf{K}_t$ in all k-dependent quantities. One can also insert these transformations into the SBEs to verify that they ensure gauge covariance of the SBEs in the comoving frame.

2.4 Summary

In this chapter we have reviewed the derivation of the single particle SBEs used to model strong field light-matter interactions in the length gauge. We have also discussed and clarified the $U(1)$ gauge structure of the SBEs, as well as the gauge transformation relations of the relevant operators and matrix elements. An advantage of formulating the SBEs in terms of the covariant derivative is that this approach elucidates the overall gauge covariance of the SBEs, in addition to simplifying derivations. In the remaining chapters we use the SBEs to study HHG phenomena in solids, and the gauge symmetry will be a recurring theme.

Chapter 3
Gauge smoothing for gapped graphene

In order to study the mechanisms shaping HHG in solids, we seek a model system where all the required matrix elements can be calculated in a smooth and periodic gauge. Tight-binding models can be diagonalized analytically, which leads to closed form expressions for the matrix elements with well-defined phases throughout the BZ. Gapped graphene has been used extensively to model 2D materials [27, 34, 42], but analytic diagonalization generally leads to a gauge in which the Berry connections are singular. Here we develop an analytic gauge transformation to obtain a smooth and periodic gauge in gapped graphene. While the Berry connections have been derived previously in the non-smooth gauge, we also obtain analytic expressions for the generalized derivatives of the TDM components in gapped graphene. This allows the matrix elements (2.63) to be calculated, which are essential for studying the mixture current.

3.1 Dipole matrix elements in tight-binding models

Before specializing to the case of gapped graphene, we consider a general tight-binding Hamiltonian with matrix elements

$$H_{\alpha\beta}(\mathbf{k}) = \langle v_{\alpha,\mathbf{k}}|H_0|v_{\beta,\mathbf{k}}\rangle, \tag{3.1}$$

represented in a basis of orbital functions [55]

$$|v_{\alpha,\mathbf{k}}\rangle = \frac{1}{\sqrt{N}}\sum_{\mathbf{R}} e^{i\mathbf{k}\cdot\mathbf{R}}|v_{\alpha,\mathbf{R}}\rangle, \tag{3.2}$$

where N is the number of lattice sites, $|v_{\alpha,\mathbf{R}}\rangle$ is an atomic-like orbital centered at lattice site $\mathbf{R}$, and the quantum number α labels the orbital character. Following the notation of Ref. [55] the label α also represents the position of the orbital within a unit cell, which we do not distinguish explicitly. Eigenfunctions of this Hamiltonian are just the Bloch functions,

$$|u_{m,\mathbf{k}}\rangle = \sum_{\alpha} U_{\alpha m}(\mathbf{k})|v_{\alpha,\mathbf{k}}\rangle, \tag{3.3}$$

where U is a unitary matrix of eigenvector coefficients, and $U^\dagger HU$ is a diagonal matrix of band energies.

Evaluating the dipole matrix elements between Bloch states, we have

$$\begin{aligned}\boldsymbol{\xi}_{nm}(\mathbf{k}) &= \langle u_{n,\mathbf{k}}|i\nabla_{\mathbf{k}}|u_{m\mathbf{k}}\rangle \\ &= i\sum_{\alpha\beta} U^*_{\alpha n}(\mathbf{k})\langle v_{\alpha,\mathbf{k}}|\nabla_{\mathbf{k}} U_{\beta m}(\mathbf{k})|v_{\beta\mathbf{k}}\rangle \\ &= i\sum_{\alpha} U^*_{\alpha n}(\mathbf{k})\nabla_{\mathbf{k}} U_{\alpha m}(\mathbf{k}) + i\sum_{\alpha\beta} U^*_{\alpha n}(\mathbf{k})U_{\beta m}(\mathbf{k})\langle v_{\alpha,\mathbf{k}}|\nabla_{\mathbf{k}}|v_{\beta\mathbf{k}}\rangle. \end{aligned} \tag{3.4}$$

Assuming the orbitals have been orthogonalized, the second term is

$$\begin{aligned}\langle v_{\alpha,\mathbf{k}}|\nabla_{\mathbf{k}}|v_{\beta\mathbf{k}}\rangle &= \frac{1}{N}\sum_{\mathbf{R},\mathbf{R}'} e^{-i\mathbf{k}\cdot\mathbf{R}}\langle v_{\alpha,\mathbf{R}}|\nabla_{\mathbf{k}} e^{i\mathbf{k}\cdot\mathbf{R}'}|v_{\beta,\mathbf{R}'}\rangle \\ &= \frac{1}{N}\sum_{\mathbf{R},\mathbf{R}'} \mathbf{R}' e^{-i\mathbf{k}\cdot(\mathbf{R}-\mathbf{R}')}\delta_{\mathbf{R}\mathbf{R}'}\delta_{\alpha\beta} \\ &= \frac{\delta_{\alpha\beta}}{N}\sum_{\mathbf{R}} \mathbf{R} \\ &= 0, \end{aligned} \tag{3.5}$$

where the remaining sum vanishes since the summand has odd parity; i.e. for each lattice site $\mathbf{R}$, there is a corresponding lattice site $-\mathbf{R}$. As a result, the dipole matrix elements in the Bloch basis can be expressed solely in terms of the eigenvector coefficients

$$\begin{aligned}\boldsymbol{\xi}_{nm}(\mathbf{k}) &= i\sum_{\alpha} U^*_{\alpha n}(\mathbf{k})\nabla_{\mathbf{k}} U_{\alpha m}(\mathbf{k}) \\ &= i\left[U^\dagger(\mathbf{k})\nabla_{\mathbf{k}} U(\mathbf{k})\right]_{nm}. \end{aligned} \tag{3.6}$$

This calculation requires the matrix of eigenvectors $U(\mathbf{k})$ to be differentiable throughout the BZ. If the Hamiltonian matrix is diagonalized numerically, the resulting eigenvector phases will be ill-determined and a gauge-smoothing algorithm [33, 36, 41] must be used to eliminate random phase jumps between neighbouring k-points. Alternatively, if the Hamiltonian can be diagonalized analytically, it is possible to obtain closed-form expressions for the dipole matrix elements.

The eigenvalue equation,

$$H(\mathbf{k})|u_{m\mathbf{k}}\rangle = E_m(\mathbf{k})|u_{m,\mathbf{k}}\rangle, \tag{3.7}$$

for a system with N_b bands leads to the simultaneous equations

$$\sum_{\alpha=1}^{N_b} \left[H_{n\alpha}(\mathbf{k}) - \delta_{n\alpha}E_m(\mathbf{k})\right] U_{\alpha m}(\mathbf{k}) = 0; \quad n = 1, ..., N_b, \tag{3.8}$$

for the eigenvector coefficients. The band energies $E_m(\mathbf{k})$ and their derivatives can be obtained from numerical diagonalization. The eigenvector equations (3.8) can then be solved using computer algebra software [1], yielding expressions for the coefficients $U_{\alpha m}$ in terms of the Hamiltonian matrix elements and the band energies E_m. This avoids the need to evaluate the band energies analytically, which can be difficult for a multiband system. Of course, there are infinitely many possible solutions of Eq. (3.8) which differ by a k-dependent phase, and choosing a specific solution will fix the Bloch gauge of the eigenvectors. Throughout this thesis we restrict our attention to 2-band tight-binding models, where it is straightforward to obtain the eigenvalues and eigenvectors analytically.

3.2 Tight-binding model for gapped graphene

The honeycomb lattice for gapped graphene can be described by two triangular sublattices [57], with each sublattice comprised of a different atomic species. Including a single p_z-orbital for each atom and restricting the sum (3.2) to nearest neighbors, the Hamiltonian matrix for gapped graphene is [27, 42]

$$H(\mathbf{k}) = \begin{bmatrix} \Delta/2 & g(\mathbf{k}) \\ g^*(\mathbf{k}) & -\Delta/2 \end{bmatrix}, \tag{3.9}$$

where Δ is the difference of on-site energies, $g(\mathbf{k}) = \gamma f(\mathbf{k})$ with γ the hopping parameter, and

$$f(\mathbf{k}) = \exp\left(i\frac{ak_x}{\sqrt{3}}\right) + 2\exp\left(-i\frac{ak_x}{2\sqrt{3}}\right)\cos\left(\frac{ak_y}{2}\right), \tag{3.10}$$

is the structure function resulting from the nearest-neighbor sum for the lattice orientation shown in Fig. 3.1a. In our calculations we use numerical values of $a = 5.97$, $\gamma = -0.0184$, and $\Delta = 0.061$ in atomic units, which are chosen to approximate the minimum bandgap and bandwidth of monolayer MoS_2. The primitive reciprocal lattice vectors for this geometry can be

[1] For example, Wolfram Mathematica [56]

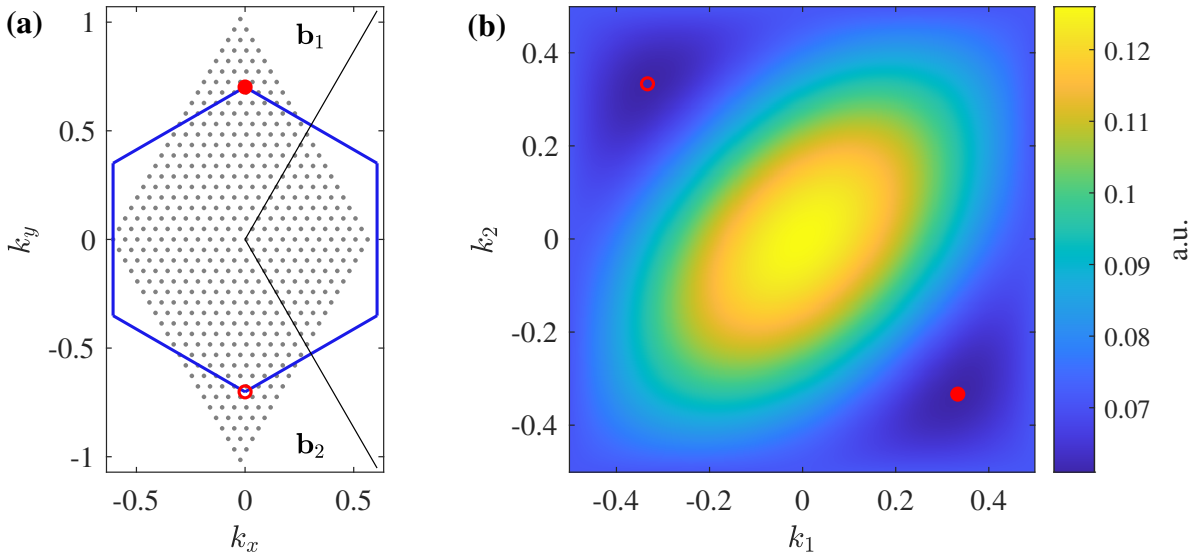

Figure 3.1: (a) Geometry of the reciprocal lattice for gapped graphene. The blue hexagon depicts the Brillouin zone, and black lines show the reciprocal lattice vectors. The discrete k-mesh in the primitive cell is illustrated, along with the $K(K')$ points depicted by full (open) circles. (b) Energy gap between conduction and valence band in the primitive basis, with K and K' points as indicated in (a).

written as a matrix of column vectors

$$B = \begin{bmatrix} \mathbf{b}_1 & \mathbf{b}_2 \end{bmatrix} = \frac{2\pi}{\sqrt{3}a} \begin{bmatrix} 1 & 1 \\ \sqrt{3} & -\sqrt{3} \end{bmatrix}, \tag{3.11}$$

and an arbitrary k-point in the primitive basis is written as

$$\mathbf{k} = k_1\mathbf{b}_1 + k_2\mathbf{b}_2, \tag{3.12}$$

where k_1 and k_2 are known as fractional coordinates. Transformations between Cartesian and primitive bases are described in App. E, and we note that

$$f(\mathbf{k}) = \exp\left(i\frac{2\pi k_+}{3}\right) + 2\exp\left(-i\frac{\pi k_+}{3}\right)\cos\left(\pi k_-\right), \tag{3.13}$$

where we have defined $k_\pm \equiv k_1 \pm k_2$. The function $f(\mathbf{k})$ vanishes at the K points, which correspond to the vertices of the hexagonal BZ as shown in Fig. 3.1a. Only two of these points are distinct; they are labeled K and K' and their locations are inverted about the origin as shown in Fig. 3.1. The remaining K and K' points are equivalent under rotations of $\pi/3$. Unless it is

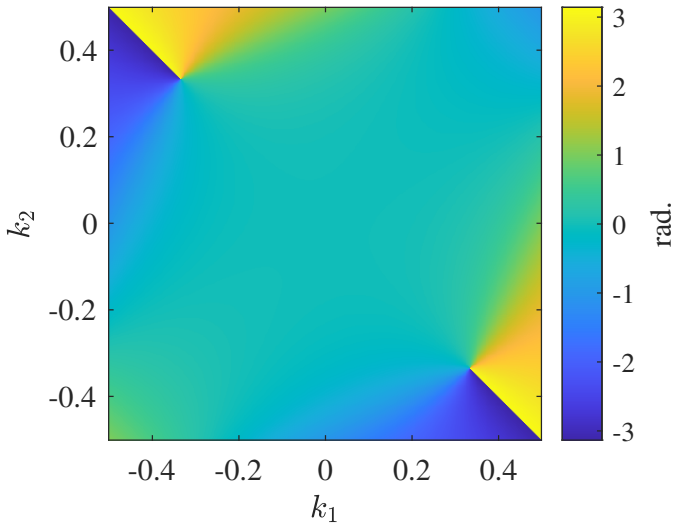

Figure 3.2: Phase factor $\phi(\mathbf{k}) = \arg[f(\mathbf{k})]$ for the gapped graphene model.

necessary to distinguish the K and K' points, we refer to them collectively as K points.

The Hamiltonian (3.9) can be diagonalized analytically, and the energy eigenvalues are $E_m(\mathbf{k}) = s_m\varepsilon(\mathbf{k})/2$, where $s_v = -1$ for the valence band and $s_c = 1$ for the conduction band, while the energy gap is

$$\varepsilon(\mathbf{k}) = 2\left[\left(\frac{\Delta}{2}\right)^2 + |g(\mathbf{k})|^2\right]^{1/2}. \tag{3.14}$$

The energy gap is plotted in Fig. 3.1b, which shows that ε is minimized at the K points and maximized at Γ (k=0). By inspection of Eq. (3.14), the minimum bandgap is Δ, while the maximum bandgap is $2\left[(\Delta/2)^2 + 9\gamma^2\right]^{1/2}$. The eigenvectors can be written as

$$|u^{\mathrm{TB}}_{m,\mathbf{k}}\rangle = \frac{1}{\sqrt{2}}\begin{bmatrix} (1 + s_m\Delta/E_g)^{1/2} \\ s_m e^{-i\phi(\mathbf{k})}\,(1 - s_m\Delta/E_g)^{1/2} \end{bmatrix}, \tag{3.15}$$

where we have defined the phase $\phi(\mathbf{k}) \equiv \arg[f(\mathbf{k})]$. The eigenvectors (3.15) are calculated in a particular Bloch gauge where the first component is chosen to be real, but we note that the phase difference between eigenvector components is clearly $\phi(\mathbf{k})$ in any gauge. We refer to the specific eigenvectors in Eq. (3.15) as the tight-binding (TB) gauge. Fig. 3.2 shows the behaviour of $\phi(\mathbf{k})$ throughout the BZ, and there is an obvious phase singularity at the K points. This ultimately leads to non-smooth behaviour of the Berry connections in the TB gauge, which we will discuss in the next section.

3.2.1 Berry connections and TDM in TB gauge

Using Eq. (3.15) for the Bloch eigenvectors, the Berry connections are given by

$$\begin{aligned}\boldsymbol{\mathcal{A}}_n^{\mathrm{TB}}(\mathbf{k}) &= \langle u_{n,\mathbf{k}}^{\mathrm{TB}} | i\nabla_{\mathbf{k}} | u_{n,\mathbf{k}}^{\mathrm{TB}} \rangle \\ &= \frac{1}{2}\left[1 - \frac{s_n\Delta}{\varepsilon(\mathbf{k})}\right]\nabla_{\mathbf{k}}\phi(\mathbf{k}),\end{aligned} \tag{3.16}$$

where $s_v = -1$ for the valence band and $s_c = 1$ for the conduction band. Working in the primitive basis, the individual components are

$$\begin{aligned}\mathcal{A}_{n,1}^{\mathrm{TB}} &= \frac{a^2}{8\pi|f|^2}\left(1 - \frac{s_n\Delta}{E_g}\right)(\cos 2\pi k_2 - \cos 2\pi k_-) \\ \mathcal{A}_{n,2}^{\mathrm{TB}} &= \frac{a^2}{8\pi|f|^2}\left(1 - \frac{s_n\Delta}{E_g}\right)(\cos 2\pi k_1 - \cos 2\pi k_-)\,.\end{aligned} \tag{3.17}$$

In this particular gauge the conduction band Berry connections are smooth and finite throughout the BZ; however, the valence band Berry connections diverge at the K points. This behaviour is depicted in Figs. 3.3(a) and (b), which compare the components $\mathcal{A}_{v,2}^{\mathrm{TB}}$ and $\mathcal{A}_{c,2}^{\mathrm{TB}}$ of the Berry connections. The divergent behaviour results from the phase singularity of $\phi(\mathbf{k})$ shown in Fig. 3.2, and further details are discussed in App. B.

The TDM is given by

$$\mathbf{d}_{cv}^{\mathrm{TB}}(\mathbf{k}) = -\frac{|g(\mathbf{k})|}{\varepsilon(\mathbf{k})}\nabla_{\mathbf{k}}\phi(\mathbf{k}) + i\frac{\Delta}{\varepsilon^2(\mathbf{k})}\nabla_{\mathbf{k}}|g(\mathbf{k})|, \tag{3.18}$$

with components

$$\begin{aligned}d_{cv,1}^{\mathrm{TB}}(\mathbf{k}) =& \frac{a^2|\gamma|}{4\pi\varepsilon|f|}(\cos 2\pi k_- - \cos 2\pi k_2) - i\frac{a^2|\gamma|\Delta}{4\pi\varepsilon^2|f|}(\sin 2\pi k_- + \sin 2\pi k_2 + 2\sin 2\pi k_1) \\ d_{cv,2}^{\mathrm{TB}}(\mathbf{k}) =& \frac{a^2|\gamma|}{4\pi\varepsilon|f|}(\cos 2\pi k_- - \cos 2\pi k_1) + i\frac{a^2|\gamma|\Delta}{4\pi\varepsilon^2|f|}(\sin 2\pi k_- - \sin 2\pi k_1 - 2\sin 2\pi k_2)\,,\end{aligned} \tag{3.19}$$

where we have suppressed explicit k-dependence in the prefactors. We remark that the two components of the TDM have a close resemblance, and are in fact made identical by substituting $k_1 \leftrightarrow k_2$ in either component. The real and imaginary parts of the TDM component $d_{cv,2}$ are shown in Fig. 3.3, and we observe that the TDM is discontinuous about the K points. The

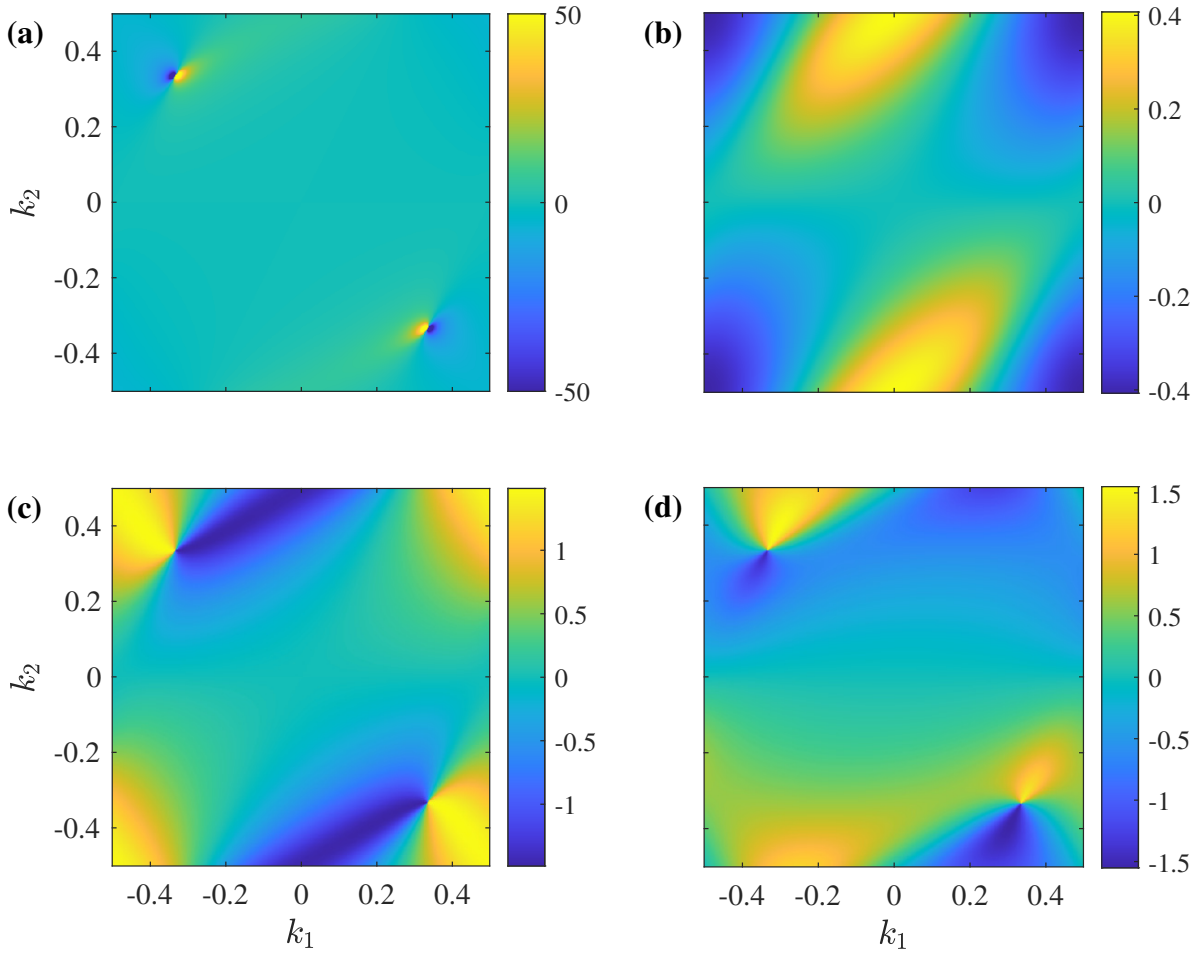

Figure 3.3: (a) component $\mathcal{A}_{v,2}$ of the valence band Berry connection, with restricted color scale; (b) component $\mathcal{A}_{c,2}$ of the conduction band Berry connection. Panels (c) and (d) show the real and imaginary parts of the TDM component $d_{cv,2}$.

component $d_{cv,2}$ exhibits a similar discontinuity at the K points, and this behaviour also results from the phase singularity of $\phi(\mathbf{k})$; as discussed in App. B.

The matrix elements (2.63) for the mixture current (2.64) are

$$\begin{aligned}\mathbf{W}_{cv}(\mathbf{k},t) &= \boldsymbol{\mathcal{D}}_{\mathbf{k}}\Omega_{cv}(\mathbf{k},t)\\ &= \boldsymbol{\mathcal{D}}_{\mathbf{k}}\left[\mathbf{F}(t)\cdot\mathbf{d}_{cv}(\mathbf{k})\right]\\ &= \sum_{i,j} g_{ij}F_i(t)\mathcal{D}_{\mathbf{k}}d_{cv,j}(\mathbf{k}),\end{aligned} \tag{3.20}$$

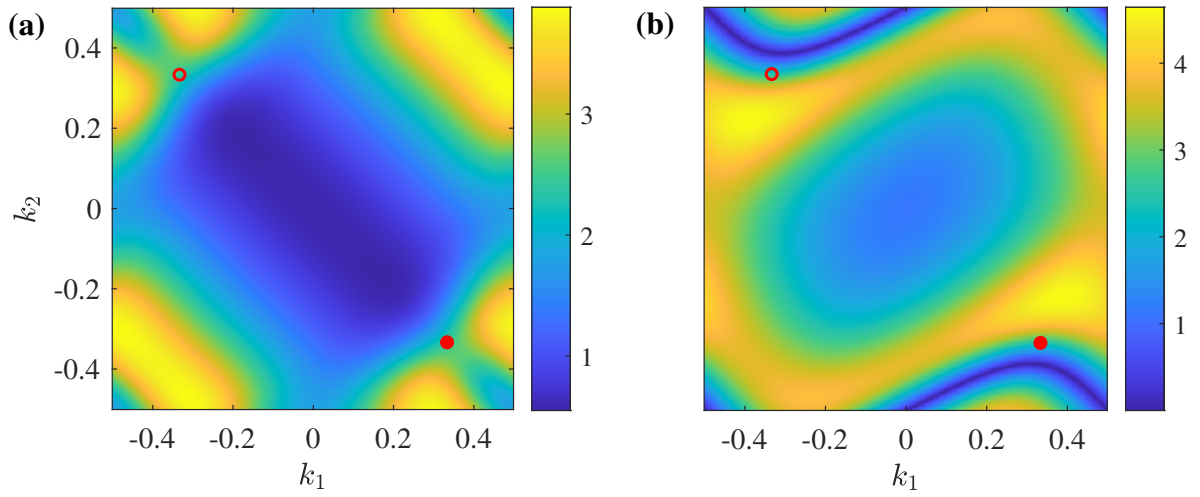

Figure 3.4: Magnitudes of the generalized derivative components (a) $|\mathcal{D}_1 d_{cv,2}|$ and (b) $|\mathcal{D}_2 d_{cv,2}|$ in the smooth gauge. Data are in atomic units, and circles indicate the K points corresponding to Fig. 3.1

where g_{ij} is the metric tensor (A.15). The components of these matrix elements are

$$W_{cv,\mu}(\mathbf{k}, t) = g_{ij} F_i(t) \mathcal{D}_\mu d_{cv,j}(\mathbf{k}), \tag{3.21}$$

where

$$\mathcal{D}_\mu d_{cv,j}(\mathbf{k}) = \mathbf{b}_\mu \cdot \boldsymbol{\mathcal{D}}_\mathbf{k} d_{cv,j}(\mathbf{k}) \tag{3.22}$$

is a component of the generalized derivative, with $\mathbf{b}_i$ a primitive vector of the reciprocal lattice. We thus conclude that in order to evaluate the mixture current, we require generalized derivatives of the TDM components. In practice, we only need to calculate the generalized derivative of one TDM component, since it is found that $\mathcal{D}_1 d_{cv,2} = \mathcal{D}_2 d_{cv,1}$, while $\mathcal{D}_2 d_{cv,2}$ is obtained from $\mathcal{D}_1 d_{cv,1}$ by interchanging $k_1 \leftrightarrow k_2$. The calculations are straightforward but tedious, and expressions for the required derivatives are provided in Sec. B.2.

One might be concerned that the mixture current involves the singular quantity $\boldsymbol{\mathcal{A}}_{cv}^{\mathrm{TB}}$, which enters the expression for the generalized derivatives in the TB gauge. However, a careful analysis shows that the singularity of the Berry connections at the K points arises from the derivative of an inverse tangent function, and this behaviour is exactly canceled by the gradient of the discontinuous TDM in the generalized derivative. The magnitudes of the generalized derivatives are gauge invariant, and Fig. 3.4 shows the components $|\mathcal{D}_1 d_{cv,2}|$ and $|\mathcal{D}_2 d_{cv,2}|$, which

are clearly smooth and finite throughout the BZ. While the magnitudes are finite near K, the real and imaginary components of the generalized derivatives are actually discontinuous about the K-points. This is similar to the behaviour of the TDM components, which is not surprising since $\mathbf{d}_{cv}$ and $\mathbf{W}_{cv}$ have identical gauge transformation relations; i.e. they both pick up a phase $\chi_{cv}(\mathbf{k})$ as a result of a gauge transformation (2.69). Comparing Figs. 3.3 and 3.4, we see that the matrix elements $\mathcal{D}_i d_{cv,j}$ have similar magnitudes to the TDM components. This implies that the linear interband response will be dominated by the polarization current, since the mixture current (2.68c) scales directly with the field strength $|\mathbf{F}| \ll 1$. However, for higher harmonics the relative contributions are not as intuitive, and this will be explored numerically in Sec. 4.1.

The non-smooth behaviour of the matrix elements $\boldsymbol{\mathcal{A}}_{cv}$ and $\mathbf{d}_{cv}$ presents a challenge for numerical integration of the SBEs. Although the singularities can be avoided by choosing a k-mesh that excludes the K-points, the behaviour is still rapidly varying in a neighbourhood of the K-points. Since this region of the BZ includes the minimum bandgap where we expect optical excitations to be most significant, the TB gauge is quite inefficient for numerical integration. Specifically, both the k-mesh and the integration time steps require small values in order to achieve convergence. These difficulties can be circumvented by transforming to a gauge in which the Berry connections are smooth and finite throughout the BZ.

3.3 Gauge smoothing transformation

To overcome the difficulty of non-smooth Berry connections in gapped graphene, we employ an analytic gauge transformation which removes the singular behaviour from the valence band Bloch functions. In appendix B it is shown that the gradient of $\arg[d_{cv,1}(\mathbf{k})]$ exactly cancels the divergence of the valence band Berry connection. This means the TDM phase can be used as a gauge transformation to achieve a smooth and periodic gauge throughout the BZ. Details of the gauge smoothing function are provided in Sec. B.3, and for the remainder of this chapter we assume to be working in the smoothed gauge,

$$|u_{m,\mathbf{k}}\rangle = e^{-i\chi_m(\mathbf{k})}|u^{\mathrm{TB}}_{m,\mathbf{k}}\rangle, \tag{3.23}$$

where χ_v is given by Eq. (B.21), while $\chi_c = 0$ as the conduction band is already smooth in the TB gauge. Although we have found that it is also possible to smooth the valence band using the discrete version of the parallel transport gauge transformation [36, 41], this introduces an undesirable finite difference error. Further, using a gauge function with a closed-form expression preserves the overall analytic nature of the tight-binding model.

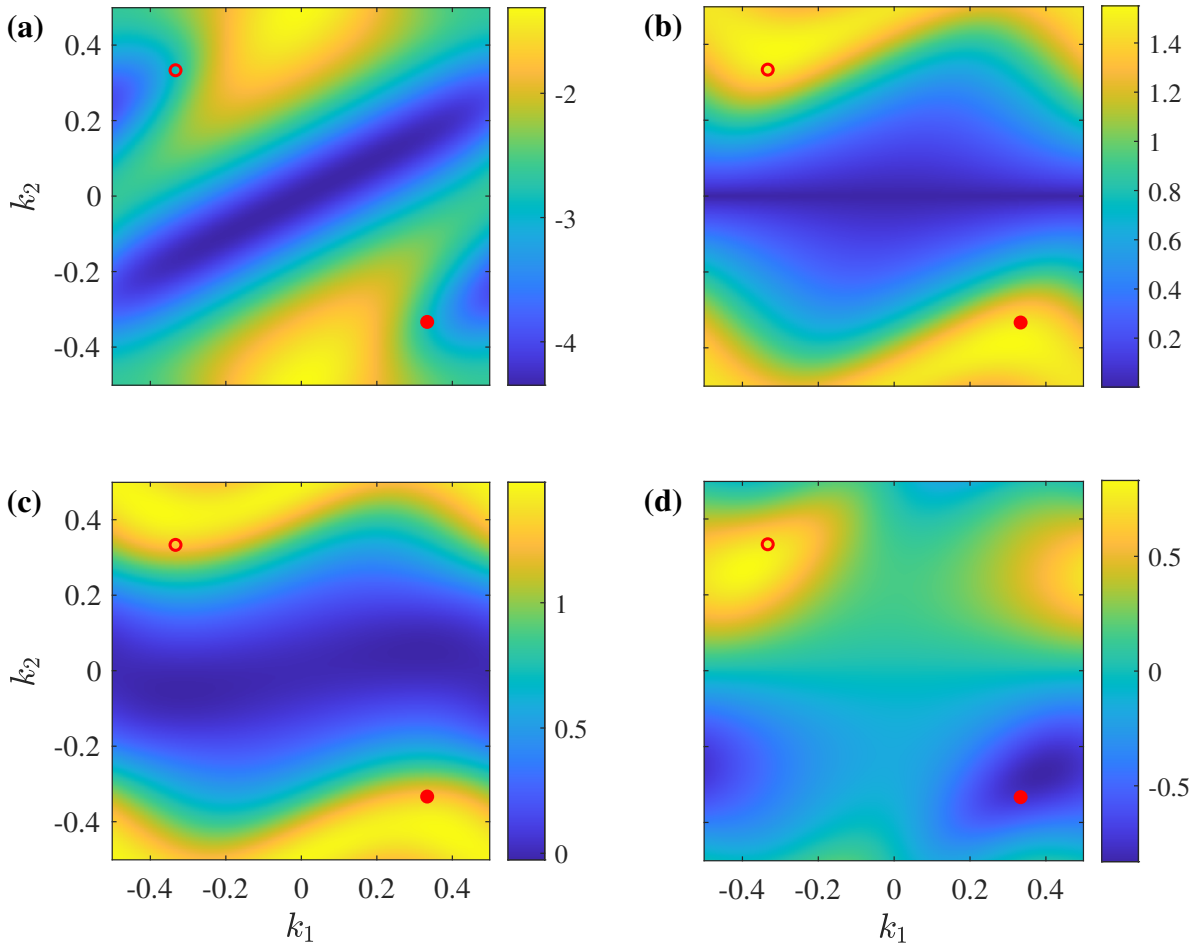

Figure 3.5: Berry connections and dipole moments in the smooth gauge. Panel (a) shows difference of Berry connections $\mathcal{A}_{cv,2} = \mathcal{A}_{c,2} - \mathcal{A}_{v,2}$; (b-d) show magnitude, real, and imaginary parts of $d_{cv,2}$, respectively. All data are in atomic units. Circles indicate the K points corresponding to Fig. 3.1.

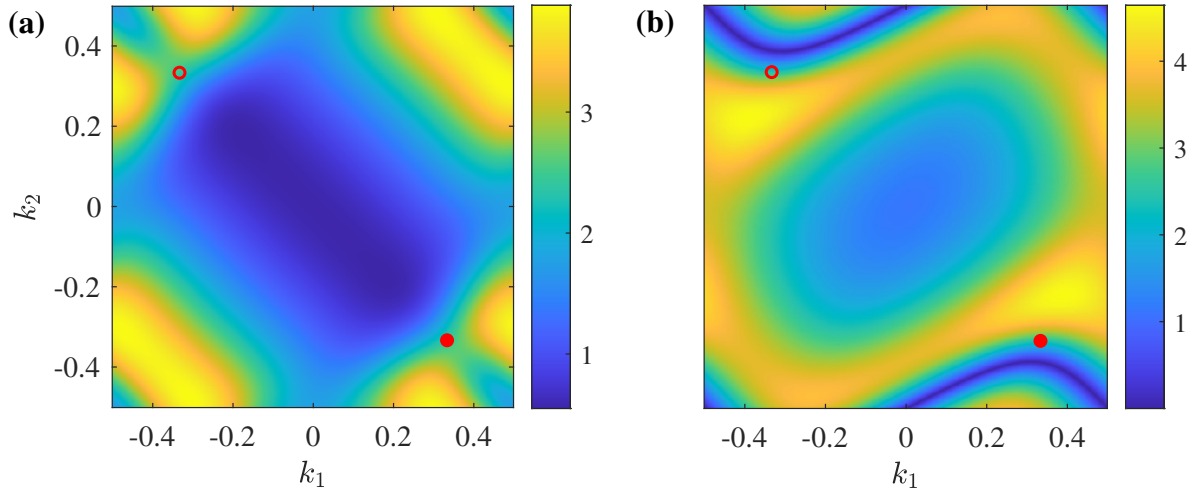

Figure 3.6: Generalized derivatives of the TDM component $d_{cv,2}$ in the smooth gauge. Panels (a,b) show the real and imaginary parts of $\mathcal{D}_1 d_{cv,2}$; (b,d) show the real and imaginary parts of $\mathcal{D}_2 d_{cv,2}$. All data are in atomic units, and circles indicate the K points corresponding to Fig. 3.1.

The Berry connections contribute to the dynamics through the difference $\boldsymbol{\mathcal{A}}_{cv}$, which is depicted in Fig. 3.5(a). We only show the second vector component, since the first component ends up being a constant in this gauge; specifically, $\mathcal{A}_{cv,1} = a^2/4\pi$. Clearly, the smooth and finite behaviour observed in Fig. 3.5 demonstrates the success of the gauge smoothing function. Fig. 3.5(b) shows the magnitude $|d_{cv,2}|$, while (c,d) show the real and imaginary parts of $d_{cv,2}$. We do not show $d_{cv,1}$ since the two TDM components have very similar behaviour.

In order to evaluate the matrix elements (2.63) for the mixture current, we also require the generalized derivatives of the TDM components $\mathcal{D}_i d_{cv,j}(\mathbf{k})$ in the smooth gauge. Since the generalized derivative was shown to be gauge covariant (2.80), it is easiest to calculate these matrix elements initially in the TB gauge, and then multiply by $e^{-i\chi_v}$ to transform to the smooth gauge. As discussed in the previous section, we only need to calculate the generalized derivative of one TDM component, since the two components are equivalent under the substitution $k_1 \leftrightarrow k_2$. The real and imaginary parts of the components $\mathcal{D}_1 d_{cv,2}$ and $\mathcal{D}_2 d_{cv,2}$ are shown in Fig. 3.6. The generalized derivative components are strongly anisotropic about the K points, which suggests that the mixture current could contribute to the orientation dependence of high harmonics. The influence of the mixture current on the HHG spectrum will be discussed in chapter 4.

3.4 Maximally localized Wannier gauge

We close this chapter by discussing a specific Bloch gauge. By Fourier transforming the Bloch functions, one obtains a complete set of orbitals in real-space known as Wannier functions [45, 49, 58]. While Bloch functions are defined at each k-point in the BZ, the Wannier functions

$$|w_{n,\mathbf{R}}\rangle = \int d\mathbf{k} e^{-i\mathbf{k}\cdot\mathbf{R}} |u_{n,\mathbf{k}}\rangle, \tag{3.24}$$

are associated with translation vectors $\mathbf{R}$ between unit cells of the real-space lattice. The centers of the Wannier functions are given by the average value of the Berry connections throughout the BZ,

$$\langle \mathbf{x}_n \rangle = \int d\mathbf{k} \boldsymbol{\mathcal{A}}_n(\mathbf{k}), \tag{3.25}$$

and they are gauge invariant up to a lattice vector [41, 49]. In contrast, the spread of each Wannier function with respect to its center, given by

$$\langle x_n^2 \rangle - \langle \mathbf{x}_n \rangle^2 = \int d\mathbf{k} \mathcal{A}_n^2(\mathbf{k}) - \left[\int d\mathbf{k} \boldsymbol{\mathcal{A}}_n(\mathbf{k}) \right]^2 + \sum_{m \neq n} \int d\mathbf{k} |d_{nm}(\mathbf{k})|^2, \tag{3.26}$$

is strongly gauge-dependent [41, 45, 49]; although we note that the third term is actually gauge invariant. The Bloch gauge corresponding to maximally localized Wannier functions (MLWFs) is unique, and is referred to as the MLWF gauge. MLWFs have received considerable attention in the condensed matter community [30, 45, 59, 60]. More recently, MLWFs have been used to improve quasi-classical models of HHG in solids [17, 18], which help to develop understanding and intuition of the physical processes shaping HHG in solids. In particular, the Wannier quasi-classical (WQC) model of HHG [18] achieves quantitative agreement with numerical simulation of the SBEs, but its success relies on strong localization of the Wannier functions. While algorithms exist to obtain MLWFs in numerical band structure calculations [44] for general crystals, this involves a highly technical optimization procedure. Here we develop a simpler algorithm for fixing the MLWF gauge in systems with non-degenerate bands. This approach avoids unnecessary complexity, and is well suited to analytic tight-binding models.

In the absence of degeneracies, it can be shown [49] that the MLWF gauge corresponds to vanishing divergence of the Berry connections; i.e.

$$\nabla_{\mathbf{k}} \cdot \bar{\boldsymbol{\mathcal{A}}}_m(\mathbf{k}) = 0, \tag{3.27}$$

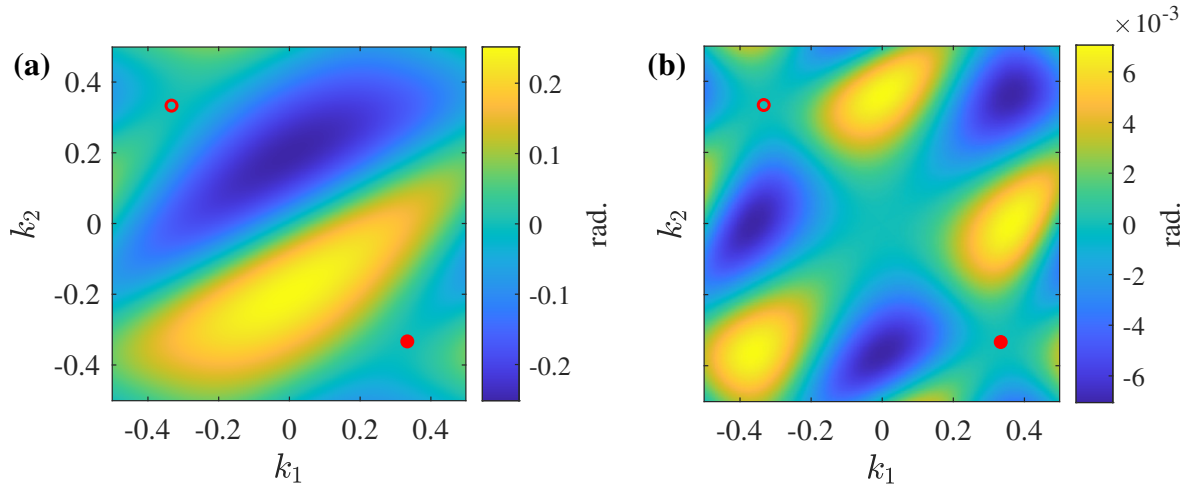

Figure 3.7: MLWF gauge functions for the valence (a) and conduction (b) bands.

where we denote $\bar{\boldsymbol{\mathcal{A}}}_m$ the Berry connection in the MLWF gauge. If the Berry connections are given by $\boldsymbol{\mathcal{A}}_m$ in some initial gauge, we can find the gauge function $\bar{\chi}_m(\mathbf{k})$ that transforms to the MLWF gauge by requiring

$$\begin{aligned} 0 &= \nabla_{\mathbf{k}} \cdot \bar{\boldsymbol{\mathcal{A}}}_m(\mathbf{k}) \\ &= \nabla_{\mathbf{k}} \cdot \left[\boldsymbol{\mathcal{A}}_m(\mathbf{k}) + \nabla_{\mathbf{k}} \bar{\chi}_m(\mathbf{k})\right]. \end{aligned} \tag{3.28}$$

The MLWF gauge function is thus the solution to the Poisson equation

$$\nabla^2_{\mathbf{k}} \bar{\chi}_m(\mathbf{k}) = -\nabla_{\mathbf{k}} \cdot \boldsymbol{\mathcal{A}}_m(\mathbf{k}) \equiv -\eta_m(\mathbf{k}), \tag{3.29}$$

where we denote η_m the divergence of the Berry connection in the initial gauge. The solution is readily obtained using the Wannier-Bloch Fourier transform [41]

$$f(\mathbf{k}) = \frac{1}{\sqrt{N}} \sum_{\mathbf{R}} e^{i\mathbf{k}\cdot\mathbf{R}} f(\mathbf{R}), \tag{3.30}$$

where N is the number of unit cells. Clearly

$$\nabla^2_{\mathbf{k}} \bar{\chi}_m(\mathbf{k}) = \sum_{\mathbf{R}} \bar{\chi}_m(\mathbf{R}) \nabla^2_{\mathbf{k}} e^{i\mathbf{k}\cdot\mathbf{R}} = -\sum_{\mathbf{R}} \bar{\chi}_m(\mathbf{R}) R^2 e^{i\mathbf{k}\cdot\mathbf{R}}, \tag{3.31}$$

and thus

$$\bar{\chi}_m(\mathbf{R}) = \frac{\eta_m(\mathbf{R})}{R^2} \tag{3.32}$$

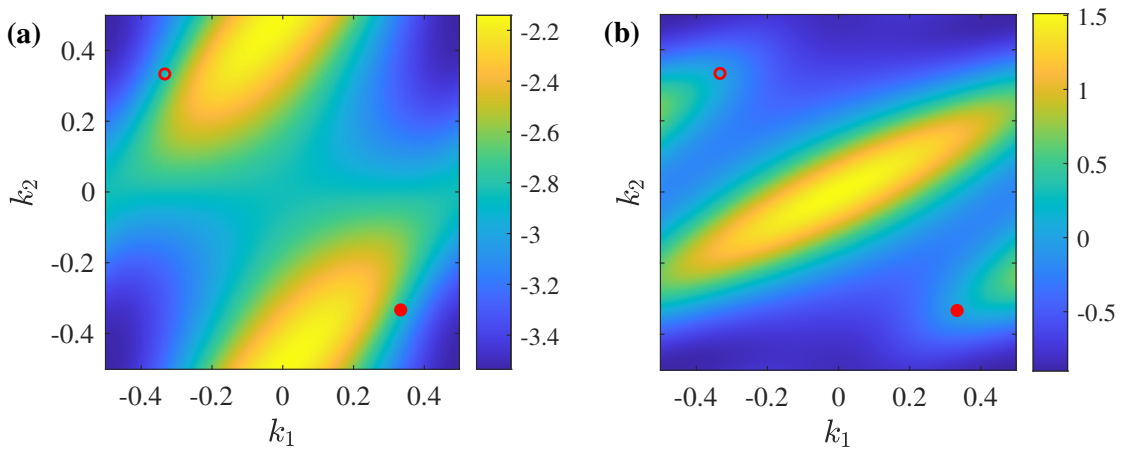

Figure 3.8: Panel (a) shows the difference of Berry connections $\bar{\mathcal{A}}_{cv,2}$ in the MLWF gauge; (b) shows the change $\bar{\mathcal{A}}_{cv,2} - \mathcal{A}_{cv,2}$ with respect to the smooth gauge of Sec. 3.3.

is the solution in real space, which decays rapidly with $|\mathbf{R}|$; provided the initial Bloch gauge used to calculate $\eta_m(\mathbf{R})$ is smooth and periodic. Transforming back to k-space, we obtain the desired MLWF gauge function

$$\begin{aligned}\bar{\chi}_m(\mathbf{k}) &= \frac{1}{N}\sum_{\mathbf{R},\mathbf{k}'} \frac{e^{i(\mathbf{k}-\mathbf{k}')\cdot\mathbf{R}}}{R^2}\eta_m(\mathbf{k}') \\ &= \frac{1}{N}\sum_{\mathbf{R},\mathbf{k}'} \frac{e^{i(\mathbf{k}-\mathbf{k}')\cdot\mathbf{R}}}{R^2}\nabla_{\mathbf{k}'}\cdot\boldsymbol{\mathcal{A}}_m(\mathbf{k}'). \end{aligned} \tag{3.33}$$

It is important to note that the Fourier transform approach only works if the Berry connection in the initial gauge is well-approximated by its Fourier series. Clearly this would not be the case for the singular valence band Berry connections of gapped graphene in the TB gauge. In contrast, the analytically smoothed gauge for gapped graphene provides an ideal starting point for implementing the MLWF gauge transformation. Fig. 3.7 shows the gauge functions $\bar{\chi}_v$ and $\bar{\chi}_c$ that transform from the smooth gauge to the MLWF gauge of gapped graphene. Clearly $|\bar{\chi}_v| \gg |\bar{\chi}_c|$, which means the difference $\bar{\chi}_{cv}$ is dominated by the valence band gauge function.

While the real and imaginary parts of the TDM are slightly modified by the MLWF gauge transformation, the behaviour of the Berry connections is more interesting. Fig. 3.8a shows the component $\bar{\mathcal{A}}_{cv,2}$ of the difference of Berry connections that contributes to the SBE dynamics. Comparing to Fig. 3.3a, the overall magnitude $|\bar{\boldsymbol{\mathcal{A}}}_{cv}|$ is significantly reduced in the MLWF gauge compared to the TB gauge. Fig. 3.8b shows the difference $\bar{\mathcal{A}}_{cv,2} - \mathcal{A}_{cv,2}$ compared to the initial

gauge, and the most significant change occurs near $k = 0$. Overall, the Berry connections are observed to vary more slowly throughout the BZ as a result of the MLWF gauge transformation.

Although the Berry connections are gauge-dependent, it is nevertheless interesting to consider the relative contribution of $\bar{\boldsymbol{\mathcal{A}}}_{cv}$ to the dynamics in the MLWF gauge. The difference of Berry connections $\bar{\boldsymbol{\mathcal{A}}}_{cv}$ is scaled by the electric field strength in the SBEs (2.44), which means $\varepsilon_{cv} \gg \mathbf{F} \cdot \bar{\boldsymbol{\mathcal{A}}}_{cv}$ for any realistic field strength; i.e. below the damage threshold. Since the bandgap is the dominant structural quantity influencing the excitation of electron-hole pairs, it is not obvious to what extent the Berry connections will contribute to the population dynamics. We can gain insight by comparing simulations of the SBEs with and without the Berry connections included. Fig. 3.9 shows the time-dependent behaviour of the conduction band population in response to a 75fs pulse with 3.5μm wavelength, polarized along the $\Gamma - M$ direction. Fig. 3.9a shows the total population $n_c(t)$ over the duration of the pulse, and we see that the intraband Berry connection plays a noticeable role in the excitation process. Not only is the final population overestimated when $\bar{\boldsymbol{\mathcal{A}}}_{cv} = 0$, but the asymmetry of the dynamics between half-cycles is also affected. This asymmetry is depicted more clearly in Fig. 3.9b, which shows the excitation rate $\dot{n}_c(t)$ over two optical cycles. In both cases there is strong asymmetry between half cycles, but the asymmetry appears to flip when the Berry connection is excluded. The most important conclusion from these results is that it is essential to include the full Berry connections when simulating strong field processes in gapped graphene.

3.5 Summary

The tight-binding model for gapped graphene is a simple and useful prototype for studying light-matter interactions in two-dimensional materials. Although this model has been used previously to study time-dependent phenomena [11, 34, 43], the non-smooth dipole matrix elements in the TB gauge create numerical difficulty; especially in the regime of HHG. In Ref. [34], HHG in gapped graphene was simulated in the TB gauge including the complex dipole moments but omitting the Berry connections. From the results of the previous section, it is clear that the Berry connections play a significant role in the dynamics, and should not be excluded. The analytic gauge smoothing transformation eliminates the numerical issues of the TB gauge, and makes gapped graphene an ideal model for investigating HHG in 2D materials. This model will be applied in the next chapter to study strong field physics in more detail.

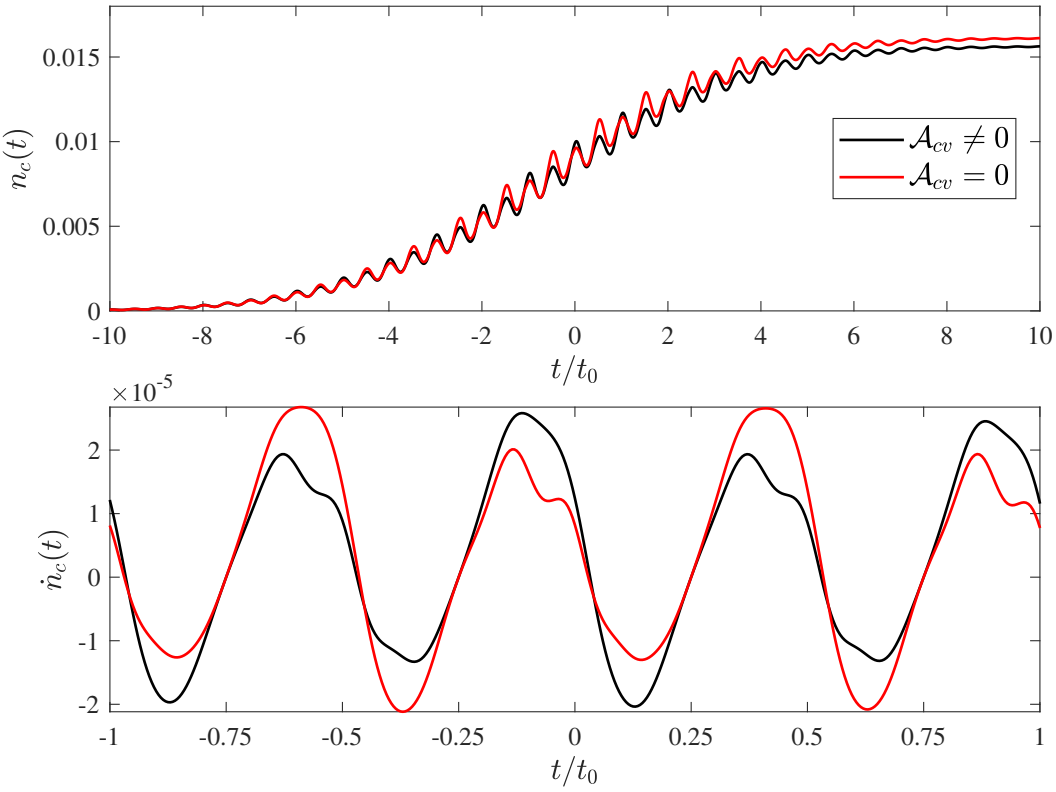

Figure 3.9: Time-dependent population dynamics in the MLWF gauge, highlighting the influence of the Berry connections. Panel (a) shows the time-dependent population $n_c(t)$ over the full pulse duration, while (b) shows the excitation rate $\dot{n}_c(t)$ over two optical cycles. The two curves in each panel correspond to simulations including (black) and excluding (red) the Berry connections.

Chapter 4
Influence of mixture current for HHG in solids

Recall from chapter 2 that the interband current contains a term arising from non-adiabatic couplings between Bloch states, known as the mixture current (2.68c). The influence of the interband mixture current [36] has been mostly ignored by the HHG community, and has only been considered recently in simulations of HHG for the linearized model of inversion-symmetric graphene [39]. In order to study the influence of the mixture current more thoroughly, we desire a model system for which we can calculate the relevant matrix elements (2.63). Although there exist sum rules to calculate generalized derivatives from DFT [37, 46], obtaining a smooth Bloch gauge suitable for numerical integration is still challenging [33, 36]. A tight-binding model is an easier starting point, and gapped graphene has been used extensively to model 2D materials with broken inversion symmetry [27, 42, 43]. The analytically smoothed gauge of gapped graphene enables efficient numerical integration of the SBEs, and also provides analytic expression for the required matrix elements. We focus on orientation dependence of HHG in order to reveal the influence of the mixture current. The orientation dependence is sensitive to details of the band structure, and provides valuable insight. Experimentally, the orientation dependence of HHG has been measured in several systems [12, 28, 61–63].

4.1 SBE simulations

We investigate HHG in gapped graphene by simulating the SBEs (2.44) for a linearly polarized optical pulse,

$$\mathbf{F}(t) = F_0 e^{-(t/\tau)^2} \cos(\omega_0 t)(\cos\theta \mathbf{e}_x + \sin\theta \mathbf{e}_y), \tag{4.1}$$

where θ is the incident polarization angle with repsect to the x-axis in Fig. 3.1a, which corresponds to the ΓM symmetry axis. The optical frequency of the pulse is $\omega_0 = \Delta/5.3 = 0.061$ a.u., and we use a Gaussian pulse envelope with 50 fs duration. Unless specified otherwise, we use a dephasing time of one optical cycle, $t_0 = 2\pi/\omega_0$. We integrate the SBEs using a fourth order Runge-Kutta method, using a k-mesh of 100×100 points.

The intensity of emitted harmonics is proportional to the spectrum of the current

$$S(\omega) \propto |\mathbf{j}(\omega)|^2, \tag{4.2}$$

where

$$\mathbf{j}(\omega) = \int_{-\infty}^{\infty} dt e^{-i\omega t} \mathbf{j}(t). \tag{4.3}$$

Focusing on the interband current, we compare the harmonic spectrum calculated using the full interband current $\mathbf{j}_{\mathrm{er}}(\omega)$ to the spectrum arising solely from the polarization current $\mathbf{j}_{\mathrm{pol}}(\omega)$. Since $\mathbf{j}_{\mathrm{er}} = \mathbf{j}_{\mathrm{pol}} + \mathbf{j}_{\mathrm{mix}}$, any discrepancy between $\mathbf{j}_{\mathrm{er}}$ and $\mathbf{j}_{\mathrm{pol}}$ can be attributed to the mixture current. We decompose the current into components parallel ($j_{\parallel}$) and perpendicular ($j_{\perp}$) to the incident polarization angle, so that the total harmonic yield arising from both vector components is given by

$$S(\omega) = |j_{\parallel}(\omega)|^2 + |j_{\perp}(\omega)|^2 \equiv |\mathbf{j}(\omega)|^2. \tag{4.4}$$

Fig. 4.1 compares the HHG spectra arising from the polarization current and the full interband current for two different crystal orientations. In Fig. 4.1a the orientation angle θ is aligned with the ΓM symmetry axis, and the induced current is entirely parallel to the driving laser. In Fig. 4.1b the orientation is along the ΓK direction, which is a mirror symmetry direction for the hexagonal lattice [27]. As a result, the parallel component of the current contains only odd harmonics, while the perpendicular current contains only even harmonics. For intermediate orientations, both the parallel and perpendicular currents contain a mixture of even and odd harmonics.

In Fig. 4.1 it is clear that higher harmonics beyond the cutoff are influenced more strongly by the mixture current. As the harmonic order increases, the polarization current tends to overestimates the harmonic yield. By contrast, in Fig. 4.1b we can see that harmonic 9 is slightly enhanced by the mixture current for $\theta \parallel \Gamma K$, although it is difficult to quantify on this scale. What we can conclude is that the effect on harmonic 9 is different for the two orientations, and this suggests that the effect of the mixture current is more complicated than a simple scale factor. Clearly, it is difficult to compare the stronger harmonics based solely on the spectrum in Fig. 4.1a due to the large dynamic range. Further, comparing the spectra for a single orientation provides limited insight for the strong anisotropy of gapped graphene. We can develop a more complete picture by studying the orientation dependence of the individual harmonic efficiencies.

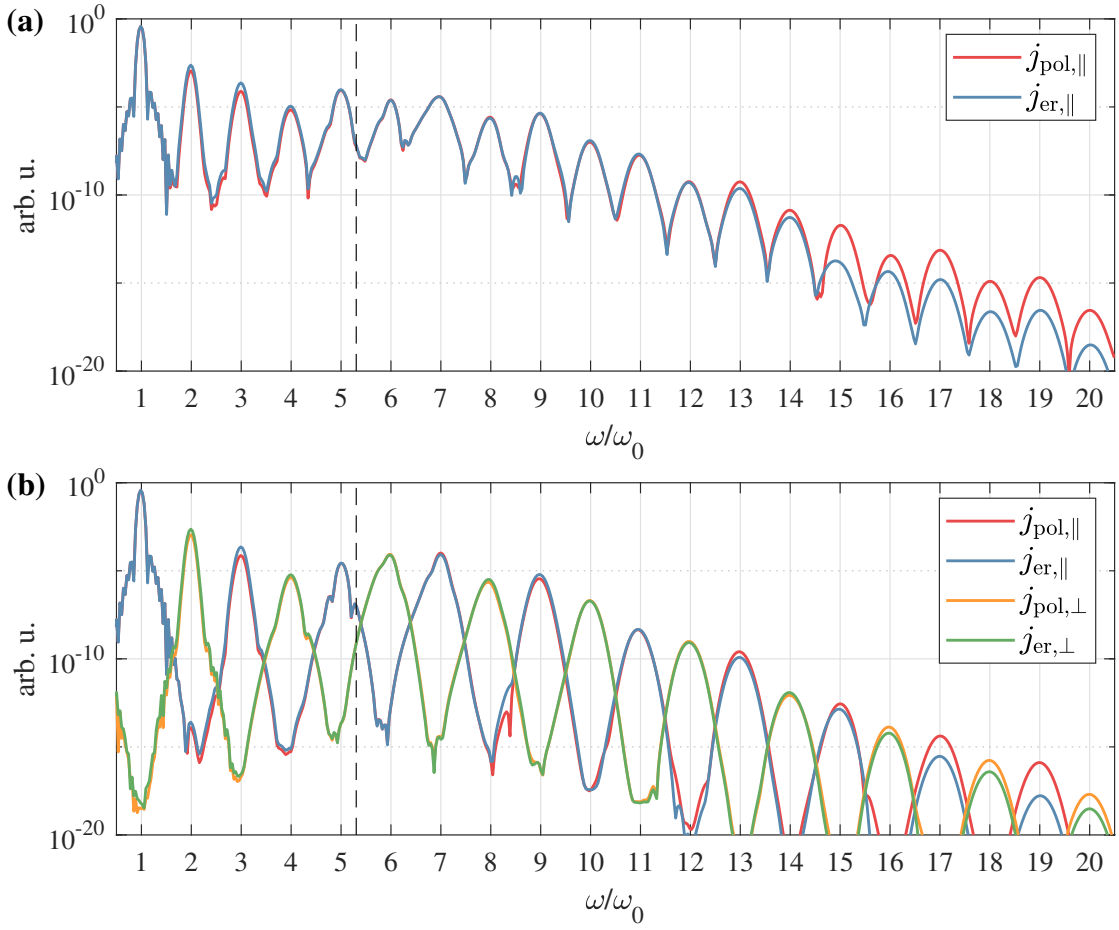

Figure 4.1: Influence of mixture current on HHG spectra for optical polarization oriented along (a) ΓM, and (b) ΓK. Field strength $F_0 = 0.0025$ in both cases.

4.2 Orientation dependence of HHG

In order to study the orientation dependence of HHG, we calculate the integrated yield of the n^{th} harmonic according to

$$S(n\omega_0) = \int_{n\omega_0-\delta\omega}^{n\omega_0+\delta\omega} d\omega S(\omega) = \int_{n\omega_0-\delta\omega}^{n\omega_0+\delta\omega} \left[|j_{\parallel}(\omega)|^2 + |j_{\perp}(\omega)|^2\right], \tag{4.5}$$

where $\delta\omega = \omega_0/4$ is the integration window, and we restrict our attention to interband HHG for harmonics above the minimum bandgap. Fig. 4.2 shows the orientation dependence of harmonics 6-14, where the full interband harmonic yield (blue) is compared to the yield arising solely from $\mathbf{j}_{\mathrm{pol}}$ (red). In each case, the harmonic yield is normalized to the largest value of S_{er} or S_{pol} over

the angular range.

For harmonics (6,7,12-14) the polarization current overestimates the total harmonic yield, and the effect of the mixture current is approximately isotropic. For harmonics (8,11) the effect of the mixture current is also isotropic, but in this case it enhances the total harmonic yield. For harmonic 10, S_{er} and S_{pol}give very similar results, and the traces actually intersect for some angles.

The most interesting case inf Fig. 4.2 is harmonic 9 (d). Overall the mixture current enhances the harmonic yield, but the behaviour is noticeably anisotropic. The enhancement is most significant for $\theta \parallel \Gamma K$, while for $\theta \parallel \Gamma M$ the efficiencies are nearly identical. Although this behaviour was also observed in Fig. 4.1, the full orientation dependence provides more insight. Specifically, the orientation dependence of S_{er} is clearly maximized along ΓK, whereas S_{pol} is more uniform with primary maxima along ΓM and secondary maxima along ΓK. Although S_{er} and S_{pol} have similar magnitudes on a logarithmic scale, we observe a qualitative change in the orientation dependence arising from the mixture current.

We can uncover more significant effects of the mixture current by examining higher harmonics. Fig. 4.3 shows the orientation dependence of harmonics 15-18, but in this case S_{er} and S_{pol} are plotted separately since they differ by at least on order of magnitude. For harmonics (15,16,18) the mixture current reverses the locations of the minima/maxima. For harmonics (16,18) the mixture current also reduces the peak-to-peak magnitude of the orientation dependence; i.e. S_{er} is more isotropic than S_{pol} for these harmonics. In contrast, S_{er} and S_{pol} are both strongly anisotropic for harmonic 15, with nearly perfect extinction between maxima. Interestingly, the orientation dependenc of harmonic 17 is essentially unaffected by the mixture current.

One inuitive mechanism shaping HHG is the ionization rate and its dependence on the band structure. Clearly, a large ionization rate will generate a greater population of excited electron-hole pairs, which can then recombine to emit high harmonics. From the Keldysh theory of ionization [64–66], we expect the ionization rate to be inversely related to the effective mass. Although the bandgap for gapped graphene shown in Fig. 3.1 is not strongly anistropic near the K-points, there is still a variation of the effective mass depending on the orientation. The total time-dependent conduction band population is given by $n_c(t) = \int d\mathbf{k}\rho_{cc}(\mathbf{k}, t)$, and Fig. 4.4a shows the excitation (ionization) rate $\dot{n}_c(t)$ for two different orientations in gapped graphene. The total excitation is clearly stronger along ΓM compared to ΓK; corresponding to $\theta = 0$ and $\theta = 30°$, respectively. Fig. 4.4b shows the maximum ionization rate during the pulse as a function of polarization angle. The ionization rate has a simple 6-fold symmetric orientation dependence, with maxima(minima) along $\Gamma M(\Gamma K)$. As a result, the orientation dependence of

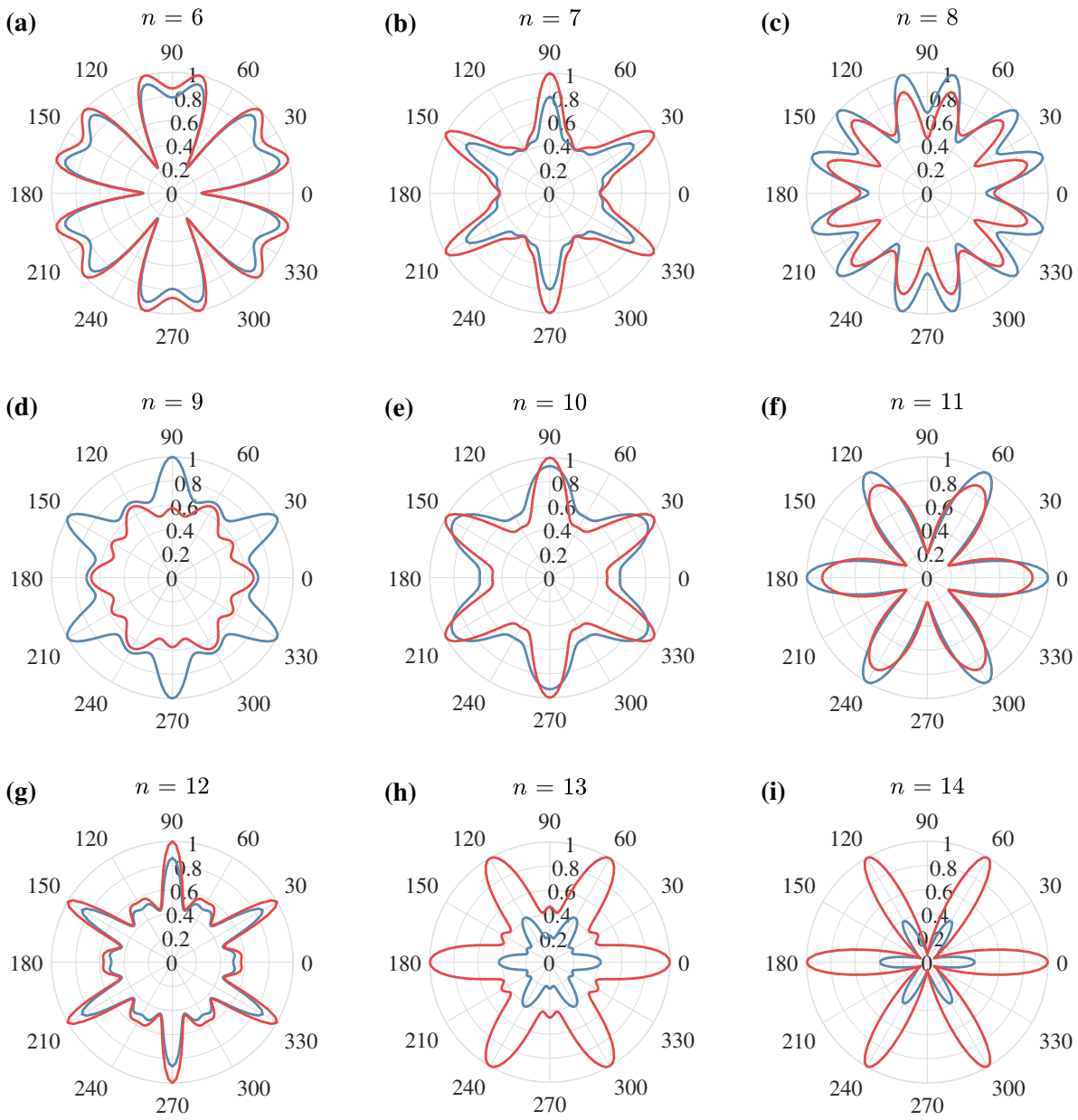

Figure 4.2: Orientation dependence of S_{er}(blue) and S_{pol}(red) for harmonics 6-14; each trace is scaled by the maximum of S_{er} or S_{pol}. The field strength $F_0 = 0.0025$ is the same used in Fig. 4.1.

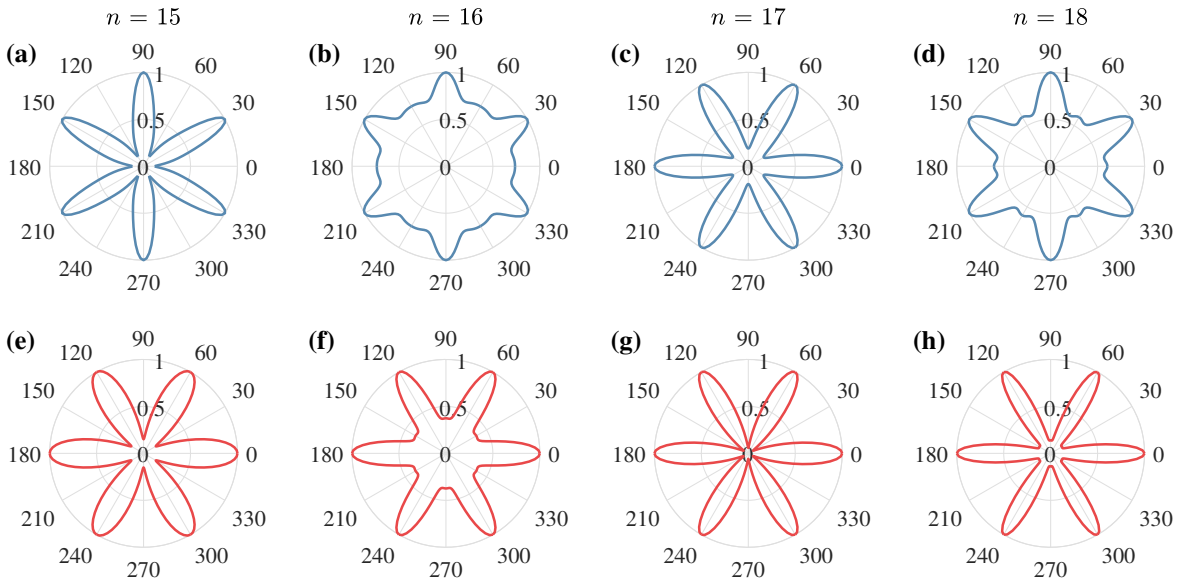

Figure 4.3: Normalized orientation dependence of S_{er}(blue) and S_{pol}(red) for harmonics 15-18. The field strength $F_0 = 0.0025$ is the same used in Fig. 4.1.

the ionization rate would have the effect of enhancing HHG when $\theta \parallel \Gamma M$. Clearly, this cannot be the dominant mechanism shaping the orientation dependence of harmonic yield, since we have already observed several harmonics with orientation dependence bearing little resemblance to Fig. 4.4b.

In Figs. 4.2 and 4.3 we identified several cases where the mixture current has a significant effect on the orientation dependence of harmonic yield. Further, the behaviour is inconsistent for different harmonic orders with no obvious trends. This suggests the overall orientation dependence is determined by an interplay of different mechanisms. The matrix elements influencing the interband HHG spectrum are the bandgap, Berry connections, TDM, and the generalized derivative of the Rabi frequency. These matrix elements have distinct behaviour throughout the BZ, and they also affect the HHG spectrum in different ways. Specifically, the bandgap, Berry connections, and TDM influence the dynamics directly via the SBEs (2.44), while the TDM and generalized derivatives enter the expressions for the interband current (2.53). Further, excited carriers are accelerated through the BZ with time-dependent crystal momentum $\mathbf{K}_t = \mathbf{K} - e\mathbf{A}(t)$ before recombining to emit harmonics. As a result, the dynamics shaping each harmonic are influenced by the band structure in different regions of the BZ. For example, harmonic 6 is only slightly above the minimum bandgap, and it will be dominated by k-space trajectories that recombine near the K-points. As the harmonic energy increases, so does the excursion distance of electron-hole pairs between excitation and recombination. We observed

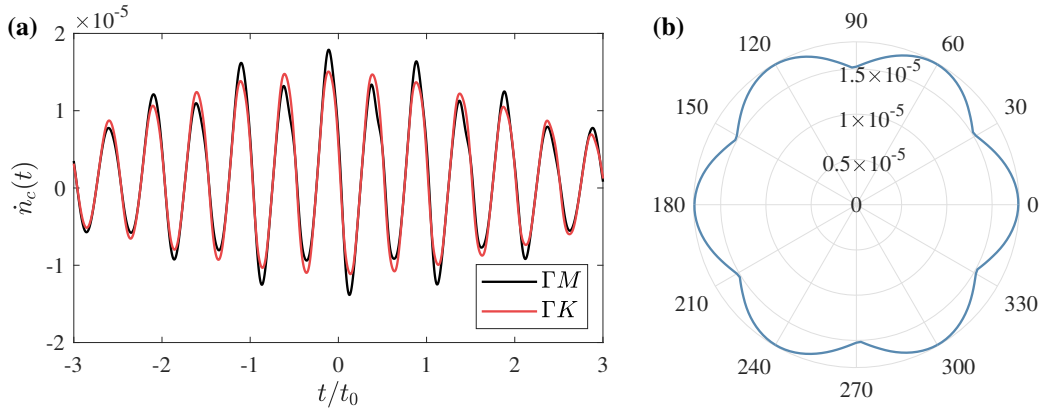

Figure 4.4: Orientation dependence of ionization rate for $F_0 = 0.0025$. Panel (a) compares $\dot{n}_c(t)$ for two orientations over 6 optical cycles; (b) shows the maximum ionization rate during the entire pulse, as a function of orientation angle θ.

in chapter 3 that the matrix elements shaping HHG in gapped graphene vary substantially throughout the BZ; especially the matrix elements influencing the mixture current. The main conclusion we can draw is that harmonic yield is influenced by the non-trivial k-dependence of the matrix elements, and this generally makes the orientation dependence non-intuitive. However, since total k-space excursion distance is directly proportional the field strength, it is safe to conclude that the orientation dependence will also depend on the field strength.

4.2.1 Influence of field strength

We remarked in Sec. 2.2 that the interplay of $\mathbf{j}_{\text{pol}}$ and $\mathbf{j}_{\text{mix}}$ is likely to vary with field strength, due to the different scalings of the relevant matrix elements. Specifically, the matrix element for $\mathbf{j}_{\text{pol}}$ is just the TDM $\mathbf{d}_{cv}$; whereas the matrix element for $\mathbf{j}_{\text{mix}}$ is the generalized derivative of $\mathbf{F}(t) \cdot \mathbf{d}_{cv}$, which is directly proportional to the field strength. However, based on the discussion of the previous section, we also expect the field strength to influence the orientation dependence via the k-space excursion distance.

Fig. 4.5 shows the orientation dependence of harmonics 6 and 9 for different applied field strengths. For harmonic 6 (a-d), the harmonic yield is maximized along ΓK for $F_0 = 0.002$, but as the field strength increases the maximum splits, and we end up with 12 distinct maxima for $F_0 = 0.003$. As the field strength is increased further, the orientation dependence for $F_0 = 0.0035$ reverts to being maximized along ΓK; similar to the case for $F_0 = 0.002$. Although the orientation dependence of harmonic 6 exhibits a non-trivial variation with field strength, the mixture current clearly has a negligible effect since both S_{pol} and S_{er} evolve similarly with F_0. In contrast, the orientation dependence of harmonic 9 (e-h) behaves quite differently. For

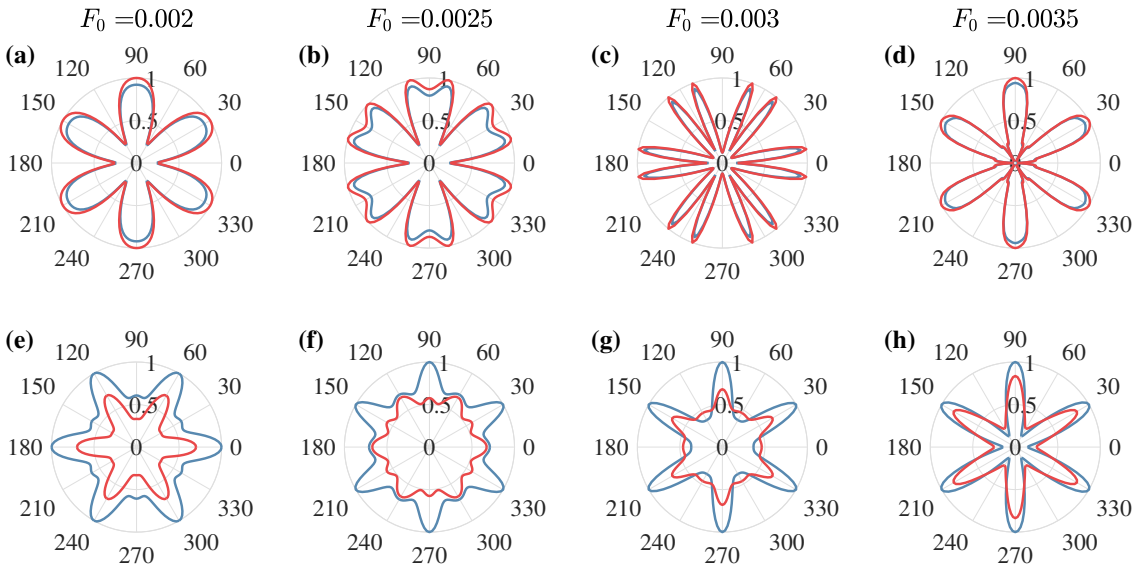

Figure 4.5: Orientation dependence of harmonics 6 (a-d) and 9 (b-h) for different applied field strengths. The full interband harmonic yield S_{er} (blue) is compared to S_{pol} (red).

$F_0 = 0.002$ both S_{pol} and S_{er} are maximized along ΓM, while for $F_0 = 0.0035$ they are both maximized along ΓK. However, we can see that the orientation dependence of S_{pol} and S_{er} evolve asynchronously for intermediate field strengths. At $F_0 = 0.0025$ the full interband harmonic yield S_{er} has already flipped the orientation of its maxima to ΓK, whereas S_{pol} is still maximized along ΓM. For both calculations the maximum orientation dependence of harmonic 9 moves from ΓM to ΓK as F_0 increases; however, S_{pol} seems to lag behind S_{er}.

We can develop a more complete picture by visualizing the harmonic yield as a function of both polarization angle θ and field strength F_0. Fig. 4.6 shows the combined orientation and field strength dependence of harmonics 6 and 9, with a side-by-side comparison of S_{er} and S_{pol}. For weaker fields harmonic 6 is maximized along ΓK, and we observe a gradual splitting of the maximum as F_0 increases. At higher field strengths the maxima recombine quite abruptly, reverting to a single maximum along ΓK. We also observe that the orientation dependence of $S_{\mathrm{er}}(6\omega_0)$ and $S_{\mathrm{pol}}(6\omega_0)$ evolve simultaneously with F_0. In contrast, harmonic 9 exhibits a single maximum that shifts from ΓM to ΓK with increasing field strengths, and these transitions occur at different field strengths for S_{er} and S_{pol}.

From Fig. 4.5 it was clear that the mixture current does not have a significant effect on the orientation dependence of harmonic 6. In contrast, the influence of the mixture current on harmonic 9 is clearly observable in Fig. 4.5, but it is difficult to characterize the nature of the effect from this limited view. From the combined picture in Fig. 4.6, we observe that the mixture

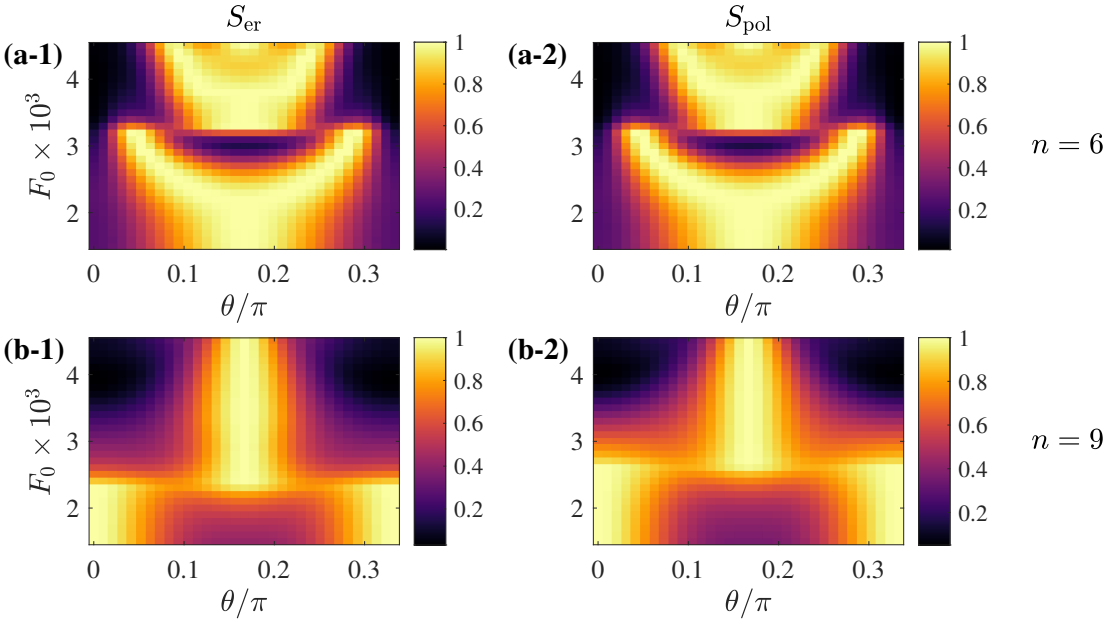

Figure 4.6: Combined orientation and field strength dependence of harmonics 6 and 9. Calculations using the full interband current S_{er} (LHS) are compared to S_{pol}(RHS), and in each case the orientation dependence is normalized to the maximum value at each field strength.

current simply shifts the field strength dependence of harmonic 9. Importantly, the mixture current does not fundamentally change the shape of the combined orientation and field strength dependence for harmonic 9. Clearly this expanded view provides valuable insight, but we note that overall scale differences between S_{er} and S_{pol} cannot be discerned due to the normalization.

Fig. 4.7 shows the combined orientation and field strength for selected higher harmonics. The mixture current has a negligible effect on harmonic 12, while for harmonic 11 the mixture current induces a considerable shift of the field strength dependence. The mixture current has a significant influence on harmonic 15, and the behaviour is distinct from the lower harmonics. The polarization current is always maximized along ΓM for harmonic 15; regardless of field strength. However, the mixture current clearly dominates at lower field strengths, where the orientation dependence is maximized along ΓK. In contrast to the lower harmonics, there is little resemblance between Figs. 4.7d-1 and d-2, and the mixture current does not simply shift the field strength dependence.

4.2.2 Influence of dephasing time

We close this chapter by considering the influence of dephasing time on the orientation dependence of HHG. We focus on harmonic 9, which has shown interesting orientation dependence in

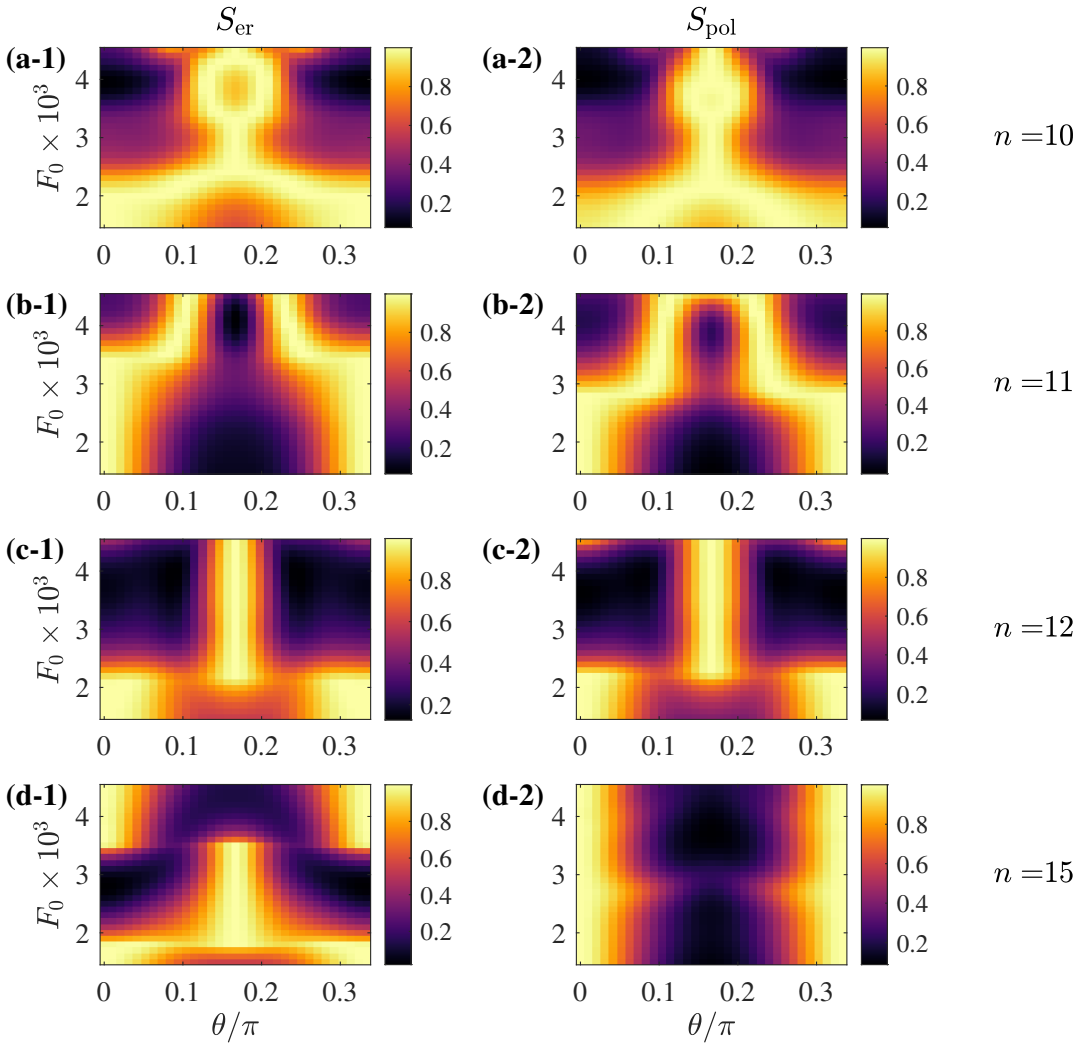

Figure 4.7: Combined orientation and field strength dependence of harmonics (10-12,15). Calculations using the full interband current S_{er} (LHS) are compared to S_{pol}(RHS), and in each case the orientation dependence is normalized to the maximum value at each field strength.

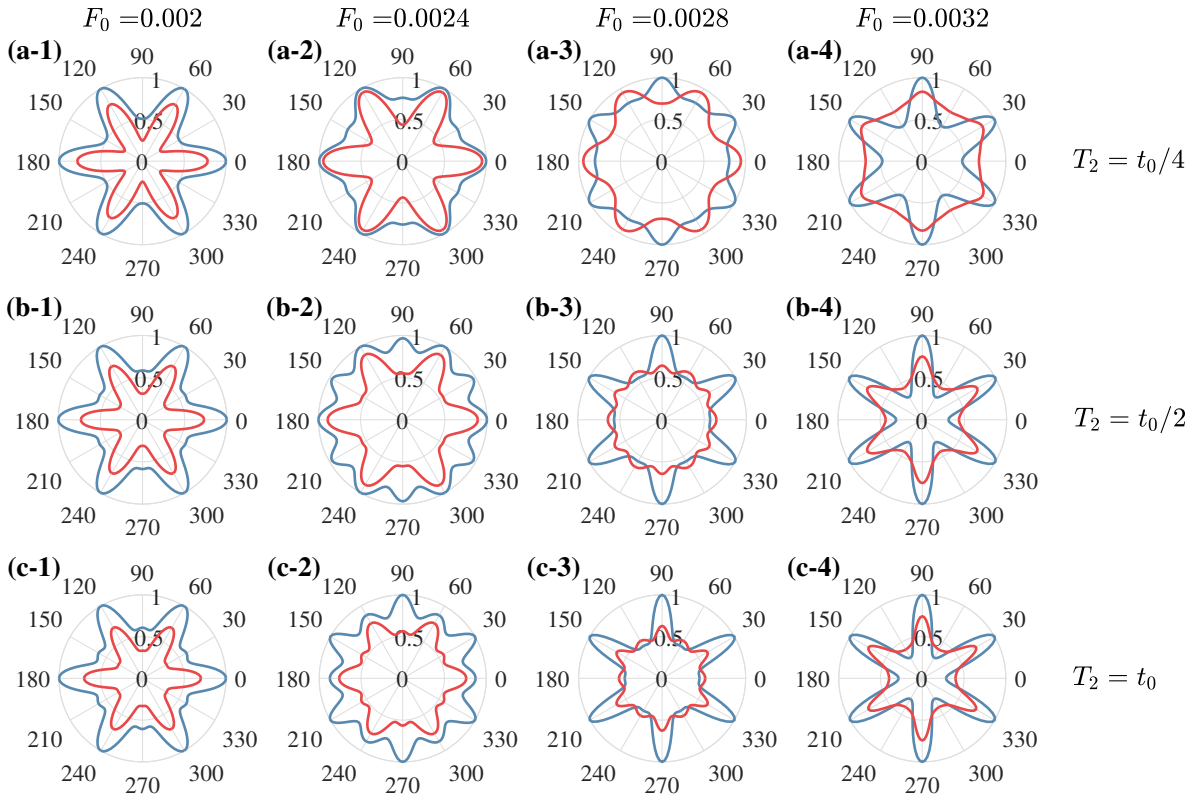

Figure 4.8: Influence of dephasing time on orientation dependence of harmonic 9. The full interband harmonic yield S_{er} (blue) is compared to S_{pol} (red).

the preceding sections. Fig. 4.8 compares the orientation dependence of S_{er} and S_{pol} for different combinations of field strengths and dephasing times. Clearly the dephasing time has a significant effect on the orientation dependence at some field strengths, but for $F_0 = 0.002$ the effect is negligible. At intermediate field strengths the orientation dependence of both S_{er} and S_{pol} depend on the dephasing time, and their behaviours are distinct. Motivated by the analysis of the previous section, we consider the combined orientation and field strength dependence in Fig. 4.9. This reveals that changing the dephasing time simply shifts the field strength dependence, and the shift is similar for both S_{er} and S_{pol}.

4.3 Summary

The smoothed gauge for gapped graphene allows effecient numerical integration of the SBEs. The tight-binding model for gapped graphene is also an ideal system for investigating the mixture current, since the matrix elements can be calculated analytically. We have shown that the mixture current has a significant influence on the orientation dependence of HHG, and this contribution

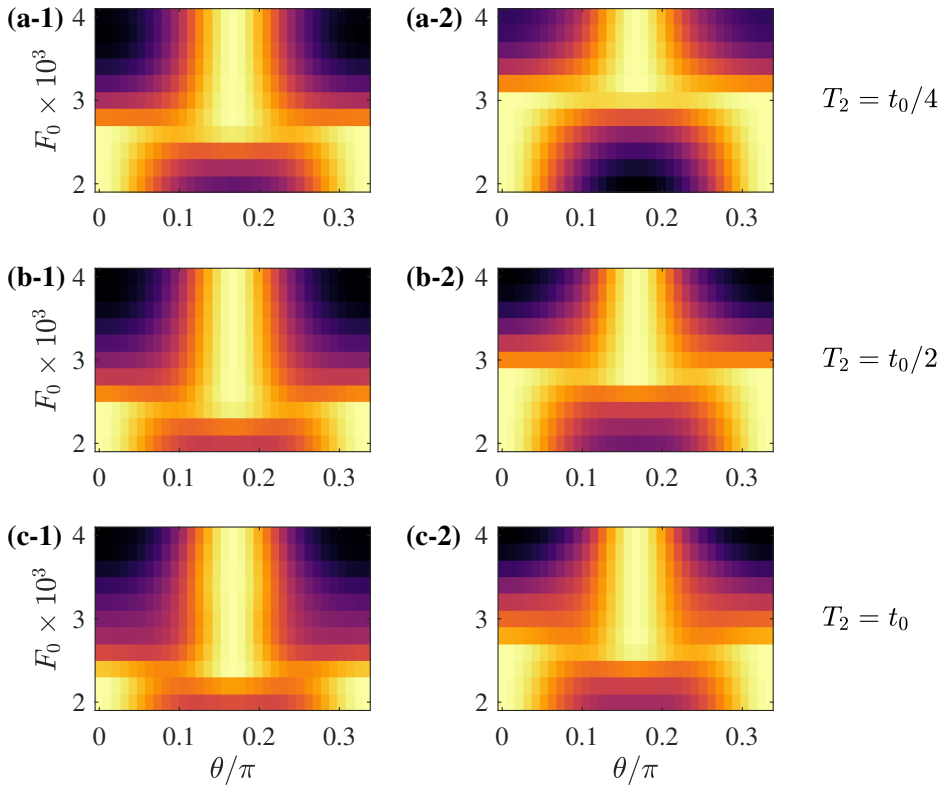

Figure 4.9: Influence of dephasing time on the combined orientation and field strength dependence of harmonic 9.

to the current should not be ignored. Finally, we have shown that the combined orientation and field strength dependence provides valuable insight for the processes influencing HHG. While the dephasing time clearly influences the orientation dependence, we observe that the main effect is simply to shift the field strength dependence of harmonic efficiencies. The results and analysis of this chapter provide useful information for the possible effects that might be observed when studying the orientation dependence of HHG in more complicated systems, which will be the subject of future work. Further, the combined orientation and field strength dependence could be an ideal candidate for comparison of simulated HHG spectra with experiment. Even if individual traces of orientation dependence show poor agreement, a shift of the field strength dependence is easy to identify and could possibly offer clues to any discrepancy between experiment and simulation.

Finally, we mention that the ellipticity of the induced current can be calculated as

$$\epsilon(\omega) = -2\mathrm{Im}\left[j_{\parallel}(\omega)j_{\perp}^{*}(\omega)\right]/S(\omega), \tag{4.6}$$

and it is found that gapped graphene can generate significant ellipticity with a strong orientation dependence. However, the mixture current is observed to have a negligible effect on ellipticity, which is not relevant to the present discussion.

Chapter 5
Semiconductor Bloch equations in the orbital basis

In this chapter we present an alternative approach for simulating the SBEs in an analytic tight-binding model. We recall from Eq. (3.3) that the Hamiltonian matrix is represented in a basis

$$|v_{\alpha,\mathbf{k}}\rangle = \frac{1}{\sqrt{N}} \sum_{\mathbf{R}} e^{i\mathbf{k}\cdot\mathbf{R}} |v_{\alpha,\mathbf{R}}\rangle, \tag{5.1}$$

where $|v_{\alpha,\mathbf{R}}\rangle$ are atomic-like orbitals. We refer to the basis $|v_{\alpha,\mathbf{k}}\rangle$ used to construct the Hamiltonian as the orbital basis, which is related to the Bloch basis $|u_{m,\mathbf{k}}\rangle$ by the unitary transformation

$$|u_{m,\mathbf{k}}\rangle = \sum_{\alpha} U_{\alpha m}(\mathbf{k}) |v_{\alpha,\mathbf{k}}\rangle, \tag{5.2}$$

where $UU^\dagger = 1$. We generalize the SBEs to simulate the dynamics directly in the orbital basis, which avoids any numerical complications due to non-smooth dipole matrix elements in the Bloch basis. This formulation of the SBEs is analogous to the approach developed in Ref. [30], which used the basis corresponding to MLWF orbitals resulting from DFT structural calculations. The two approaches are complementary; the orbital basis applies to tight-binding models, while the MLWF basis is used for numerically calculated band structure.

5.1 Dynamics in an arbitrary basis

In the previous chapters we have assumed to be working in the basis of Bloch functions, which are eigenstates of the crystal Hamiltonian. In this section we generalize the SBEs to consider a more arbitrary basis, in which the off-diagonal Hamiltonian matrix elements are non-zero. It is convenient to work with the $\mathbf{k}\cdot\mathbf{p}$ Hamiltonian [36, 48, 49]

$$H(\mathbf{k}) = e^{-i\mathbf{k}\cdot\mathbf{x}} H_0 e^{i\mathbf{k}\cdot\mathbf{x}} = H_0 + \mathbf{k}\cdot\mathbf{p} + \frac{k^2}{2}, \tag{5.3}$$

so that

$$\begin{aligned}\langle u_{m,\mathbf{k}}|H(\mathbf{k})|u_{n,\mathbf{k}}\rangle &= \langle u_{m,\mathbf{k}}|e^{-i\mathbf{k}\cdot\mathbf{x}}H_0e^{i\mathbf{k}\cdot\mathbf{x}}|u_{n,\mathbf{k}}\rangle \\ &= \langle \Phi_{m,\mathbf{k}}|H_0|\Phi_{n,\mathbf{k}}\rangle \\ &= \delta_{mn}E_m(\mathbf{k}).\end{aligned} \tag{5.4}$$

The matrix elements of $H(\mathbf{k})$ can be represented in any basis related to the Bloch functions by a unitary transformation. To be specific, consider the change of basis

$$|\bar{u}_{m,\mathbf{k}}\rangle = \sum_{\mu} U^{\dagger}_{\mu m}(\mathbf{k})|u_{\mu,\mathbf{k}}\rangle, \tag{5.5}$$

with the inverse transformation

$$|u_{m,\mathbf{k}}\rangle = \sum_{\nu} U_{\nu m}(\mathbf{k})|\bar{u}_{\nu,\mathbf{k}}\rangle. \tag{5.6}$$

If the unitary matrices $U(\mathbf{k})$ are diagonal, these transformations reduce to the phase transformations considered in Eq. (2.69). Throughout this chapter, $u_{m,\mathbf{k}}$ refers to a basis of Bloch functions that diagonalize the $H(\mathbf{k})$, while $\bar{u}_{m,\mathbf{k}}$ is a non-diagonal basis related to $u_{m,\mathbf{k}}$ by a unitary matrix. The transformations (5.5) and (5.6) have been described as a "generalized" gauge transformation in previous work [41, 45, 59, 60] concerning maximally localized Wannier functions.

In the Bloch basis we study the dynamics using the Ansatz

$$|\psi(t)\rangle = \sum_{m,\mathbf{k}} a_m(\mathbf{k},t)|\Phi_{m,\mathbf{k}}\rangle, \tag{5.7}$$

where $a_m(\mathbf{k},t)$ is the time-dependent probability amplitude for the Bloch state $\Phi_{m,\mathbf{k}}$. This leads to the familiar SBEs introduced in chapter 2. Alternatively, one can formulate the dynamics in the transformed basis using the Ansatz

$$\begin{aligned}|\psi(t)\rangle &= \sum_{m,\mathbf{k}} \bar{a}_m(\mathbf{k},t)|\bar{\Phi}_{m,\mathbf{k}}\rangle \\ &= \sum_{\mu,m,\mathbf{k}} U^{\dagger}_{\mu m}(\mathbf{k})\bar{a}_m(\mathbf{k},t)|\Phi_{\mu,\mathbf{k}}\rangle.\end{aligned} \tag{5.8}$$

Equating (5.7) and (5.8), we obtain the transformation between probability amplitudes

$$\begin{aligned} a_m(\mathbf{k},t) &= \sum_\mu U^\dagger_{m\mu}(\mathbf{k})\bar{a}_\mu(\mathbf{k},t) \\ \bar{a}_m(\mathbf{k},t) &= \sum_\mu U_{m\mu}(\mathbf{k})a_\mu(\mathbf{k},t), \end{aligned} \tag{5.9}$$

while the density matrix elements transform according to

$$\begin{aligned} \rho_{nm}(\mathbf{k},t) &= \left[\sum_\mu U^\dagger_{m\mu}(\mathbf{k})\bar{a}_\mu(\mathbf{k},t)\right]^* \left[\sum_\nu U^\dagger_{n\nu}(\mathbf{k})\bar{a}_\nu(\mathbf{k},t)\right] \\ &= \sum_{\mu\nu} U^\dagger_{n\nu}(\mathbf{k})U_{\mu m}(\mathbf{k})\bar{\rho}_{\nu\mu}(\mathbf{k},t), \end{aligned} \tag{5.10}$$

and

$$\begin{aligned} \bar{\rho}_{nm}(\mathbf{k},t) &= \left[\sum_\mu U_{m\mu}(\mathbf{k})a_\mu(\mathbf{k},t)\right]^* \left[\sum_\nu U_{n\nu}(\mathbf{k})a_\nu(\mathbf{k},t)\right] \\ &= \sum_{\mu,\nu} U_{n\nu}(\mathbf{k})U^\dagger_{\mu m}(\mathbf{k})\rho_{\nu\mu}(\mathbf{k},t). \end{aligned} \tag{5.11}$$

These transformations can be written more succinctly as

$$\begin{aligned} \rho_{nm}(\mathbf{k},t) &= \left[U^\dagger(\mathbf{k})\bar{\rho}(\mathbf{k},t)U(\mathbf{k})\right]_{nm} \\ \bar{\rho}_{nm}(\mathbf{k},t) &= \left[U(\mathbf{k})\rho(\mathbf{k},t)U^\dagger(\mathbf{k})\right]_{nm}, \end{aligned} \tag{5.12}$$

and it is also straightforward to verify that the Hamiltonian transforms according to

$$\bar{H}(\mathbf{k}) = U(\mathbf{k})H(\mathbf{k})U^\dagger(\mathbf{k}). \tag{5.13}$$

The transformation of the dipole matrix elements is more subtle due to the gradient term;

specifically,

$$\begin{aligned}\bar{\boldsymbol{\xi}}_{nm}(\mathbf{k}) &= \langle \bar{u}_{n,\mathbf{k}} | i\nabla_{\mathbf{k}} | \bar{u}_{m,\mathbf{k}} \rangle \\ &= \sum_{\mu,\nu} U_{n\nu}(\mathbf{k}) \langle u_{\nu,\mathbf{k}} | i\nabla_{\mathbf{k}} U^{\dagger}_{\mu m}(\mathbf{k}) | u_{\mu,\mathbf{k}} \rangle \\ &= \sum_{\mu,\nu} \left[U_{n\nu}(\mathbf{k}) \boldsymbol{\xi}_{\nu\mu}(\mathbf{k}) U^{\dagger}_{\mu m}(\mathbf{k}) + i U_{n\nu}(\mathbf{k}) \langle u_{\nu,\mathbf{k}} | u_{\mu,\mathbf{k}} \rangle \nabla_{\mathbf{k}} U^{\dagger}_{\mu m}(\mathbf{k}) \right] \\ &= \left[U(\mathbf{k}) \boldsymbol{\xi}(\mathbf{k}) U^{\dagger}(\mathbf{k}) \right]_{nm} + i \left[U(\mathbf{k}) \nabla_{\mathbf{k}} U(\mathbf{k}) \right]_{nm}, \end{aligned} \tag{5.14}$$

from which we conclude

$$\bar{\boldsymbol{\xi}}(\mathbf{k}) = U(\mathbf{k}) \boldsymbol{\xi}(\mathbf{k}) U^{\dagger}(\mathbf{k}) + i U(\mathbf{k}) \nabla_{\mathbf{k}} U(\mathbf{k}). \tag{5.15}$$

The transformations (5.12) and (5.13) are covariant, but the dipole matrix is not covariant due to the gradient term in (5.15) [30, 59]. It should be emphasized that there is no separation of intra- and interband dipole matrix elements in an arbitrary basis, since energy bands are specific to the basis which diagonalizes the Hamiltonian.

5.1.1 SBEs in comoving frame

Since the basis functions $\bar{\Phi}_{m\mathbf{k}}$ are not eigenvectors of $H(\mathbf{k})$, the SBEs need to be generalized accordingly. This was demonstrated in Ref. [30] in the static momentum frame, but here we present an analogous formulation in the comoving frame. Recalling the time-dependent Hamiltonian $H(t) = H_0 - e\mathbf{F}(t) \cdot \mathbf{x}$, the matrix elements of the density matrix equation $\dot{\rho}(t) = -i\,[H(t), \rho(t)]$ are most generally given by

$$\partial_t \bar{\rho}_{nm}(\mathbf{k}, t) = -i \left[H_0, \rho(\mathbf{k}, t) \right]_{\bar{n}\bar{m}} - e \left[\mathbf{F}(t) \cdot \mathbf{D}_{\mathbf{k}}, \rho(\mathbf{k}, t) \right]_{\bar{n}\bar{m}}, \tag{5.16}$$

where we denote

$$\bar{\mathcal{O}}_{nm}(\mathbf{k}) = \left[\mathcal{O}(\mathbf{k}) \right]_{\bar{n}\bar{m}} = \langle \bar{\Phi}_{n,\mathbf{k}} | \mathcal{O}(\mathbf{k}) | \bar{\Phi}_{m,\mathbf{k}} \rangle, \tag{5.17}$$

to indicate that matrix elements are evaluated in the non-diagonal basis. In the Bloch basis the first term on the RHS of Eq. (5.16) simplifies to $\varepsilon_{nm}(\mathbf{k}) \rho_{nm}(\mathbf{k}, t)$, and we recover the regular SBEs (2.32). To continue in a non-diagonal basis, we evaluate

$$\left[\mathbf{F}(t) \cdot \mathbf{D}_{\mathbf{k}}, \rho(\mathbf{k}, t) \right]_{\bar{n}\bar{m}} = \mathbf{F}(t) \cdot \nabla_{\mathbf{k}} \bar{\rho}_{nm}(\mathbf{k}, t) - i \left[\mathbf{F}(t) \cdot \boldsymbol{\xi}(\mathbf{k}), \rho(\mathbf{k}, t) \right]_{\bar{n}\bar{m}}, \tag{5.18}$$

where we do not separate diagonal and off-diagonal components of the dipole matrix elements. Defining the combined matrix elements

$$G_{nm}(\mathbf{k},t) = H_{nm}(\mathbf{k}) - e\mathbf{F}(t)\cdot\boldsymbol{\xi}_{nm}(\mathbf{k}), \tag{5.19}$$

and transforming Eq. (5.16) to the comoving frame, we obtain the generalized SBEs

$$\partial_t\bar{\rho}_{nm}(\mathbf{K},t) = -i\left[G(\mathbf{K}_t,t),\rho(\mathbf{k},t)\right]_{\bar{n}\bar{m}} + \partial_t\bar{\rho}^{(d)}_{nm}(\mathbf{K},t), \tag{5.20}$$

where we have added a phenomenological dephasing term.

The dephasing term is most easily propagated in the Bloch basis according to

$$\partial_t\rho^{(d)}_{nm}(\mathbf{K},t) = -\frac{(1-\delta_{nm})}{T_2}\rho_{nm}(\mathbf{K},t). \tag{5.21}$$

To transform the dephasing term to an arbitrary basis, we use the transformation (5.12) in the comoving frame,

$$\begin{aligned}\rho_{nm}(\mathbf{K},t) &= \left[U^\dagger(\mathbf{K}_t)\bar{\rho}(\mathbf{K},t)U(\mathbf{K}_t)\right]_{nm}\\ \bar{\rho}_{nm}(\mathbf{K},t) &= \left[U(\mathbf{K}_t)\rho(\mathbf{K},t)U^\dagger(\mathbf{K}_t)\right]_{nm},\end{aligned} \tag{5.22}$$

which gives

$$\begin{aligned}\partial_t\bar{\rho}^{(d)}_{nm}(\mathbf{K},t) &= \sum_{\mu,\nu} U_{n\nu}(\mathbf{K}_t)U^\dagger_{\mu m}(\mathbf{K}_t)\partial_t\rho^{(d)}_{\nu\mu}(\mathbf{K},t)\\ &= -\frac{1}{T_2}\sum_{\mu,\nu}(1-\delta_{\mu\nu})U_{n\nu}(\mathbf{K}_t)U^\dagger_{\mu m}(\mathbf{K}_t)\rho_{\nu\mu}(\mathbf{K},t)\\ &= -\frac{1}{T_2}\sum_{\mu,\nu,a,b}(1-\delta_{\mu\nu})U_{n\nu}(\mathbf{K}_t)U^\dagger_{\mu m}(\mathbf{K}_t)U^\dagger_{\nu b}(\mathbf{K}_t)U_{a\mu}(\mathbf{K}_t)\bar{\rho}_{ba}(\mathbf{K},t).\end{aligned} \tag{5.23}$$

The dephasing term involves a 4-dimensional sum, which becomes computationally expensive to evaluate as the number of bands increases. Further, since the unitary matrix elements are evaluated at the time-dependent momentum, they must be calculated independently for each time step. This approach is well suited for tight-binding Hamiltonians that can be diagonalized analytically, which results in closed-form expressions for U. In contrast, the static momentum frame is better suited for Hamiltonians requiring numerical diagonalization, since the unitary matrix is only required on a fixed momentum grid. Our approach is thus complementary to that of Ref. [30], which employed the static frame to propagate the SBEs in the MLWF basis

resulting from numerical band structure calculations.

5.1.2 Change of basis

The generalized SBEs (5.20) can also be derived by applying a covariant transformation to the SBEs in the Bloch basis. We start by writing the coherent part of the SBEs in the Bloch basis as

$$\dot{\rho}_{nm}(\mathbf{K},t) = -i\left[G(\mathbf{K}_t,t),\rho(\mathbf{K},t)\right]_{nm}, \tag{5.24}$$

where $\dot{\rho} = \partial_t\rho$, and hereafter we suppress explicit (k,t)-dependence to simplify notation; it should also be understood that $G(\mathbf{K}_t)$ and $U(\mathbf{K}_t)$ are always evaluated at the time-dependent momentum $\mathbf{K}_t$ in the comoving frame. We transform both sides of Eq. (5.24) according to

$$\begin{aligned}\left[U\dot{\rho}U^\dagger\right]_{nm} &= -i\left\{U\left[G,\rho\right]U^\dagger\right\}_{nm}\\ &= -i\left[UG\rho U^\dagger - U\rho GU^\dagger\right]_{nm}\\ &= -i\left[UGU^\dagger U\rho U^\dagger - U\rho U^\dagger UGU^\dagger\right]_{nm}\\ &= -i\left[UGU^\dagger,\bar{\rho}\right]_{nm},\end{aligned} \tag{5.25}$$

where we have identified the transformed density matrix using the Eq. (5.22). Now, the matrix on the LHS can be written as

$$\begin{aligned}U\dot{\rho}U^\dagger &= \partial_t(U\rho U^\dagger) - \dot{U}\rho U^\dagger - U\rho\dot{U}^\dagger\\ &= \partial_t\bar{\rho} - \dot{U}U^\dagger U\rho U^\dagger - U\rho U^\dagger U\dot{U}^\dagger\\ &= \partial_t\bar{\rho} - \dot{U}U^\dagger\bar{\rho} - \bar{\rho}U\dot{U}^\dagger,\end{aligned} \tag{5.26}$$

where we have used $U^\dagger U = 1$. Clearly $\partial_t(UU^\dagger) = 0$, which implies $\dot{U}U^\dagger = -U\dot{U}^\dagger$,and thus

$$U\dot{\rho}U^\dagger = \partial_t\bar{\rho} + \left[U\dot{U}^\dagger,\bar{\rho}\right]. \tag{5.27}$$

In the comoving frame we have

$$\begin{aligned}\dot{U}^\dagger(\mathbf{K}_t) &= \dot{\mathbf{K}}_t\cdot\nabla_{\mathbf{K}_t}U^\dagger(\mathbf{K}_t)\\ &= e\mathbf{F}(t)\cdot\nabla_{\mathbf{K}_t}U^\dagger(\mathbf{K}_t),\end{aligned} \tag{5.28}$$

and so

$$U\dot{\rho}U^\dagger = \partial_t\bar{\rho} + e\mathbf{F}\cdot\left[U\nabla U^\dagger,\bar{\rho}\right]. \tag{5.29}$$

Inserting this result into Eq. (5.25) gives

$$\partial_t \bar{\rho}_{nm} = -i \left[U G U^\dagger, \bar{\rho} \right]_{nm} - e\mathbf{F} \cdot \left[U \nabla U^\dagger, \bar{\rho} \right]_{nm}, \tag{5.30}$$

or

$$\partial_t \bar{\rho}_{nm}(\mathbf{K}, t) = -i \left[G(\mathbf{K}_t, t), \rho(\mathbf{K}, t) \right]_{\bar{n}\bar{m}}, \tag{5.31}$$

where we have identified the transformations

$$\begin{aligned} \bar{H}(\mathbf{K}_t) &= U(\mathbf{K}_t) H(\mathbf{K}_t) U^\dagger(\mathbf{K}_t) \\ \bar{\boldsymbol{\xi}}(\mathbf{K}_t) &= U(\mathbf{K}_t) \boldsymbol{\xi}(\mathbf{K}_t) U^\dagger(\mathbf{K}_t) + i U(\mathbf{K}_t) \nabla_{\mathbf{K}_t} U^\dagger(\mathbf{K}_t), \end{aligned} \tag{5.32}$$

in the comoving frame. Although these transformations can also be obtained by applying the boost operator to Eqs. (5.13) and (5.15), this derivation highlights that the correct operator transformations ensure covariance of the SBEs.

5.1.3 Initial condition and calculation of observables

In order to integrate the generalized SBEs, we must specify an initial condition for the density matrix elements. The initial condition is most intuitive in the Bloch basis, where the off-diagonal matrix elements are zero and the diagonal elements are the band occupations of an unperturbed system. At zero temperature the valence bands are occupied and the conduction bands are empty, while at non-zero temperature the band occupations can be specified by a thermal distribution [21, 30]. In any case, for an initial condition $\rho(\mathbf{K}, t_0)$ specified in the Bloch basis, we have

$$\begin{aligned} \bar{\rho}_{nm}(\mathbf{K}, t_0) &= \sum_{\mu,\nu} U_{n\nu}(\mathbf{K}) U^\dagger_{\mu m}(\mathbf{K}) \rho_{\nu\mu}(\mathbf{K}, t_0) \\ &= \sum_{\mu} U_{n\mu}(\mathbf{K}) U^\dagger_{\mu m}(\mathbf{K}) \rho_{\mu\mu}(\mathbf{K}, t_0), \end{aligned} \tag{5.33}$$

where the unitary matrices are evaluated at the initial (field-free) k-space coordinates. At zero temperature this simplifies to

$$\bar{\rho}_{nm}(\mathbf{K}, t_0) = \sum_{\mu \leq N_v} U_{n\mu}(\mathbf{K}) U^\dagger_{\mu m}(\mathbf{K}),$$

where N_v is the number of valence bands.

When the SBEs are propagated in an arbitrary basis, the band occupations can be obtained

using the transformation

$$\rho_{nn}(\mathbf{K},t) = U^{\dagger}_{n\mu}(\mathbf{K}_t)U_{\nu n}(\mathbf{K}_t)\bar{\rho}_{\mu\nu}(\mathbf{K},t). \tag{5.34}$$

In principle the total current can be calculated by generalizing Eq. (2.49) according to

$$\begin{aligned}\mathbf{j}(t) =& e\int d\mathbf{k}\mathrm{Tr}\left\{[\mathbf{D}, H(t)]\,\rho(t)\right\}\\ =& e\sum_{n,m}\int d\mathbf{k}\left\{\nabla_{\mathbf{k}}\bar{H}(\mathbf{k}) - i\left[\bar{\boldsymbol{\xi}}(\mathbf{k}), \bar{H}(\mathbf{k})\right]\right\}_{nm}\bar{\rho}_{mn}(\mathbf{k},t)\\ &- i\sum_{n,m}\int d\mathbf{k}\left\{\nabla_{\mathbf{k}} - i\bar{\boldsymbol{\xi}}(\mathbf{k}), \mathbf{F}(t)\cdot\left[\nabla_{\mathbf{k}} - i\bar{\boldsymbol{\xi}}(\mathbf{k})\right]\right\}_{nm}\bar{\rho}_{mn}(\mathbf{k},t).\end{aligned} \tag{5.35}$$

We note that only the first integral on the RHS was considered in Ref. [30], which simulated HHG in the MLWF basis. There are additional contributions to the current arising from the commutator $[\mathbf{x}, \mathbf{F}\cdot\mathbf{x}]$, which does not vanish within the crystal momentum representation [36, 37, 46]. In Sec. 2.2 we saw that this commutator yields the anomalous intraband and the interband mixture currents in the Bloch basis; however, an arbitrary basis does not admit an intuitive decomposition of the current. In fact, one cannot even separate intra and interband contributions in a non-diagonal basis, since the band picture is exclusive to the Bloch basis which diagonalizes the Hamiltonian.

It is preferable to calculate the current starting from Eq. (2.68) in the Bloch basis. We then transform the density matrix elements using Eq. (5.22), resulting in

$$\mathbf{j}_{\text{ra}}(t) = e\sum_{n,\mu,\nu}\int_{\overline{BZ}} d\mathbf{K}\mathbf{v}_n(\mathbf{K}_t)U^{\dagger}_{n\mu}(\mathbf{K}_t)U_{\nu n}(\mathbf{K}_t)\bar{\rho}_{\mu\nu}(\mathbf{K},t) \tag{5.36a}$$

$$\mathbf{j}_{\text{an}}(t) = -\sum_{n,\mu,\nu}\int_{\overline{BZ}} d\mathbf{K}\mathbf{v}^a_n(\mathbf{K}_t,t)U^{\dagger}_{n\mu}(\mathbf{K}_t)U_{\nu n}(\mathbf{K}_t)\bar{\rho}_{\mu\nu}(\mathbf{K},t) \tag{5.36b}$$

$$\mathbf{j}_{\text{mix}}(t) = -\sum_{n,m,\mu,\nu}\int_{\overline{BZ}} d\mathbf{K}\mathbf{W}_{nm}(\mathbf{K}_t,t)U^{\dagger}_{m\mu}(\mathbf{K}_t)U_{\nu n}(\mathbf{K}_t)\bar{\rho}_{\mu\nu}(\mathbf{K},t) \tag{5.36c}$$

$$\mathbf{j}_{\text{pol}}(t) = e\frac{d}{dt}\sum_{n,m,\mu,\nu}\int_{\overline{BZ}} d\mathbf{K}\mathbf{d}_{nm}(\mathbf{K}_t)U^{\dagger}_{m\mu}(\mathbf{K}_t)U_{\nu n}(\mathbf{K}_t)\bar{\rho}_{\mu\nu}(\mathbf{K},t). \tag{5.36d}$$

This way, the contributions to the current can still be resolved in the Bloch basis, but using the density matrix elements calculated in an arbitrary basis. In other words, the basis transformation is used only for the propagation of the SBEs, and we transform the numerical results back to the Bloch basis in order to evaluate the current.

5.2 Tight-binding orbital basis

We now discuss the considerable advantage afforded by a non-diagonal basis when applied to analytic tight-binding models. Recall from Sec. 3.1 that for a tight-binding Hamiltonian matrix $\bar{H}(\mathbf{k})$ diagonalized by a unitary matrix $U(\mathbf{k})$, the Bloch eigenvectors are given by

$$|u_{m,\mathbf{k}}\rangle = \sum_{\alpha} U_{\alpha m}(\mathbf{k})|v_{\alpha,\mathbf{k}}\rangle, \tag{5.37}$$

where $|v_{\alpha,\mathbf{k}}\rangle$ is the basis in which the tight-binding Hamiltonian matrix $\bar{H}(\mathbf{k})$ is represented. Since the k-dependent basis states $|v_{\alpha,\mathbf{k}}\rangle$ are related to the tight-binding orbitals via,

$$|v_{\alpha,\mathbf{k}}\rangle = \frac{1}{\sqrt{N}} \sum_{\mathbf{R}} e^{i\mathbf{k}\cdot\mathbf{R}}|v_{\alpha,\mathbf{R}}\rangle,$$

we refer to this basis as the orbital basis. Naturally, we can use this unitary matrix to transform the SBEs from the Bloch basis to the orbital basis. It was shown in Sec. 3.1 that the dipole matrix elements between Bloch functions are simply

$$\boldsymbol{\xi}_{nm}(\mathbf{k}) = i \sum_{\alpha} U^{*}_{\alpha n}(\mathbf{k}) \nabla_{\mathbf{k}} U_{\alpha m}(\mathbf{k}) = i \left[U^{\dagger}(\mathbf{k}) \nabla_{\mathbf{k}} U(\mathbf{k})\right]_{nm}, \tag{5.38}$$

since the dipole matrix elements vanish in the orbital basis, by virtue of Eq. (3.5). As a result, the SBEs in the orbital basis are simply

$$\partial_t \bar{\rho}_{nm}(\mathbf{K}, t) = -i \left[\bar{H}(\mathbf{K}_t), \bar{\rho}(\mathbf{K}, t)\right]_{nm} + \partial_t \bar{\rho}^{(d)}_{nm}(\mathbf{K}, t),$$

where $\bar{H}(\mathbf{k})$ is the tight-binding Hamiltonian matrix, and $\bar{\rho}$ is the density matrix in the orbital basis. To see why it is always possible to obtain a basis with vanishing dipole matrix elements, we set $\bar{\boldsymbol{\xi}}(\mathbf{k}) = 0$ in the transformation (5.15) to get

$$\nabla_{\mathbf{k}} U(\mathbf{k}) = i\boldsymbol{\xi}(\mathbf{k}) U^{\dagger}(\mathbf{k}). \tag{5.39}$$

The solution to this matrix differential equation provides a unitary transformation that eliminates the dipole matrix elements. Comparing Eq. (5.38) to (5.15), it is clear that the matrix of eigenvectors for a tight-binding Hamiltonian matrix is an example of such a solution.

Eliminating the dipole matrix elements from the SBEs avoids any complications that might arise from non-smooth behaviour. In Chapter 4 we saw that gapped graphene has singular Berry connections and discontinuous TDMs in the Bloch gauge resulting from analytic diagonalization of the Hamiltonian. We developed a gauge smoothing transformation to eliminate the singular behaviour, and this facilitated efficient numerical integration of the SBEs. Although this approach was successful, deriving this gauge function was laborious even for the simple 2-band Hamiltonian of the gapped graphene model. It is reasonable to assume that analytic gauge smoothing of multi-band tight-binding models would be even more complicated; assuming it is even possible. Numerical gauge-smoothing algorithms based on the parallel transport gauge transformation [33, 36, 41] have been developed, but their implementation is quite technical and they ultimately restrict the model to a discretized k-mesh. The tight-binding orbital basis makes gauge smoothing unecessary, as we only need the Hamiltonian to propagate the SBEs. Not only are the Hamiltonian matrix elements smooth and periodic, but they are also slowly varying compared to the dipole matrix elements; even in the analytically smoothed gauge for gapped graphene. As a result, the orbital basis can significantly reduce the number of k-points required to achieve convergence. Further, while non-smooth Berry connections and TDMs are strongly detrimental to numerical integration of the SBEs, they do not affect the calculation of the current using Eq. (5.36). Most importantly, integration of the SBEs using the orbital basis is feasible even for systems with non-vanishing topological invariants, which do not admit a smooth Bloch gauge throughout the BZ [41, 53, 67].

5.3 Results for gapped graphene

In this section we use the orbital basis to simulate HHG in gapped graphene discussed in Chapter 3, where the 2×2 Hamiltonian is represented in a basis of p_z orbitals at each atomic position in the lattice. Gapped graphene is a natural example to verify the orbital basis approach, since we can compare to the results of Chapter 4 using the smoothed Bloch gauge. We calculate the total harmonic efficiency arising from both the parallel and perpendicular components of the current; i.e.

$$S(\omega) = |j_{\parallel}(\omega)|^2 + |j_{\perp}(\omega)|^2, \tag{5.40}$$

and we consider incident optical polarization along two different orientations; ΓM and ΓK. Fig. 5.1 compares HHG spectra calculated using the orbital and Bloch bases, and the results are clearly equivalent over the full harmonic range. Although the noise floor is not discernible in this plot, it is generally found that the orbital basis results in a lower noise floor. In terms of numerical efficiency, the integration times are similar for the Bloch and orbital calculations in

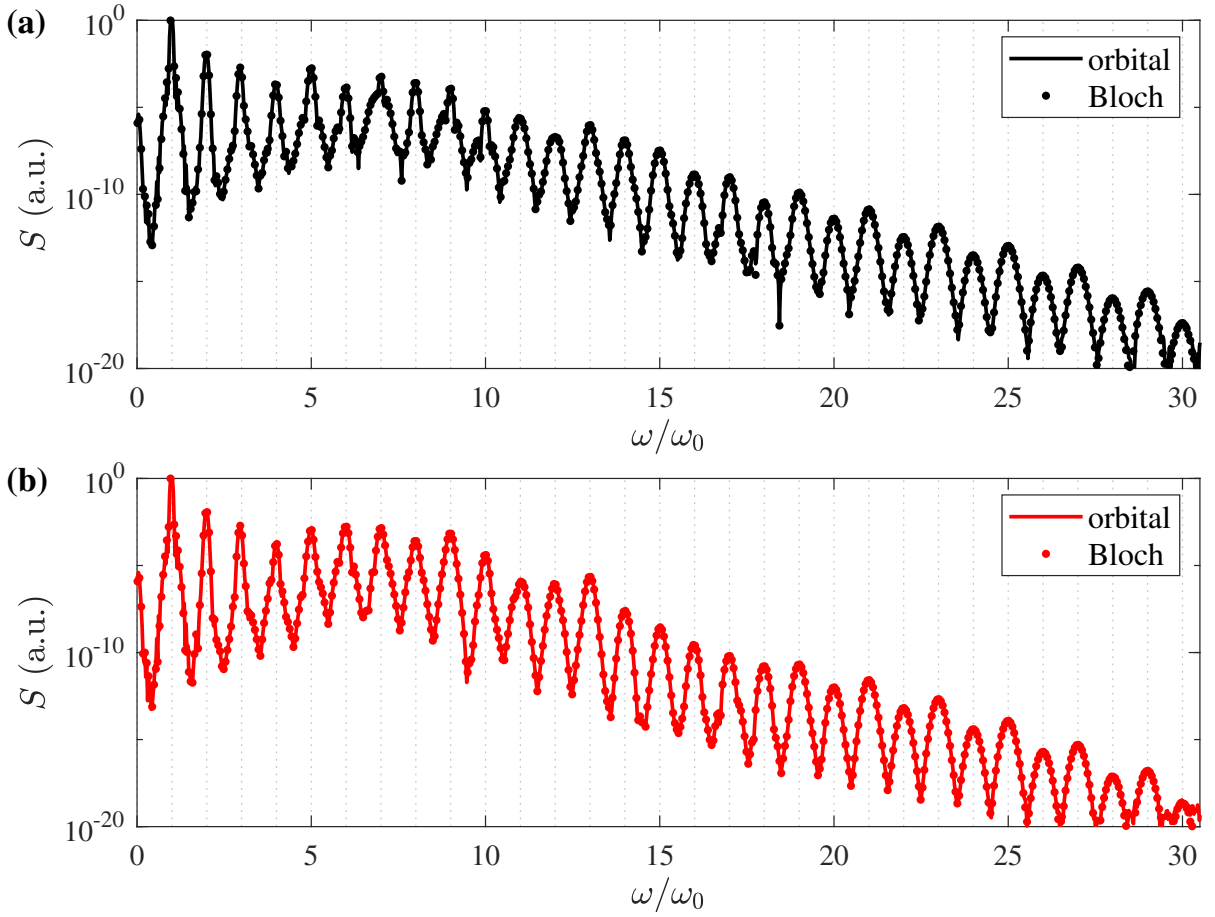

Figure 5.1: Comparison of Bloch and orbital basis calculations for HHG spectra in gapped graphene for two different orientations; (a) $\Gamma - M$, (b) $\Gamma - K$.

this example. This is due to competing effects affecting performance. The gauge smoothing function for the Bloch basis is costly to evaluate, whereas the dephasing term adds computation time in the orbital basis. However, the full simulation takes longer for the orbital basis, since the calculation of observables also involves the U matrix. While both calculations take longer in models with a larger number of bands, the computation time in the orbital basis increases more rapidly. Further, if the Bloch structure is evaluated using cubic spline interpolation rather than evaluating the full analytic expressions in the smoothed gauge, the performance can be improved significantly.

We can also calculated the integrated harmonic yield

$$S_n = \int_{n\omega_0-\delta\omega}^{n\omega_0+\delta\omega} d\omega S(\omega), \tag{5.41}$$

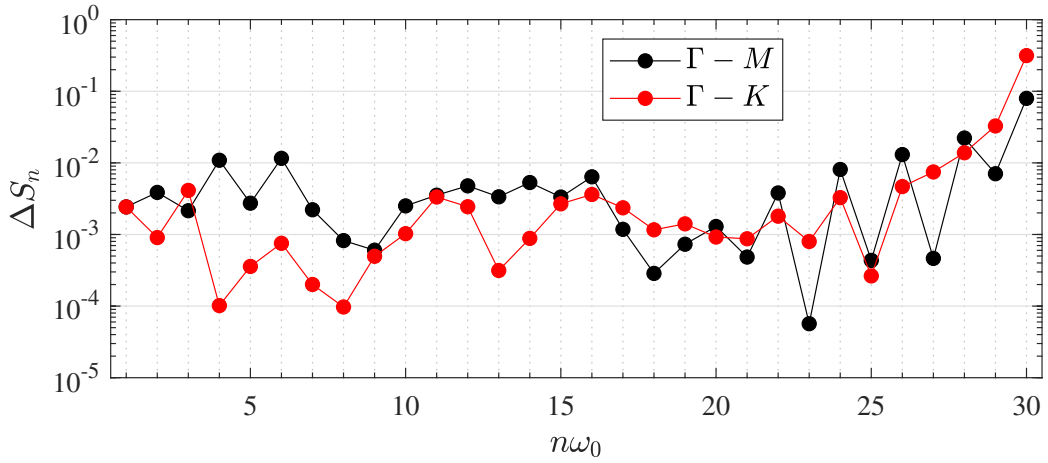

Figure 5.2: Relative difference of harmonic yields calculating using orbital vs. Bloch basis.

and from this the relative difference

$$\Delta S_n = \frac{|S_n^{\text{orb}} - S_n^{\text{Bloch}}|}{S_n^{\text{orb}}}, \tag{5.42}$$

between the two calculations. The difference ΔS is shown in Fig. 5.2, and we observe that the discrepancy only becomes significant when the harmonics approach the noise floor. For all practical purposes, we conclude that the Bloch and orbital calculations give identical results.

5.4 Results for QWZ model

An interesting application of the orbital basis is to study HHG in topological materials with non-zero Chern number, which do not admit a smooth and periodic gauge in the Bloch basis [41, 53]. As a simple example we consider the Qi-Wu-Zhang (QWZ) model for a topological insulator [68, 69],

$$\begin{aligned} H(\mathbf{k}) &= \alpha \left[\sin ak_x \sigma_x + \sin ak_y \sigma_y + (\gamma + \cos ak_x + \cos ak_y)\, \sigma_z\right] \\ &= \alpha \begin{bmatrix} \gamma + \cos ak_x + \cos ak_y & \sin ak_x + i \sin ak_y \\ \sin ak_x + i \sin ak_y & -\gamma - \cos ak_x + \cos ak_y \end{bmatrix} \\ &\equiv \begin{bmatrix} \Delta(\mathbf{k}) & q(\mathbf{k}) \\ q^*(\mathbf{k}) & -\Delta(\mathbf{k}) \end{bmatrix}, \end{aligned} \tag{5.43}$$

where α is a scale factor used to tune the energy scale, while the parameter γ controls the characteristics of the model. This tight-binding model does not correspond to a basis of atomic

orbitals. Rather, the QWZ model describes a spin-1/2 particle with two internal spin states hopping on a square lattice, and the energy bands result from the spin degree of freedom. The QWZ model can be interpreted as a simple model for a paramagnetic semiconductor. Although the real-space interpretation of the QWZ model is not inuitive [69], it is valuable as a simple 2D model with tunable topological properties. The symmetry points of the BZ for the square lattice are indicated in Fig. 5.3a.

The bandgap of the QWZ model is given by

$$\begin{aligned}\varepsilon(\mathbf{k}) &= \sqrt{\Delta^2(\mathbf{k}) + |q|^2(\mathbf{k})} \\ &= \alpha\sqrt{\sin^2 ak_x + \sin^2 ak_y + (\gamma + \cos ak_x + \cos ak_y)^2},\end{aligned} \tag{5.44}$$

where $s_m = -1(+1)$ for the valence (conduction) band. The energy gap closes when $\gamma = -2, 0, +2$; with Dirac cones [53, 69] located at different points in the BZ for each case. When $\gamma = -2$ there is a single Dirac point at Γ ($k = 0$); for $\gamma = 0$ there are 2 inequivalent Dirac points at the midpoints (X) of each band edge; while for $\gamma = 2$ the bandgap closes at the M points of the BZ, which comprise a single Dirac point. The Chern number Q also depends on the value of γ according to [69]

$$\begin{aligned}\gamma < -2, &\quad Q = 0 \\ -2 < \gamma < 0, &\quad Q = -1 \\ 0 < \gamma < 2, &\quad Q = +1 \\ \gamma > 2, &\quad Q = 0.\end{aligned} \tag{5.45}$$

To simulate HHG spectra in the QWZ model we use a lattice constant $a = 7$ a.u., and we consider two different combinations of parameters,

$$\begin{aligned}\text{I}: &\quad \alpha = 0.0367, \gamma = -3.5 \\ \text{II}: &\quad \alpha = 0.0735, \gamma = -1.2,\end{aligned} \tag{5.46}$$

where I is a trivial phase, while II is a topological phase. Fig. 5.3 shows the 2D bandgap throughout the BZ for phases I and II. The parameters for each phase were chosen to give similar maximum and minimum bandgaps. In both cases, the bandgap is minimized at Γ and maximized at M. We note that the 1D bandgap along $\Gamma - K$ is similar for phases I and II; whereas the bandgap along $\Gamma - X$ is much flatter in phase II than phase I.

Fig. 5.4 shows the x-component of the Berry connections for each phase. Although the Berry

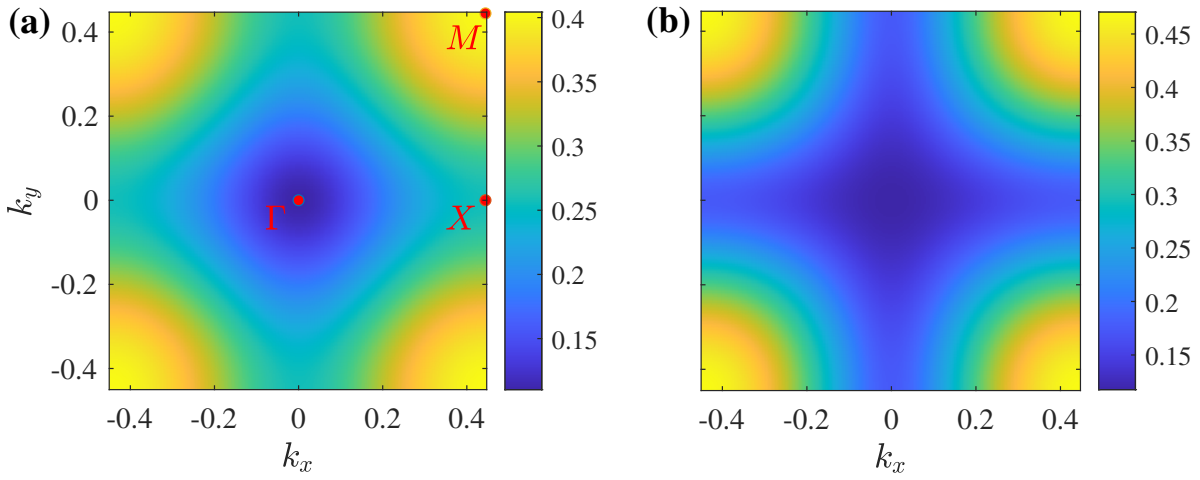

Figure 5.3: Bandgap of the QWZ for (a) phase I, and (b) phase II; as described by Eq. (5.46). Symmetry points of the BZ are illustrated in (a).

connections do not enter the orbital basis SBEs, it is instructive to demonstrate the singular behaviour of the QWZ model. In phase I the valence band Berry connection is finite, while the conduction Berry connection diverges at the Γ, X and M points. In phase II the valence band Berry connection diverges at Γ, while the conduction band Berry connection is singular at the X and M point. Although both phases have singular points, the locations (both in k-space and band indices) are different for each phase. The y-component is not shown, since it can be obtained from a $\pi/2$ rotation of the x-component.

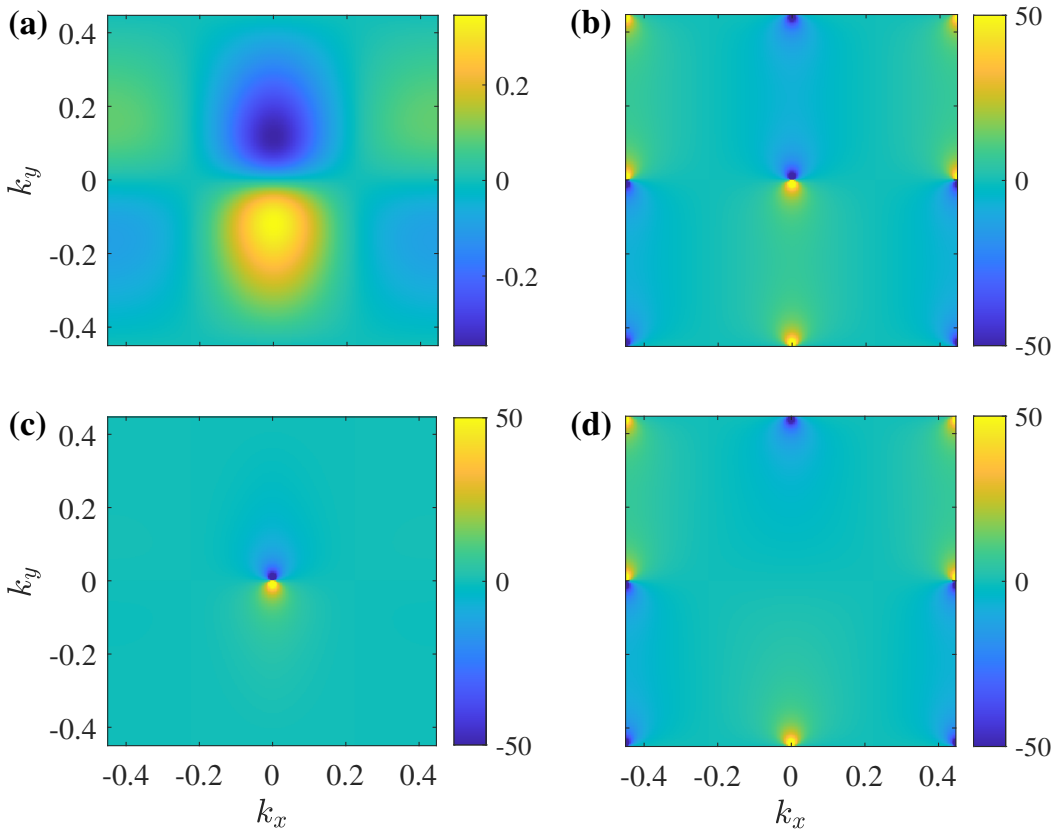

Figure 5.4: Berry connections for the QWZ model. Panels (a,b) show $\mathcal{A}_{v,x}$ and $\mathcal{A}_{c,x}$ for phase I; (c,d) show $\mathcal{A}_{v,x}$ and $\mathcal{A}_{c,x}$ for phase II.

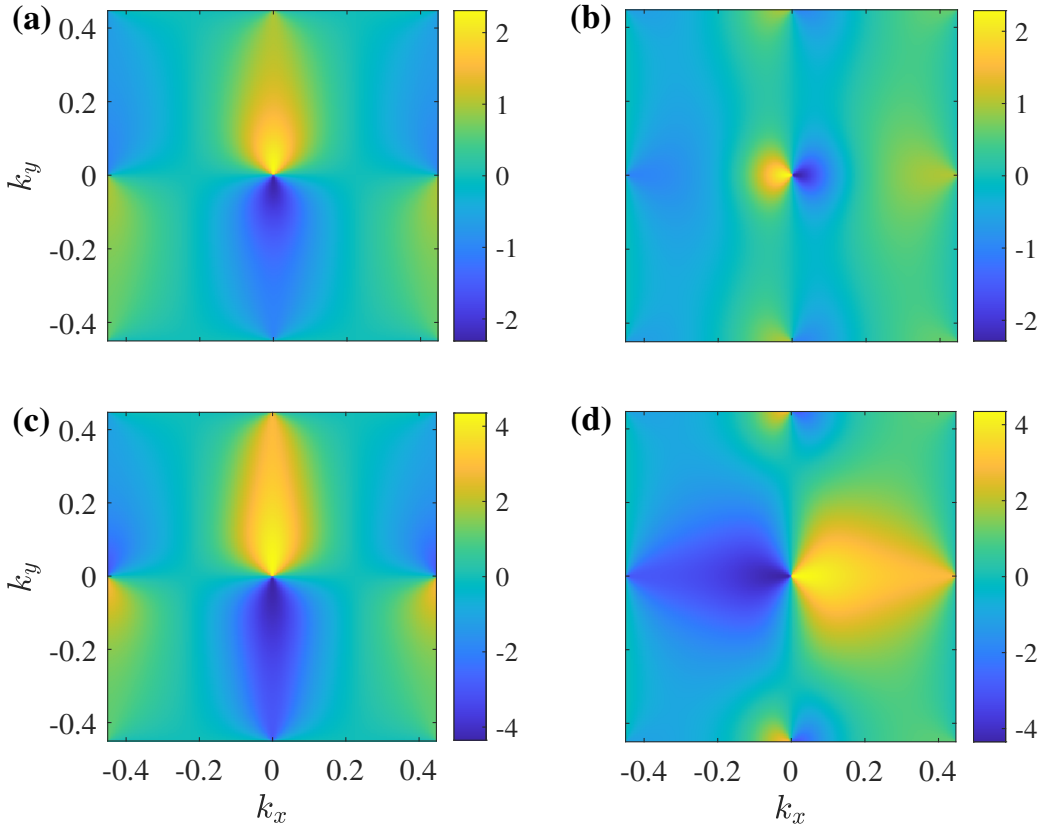

Figure 5.5: TDM component $d_{cv,x}$ for the QWZ model. Panels (a) and (b) show the real and imaginary parts of $d_{cv,x}$ for phase I; panels (c) and (d) correspond to phase II.

The x-component of the TDM is shown in Fig. 5.5 for both phases. The maximum value of the TDM for phase II is roughly two times larger than for phase I. For phase I the imaginary part is localized near Γ, while for phase II the imaginary has a larger distribution throughout the BZ. We also observe that for both phases the TDM is discontinuous at high symmetry points of the BZ. This is similar to the non-smooth behaviour of gapped graphene in the TB gauge, where the singular Berry connections at the K points are accompanied by discontinuous TDMs.

To demonstrate the orbital basis approach in the QWZ model, HHG spectra were simulated for a 3μm optical pulse with 50fs duration. We consider input polarization along ΓX, for which the bandgaps are most similar for the two phases. The simulated harmonic spectra for both phases are shown in Fig. 5.6a. Despite the non-smooth behaviour of the QWZ model, the orbital basis SBEs succeed in calculating the HHG spectra to high precision. Although the HHG spectra exhibit slight differences for the two phases, there is no obvious qualitative indicator that distinguishes the topological phase. Indeed, the influence of topological phases on HHG is generally not obvious based on inspection of HHG spectra [35, 67]. It is more interesting to

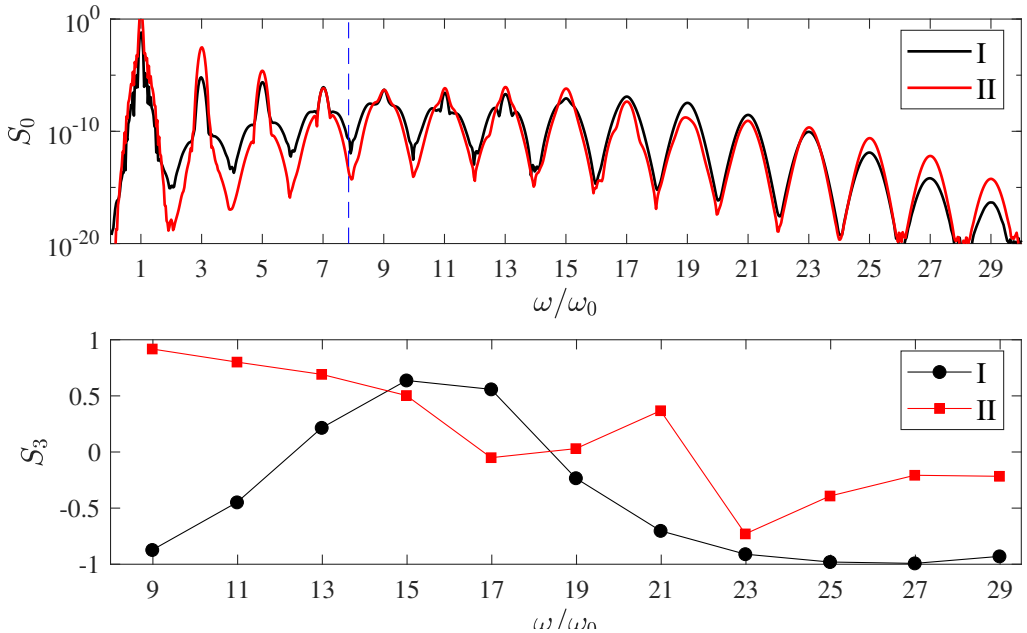

Figure 5.6: (a) simulated HHG spectra for two phases of QWZ model with input polarization along $\Gamma - M$ orientation; maximum bandgap indicated by dashed blue line. Panel (b) shows simulated ellipticity of harmonics above the maximum bandgap.

examine the ellipticity of each harmonic order, given by the Stokes parameter

$$S_3(\omega) = -2\text{Im}\left[j_{\parallel}(\omega)j_{\perp}^*(\omega)\right]/S_0(\omega), \tag{5.47}$$

where the normalization $S_0(\omega) = S(\omega) = |j_{\parallel}(\omega)|^2 + |j_{\perp}(\omega)|^2$ is the Stokes parameter for the harmonic intensity. The simulated ellipticity for the two phases of the QWZ model are shown in Fig. 5.6b. Although the input polarization is linear, harmonics are generated with significant ellipticity. Interestingly, the two phases generate low order harmonics with opposite ellipticity. As the harmonic order increases, the overall magnitude of ellipticity varies in each phase.

The main goal of this section is to demonstrate the validity of the orbital basis SBEs, and exploring the influence of the topological phase on the HHG spectrum will be the subject of future work. Here we have only considered linear polarization, but the HHG spectrum resulting from excitation by a circularly polarized pulse can be more sensitive to topological phase [67]. Time-frequency analysis of HHG emission can also provide insight for the role of topological phase in HHG [35]. Finally, it will be particularly interesting to explore the role of the mixture current in HHG for different material phases.

Chapter 6
Gauge invariant semiconductor Bloch equations

In the previous chapters we have exploited gauge freedom to facilitate numerical integration of the SBEs. In chapter 3 we used a specific gauge transformation to remove singular behaviour from the tight-binding model of gapped graphene, while in chapter 5 we transformed the SBEs to a non-diagonal basis. In this chapter we take a different approach, and derive a gauge invariant formulation of the SBEs. Using a simple transformation of the density matrix, we obtain modified SBEs containing only gauge invariant structural matrix elements. As we shall see, the TDM phases and Berry connections are replaced by a gauge invariant quantity known as the shift vector [35, 46, 47]. The transformation also removes gauge dependent phases from the interband current, which means HHG in solids can be described using only gauge invariant structural quantities. For completenes we present gauge invariant SBEs in both the static and comoving momentum frames, although we perform numerical calculations only in the comoving frame.

6.1 Gauge invariant SBEs in the static frame

Starting from Eq. (2.32) in the static frame, we separate the SBEs into diagonal (intraband) components

$$\dot{\rho}_{nn}(\mathbf{k},t) = -e\mathbf{F}(t)\cdot\nabla_{\mathbf{k}}\rho_{nn}(\mathbf{k},t) - 2e\sum_{l}\mathrm{Im}\left[\Omega_{nl}(\mathbf{k},t)\rho_{ln}(\mathbf{k},t)\right], \tag{6.1}$$

and off-diagonal (interband) components

$$\begin{aligned}\dot{\rho}_{nm}(\mathbf{k},t) = &-i\left[\varepsilon_{nm}(\mathbf{k}) - e\mathbf{F}(t)\cdot\boldsymbol{\mathcal{A}}_{nm}(\mathbf{k})\right]\rho_{nm}(\mathbf{k},t) - e\mathbf{F}(t)\cdot\nabla_{\mathbf{k}}\rho_{nm}(\mathbf{k},t)\\ &+ ie\Omega_{nm}(\mathbf{k},t)\left[\rho_{mm}(\mathbf{k},t) - \rho_{nn}(\mathbf{k},t)\right]\\ &+ ie\sum_{l\neq n,m}\left[\Omega_{nl}(\mathbf{k},t)\rho_{lm}(\mathbf{k},t) - \Omega_{lm}(\mathbf{k},t)\rho_{nl}(\mathbf{k},t)\right]\\ &+ \dot{\rho}^{(d)}_{nm}(\mathbf{k},t),\end{aligned} \tag{6.2}$$

where we recall that $\varepsilon_{nm} = E_n - E_m$ is the bandgap, $\boldsymbol{\mathcal{A}}_{nm} = \boldsymbol{\mathcal{A}}_n - \boldsymbol{\mathcal{A}}_m$ is the difference of Berry connections, and $\Omega_{nm} = \mathbf{F} \cdot \mathbf{d}_{nm}$ is the Rabi frequency. In Eq. 6.2 we have also added a phenomenological dephasing term

$$\dot{\rho}^{(d)}_{nm}(\mathbf{k}, t) = -\frac{(1 - \delta_{nm})}{T_2} \rho_{nm}(\mathbf{k}, t). \tag{6.3}$$

It is convenient to write the Rabi frequency as

$$\Omega_{nm}(\mathbf{k}, t) = F(t) \bar{\Omega}_{nm}(\mathbf{k}, t), \tag{6.4}$$

where the reduced Rabi frequency

$$\bar{\Omega}_{nm}(\mathbf{k}, t) = \mathbf{n}(t) \cdot \mathbf{d}_{nm}(\mathbf{k}), \tag{6.5}$$

is simply the component of the TDM parallel to the polarization vector $\mathbf{n}(t)$ of the applied electric field. Next, we decompose the reduced Rabi frequency according to

$$\bar{\Omega}_{nm}(\mathbf{k}, t) = |\bar{\Omega}_{nm}(\mathbf{k}, t)| e^{i\phi_{nm}(\mathbf{k},t)}, \tag{6.6}$$

where

$$\phi_{nm}(\mathbf{k}, t) = \arg \left[\bar{\Omega}_{nm}(\mathbf{k}, t) \right], \tag{6.7}$$

is the phase of the TDM component parallel to the polarization vector. Note that the magnitude of the Rabi frequency is a gauge invariant quantity, so the phase ϕ_{nm} represents the full gauge-dependence of the Rabi frequency. Next we transform the density matrix according to

$$\varrho_{nm}(\mathbf{k}, t) = \left[\delta_{nm} + (1 - \delta_{nm}) e^{-i\phi_{nm}(\mathbf{k},t)} \right] \rho_{nm}(\mathbf{k}, t), \tag{6.8}$$

where the off-diagonal components are transformed by the phase of the Rabi frequency, while the diagonal elements are unchanged. Eq. (6.8) can be interpreted as a specific gauge transformation that removes the parallel TDM phase from the Rabi frequency and the density matrix; both of which are gauge covariant quantities.

Using the transformation (6.8), the SBE for the population becomes

$$\dot{\varrho}_{nn}(\mathbf{k}, t) = -e\mathbf{F}(t) \cdot \nabla_{\mathbf{k}} \varrho_{nn}(\mathbf{k}, t) - 2eF(t) \sum_l \left| \bar{\Omega}_{nl}(\mathbf{k}, t) \right| \mathrm{Im} \left[\varrho_{ln}(\mathbf{k}, t) \right], \tag{6.9}$$

where the only structural matrix elements on the RHS are the gauge invariant magnitudes of the

reduced Rabi frequency. For the off-diagonal components of the density matrix, we calculate

$$\dot{\varrho}_{nm}(\mathbf{k},t) = e^{-i\phi_{nm}(\mathbf{k},t)}\dot{\rho}_{nm}(\mathbf{k},t) + \dot{\varrho}^{(\mathrm{pol})}_{nm}(\mathbf{k},t), \tag{6.10}$$

where the term

$$\dot{\varrho}^{(\mathrm{pol.})}_{nm}(\mathbf{k},t) = -\dot{\phi}_{nm}(\mathbf{k},t)\varrho_{nm}(\mathbf{k},t), \tag{6.11}$$

accounts for time-dependent polarization, since $\dot{\phi}_{nm}(\mathbf{k},t)$ vanishes unless $\partial_t \mathbf{n}(t) \neq 0$. We will revisit this term later in this section, but for now we focus on the first term of Eq. (6.10).

Using the RHS of Eq. (6.2) in (6.10), we have

$$\begin{aligned}\dot{\varrho}_{nm} - \dot{\varrho}^{(\mathrm{pol})}_{nm} =& -i\left[\varepsilon_{nm} - e\mathbf{F}\cdot\boldsymbol{\mathcal{A}}_{nm}\right]\varrho_{nm} - e^{-i\phi_{nm}}\left(e\mathbf{F}\cdot\nabla_{\mathbf{k}}\right)\rho_{nm} \\ &+ ie\Omega_{nm}\left(\varrho_{mm}-\varrho_{nn}\right)e^{-i\phi_{nm}} + ie\sum_{l\neq n,m}\left(\Omega_{nl}\rho_{lm} - \Omega_{lm}\rho_{nl}\right)e^{-i\phi_{nm}},\end{aligned} \tag{6.12}$$

where we have suppressed explicit (k,t)-dependence for notational brevity. To evaluate the term containing derivatives, we invert the transformation (6.8) to write

$$\begin{aligned}e^{-i\phi_{nm}}\left(e\mathbf{F}\cdot\nabla_{\mathbf{k}}\right)\rho_{nm} &= e^{-i\phi_{nm}}\left(e\mathbf{F}\cdot\nabla_{\mathbf{k}}\right)e^{i\phi_{nm}}\varrho_{nm} \\ &= \left(e\mathbf{F}\cdot\nabla_{\mathbf{k}}\right)\varrho_{nm} + i\varrho_{nm}\left(e\mathbf{F}\cdot\nabla_{\mathbf{k}}\phi_{nm}\right),\end{aligned}$$

and inserting this into Eq. (6.12) gives

$$\begin{aligned}\dot{\varrho}_{nm} - \dot{\varrho}^{(\mathrm{pol})}_{nm} =& -i\left[\varepsilon_{nm} - e\mathbf{F}(t)\cdot\mathbf{R}_{nm}\right]\varrho_{nm} - e\mathbf{F}\cdot\nabla_{\mathbf{k}}\varrho_{nm} \\ &+ ie\Omega_{nm}\left[\tilde{\rho}_{mm}-\tilde{\rho}_{nn}\right]e^{-i\phi_{nm}} + ie\sum_{l\neq n,m}\left[\Omega_{nl}\rho_{lm} - \Omega_{lm}\rho_{nl}\right]e^{-i\phi_{nm}},\end{aligned} \tag{6.13}$$

where we have identified the shift vector [46, 47]

$$\mathbf{R}_{nm}(\mathbf{k}) = \boldsymbol{\mathcal{A}}_{nm}(\mathbf{k}) - \nabla_{\mathbf{k}}\phi_{nm}(\mathbf{k}). \tag{6.14}$$

Properties of the shift vector are discussed in App. E, where it is shown explicitly that $\mathbf{R}_{nm}$ is

gauge invariant. Finally, using Eqs. (6.6) and (6.8), we obtain

$$\begin{aligned}\dot{\varrho}_{nm} - \dot{\varrho}_{nm}^{(\mathrm{pol})} = &- i\left[\varepsilon_{nm} - e\mathbf{F}(t)\cdot\mathbf{R}_{nm}\right]\varrho_{nm} - e\mathbf{F}(t)\cdot\nabla_{\mathbf{k}}\varrho_{nm} + ieF(t)\left|\bar{\Omega}_{nm}\right|\left(\varrho_{mm}-\varrho_{nn}\right)\\ &+ ieF(t)\sum_{l\neq n,m}\left(|\bar{\Omega}_{nl}|\varrho_{lm} - |\bar{\Omega}_{lm}|\varrho_{nl}\right)T_{nlm},\end{aligned} \tag{6.15}$$

where we have defined the triple product of dipole phases

$$T_{nlm}(\mathbf{k}) = e^{i\phi_{nl}(\mathbf{k})}e^{i\phi_{lm}(\mathbf{k})}e^{i\phi_{mn}(\mathbf{k})}, \tag{6.16}$$

which is also gauge invariant; see App. F. We note that a similar triple product of dipole moments was encountered in Ref. [70], where its gauge invariance was used to avoid random TDM phases resulting from numerical band structure calculations. As a result of the transformation (6.8), the roles of the Berry connections and dipole phases have been replaced by the shift vector, as well as the circular product of dipole phases.

To see that the time-dependent polarization term in Eq. (6.10) is also gauge invariant, we start from

$$\begin{aligned}\dot{\varrho}_{nm}^{(\mathrm{pol.})} &= -\left[\partial_t \arg\left(\bar{\Omega}_{nm}\right)\right]\varrho_{nm}\\ &= -\mathrm{Im}\left[\partial_t \ln\bar{\Omega}_{nm}\right]\varrho_{nm}\\ &= -\mathrm{Im}\left[\frac{\partial_t\bar{\Omega}_{nm}}{\bar{\Omega}_{nm}}\right]\varrho_{nm}.\end{aligned} \tag{6.17}$$

Writing the vector components of the dipole moment as

$$\mathbf{e}_i\cdot\mathbf{d}_{nm} = d_{nm,i} = |d_{nm,i}|e^{i\phi_{nm,i}}, \tag{6.18}$$

we have

$$\dot{\varrho}_{nm}^{(\mathrm{pol.})} = -\mathrm{Im}\left[\frac{\sum_i \dot{n}_i d_{nm,i}}{\sum_j n_j d_{nm,j}}\right]\varrho_{nm}. \tag{6.19}$$

The term in square brackets on the RHS can be expressed as

$$\frac{\sum_i \dot{n}_i d_{nm,i}}{\sum_j n_j d_{nm,j}} = \frac{\sum_i \dot{n}_i |d_{nm,i}|e^{i\phi_{nm,i}}}{\sum_j n_j |d_{nm,j}|e^{i\phi_{nm,j}}} = \frac{\sum_i \dot{n}_i |d_{nm,i}|}{\sum_j n_j |d_{nm,j}|e^{i(\phi_{nm,j}-\phi_{nm,i})}}, \tag{6.20}$$

where the difference of phases is clearly a gauge invariant quantity. Together with Eq. (6.15), this shows that the transformed SBEs only involve gauge invariant structural matrix elements.

Clearly the transformed density matrix ϱ can be propagated using only gauge invariant quantities, but for a fully gauge invariant description of HHG we must also consider the calculation of observables. The intraband current is

$$\mathbf{j}_{ra}(t) = e \sum_n \int d\mathbf{k} \mathbf{v}_n(\mathbf{k}) \rho_{nn}(\mathbf{k}, t), \tag{6.21}$$

where $\mathbf{v}_n(\mathbf{k})$ is the band velocity, and $\rho_{nn} = \varrho_{nn}$ are the band occupations. Since the both the band velocities and occupations are gauge invariant, it is obvious that the intraband current does not involve any gauge dependent matrix elements. More interesting is the interband polarization

$$\mathbf{p}_{er}(t) = e \sum_{m \neq n} \int d\mathbf{k} \mathbf{d}_{nm}(\mathbf{k}) \rho_{mn}(\mathbf{k}, t), \tag{6.22}$$

in which both the TDM $\mathbf{d}_{nm}$ and the density matrix elements ρ_{mn} are gauge covariant. To eliminate this gauge dependence, we consider a single vector component of the interband polarization,

$$\begin{aligned} p_{er,j}(t) &= e \sum_{m \neq n} \int d\mathbf{k} d_{nm,j}(\mathbf{k}) \rho_{mn}(\mathbf{k}, t) \\ &= e \sum_{m \neq n} \int d\mathbf{k} |d_{nm,j}(\mathbf{k})| \varrho_{mn}(\mathbf{k}, t) e^{i\phi_{nm,j}(\mathbf{k})} e^{i\phi_{mn}(\mathbf{k})}, \end{aligned} \tag{6.23}$$

where we have used Eqs. (6.6) and (6.18). The phase difference is a gauge invariant quantity, which means each vector component of the interband polarization can be calculated using only gauge invariant structural matrix elements. We note in particular that the parallel component of the polarization is simply

$$\mathbf{n} \cdot \mathbf{p}_{er}(t) = e \sum_{m \neq n} \int d\mathbf{k} |\mathbf{n} \cdot \mathbf{d}_{nm}(\mathbf{k})| \varrho_{mn}(\mathbf{k}, t), \tag{6.24}$$

since the phase factors cancel for this component. We also note that the total interband current can be written as

$$\mathbf{j}_{er}(t) = e \sum_{m \neq n} \int d\mathbf{k} \mathbf{p}_{nm}(\mathbf{k}) \rho_{mn}(\mathbf{k}, t), \tag{6.25}$$

where the momentum matrix elements are

$$\mathbf{p}_{nm}(\mathbf{k}) = i\varepsilon_{nm}(\mathbf{k})\mathbf{d}_{nm}(\mathbf{k}). \tag{6.26}$$

Clearly, the total current will involve the same gauge invariant combination of phases as the interband polarization. We thus conclude that all observables relevant to HHG can be calculated using only gauge invariant structural matrix elements.

6.2 Gauge invariant SBEs in the comoving frame

The gauge invariant SBEs can also be formulated in the comoving frame, starting from the covariant SBEs (2.44). In this case the Rabi frequency is evaluated at the time-dependent momentum,

$$\Omega_{nm}(\mathbf{K}_t, t) = \mathbf{F}(t) \cdot \mathbf{d}_{nm}(\mathbf{K}_t), \tag{6.27}$$

and we recall that $\mathbf{K}_t = \mathbf{K} - e\mathbf{A}(t)$. To obtain gauge invariant SBEs in the comoving frame, we perform the decomposition

$$\bar{\Omega}(\mathbf{K}_t) = |\bar{\Omega}_{nm}(\mathbf{K}_t)|e^{i\phi_{nm}(\mathbf{K}_t)}, \tag{6.28}$$

and transform the density matrix according to

$$\varrho_{nm}(\mathbf{K}, t) = \left[\delta_{nm} + (1 - \delta_{nm})e^{-i\phi_{nm}(\mathbf{K}_t)}\right] \rho_{nm}(\mathbf{K}, t). \tag{6.29}$$

The difference compared to the transformation (6.8) in the static frame is that the phase

$$\phi_{nm}(\mathbf{K}_t, t) = \arg\left[\mathbf{n}(t) \cdot \mathbf{d}_{nm}(\mathbf{K}_t)\right] \tag{6.30}$$

is now evaluated at the time-dependent momentum $\mathbf{K}_t$. For the diagonal elements of the density matrix, we have

$$\dot{\varrho}_{nn}(\mathbf{K}, t) = -2eF(t) \sum_l \left|\bar{\Omega}_{nl}(\mathbf{K}_t)\right| \mathrm{Im}\left[\varrho_{ln}(\mathbf{K}, t)\right]. \tag{6.31}$$

For the off-diagonal elements, we calculate

$$\begin{aligned}\dot{\varrho}_{nm}(\mathbf{K}, t) =& \frac{d}{dt} e^{-i\phi_{nm}(\mathbf{K}_t)} \rho_{nm}(\mathbf{K}, t) \\ =& e^{-i\phi_{nm}(\mathbf{K}_t)} \dot{\rho}_{nm}(\mathbf{K}, t) - i\dot{\phi}_{nm}(\mathbf{K}_t)\varrho_{nm}(\mathbf{K}, t),\end{aligned} \tag{6.32}$$

where

$$\begin{aligned}\frac{d}{dt}\phi_{nm}(\mathbf{K}_t) &= \partial_t\phi_{nm}(\mathbf{K}_t) + e\mathbf{F}(t)\cdot\left[\nabla_{\mathbf{k}}\phi_{nm}(\mathbf{k})\right]_{\mathbf{k}=\mathbf{K}_t} \\ &= \dot{\varrho}_{nm}^{(\mathrm{pol.})}(\mathbf{K}_t) + e\mathbf{F}(t)\cdot\left[\nabla_{\mathbf{k}}\phi_{nm}(\mathbf{k})\right]_{\mathbf{k}=\mathbf{K}_t}, \end{aligned} \tag{6.33}$$

and we have recognized that the phase $\phi_{nm}(\mathbf{K}_t)$ only has explicit time-dependence if $\dot{\mathbf{n}}(t) \neq 0$. The rest of the derivation proceeds analogously to Sec. 6.1, with the result

$$\begin{aligned}\dot{\varrho}_{nm}(\mathbf{K},t) =& -i\left[\varepsilon_{nm}(\mathbf{K}_t) - e\mathbf{F}(t)\cdot\mathbf{R}_{nm}(\mathbf{K}_t)\right]\varrho_{nm}(\mathbf{K},t) \\ &+ ieF(t)\left|\bar{\Omega}_{nm}(\mathbf{K}_t)\right|\left[\varrho_{mm}(\mathbf{K},t) - \varrho_{nn}(\mathbf{K},t)\right] \\ &+ ieF(t)\sum_{l\neq n,m}\left[|\bar{\Omega}_{nl}(\mathbf{K}_t)|\varrho_{lm}(\mathbf{K},t) - |\bar{\Omega}_{lm}(\mathbf{K}_t)|\varrho_{nl}(\mathbf{K},t)\right]T_{nlm}(\mathbf{K}_t), \end{aligned} \tag{6.34}$$

where we have assumed constant polarization. Similarly to the covariant SBEs discussed in chapter 2, the frame transformation eliminates the gradient term and the resulting equations are entirely decoupled for different $\mathbf{K}$ points.

To demonstrate that observables can also be calculated using gauge invariant quantities in the comoving frame, we consider the interband polarization

$$\begin{aligned}p_{er,j}(t) =& e\sum_{m\neq n}\int d\mathbf{K} d_{nm,j}(\mathbf{K}_t)\rho_{mn}(\mathbf{K},t) \\ =& e\sum_{m\neq n}\int d\mathbf{K}|d_{nm,j}(\mathbf{K}_t)|\varrho_{mn}(\mathbf{K},t)e^{i\phi_{nm,j}(\mathbf{K}_t)}e^{i\phi_{mn}(\mathbf{K}_t)} \end{aligned} \tag{6.35}$$

which is clearly analogous to Eq. (6.23), but with the structural matrix elements evaluated at the time-dependent momentum coordinates. We conclude that in either the static or comoving frame, the SBEs and observables can be calculated using only gauge invariant structural matrix elements.

6.3 Two-band model

It is worthwhile to examine the simple case of a two-band model with a single valence (v) and conduction (c) band. Working in the comoving frame, the covariant SBEs simplify to

$$\begin{aligned}\dot{n}_c(\mathbf{K},t) =& -2e\mathrm{Im}\left[\Omega_{cv}(\mathbf{K}_t,t)\rho^*_{cv}(\mathbf{K},t)\right]\\ \dot{\rho}_{cv}(\mathbf{K},t) =& -i\left[\varepsilon_{cv}(\mathbf{K}_t) - e\mathbf{F}(t)\cdot\boldsymbol{\mathcal{A}}_{cv}(\mathbf{K}_t)\right]\rho_{cv}(\mathbf{K},t) + ie\Omega_{cv}(\mathbf{K}_t,t)w(\mathbf{K},t),\end{aligned} \tag{6.36}$$

where $n_m = \rho_{mm}$ is the band population, and $w = n_v - n_c$ is the population difference. The equations can be transformed using the Ansatz [16]

$$\pi_{cv}(\mathbf{K},t) = e^{iS_{cv}(\mathbf{K},t)}\rho_{cv}(\mathbf{K},t), \tag{6.37}$$

where

$$S_{cv}(\mathbf{K},t) = \int_{-\infty}^{t} dt' \left[\varepsilon_{cv}(\mathbf{K}_{t'}) - e\mathbf{F}(t')\cdot\boldsymbol{\mathcal{A}}_{cv}(\mathbf{K}_{t'})\right], \tag{6.38}$$

is the classical action, and π_{cv} is known as the interband coherence matrix. This leads to a new system of differential equations

$$\begin{aligned}\dot{\pi}_{cc}(\mathbf{K},t) =& -2e\mathrm{Im}\left[\Omega_{cv}(\mathbf{K}_t,t)e^{iS_{cv}(\mathbf{K},t)}\pi^*_{cv}(\mathbf{K},t)\right]\\ \dot{\pi}_{cv}(\mathbf{K},t) =& -ie\Omega_{cv}(\mathbf{K}_t,t)e^{iS_{cv}(\mathbf{K},t)}w(\mathbf{K},t),\end{aligned} \tag{6.39}$$

in which the intraband matrix elements ε_{cv} and $\boldsymbol{\mathcal{A}}_{cv}$ only appear in the action, while the (interband) Rabi frequency is pre-exponential. These two band equations are the starting point of the strong field approximation (SFA) [16], which has been used extensively to study HHG in solids [16, 18, 24, 31, 36].

At this point one might wonder if the phase of the Rabi frequency could be pulled inside the action integral, and if this would result in gauge invariant dynamical equations. Specifically, write

$$\Omega_{cv}(\mathbf{K}_t,t)e^{iS_{cv}(\mathbf{K},t)} = F(t)|\bar{\Omega}(\mathbf{K}_t,t)|e^{i\theta(\mathbf{K}_t,t)}, \tag{6.40}$$

where the total phase is

$$\theta(\mathbf{K}_t,t) = \phi_{cv}(\mathbf{K}_t) + S_{cv}(\mathbf{K},t). \tag{6.41}$$

Using the fundemantal theorem of calculus, we can write

$$\phi_{cv}(\mathbf{K}_t) = \phi_{cv}(\mathbf{K}_{t=-\infty}) + \int_{-\infty}^{t} dt' \dot{\phi}_{cv}(\mathbf{K}_{t'}), \tag{6.42}$$

and we emphasize that the first term cannot be neglected, since the TDM phase evaluated at the initial (static) crystal momentum coordinates is non-vanishing. Now, recalling Eq. (6.33) and assuming time-independent polarization, we can write the total phase as

$$\begin{aligned}\theta(\mathbf{K}_t, t) &= \phi_{cv}(\mathbf{K}) + \int_{-\infty}^{t} dt' \left[\varepsilon_{cv}(\mathbf{K}_{t'}) - e\mathbf{F}(t') \cdot \mathbf{R}_{cv}(\mathbf{K}_{t'})\right] \\ &\equiv \phi_{cv}(\mathbf{K}) + \mathcal{S}_{cv}(\mathbf{K}, t),\end{aligned} \tag{6.43}$$

where $\mathcal{S}_{cv}$ is a modified action that is clearly gauge invariant, since it depends only on the bandgap and the shift vector. The DEs for the coherence matrix can thus be written as

$$\begin{aligned}\dot{\pi}_{cc}(\mathbf{K}, t) &= -2e\mathrm{Im}\left[\Omega_{cv}(\mathbf{K}_t, t)e^{i\theta(\mathbf{K}_t,t)}\pi^*_{cv}(\mathbf{K}, t)\right] \\ \dot{\pi}_{cv}(\mathbf{K}, t) &= -ie\Omega_{cv}(\mathbf{K}_t, t)e^{i\theta(\mathbf{K}_t,t)}w(\mathbf{K}, t).\end{aligned} \tag{6.44}$$

Although the modified action is gauge invariant, the total phase θ is gauge dependent due to the first term in Eq. (6.43). Omitting the initial phase would violate the gauge symmetry of a periodic crystal, so we conclude that this approach does not lead to gauge invariant dynamic equations.

A better approach for obtaining gauge invariant two-band equations with the action Ansatz starts from Eqs. (6.31) and (6.34), which simplify to

$$\dot{\varrho}_{cc}(\mathbf{K}, t) = 2eF(t)\left|\bar{\Omega}_{cv}(\mathbf{K}_t)\right| \mathrm{Im}\left[\varrho_{cv}(\mathbf{K}, t)\right], \tag{6.45}$$

and

$$\dot{\varrho}_{cv}(\mathbf{K}, t) = -\,i\left[\varepsilon_{cv}(\mathbf{K}_t) - e\mathbf{F}(t) \cdot \mathbf{R}_{cv}(\mathbf{K}_t)\right]\varrho_{cv}(\mathbf{K}, t) + ieF(t)\left|\bar{\Omega}_{cv}(\mathbf{K}_t)\right| w(\mathbf{K}, t). \tag{6.46}$$

in a two band system. We now consider the modified action Ansatz

$$\zeta_{cv}(\mathbf{K}, t) = e^{i\mathcal{S}_{cv}(\mathbf{K},t)}\varrho_{cv}(\mathbf{K}, t), \tag{6.47}$$

which is similar to Eq. (6.37), except here $\mathcal{S}_{cv}$ is the gauge invariant action defined in Eq. (6.43). Further, the RHS of Eq. (6.47) contains the transformed density matrix ϱ_{cv}, which means the corresponding coherence matrix ζ_{cv} is analogous to (but distinct from) π_{cv} defined in Eq. (6.37).

The dynamic equations for this transformed coherence matrix are

$$\begin{aligned}\dot{n}_c(\mathbf{K},t) &= -2eF(t)|\bar{\Omega}_{cv}(\mathbf{K}_t)|\mathrm{Im}\left[e^{i\mathcal{S}_{cv}(\mathbf{K},t)}\zeta^*_{cv}(\mathbf{K},t)\right]\\ \dot{\zeta}_{cv}(\mathbf{K},t) &= -ieF(t)|\bar{\Omega}_{cv}(\mathbf{K}_t)|e^{i\mathcal{S}_{cv}(\mathbf{K},t)}w(\mathbf{K},t),\end{aligned} \tag{6.48}$$

which only contain gauge invariant structural matrix elements. Finally, the components of the interband polarization are

$$\begin{aligned}p_{er,j}(t) &= e\int d\mathbf{K} d_{cv,j}(\mathbf{K}_t)\rho_{vc}(\mathbf{K},t) + \mathrm{c.c.}\\ &= e\int d\mathbf{K}|d_{cv,j}(\mathbf{K}_t)|e^{i\phi_{cv,j}(\mathbf{K}_t)}e^{i\phi_{vc}(\mathbf{K}_t)}\varrho^*_{cv}(\mathbf{K},t) + \mathrm{c.c.}\\ &= e\int d\mathbf{K}|d_{cv,j}(\mathbf{K}_t)|e^{i\phi_{cv,j}(\mathbf{K}_t)}e^{i\phi_{vc}(\mathbf{K}_t)}\zeta^*_{cv}(\mathbf{K},t)e^{i\mathcal{S}_{cv}(\mathbf{K},t)} + \mathrm{c.c.},\end{aligned} \tag{6.49}$$

where the second line is simply Eq. (6.35) for two-band system, and in the third line we have used Eq. (6.47). We thus conclude that the dynamic equations for the coherence matrix can also be formulated in terms of gauge invariant structural matrix elements.

6.3.1 Strong field approximation

Next we discuss the strong field approximation (SFA) for HHG in solids, in which we neglect depletion of valence band population [16]. We will show that formulating the SFA in terms of the shift vector helps to clarify the gauge invariance of the SFA.

Approximating $w(\mathbf{K},t) \simeq 1$, Eq. (6.39) for the interband coherence function can be integrated directly to give

$$\pi_{cv}(\mathbf{K},t) = -ie\int_{-\infty}^{t} dt' \Omega_{cv}(\mathbf{K}_{t'},t')e^{iS_{cv}(\mathbf{K},t')}. \tag{6.50}$$

The interband polarization is then

$$\begin{aligned}\mathbf{p}_{er}(t) &= e\int d\mathbf{K}\mathbf{d}_{cv}(\mathbf{K}_t)\rho^*_{cv}(\mathbf{K},t)\\ &= e\int d\mathbf{K}\mathbf{d}_{cv}(\mathbf{K}_t)\left[\pi_{cv}(\mathbf{K},t)e^{-iS_{cv}(\mathbf{K},t)}\right]^*\\ &= i\int d\mathbf{K}\mathbf{d}_{cv}(\mathbf{K}_t)\int_{-\infty}^{t} dt'\Omega^*_{cv}(\mathbf{K}_{t'},t')e^{iS(\mathbf{K},t',t)}\end{aligned} \tag{6.51}$$

where

$$S(\mathbf{K},t',t) = \int_{t'}^{t} d\tau\left[\varepsilon(\mathbf{K}_\tau) - e\mathbf{F}(\tau)\cdot\boldsymbol{\mathcal{A}}_{cv}(\mathbf{K}_\tau)\right] \tag{6.52}$$

is the gauge-dependent SFA action integral. A vector component of the polarization is

$$\begin{aligned} p_{er,j}(t) &= i \int d\mathbf{K} d_{cv,j}(\mathbf{K}_t) \int_{-\infty}^{t} dt' \Omega_{cv}^{*}(\mathbf{K}_{t'}, t') e^{iS(\mathbf{K},t',t)} + \text{c.c.} \\ &= i \int d\mathbf{K} \left| d_{cv,j}(\mathbf{K}_t) \right| e^{i\phi_{cv,j}(\mathbf{K}_t)} \int_{-\infty}^{t} dt' \left| \Omega_{cv}(\mathbf{K}_{t'}, t') \right| e^{-i\phi_{cv}(\mathbf{K}_{t'})} e^{iS(\mathbf{K},t',t)} + \text{c.c.}, \end{aligned} \tag{6.53}$$

where we have extracted the TDM phases. The TDM phases are evaluated at different time-dependent momenta, so this combination of phases is not gauge invariant. However, we can write one of these TDM phases as

$$\begin{aligned} -\phi_{cv}(\mathbf{K}_{t'}) &= \int_{t'}^{t} d\tau \partial_\tau \phi_{cv}(\mathbf{K}_\tau) - \phi_{cv}(\mathbf{K}_t) \\ &= e \int_{t'}^{t} d\tau \mathbf{F}(\tau) \cdot \nabla_{\mathbf{K}_\tau} \phi_{cv}(\mathbf{K}_\tau) - \phi_{cv}(\mathbf{K}_t), \end{aligned} \tag{6.54}$$

and combining this integral with Eq. (6.52) gives the gauge invariant SFA action integral

$$\mathcal{S}(\mathbf{K}, t', t) = \int_{t'}^{t} d\tau \left[\varepsilon(\mathbf{K}_\tau) - e\mathbf{F}(\tau) \cdot \mathbf{R}_{cv}(\mathbf{K}_\tau) \right], \tag{6.55}$$

which involves the shift vector. The interband polarization is thus

$$p_{er,j}(t) = i \int d\mathbf{K} \left| d_{cv,j}(\mathbf{K}_t) \right| \int_{-\infty}^{t} dt' \left| \Omega_{cv}(\mathbf{K}_{t'}, t') \right| e^{i\vartheta(\mathbf{K},t',t)} + \text{c.c.}, \tag{6.56}$$

where we have defined the total SFA phase

$$\vartheta_j(\mathbf{K}, t', t) = \mathcal{S}(\mathbf{K}, t', t) + \phi_{cv,j}(\mathbf{K}_t) - \phi_{cv}(\mathbf{K}_t), \tag{6.57}$$

which is gauge invariant, since the TDM phases are evaluated at the same time-dependent momenta. Clearly, the phase difference is zero for the component of the current parallel to the input polarization, but for other components the phase difference cannot be neglected. Gauge invariance of the SFA phase corresponding to the parallel current has been considered previously [35, 67], but Eq. (6.57) is a more general result. The SFA phase is gauge invariant for all components of the current, and we emphasize that this result does not rely on the gauge invariant SBEs. In Eq. (6.51) we started from the gauge covariant SBEs, but we encounter the shift vector

naturally when formulating the SFA. The gauge invariant SBEs are distinct from the gauge invariant SFA, even though they both involve the shift vector.

6.3.2 Influence of shift vector on cycle symmetry

Finally, we investigate the influence of crystal inversion symmetry in a two band system. In appendix E it is shown that the shift vector always has even inversion symmetry, $\mathbf{R}_{cv}(-\mathbf{k}) = \mathbf{R}_{cv}(\mathbf{k})$; but in centrosymmetric crystals the shift vector necessarily vanishes. As a result, we expect the shift vector to play an important role in distinguishing the optical response of crystals with broken inversion symmetry. Our goal is to compare the excitation rate $\dot{n}_c(t)$ and the interband polarization $\mathbf{p}_{er}(t)$ between half cycles. For simplicity, we work in the cw limit where the applied field has odd parity between half cycles; i.e. $\mathbf{F}(t \pm t_0/2) = -\mathbf{F}(t)$.

The total excitation rate is given by

$$\begin{aligned}\dot{n}_c(t) &= \int d\mathbf{K} \dot{n}_c(\mathbf{K}, t) \\ &= -2eF(t) \int d\mathbf{K} |\bar{\Omega}_{cv}(\mathbf{K}_t)| \mathrm{Im}\left[e^{i\mathcal{S}_{cv}(\mathbf{K},t)} \zeta^*_{cv}(\mathbf{K}, t)\right]. \end{aligned} \tag{6.58}$$

Shifting both sides by half of an optical cycle, we find

$$\begin{aligned}\dot{n}_c(t + t_0/2) =& -2eF(t + t_0/2) \int d\mathbf{K} \left|\bar{\Omega}_{cv}(\mathbf{K}_{t+t_0/2})\right| \mathrm{Im}\left[e^{i\mathcal{S}_{cv}(\mathbf{K},t+t_0/2)} \zeta^*_{cv}(\mathbf{K}, t + t_0/2)\right] \\ =& 2eF(t) \int d\mathbf{K} \left|\bar{\Omega}_{cv}[\mathbf{K} + e\mathbf{A}(t)]\right| \mathrm{Im}\left[e^{i\mathcal{S}_{cv}(\mathbf{K},t+t_0/2)} \zeta^*_{cv}(\mathbf{K}, t + t_0/2)\right] \\ =& 2eF(t) \int d\mathbf{K} \left|\bar{\Omega}_{cv}(-\mathbf{K}_t)\right| \mathrm{Im}\left[e^{i\mathcal{S}_{cv}(-\mathbf{K},t+t_0/2)} \zeta^*_{cv}(-\mathbf{K}, t + t_0/2)\right], \end{aligned} \tag{6.59}$$

where have have substituted $\mathbf{K} \to -\mathbf{K}$, and note that the sign change of $d\mathbf{K}$ is canceled by the change of integration limits. Clearly $|\bar{\Omega}(-\mathbf{k})| = |\bar{\Omega}(\mathbf{k})|$, and from here onwards we consider an inversion symmetric system with vanishing shift vector. As a result, the action on the RHS of

Eq. (6.59) is simply

$$\begin{aligned}\mathcal{S}_{cv}(-\mathbf{K}, t+t_0/2) &= \int_{-\infty}^{t+t_0/2} dt' \varepsilon_{cv}\left[-\mathbf{K} - e\mathbf{A}(t')\right] \\ &= \int_{-\infty}^{t} d\tau \varepsilon_{cv}\left[-\mathbf{K} - e\mathbf{A}(\tau + t_0/2)\right] \\ &= \int_{-\infty}^{t} d\tau \varepsilon_{cv}\left[-\mathbf{K} + e\mathbf{A}(\tau)\right] \\ &= \int_{-\infty}^{t} d\tau \varepsilon_{cv}(-\mathbf{K}_\tau) \\ &= \mathcal{S}_{cv}(\mathbf{K}, t), \end{aligned} \tag{6.60}$$

since $\varepsilon_{cv}(-\mathbf{k}) = \varepsilon(\mathbf{k})$. From this, we obtain the relation

$$\begin{aligned}\dot{\zeta}_{cv}(-\mathbf{K}, t+t_0/2) &= ieF(t)|\bar{\Omega}_{cv}(\mathbf{K}_t)|e^{i\mathcal{S}_{cv}(-\mathbf{K}, t+t_0/2)} \\ &= -\dot{\zeta}_{cv}(\mathbf{K}, t), \end{aligned} \tag{6.61}$$

and, since both the LHS and RHS evolve from the same initial condition, this implies

$$\zeta_{cv}(-\mathbf{K}, t+t_0/2) = -\zeta_{cv}(\mathbf{K}, t). \tag{6.62}$$

Returning to the excitation rate, we obtain the result

$$\dot{n}_c(t+t_0/2) = \dot{n}(t), \tag{6.63}$$

which shows that the excitation rates in the positive/negative half-cycles are identical in a centrosymmetric crystal.

For the interband polarization, we have

$$\begin{aligned}p_{er,j}(t+t_0/2) =& i\int d\mathbf{K}|d_j(\mathbf{K}_{t+t_0/2})|\int_{-\infty}^{t+t_0/2} dt' F(t')|\bar{\Omega}(\mathbf{K}_{t'})|e^{i\vartheta_j(\mathbf{K},t',t+t_0/2)} + \text{c.c.} \\ =& i\int d\mathbf{K}|d_j(\mathbf{K}_{t+t_0/2})|\int_{-\infty}^{t} d\tau F(\tau+t_0/2)|\bar{\Omega}(\mathbf{K}_{\tau-t_0/2})|e^{i\vartheta_j(\mathbf{K},\tau+t_0/2,t+t_0/2)} + \text{c.c.} \\ =& -i\int d\mathbf{K}|d_j(\mathbf{K}_t)|\int_{-\infty}^{t} d\tau F(\tau)|\bar{\Omega}(\mathbf{K}_\tau)|e^{i\vartheta_j(-\mathbf{K},\tau+t_0/2,t+t_0/2)} + \text{c.c.}, \end{aligned} \tag{6.64}$$

where have again substituted $\mathbf{K} \to -\mathbf{K}$. Since the shift vector vanishes for an inversion

symmetric system, the SFA phase satisfies

$$\begin{aligned}\vartheta_j(-\mathbf{K},\tau+t_0/2,t+t_0/2) =&\mathcal{S}(-\mathbf{K},\tau+t_0/2,t+t_0/2)+\phi_{cv,j}[-\mathbf{K}-e\mathbf{A}(\tau+t_0/2)]\\ &-\phi_{cv}[-\mathbf{K}-e\mathbf{A}(t+t_0/2)]\\ =&\mathcal{S}(\mathbf{K},\tau,t)+\phi_{cv,j}(-\mathbf{K}_\tau)-\phi_{cv}(-\mathbf{K}_t). \end{aligned} \tag{6.65}$$

For the difference of dipole phases, we can use the inversion relation (E.8) for centro-symmetric crystals to deduce

$$\begin{aligned}\phi_{cv,j}(-\mathbf{k})-\phi_{cv}(-\mathbf{k}) =&\arg\left\{[\mathbf{e}_j\cdot\mathbf{d}_{cv}(-\mathbf{k})]\,[\mathbf{n}\cdot\mathbf{d}^*_{cv}(-\mathbf{k})]\right\}\\ =&\arg\left\{\left[\mathbf{e}_j\cdot\mathbf{d}_{cv}(\mathbf{k})\left(-e^{i\bar{\sigma}(\mathbf{k})}\right)\right]\left[\mathbf{n}\cdot\mathbf{d}^*_{cv}(\mathbf{k})\left(-e^{i\bar{\sigma}(\mathbf{k})}\right)^*\right]\right\}\\ =&\phi_{cv,j}(\mathbf{k})-\phi_{cv}(\mathbf{k}). \end{aligned} \tag{6.66}$$

The total SFA phase is thus symmetric between half cycles,

$$\vartheta_j(-\mathbf{K},\tau+t_0/2,t+t_0/2)=\vartheta_j(\mathbf{K},\tau,t), \tag{6.67}$$

and this leads to the simple relation

$$p_{er,j}(t+t_0/2)=-p_{er,j}(t), \tag{6.68}$$

which shows that the interband polarization has negative parity between half-cycles. From this, it is straightforward to show that the harmonic amplitudes in the cw-limit

$$j_{er,j}(n\omega_0)=in\omega_0\int_0^{t_0}dte^{-in\omega_0 t}p_{er,j}(t), \tag{6.69}$$

are non-vanishing only for odd values of n. Although it is not a new observation that even order interband harmonics vanish in an inversion symmetric system, it is interesting to observe that: 1) this selection rule holds for all components of the current in multiple dimensions; and 2) the selection rule can be derived without any assumptions of the Bloch gauge, since all gauge-dependent phases cancel. This analysis generalizes previous results which considered only the parallel component [35], or relied on implicit assumptions about the Bloch gauge [27].

6.4 Application of the gauge invariant SBEs

To demonstrate the validity of the gauge invariant SBEs in an example system, we use the 6-band tight-binding model for ZnO developed in Ref. [28]. ZnO has a hexagonal crystal structure, and this simplified tight-binding model approximates the band structure in the rectangular ΓALM cross section of the BZ, as illustrated in Fig. 6.1. After diagonalizing the Hamiltonian analytically, it is straightforward to obtain expressions for the Berry connections and shift vectors. The Berry connections are calculated in a particular Bloch gauge used to diagonalize the tight-binding Hamiltonian, and we refer to this as the TB gauge.

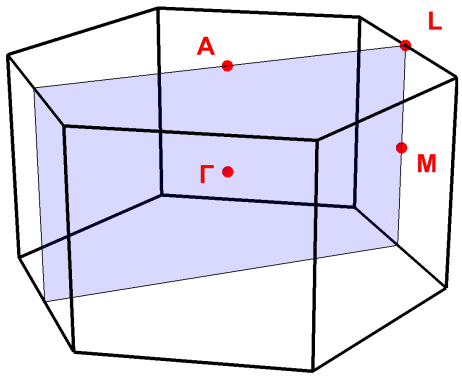

Figure 6.1: Brillouin zone of the hexagonal lattice for ZnO, indicating the cross section defined by the symmetry points ΓALM.

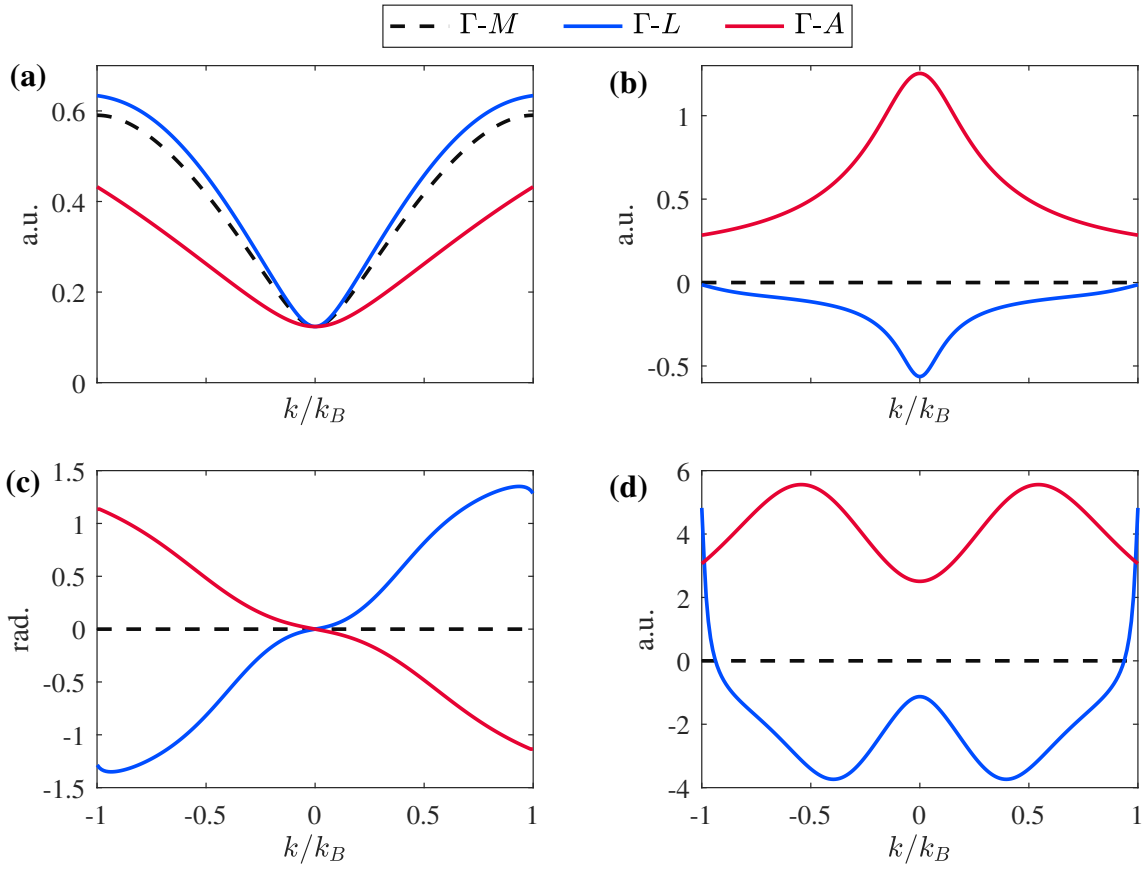

Figure 6.2: 1D band structure of ZnO along symmetry axes of BZ: panel (a) shows the bandgap; (b) is the difference of Berry connections $\mathcal{A}_{cv} = \mathcal{A}_c - \mathcal{A}_v$; (c) is the TDM phase; and (d) shows the shift vector $\mathbf{R}_{cv}$. The scale factor k_B is the boundary of the BZ along each direction.

We simulate the dynamics using the SBEs formulated in the comoving frame, with the goal of demonstrating the validity of the gauge invariant SBEs (GI-SBEs) by comparing the resulting HHG spectra to calculations using the covariant SBEs in the TB gauge (TB-SBEs). Assuming linear input polarization, we consider one-dimensional approximations of the band structure for different polarization angles. Fig. 6.2 shows the relevant band structure along three symmetry axes containing the minimum bandgap; namely ΓM, ΓL, and ΓA. We note that there is a reflection symmetry operation along the ΓM direction, and the shift vector vanishes as a result. The TDM phase and Berry connections also vanish along the symmetry direction; however, these results depend on the specific TB gauge. One could transform to a different gauge in which the TDM phase and Berry connections would be nonzero. The axes ΓL and ΓA have no special symmetry operations, and the corresponding shift vectors shown in Fig. 6.2d are non-zero as a result. In our calculations the system was excited by a 75fs pulse with 2.07μm wavelength, and a

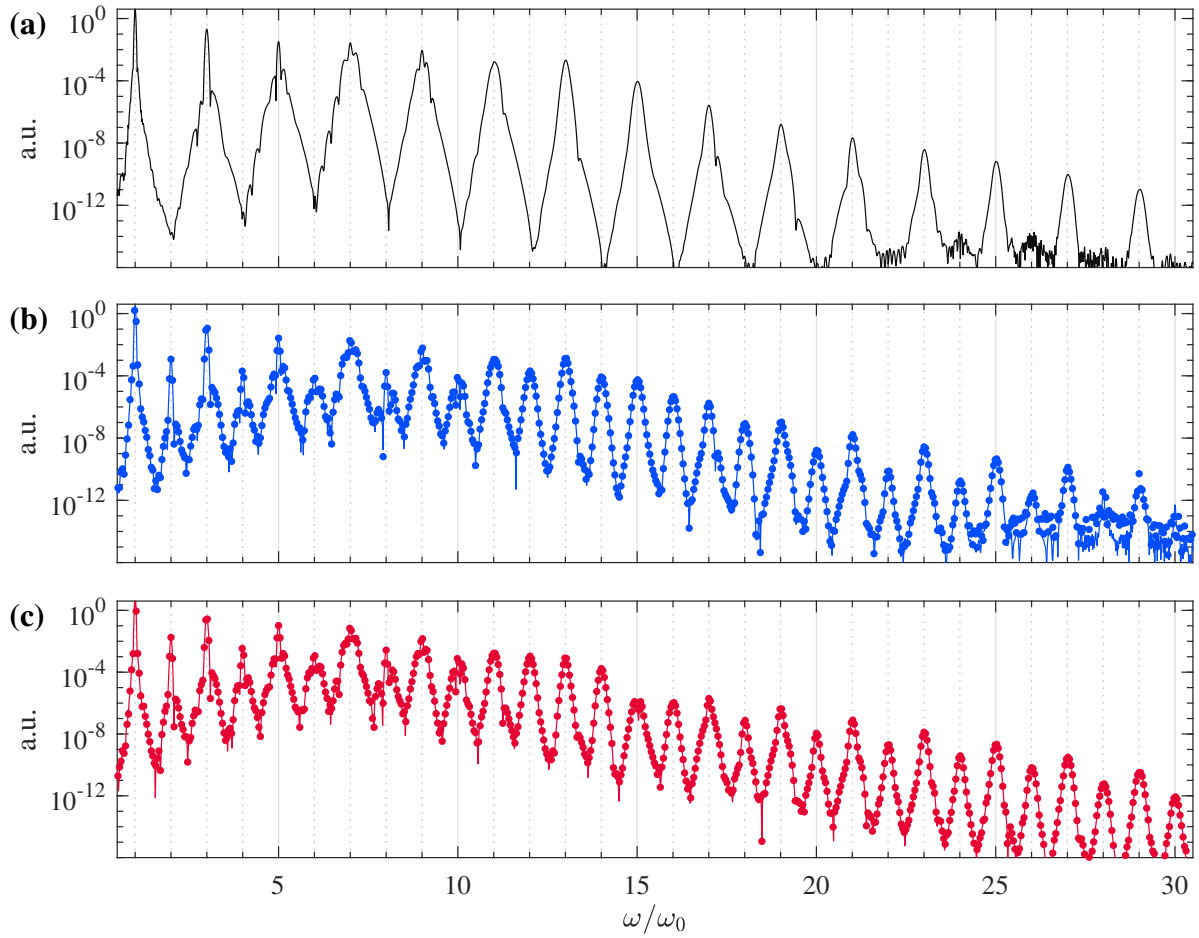

Figure 6.3: HHG spectra along different symmetry directions of ZnO; (a) ΓM, (b) ΓL, (c) ΓA. In (b,c) the lines are calculated using the covariant SBEs, while the filled circles result from the gauge invariant SBEs

phenomenological dephasing time of 0.5 optical cycles was used.

The simulated interband HHG spectra along the different orientations are shown in Fig. 6.3. For the ΓM direction with 1D inversion symmetry, Fig. 6.3a exhibits only odd-order harmonics, as expected. For this orientation the TB-SBEs are identical to the GI-SBEs, since only the bandgap and TDM magnitude are non-zero. It is more interesting to compare the simulations results for the ΓL and ΓA directions, where the broken inversion symmetry gives rise to even harmonics. Figs. 6.3b-c show that the TB-SBEs and GI-SBEs give equivalent results for the HHG spectrum. A small discrepancy arises for harmonics approaching the noise floor of the spectrum, which can be seen for the highest harmonics in Fig. 6.3b. This is simply a convergence issue of the numerical integrator, and not a shortcoming of the gauge invariant formalism.

We can also observe in Fig. 6.3 that the even harmonics appear stronger along the ΓA

orientation compared to ΓL. The shift vector provides an inuitive and gauge invariant explanation for this observation. For these simulation parameters the dynamics fall within the SFA. As a result, excited population is expected to be largest near the minimum bandgap at $k = 0$, and even order harmonics are necessarily generated by the shift vector. Since Fig. (6.2d) shows that the shift vector near $k = 0$ is larger along ΓA compared to ΓL, we expect the overall influence of the shift vector to be more significant along ΓA. Although Fig. (6.2) also shows that $\mathcal{A}_{cv}$ is larger for ΓA, the behaviour of the TDM phase is less intuitive. More importantly, these quantities are gauge-dependent, which makes interpretation somewhat ambiguous. Clearly, it is preferable to study the behaviour of gauge invariant structure in relation to observables, and in this example the shift vector provides an unambiguous connection between band structure and HHG phenomena.

We can gain further insight for the role of the shift vector in HHG by comparing simulations with $\mathbf{R}_{cv} = 0$ and $\mathbf{R}_{cv} \neq 0$. Specifically, we simulate the gauge invariant SBEs along the ΓA orientation, and we compare the results to a modified calculation in which the shift vector is artificially set to zero. Fig. 6.4a shows time-dependent excitation rate $\dot{n}_c(t)$ for two optical cycles. When the shift vector is zero (black curve), the excitation rate is equivalent between half cycles; in agreement with the analysis of Sec. 6.3.2. When $\mathbf{R}_{cv} \neq 0$, the rate in the positive (negative) half cycle is enhanced (suppressed) compared to the rate using $\mathbf{R}_{cv} = 0$.

Fig. 6.4b compares the HHG spectra with and without the shift vector. As expected, the shift vector must be non-zero in order for even harmonics to be generated. However, we also observe the interesting result that the odd harmonics are mostly unaffected by the shift vector. In Fig. 6.4b we see that harmonic 15 shows the most noticeable discrepancy when the shift vector is set to zero, but most of the odd harmonics have negligible discrepancy. To study the discrepancy more directly, we define the integrated efficiency for each integer harmonic order n,

$$S(n\omega_0) = \int_{n\omega_0-\delta\omega}^{n\omega_0+\delta\omega} d\omega S(\omega), \tag{6.70}$$

where $\delta\omega$ is an integration window. Further, we denote $S^0(\omega)$ harmonic efficiency resulting from simulation with the shift vector set to zero, and the discrepancy between simulations with/without the shift vector is quantified as

$$\Delta S = \frac{S - S^0}{S + S^0}. \tag{6.71}$$

Fig. 6.4c shows the discrepancy for the odd harmonic orders. The dashed black line indicates the semiclassical cutoff, which is the maximum harmonic energy beyond which the saddle point equations for the SFA phase (6.57) have no solutions. A brief discussion of the saddle point

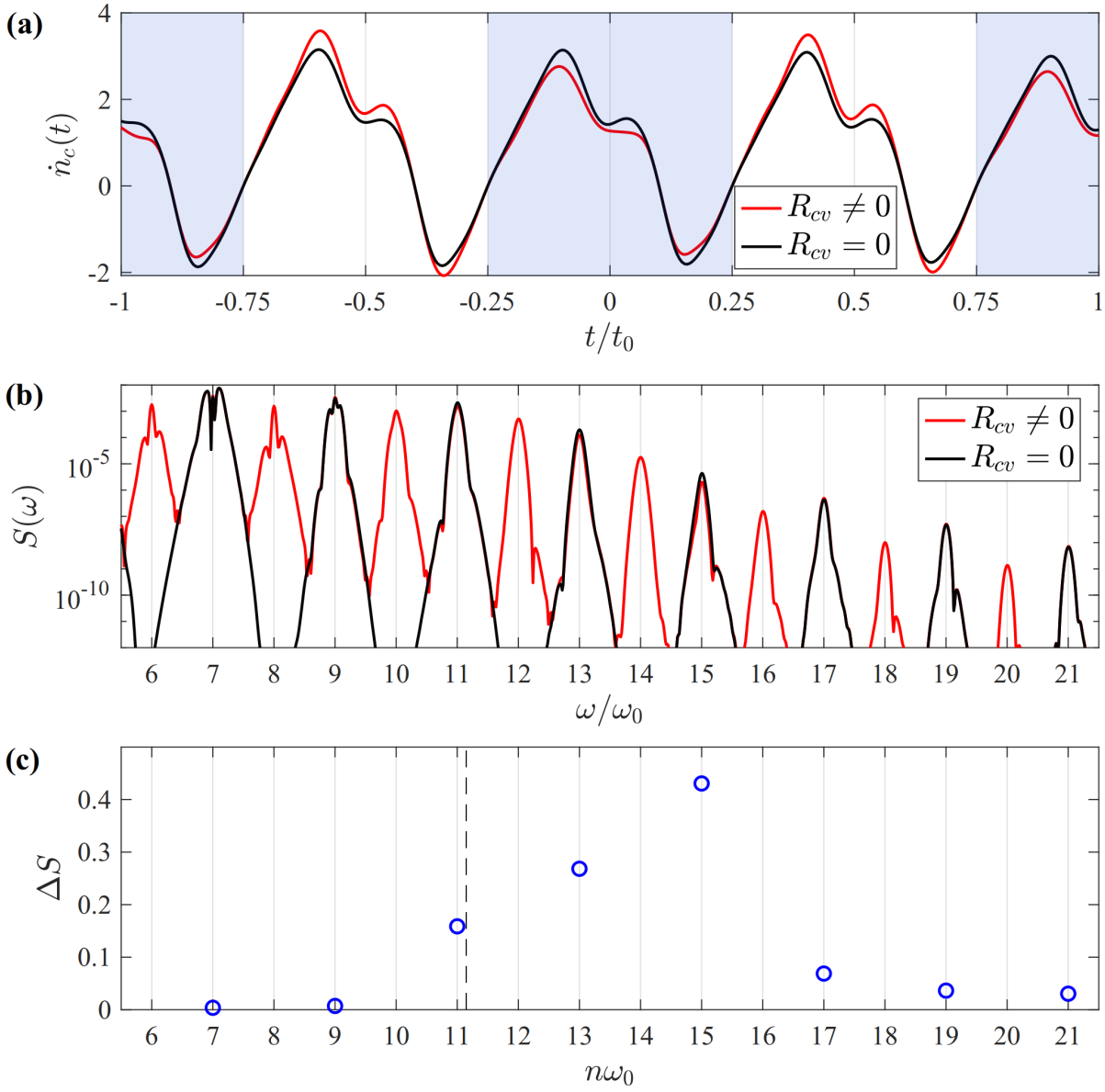

Figure 6.4: Comparison of HHG simulations with and without the shift vector included; using 75fs pulse polarized along ΓA, with field strength $F_0 = 0.0023$. Panel (a) shows the excitation rate $\dot{n}_c(t)$ for two optical cycles, where the shaded regions indicate the negative half-cycle. Panel (b) compares the harmonic efficiency $S(\omega)$ with (red) and without (black) the shift vector included; while (c) shows the discepancy ΔS for the odd harmonics. In (b,c) we only includeharmonics above the minimum bandgap, and the black dashed line in (c) indicates the semiclassical cutoff.

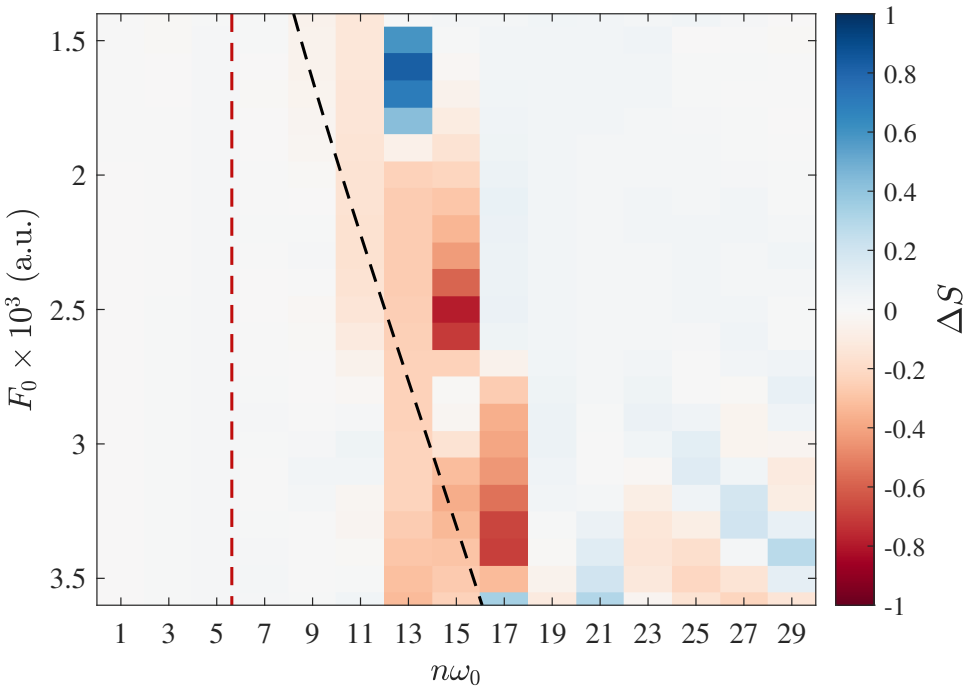

Figure 6.5: Discrepancy ΔS of odd harmonics as a function of applied field strength. The red dashed line indicates the minumum bandgap, while the black dashed line indicates the semiclassical cutoff.

equations is provided in appendix F for reference. In Fig. 6.4c we observe that the harmonic discrepancy begins to increase approaching the cutoff, and is then maximized slightly above the cutoff before it begins to decrease with harmonic order.

Since the cutoff depends on the applied field strength by virtue of Eq. (F.9), we might expect discrepancy to vary with field strength as well. Fig. 6.5 shows the discrepancy ΔS as a function of field strength for each odd harmonic order. Odd harmonics below the cutoff have very little discrepancy, which indicates they are insensitive to the shift vector. As the field strength increases, we observe that the harmonic order showing the largest discrepancy also increases. Overall, we observe a trend that the discrepancy is maximized slighly above the cutoff, but away from this region the odd harmonics are not influenced significantly by the shift vector.

6.5 Summary

We have derived a novel formulation of the 1-body SBEs which only involve gauge invariant structural quantities. In the gauge invariant SBEs the TDM phase and Berry connections are replaced by the gauge invariant shift vector. We also clarified the gauge invariance of the strong field approximation for HHG in solids, in which the shift vector also plays an important role.

The gauge invariant SBEs were successfully demonstrated for a simple 1D two-band system,

It should be mentioned that implementing the gauge invariant SBEs for more general systems will present numerical challenges. For multiband systems the triple product of TDM phases in Eq. 6.15 does not vanish, and must be included in the calculation. Although this quantity is gauge invariant, it may not be smooth throughout the BZ. Specifically, the phase of a TDM component can exhibit a discontinuous jump at a zero-crossing. As a result, the product of TDM phases can have a phase jump of π at k-points where the TDM magnitude vanishes. Clearly a discontinuity is undesirable for numerical integration of the SBEs; however, the dynamics at such points should be trivial since a vanishing TDM cannot excite electron-hole pairs. One possible technique might be to suppress such points in the SBEs, since their contribution is expected to be negligible.

Higher dimensions also require careful consideration due to the complicated behaviour of the shift vector. Since the shift vector depends on the gradient of the TDM phase, the shift vector can be singular where the TDM magnitude vanishes. Again, these points should not contribute meaningfully to the dynamics, and developing a numerical technique to suppress these k-space regions will be the focus of future work. The existing literature involving the shift vector has focused primarily on the bulk photovoltaic effect [47, 71, 72], and only recently has the shift vector been studied in the context of HHG [35]. The role of the shift vector in HHG deserves further study; both from the perspective of the gauge invariant SBEs, as well as the SFA.

In theory, the gauge invariant SBEs eliminate the random phase issue for band structure calculated from numerical diagonalization. Whereas the Berry connections can only be calculated using finite differences in a smooth Bloch gauge, the shift vector should not be susceptible to this issue since it is gauge invariant. Indeed, techniques have been developed to calculate the shift vector directly from DFT [47, 60], without the need for gauge smoothing. Finally, the gauge invariant SBEs also open up new possibilities for the prospect of reconstructing band structure from HHG measurements. Reconstruction of the TDM is complicated due to its gauge dependent phase, and any reconstruction algorithm must fix the gauge of the SBEs. Ref. [73] demonstrated an approach for a 1D system using the parallel transport gauge, but the generalization to higher dimensions is not trivial. In contrast, reconstruction of the shift vector is unambiguous since it is gauge invariant. Further, we have shown that most of the odd harmonics are insensitive to the shift vector. This suggests the possibility of an iterated approach to reconstruction where the bandgap and TDM amplitudes are optimized to match the measured odd harmonics, while the reconstruction of the shift vector is based on even harmonics.

Chapter 7
Concluding remarks

The semiconductor Bloch equations provide an efficient and insightful formalism for studying light-matter interactions in solids. The SBEs in the single particle approximation are particularly well-suited to model high harmonic generation in semiconductors, where the intense driving laser is tuned below the bandgap. The $U(1)$ gauge symmetry of a periodic solid plays an important role when the SBEs are formulated in the length gauge. On one hand, this gauge freedom can complicate numerical analysis of the SBEs, since the matrix elements of the position operator are not uniquely defined. However, in this thesis we have shown that this gauge freedom can also be beneficial, and we have exploited it to develop novel approaches for analyzing and formulating the SBEs.

The smoothed gauge for gapped graphene provides a suitable test platform to investigate the orientation dependence of HHG. In particular, we obtained explicit expressions for the generalized derivatives of the TDM components, which facililated a thorough characterization of the mixture current in gapped graphene. When gapped graphene is subject to a linearly polarized optical pulse, the orientation dependence of harmonic efficiency exhibits 6-fold symmetry. The orientation dependent patterns are complicated and non-intuitive, with significant variation for different harmonic orders. Further, the orientation dependence of several harmonics exhibit rapid transitions in response to modulation of the applied field strength. For example, in Fig. 3.6 we observed that the efficiency of harmonic 9 is maximized along ΓM and minimized along ΓK at weak fields; but as the field strength increases, the maxima and minima flip. This behaviour can be interpreted is a field-induced transition of the material response, and will be a significant focus of future work.

Although the mixture current clearly influences the orientation dependence of some harmonics, in most cases it simply shifts the field strength at which these transitions occur. Changing the dephasing time has a similar effect, and does not modify the combined orientation and field-strength dependence in a qualitative way. This suggests that the overall response of harmonic efficiency to orientation and field strength is quite stable. It is an open question if these observations are specific to the model of gapped graphene, or if they also manifest in more

realistic materials. Future work will generalize this analysis of orientation dependence to band structure calculated from DFT.

In Chapter 5 we discussed the orbital basis approach for simulating the HHG in analytic tight-binding models. This is complementary to the MLWF basis used to obtain a smooth gauge for DFT band structure. Although tight-binding models do not reproduce all the features of DFT calculations, they can be easier to work with than numerical band structure. Further, a tight-binding model that reproduces essential features of the band structure can be used as an exploratory model to develop intuition and understanding. In future work we will apply the orbital basis to more sophisticated tight-binding models, such as the 6-band model for transition metal dichalcogenides developed in Ref. [74]. Since the orbital basis is not susceptible to the numerical complications of singular Berry connections, this approach is particularly well-suited for studying topological materials. This avoids the need for complex gauge-stitching procedures, as used in Ref. [67] for simulating HHG in the Haldane model [75].

The gauge invariant SBEs provide a description of HHG in solids that involves only gauge invariant structural quantities, and the shift vector plays a central role in this formalism. Since the shift vector is gauge invariant, it can be obtained directly from numerical band structure calculations [47]. This avoids the need for complicated gauge smoothing algorithms when simulating the gauge covariant SBEs with numerical band structure. Although the shift vector was identified over 20 years ago by Sipe et al [46], its relevance to HHG was only identified very recently [35]. The shift vector has received more attention from the photovoltaic community [47, 71, 72], and further work is required to develop more familiarity with its behaviour.

By simulating the gauge invariant SBEs in a model system, we saw that the shift vector is responsible for generating even harmonics in the absence of inversion symmetry. Since the shift vector is gauge invariant, its prominent role in HHG raises new possibilities for tomographic reconstruction of band structure. Previous studies have demonstrated reconstruction of other gauge invariant structural quantities, such as the band energy [13, 63] and Berry curvature [14, 15]. Reconstruction of the TDM is significantly more complicated due to its gauge dependence. Ref. [73] demonstrated an approach for extracting the TDM in a 1D system by fixing the gauge of the SBEs to the parallel transport gauge [41]. Unfortunately, this gauge is particularly simple in 1D since it corresponds to vanishing Berry connections, and the generalization to higher dimensions is not obvious. One possibility could be to fix the SBEs to the MLWF gauge using the approach of Sec. 3.4, which specifies a unique gauge in higher dimensions. However, reconstruction of the shift vector would avoid these complications entirely since it is gauge invariant. Further, we observed that the shift vector has a negligible influence on the majority of the odd harmonics, which are determined primarily by the bandgap and the magnitude of

the TDM. As a result, one could envision an iterative scheme for reconstructing band structure; where the odd harmonics are used to reconstruct the bandgap and TDM magnitude, while the shift vector is reconstructed from the even harmonics. Future work will apply the gauge invariant SBEs to more realistic structural models, where tomographic reconstruction of the shift vector will also be investigated in more detail.

Bibliography

1. S. Ghimire, A. D. Dichiara, E. Sistrunk, P. Agostini, L. F. Dimauro, and D. A. Reis, "Observation of high-order harmonic generation in a bulk crystal," *Nature Physics*, vol. 7, no. 2, pp. 138–141, 2011. DOI: 10.1038/nphys1847

2. T. T. Luu, M. Garg, S. Yu. Kruchinin, A. Moulet, M. T. Hassan, and E. Goulielmakis, "Extreme ultraviolet high-harmonic spectroscopy of solids," *Nature*, vol. 521, no. 7553, pp. 498–502, 2015. DOI: 10.1038/nature14456

3. M. Garg, M. Zhan, T. T. Luu, H. Lakhotia, T. Klostermann, A. Guggenmos, and E. Goulielmakis, "Multi-petahertz electronic metrology," *Nature*, vol. 538, p. 359, 2016.

4. H. Liu, Y. Li, Y. S. You, S. Ghimire, T. F. Heinz, and D. A. Reis, "High-harmonic generation from an atomically thin semiconductor," vol. 13, no. November 2016, 2017. DOI: 10.1038/NPHYS3946

5. N. Yoshikawa, K. Nagai, K. Uchida, Y. Takaguchi, S. Sasaki, Y. Miyata, and K. Tanaka, "Interband resonant high-harmonic generation by valley polarized electron-hole pairs," *Nature Communications*, vol. 10, p. 3709, 2019.

6. G. Vampa, B. G. Ghamsari, S. S. Mousavi, T. J. Hammond, and A. Olivieri, "Plasmon-enhanced high-harmonic generation from silicon," *Nature Physics*, vol. 13, p. 659, 2017. DOI: 10.1038/NPHYS4087

7. D. Franz, S. Kaassamani, D. Gauthier, R. Nicolas, M. Kholodtsova, L. Douillard, J.-t. Gomes, L. Lavoute, D. Gaponov, N. Ducros, S. Février, J. Biegert, L. Shi, M. Kovacev, W. Boutu, and H. Merdji, "All semiconductor enhanced high- harmonic generation from a single nanostructured cone," pp. 6–12, 2019.

8. M. Schultze, E. M. Bothschafter, A. Sommer, S. Holzner, W. Schweinberger, M. Fiess, M. Hofstetter, R. Kienberger, V. Apalkov, V. S. Yakovlev, M. I. Stockman, and F. Krausz, "Controlling dielectrics with the electric field of light," *Nature*, vol. 493, no. 7430, pp. 75–78, 2013. DOI: 10.1038/nature11720

9. M. Hohenleutner, F. Langer, O. Schubert, M. Knorr, U. Huttner, S. W. Koch, M. Kira, and R. Huber, "Real-time observation of interfering crystal electrons in high-harmonic generation," 2015. DOI: 10.1038/nature14652

10. H. K. Kelardeh, V. Apalkov, and M. I. Stockman, "Attosecond strong-field interferometry in graphene: Chirality, singularity, and Berry phase," *Physical Review B*, vol. 93, no. 15, pp. 1–7, 2016. DOI: 10.1103/PhysRevB.93.155434

11. T. Higuchi, C. Heide, K. Ullmann, H. B. Weber, and P. Hommelhoff, "Light-field-driven currents in graphene," *Nature*, vol. 550, no. 7675, pp. 224–228, 2017. DOI: 10.1038/nature23900

12. F. Langer, M. Hohenleutner, U. Huttner, S. W. Koch, M. Kira, and R. Huber, "Symmetry-controlled temporal structure of high-harmonic carrier fields from a bulk crystal," *Nature Photonics*, vol. 11, no. 4, pp. 227–231, 2017. DOI: 10.1038/nphoton.2017.29

13. G. Vampa, T. J. Hammond, N. Thiré, B. E. Schmidt, F. Légaré, C. R. McDonald, T. Brabec, D. D. Klug, and P. B. Corkum, "All-Optical Reconstruction of Crystal Band Structure," *Physical Review Letters*, vol. 115, no. 19, pp. 1–5, 2015. DOI: 10.1103/PhysRevLett.115.193603

14. H. B. Banks, Q. Wu, D. C. Valovcin, S. Mack, A. C. Gossard, L. Pfeiffer, R. B. Liu, and M. S. Sherwin, "Dynamical birefringence: Electron-hole recollisions as probes of berry curvature," *Physical Review X*, vol. 7, no. 4, pp. 1–21, 2017. DOI: 10.1103/PhysRevX.7.041042

15. T. T. Luu and H. J. Wörner, "Measurement of the Berry curvature of solids using high-harmonic spectroscopy," *Nature Communications*, vol. 9, no. 1, pp. 1–6, 2018. DOI: 10.1038/s41467-018-03397-4

16. G. Vampa, C. R. McDonald, G. Orlando, D. D. Klug, P. B. Corkum, and T. Brabec, "Theoretical analysis of high-harmonic generation in solids," *Physical Review Letters*, vol. 113, no. 7, p. 073901, 2014. DOI: 10.1103/PhysRevLett.113.073901

17. E. N. Osika, A. Chacón, L. Ortmann, N. Suárez, J. A. Pérez-Hernández, B. Szafran, M. F. Ciappina, F. Sols, A. S. Landsman, and M. Lewenstein, "Wannier-bloch approach to localization in high-harmonics generation in solids," *Physical Review X*, vol. 7, no. 2, pp. 1–14, 2017. DOI: 10.1103/PhysRevX.7.021017

18. A. M. Parks, G. Ernotte, A. Thorpe, C. R. McDonald, P. B. Corkum, M. Taucer, and T. Brabec, "Wannier quasi-classical approach to high harmonic generation in semiconductors," *Optica*, vol. 7, no. 12, p. 1764, 2020. DOI: 10.1364/optica.402393

19. N. Tancogne-Dejean, O. D. Mücke, F. X. Kärtner, and A. Rubio, "Ellipticity dependence of high-harmonic generation in solids originating from coupled intraband and interband dynamics," *Nature Communications*, vol. 8, no. 1, 2017. DOI: 10.1038/s41467-017-00764-5

20. N. Tancogne-dejean and A. Rubio, "Atomic-like high-harmonic generation from two-dimensional materials," no. February, pp. 1–7, 2018.

21. H. Haug and S. W. Koch, *Quantum theory of the optical and electronic properties of semiconductors, fifth edition*, 5th ed. WORLD SCIENTIFIC, 2009. DOI: 10.1142/7184

22. D. Golde, T. Meier, and S. W. Koch, "High harmonics generated in semiconductor nanostructures by the coupled dynamics of optical inter- and intraband excitations," *Physical Review B - Condensed Matter and Materials Physics*, vol. 77, no. 7, pp. 1–6, 2008. DOI: 10.1103/PhysRevB.77.075330

23. M. Lindberg and S. W. Koch, "Effective Bloch equations for semiconductors," *Physical Review B*, vol. 38, no. 5, pp. 3342–3350, 1988. DOI: 10.1103/PhysRevB.38.3342

24. G. Vampa, C. R. McDonald, G. Orlando, P. B. Corkum, and T. Brabec, "Semiclassical analysis of high harmonic generation in bulk crystals," *Physical Review B - Condensed Matter and Materials Physics*, vol. 91, no. 6, p. 064302, 2015. DOI: 10.1103/PhysRevB.91.064302

25. G. Vampa, T. J. Hammond, N. Thiré, B. E. Schmidt, F. Légaré, C. R. McDonald, T. Brabec, and P. B. Corkum, "Linking high harmonics from gases and solids," *Nature*, vol. 522, no. 7557, pp. 462–464, 2015. DOI: 10.1038/nature14517

26. C. R. McDonald, G. Vampa, P. B. Corkum, and T. Brabec, "Intense-Laser Solid State Physics: Unraveling the Difference between Semiconductors and Dielectrics," *Physical Review Letters*, vol. 118, no. 17, p. 173601, 2017. DOI: 10.1103/PhysRevLett.118.173601

27. S. Jiang, H. Wei, J. Chen, C. Yu, R. Lu, and C. D. Lin, "Effect of transition dipole phase on high-order-harmonic generation in solid materials," *Physical Review A*, vol. 96, no. 5, pp. 1–11, 2017. DOI: 10.1103/PhysRevA.96.053850

28. S. Jiang, J. Chen, H. Wei, C. Yu, R. Lu, and C. D. Lin, "Role of the Transition Dipole Amplitude and Phase on the Generation of Odd and even High-Order Harmonics in Crystals," *Physical Review Letters*, vol. 120, no. 25, p. 253201, 2018. DOI: 10.1103/PhysRevLett.120.253201

29. S. Almalki, A. M. Parks, T. Brabec, and C. R. McDonald, "Nanoengineering of strong field processes in solids," *Journal of Physics B: Atomic, Molecular and Optical Physics*, vol. 51, no. 8, p. 84001, 2018. DOI: 10.1088/1361-6455/aab41b

30. R. E. Silva, F. Martín, and M. Ivanov, "High harmonic generation in crystals using maximally localized Wannier functions," *Physical Review B*, vol. 100, no. 19, pp. 1–6, 2019. DOI: 10.1103/PhysRevB.100.195201

31. J. Li, X. Zhang, S. Fu, Y. Feng, B. Hu, and H. Du, "Phase invariance of the semiconductor Bloch equations," *Physical Review A*, vol. 100, no. 4, p. 43404, 2019. DOI: 10.1103/PhysRevA.100.043404

32. L. Yue and M. B. Gaarde, "Structure gauges and laser gauges for the semiconductor Bloch equations in high-order harmonic generation in solids," *Physical Review A*, vol. 101, no. 5, p. 53411, 2020. DOI: 10.1103/PhysRevA.101.053411

33. L. H. Thong, C. Ngo, H. T. Duc, X. Song, and T. Meier, "Microscopic analysis of high harmonic generation in semiconductors with degenerate bands," *Physical Review B*, vol. 103, no. 8, p. 85201, 2021. DOI: 10.1103/PhysRevB.103.085201

34. T.-m. Dichalcogenides, Y. Kobayashi, C. Heide, H. K. Kelardeh, A. Johnson, F. Liu, T. F. Heinz, D. A. Reis, and S. Ghimire, "Polarization Flipping of Even-Order Harmonics in Monolayer," vol. 2021, 2021.

35. C. Qian, C. Yu, S. Jiang, T. Zhang, J. Gao, S. Shi, H. Pi, H. Weng, and R. Lu, "Role of Shift Vector in High-Harmonic Generation from Noncentrosymmetric Topological Insulators under Strong Laser Fields," *Physical Review X*, vol. 12, no. 2, p. 21030, 2022. DOI: 10.1103/PhysRevX.12.021030

36. L. Yue and M. B. Gaarde, "Introduction to theory of high-harmonic generation in solids: tutorial," *Journal of the Optical Society of America B*, vol. 39, no. 2, p. 535, 2022. DOI: 10.1364/josab.448602

37. Y. Shen, "Nonlinear Optical Susceptibilities," *Encyclopedia of Materials: Science and Technology*, vol. 52, no. 20, pp. 6249–6255, 2001. DOI: 10.1016/b0-08-043152-6/01109-8

38. K. S. Virk and J. E. Sipe, "Semiconductor optics in length gauge: A general numerical approach," *Physical Review B - Condensed Matter and Materials Physics*, vol. 76, no. 3, pp. 1–11, 2007. DOI: 10.1103/PhysRevB.76.035213

39. J. Wilhelm, P. Grössing, A. Seith, J. Crewse, M. Nitsch, L. Weigl, C. Schmid, and F. Evers, "Semiconductor Bloch-equations formalism: Derivation and application to high-harmonic generation from Dirac fermions," *Physical Review B*, vol. 103, no. 12, pp. 1–19, 2021. DOI: 10.1103/PhysRevB.103.125419

40. H. J. Rothe, *Lattice Gauge Theories*, 4th ed. WORLD SCIENTIFIC, 2021, vol. 992.

41. D. Vanderbilt, *BERRY PHASES IN ELECTRONIC STRUCTURE THEORY: Electric Polarization, Orbital Magnetization and Topological Insulators*. Cambridge University Press, 2018. DOI: 10.1017/9781316662205

42. T. G. Pedersen, A. P. Jauho, and K. Pedersen, "Optical response and excitons in gapped graphene," *Physical Review B - Condensed Matter and Materials Physics*, vol. 79, no. 11, pp. 11–14, 2009. DOI: 10.1103/PhysRevB.79.113406

43. S. A. Oliaei Motlagh, F. Nematollahi, A. Mitra, A. J. Zafar, V. Apalkov, and M. I. Stockman, "Ultrafast optical currents in gapped graphene," *Journal of Physics Condensed Matter*, vol. 32, no. 6, 2020. DOI: 10.1088/1361-648X/ab4fc7

44. G. Pizzi, V. Vitale, R. Arita, S. Blügel, F. Freimuth, G. Géranton, M. Gibertini, D. Gresch, C. Johnson, T. Koretsune, J. Ibanez-Azpiroz, H. Lee, J. M. Lihm, D. Marchand, A. Marrazzo, Y. Mokrousov, J. I. Mustafa, Y. Nohara, Y. Nomura, L. Paulatto, S. Poncé, T. Ponweiser, J. Qiao, F. Thöle, S. S. Tsirkin, M. Wierzbowska, N. Marzari, D. Vanderbilt, I. Souza, A. A. Mostofi, and J. R. Yates, "Wannier90 as a community code: New features and applications," *Journal of Physics Condensed Matter*, vol. 32, no. 16, 2020. DOI: 10.1088/1361-648X/ab51ff

45. N. Marzari and D. Vanderbilt, "Maximally localized generalized Wannier functions for composite energy bands," *Physical Review B - Condensed Matter and Materials Physics*, vol. 56, no. 20, pp. 12 847–12 865, 1997. DOI: 10.1103/PhysRevB.56.12847

46. J. L. Cabellos, "Optical Response in Semiconductors," *Centro de Investigaciones en Óptica, PhD Thesis*, vol. 61, no. 8, 2009.

47. S. M. Young and A. M. Rappe, "First principles calculation of the shift current photovoltaic effect in ferroelectrics," *Physical Review Letters*, vol. 109, no. 11, pp. 1–5, 2012. DOI: 10.1103/PhysRevLett.109.116601

48. G. B. Ventura, D. J. Passos, J. M. Lopes Dos Santos, J. M. Viana Parente Lopes, and N. M. Peres, "Gauge covariances and nonlinear optical responses," *Physical Review B*, vol. 96, no. 3, pp. 1–11, 2017. DOI: 10.1103/PhysRevB.96.035431

49. E. I. Blount, "Formalisms of Band Theory," *Solid State Physics - Advances in Research and Applications*, vol. 13, no. C, pp. 305–373, 1962. DOI: 10.1016/S0081-1947(08)60459-2

50. R. Loudon and T. von Foerster, *The Quantum Theory of Light*. Oxford: Oxford University Press, 1974, vol. 42, no. 11. DOI: 10.1119/1.1987930

51. B. Gu, N. H. Kwong, and R. Binder, "Relation between the interband dipole and momentum matrix elements in semiconductors," *Physical Review B - Condensed Matter and Materials Physics*, vol. 87, no. 12, pp. 1–17, 2013. DOI: 10.1103/PhysRevB.87.125301

52. D. Xiao, M. C. Chang, and Q. Niu, "Berry phase effects on electronic properties," *Reviews of Modern Physics*, vol. 82, no. 3, pp. 1959–2007, 2010. DOI: 10.1103/RevModPhys.82.1959

53. B. A. Bernevig and T. L. Hughes, *Topological insulators and topological superconductors*. Princeton: Princeton University Press, 2013. DOI: 10.1515/9781400846733

54. C. Heide, T. Eckstein, T. Boolakee, C. Gerner, H. B. Weber, I. Franco, and P. Hommelhoff, "Electronic Coherence and Coherent Dephasing in the Optical Control of Electrons in Graphene," *Nano Letters*, vol. 21, no. 22, pp. 9403–9409, 2021. DOI: 10.1021/acs.nanolett.1c02538

55. T. G. Pedersen, K. Pedersen, and T. Brun Kriestensen, "Optical matrix elements in tight-binding calculations," *Physical Review B - Condensed Matter and Materials Physics*, vol. 63, no. 20, p. 201101, 2001. DOI: 10.1103/PhysRevB.63.201101

56. W. R. Inc., "Mathematica," Champaign, IL, 2022. URL: https://www.wolfram.com/mathematica

57. P. Hewageegana and V. Apalkov, *Graphene quantum dots*. Berlin: Springer-Verlag, 2010. DOI: 10.1201/b19679-4

58. G. H. Wannier, "The structure of electronic excitation levels in insulating crystals," *Physical Review*, vol. 52, no. 3, pp. 191–197, 1937. DOI: 10.1103/PhysRev.52.191

59. X. Wang, J. R. Yates, I. Souza, and D. Vanderbilt, "Ab initio calculation of the anomalous Hall conductivity by Wannier interpolation," *Physical Review B - Condensed Matter and Materials Physics*, vol. 74, no. 19, pp. 1–15, 2006. DOI: 10.1103/PhysRevB.74.195118

60. C. Wang, X. Liu, L. Kang, B. L. Gu, Y. Xu, and W. Duan, "First-principles calculation of nonlinear optical responses by Wannier interpolation," *Physical Review B*, vol. 96, no. 11, pp. 1–9, 2017. DOI: 10.1103/PhysRevB.96.115147

61. Y. S. You, D. A. Reis, and S. Ghimire, "Anisotropic high-harmonic generation in bulk crystals," *Nature Physics*, vol. 13, no. 4, pp. 345–349, 2017. DOI: 10.1038/nphys3955

62. Y. S. You, E. Cunningham, D. A. Reis, and S. Ghimire, "Probing periodic potential of crystals via strong-field re-scattering," *Journal of Physics B: Atomic, Molecular and Optical Physics*, vol. 51, no. 11, 2018. DOI: 10.1088/1361-6455/aac11d

63. C. Yu, S. Jiang, T. Wu, G. Yuan, Z. Wang, C. Jin, and R. Lu, "Two-dimensional imaging of energy bands from crystal orientation dependent higher-order harmonic spectra in h-BN," *Physical Review B*, vol. 98, no. 8, pp. 1–9, 2018. DOI: 10.1103/PhysRevB.98.085439

64. L. V. Keldysh, "Ionization in the field of a strong electromagnetic wave," *Sov. Phys. JETP*, vol. 20, p. 1307, 1964.

65. N. Boroumand, A. Thorpe, A. M. Parks, and T. Brabec, "Keldysh ionization theory of atoms: Mathematical details," *Journal of Physics B: Atomic, Molecular and Optical Physics*, vol. 55, no. 21, 2022. DOI: 10.1088/1361-6455/ac9205

66. S. M. Golin, S. E. Kirkwood, D. D. Klug, D. M. Villeneuve, D. M. Rayner, C. A. Herrero, and P. B. Corkum, "Strong field processes inside gallium arsenide," *Journal of Physics B: Atomic, Molecular and Optical Physics*, vol. 47, no. 20, 2014. DOI: 10.1088/0953-4075/47/20/204025

67. A. Chacón, D. Kim, W. Zhu, S. P. Kelly, A. Dauphin, E. Pisanty, A. S. Maxwell, A. Picón, M. F. Ciappina, D. E. Kim, C. Ticknor, A. Saxena, and M. Lewenstein, "Circular dichroism in higher-order harmonic generation: Heralding topological phases and transitions in Chern insulators," *Physical Review B*, vol. 102, no. 13, p. 134115, 2020. DOI: 10.1103/PhysRevB.102.134115

68. X. L. Qi, Y. S. Wu, and S. C. Zhang, "Topological quantization of the spin Hall effect in two-dimensional paramagnetic semiconductors," *Physical Review B - Condensed Matter and Materials Physics*, vol. 74, no. 8, pp. 1–7, 2006. DOI: 10.1103/PhysRevB.74.085308

69. J. K. Asbóth, L. Oroszlány, and A. Pályi, *A Short Course on Topological Insulators: Band-structure topology and edge states in one and two dimensions*. Springer Cham, 2015. DOI: 10.1007/978-3-319-25607-8

70. S. C. Liebscher, M. K. Hagen, J. Hader, J. V. Moloney, and S. W. Koch, “Microscopic theory for the incoherent resonant and coherent off-resonant optical response of tellurium,” *Physical Review B*, vol. 104, no. 16, pp. 1–10, 2021. DOI: 10.1103/PhysRevB.104.165201

71. L. Z. Tan and A. M. Rappe, “Enhancement of the Bulk Photovoltaic Effect in Topological Insulators,” *Physical Review Letters*, vol. 116, no. 23, pp. 1–5, 2016. DOI: 10.1103/PhysRevLett.116.237402

72. L. Z. Tan, F. Zheng, S. M. Young, F. Wang, S. Liu, and A. M. Rappe, “Shift current bulk photovoltaic effect in polar materials-hybrid and oxide perovskites and beyond,” *npj Computational Materials*, vol. 2, no. July, 2016. DOI: 10.1038/npjcompumats.2016.26

73. D. Wu, L. Li, Y. Zhan, T. Huang, H. Cui, J. Li, P. Lan, and P. Lu, “Determination of transition dipole moments of solids with high-order harmonics driven by multicycle ultrashort pulses,” *Physical Review A*, vol. 105, no. 6, pp. 31–33, 2022. DOI: 10.1103/PhysRevA.105.063101

74. M. Bieniek, M. Korkusiński, L. Szulakowska, P. Potasz, I. Ozfidan, and P. Hawrylak, “Band nesting, massive Dirac fermions, and valley Landé and Zeeman effects in transition metal dichalcogenides: A tight-binding model,” *Physical Review B*, vol. 97, no. 8, pp. 1–9, 2018. DOI: 10.1103/PhysRevB.97.085153

75. F. D. Haldane, “Model for a quantum hall effect without landau levels: Condensed-matter realization of the "parity anomaly",” *Physical Review Letters*, vol. 61, no. 18, pp. 2015–2018, 1988. DOI: 10.1103/PhysRevLett.61.2015

Appendix A
Analysis in primitive basis

This appendix provides background for working in the primitive basis, which is not necessarily orthogonal. The primitive vectors of the reciprocal lattice are written as

$$\mathbf{b}_j = b_{j,\mu}\boldsymbol{e}_\mu, \tag{A.1}$$

where $\boldsymbol{e}_1, \boldsymbol{e}_2, \boldsymbol{e}_3$ are the Cartesian unit vectors, and we define the matrix of column vectors

$$B = \begin{bmatrix} \mathbf{b}_1 & \mathbf{b}_2 & \mathbf{b}_3 \end{bmatrix}, \tag{A.2}$$

with components $B_{ij} = b_{j,i}$. Writing a k-vector in the Cartesian basis as

$$\mathbf{k} = k_\mu \boldsymbol{e}_\mu, \tag{A.3}$$

and a fractional k-vector as

$$\bar{\mathbf{k}} = \bar{k}_\mu \mathbf{b}_\mu, \tag{A.4}$$

we have the relation

$$\mathbf{k} = B\bar{\mathbf{k}}, \tag{A.5}$$

where $\mathbf{k}$ and $\bar{\mathbf{k}}$ are interpreted as column vectors in their respective bases. In this appendix we distinguish vectors in the Cartesian and fractional representations by $\mathbf{k}$ and $\bar{\mathbf{k}}$, respectively; however, in the main text we assume the primitive basis is used throughout.

The covariant components of the metric tensor are

$$g_{ij} = \mathbf{b}_i \cdot \mathbf{b}_j = B_{\mu i} B_{\mu j}, \tag{A.6}$$

and thus

$$g = B^T B,$$

where B^T denotes the transpose of B, and the dot product of two k-vectors is given by

$$\mathbf{k} \cdot \mathbf{k}' = g_{\mu\nu} \bar{k}_\mu \bar{k}'_\nu. \tag{A.7}$$

The contravariant (inverse) components of g are given by

$$g^{ij} = (g^{-1})_{ij} = (B^{-1})^T B^{-1},$$

which is used to evaluate the gradient.

To study calculus in reciprocal space, we denote partial derivatives in the Cartesian basis as

$$\partial_j = \frac{\partial}{\partial k_j}, \tag{A.8}$$

while partial derivatives in the primitive basis are

$$\bar{\partial}_j = \frac{\partial}{\partial \bar{k}_j}. \tag{A.9}$$

Writing the components of the Jacobian matrix as

$$J_{ij} = \frac{\partial \bar{k}_i}{\partial k_j} = B^{-1}_{ij}, \tag{A.10}$$

we have

$$\partial_j = J^T_{j\mu} \bar{\partial}_\mu = \left(B^{-1}\right)^T_{j\mu} \bar{\partial}_\mu. \tag{A.11}$$

Note that the Jacobian determinant is just the volume of the first Brillouin zone; i.e. $|J| = |B| = V_{BZ}$, which gives the transformation $(1/V_{BZ}) \int d\mathbf{k} f(\mathbf{k}) = \int d\bar{\mathbf{k}} f(\bar{\mathbf{k}})$; as expected, since the fractional coordinates are by definition normalized with respect to the BZ.

The gradient is the vector field satisfying $\mathbf{b}_j \cdot \nabla = \bar{\partial}_j$; that is, taking the dot product of ∇ with a basis vector gives the partial derivative along the corresponding basis direction. Writing the gradient in the primitive basis as $\nabla = c_\nu \mathbf{b}_\nu$, we can determine the unknown components c_ν by requiring

$$\partial_\mu = \mathbf{b}_\mu \cdot \nabla = c_\nu \mathbf{b}_\mu \cdot \mathbf{b}_\nu = c_\nu g_{\mu\nu}.$$

Solving this linear system gives $c_\nu = g^{\mu\nu} \partial_\mu$, and thus

$$\nabla = g^{\mu\nu} \partial_\mu \mathbf{b}_\nu, \tag{A.12}$$

and we label a component of the gradient

$$\nabla_\nu = \mathbf{b}_\nu \cdot \nabla = g^{\mu\nu}\partial_\mu. \tag{A.13}$$

For the 2D hexagonal lattice geometry depicted in Fig. 3.1, the matrix of lattice vectors and its inverse are

$$B = \frac{2\pi}{\sqrt{3}a}\begin{bmatrix} 1 & 1 \\ \sqrt{3} & -\sqrt{3} \end{bmatrix} \qquad B^{-1} = \frac{a}{4\pi}\begin{bmatrix} \sqrt{3} & 1 \\ \sqrt{3} & -1 \end{bmatrix}, \tag{A.14}$$

while the metric tensor and its inverse are

$$g = \frac{8\pi^2}{3a^2}\begin{bmatrix} 2 & -1 \\ -1 & 2 \end{bmatrix}, \qquad g^{-1} = \frac{a^2}{8\pi^2}\begin{bmatrix} 2 & 1 \\ 1 & 2 \end{bmatrix}. \tag{A.15}$$

Appendix B
Matrix elements connections in gapped graphene

In this appendix we provide further details and background of the Berry connections, TDM, and generalized derivatives discussed in Chapter 4. In Sec. B.1 we analyze the non-smooth behaviour of the Berry connections in the TB gauge near the K points. Sec. B.2 provides expressions for the generalized derivatives of the TDM components, and B.3 discusses the analytic gauge smoothing function used to remove the singular behaviour from the valence band.

B.1 Behaviour of Berry connections and TDM at K-points

To study the behaviour of the intraband Berry connections at the K point $\mathbf{K} = (1/3)(\mathbf{b}_1 - \mathbf{b}_2)$, we Taylor expand the structure function (3.13) according to

$$f(\mathbf{K}+\mathbf{q}) \simeq \pi\left(i-\sqrt{3}\right) q_1 + \pi\left(i+\sqrt{3}\right) q_2. \tag{B.1}$$

Defining $q_1 = q\cos\varphi_q$ and $q_2 = q\sin\varphi_q$, the magnitude is

$$\begin{aligned} |f(\mathbf{K}+\mathbf{q})| &= 2\pi\sqrt{q_1^2+q_2^2-q_1q_2} \\ &= 2\pi q\sqrt{1-\cos\varphi_q\sin\varphi_q}, \end{aligned} \tag{B.2}$$

which goes to zero linearly at the K points. Focusing on the first component of the Berry connection in the TB gauge, we have

$$\mathcal{A}^{\mathrm{TB}}_{n,1}(\mathbf{K}+\mathbf{q}) = \frac{a^2}{8\pi}\left[1-\frac{s_n\Delta}{\varepsilon(\mathbf{K}+\mathbf{q})}\right]\frac{A_1(\mathbf{K}+\mathbf{q})}{|f(\mathbf{K}+\mathbf{q})|^2}, \tag{B.3}$$

where we have defined $A_1(\mathbf{k}) = \cos 2\pi k_2 - \cos 2\pi k_-$. The bandgap is

$$\varepsilon(\mathbf{K}+\mathbf{q}) \simeq \Delta + \frac{2\gamma^2}{\Delta}|f(\mathbf{K}+\mathbf{q})|^2 \tag{B.4}$$

and so for the conduction band, we have

$$\begin{aligned}\mathcal{A}^{\mathrm{TB}}_{c,1}(\mathbf{K}+\mathbf{q}) &\simeq \frac{a^2}{8\pi}\left[\frac{2\gamma^2|f(\mathbf{K}+\mathbf{q})|^2}{\Delta^2}\right]\frac{A_1(\mathbf{K}+\mathbf{q})}{|f(\mathbf{K}+\mathbf{q})|^2} \\ &= \frac{a^2\gamma^2}{4\pi\Delta^2}A_1(\mathbf{K}+\mathbf{q}),\end{aligned} \tag{B.5}$$

which is clearly finite, since the term in square brackets cancels the $1/|f|^2$. In contrast, the valence band Berry connection is

$$\mathcal{A}^{\mathrm{TB}}_{v,1}(\mathbf{K}+\mathbf{q}) \simeq \frac{a^2}{4\pi}\frac{A_1(\mathbf{K}+\mathbf{q})}{|f(\mathbf{K}+\mathbf{q})|^2}, \tag{B.6}$$

and there is no cancellation of the divergent $1/|f|^2$ term. To gain more insight about the nature of the divergence, we expand

$$\begin{aligned}A_1(\mathbf{K}+\mathbf{q}) &= \sqrt{3}\pi(q_1-2q_2)+\mathcal{O}(q^2) \\ &\simeq \sqrt{3}\pi q(\cos\varphi_q - 2\sin\varphi_q),\end{aligned} \tag{B.7}$$

which shows that $\mathcal{A}_{v,1}$ diverges as $1/q$. The leading order approximation near the K point is thus

$$\mathcal{A}^{\mathrm{TB}}_{v,1}(\mathbf{K}+\mathbf{q}) = \frac{\sqrt{3}a^2}{(4\pi)^2}\frac{q_1-2q_2}{q_1^2+q_2^2-q_1q_2}, \tag{B.8}$$

while a similar analysis for the second vector component results in

$$\mathcal{A}^{\mathrm{TB}}_{v,2}(\mathbf{K}+\mathbf{q}) = \frac{\sqrt{3}a^2}{(4\pi)^2}\frac{\sqrt{3}a^2}{(4\pi)^2}\frac{2q_1-q_2}{q_1^2+q_2^2-q_1q_2}. \tag{B.9}$$

Next we consider the behaviour of the TDM near the K point. Specifically, the phase of the TDM component $d_{cv,1}(\mathbf{k})$ is given by

$$\arg\left[d^{\mathrm{TB}}_{cv,1}(\mathbf{k})\right] = \arctan\left[\frac{-\Delta\left(\sin 2\pi k_- + \sin 2\pi k_2 + 2\sin 2\pi k_1\right)}{\varepsilon(\mathbf{k})\left(\cos 2\pi k_- - \cos 2\pi k_2\right)}\right], \tag{B.10}$$

which is approximated by

$$\arg\left[d^{\mathrm{TB}}_{cv,1}(\mathbf{K}+\mathbf{q})\right] \simeq \arctan\left[\frac{\sqrt{3}q_1}{2q_2-q_2}\right], \tag{B.11}$$

near the K point. There is clearly a phase singularity about the K point, which also means the

real and imaginary parts of the TDM are discontinuous. To calculate the gradient of the TDM phase, we first note that

$$\nabla_{\mathbf{k}} = \frac{a^2}{8\pi^2}\left[(2\partial_1 + \partial_2)\mathbf{b}_1 + (\partial_1 + 2\partial_2)\mathbf{b}_2\right],$$

which results from the metric (3.13) for gapped graphene. To leading order, the gradient of the dipole phase near the K points is found to be

$$\nabla_{\mathbf{k}} \arg\left[d^{\mathrm{TB}}_{cv,1}(\mathbf{k})\right]\big|_{\mathbf{k}=\mathbf{K}+\mathbf{q}} = \frac{\sqrt{3}a^2}{(4\pi)^2}\left[\frac{2q_2 - q_1}{q_1^2 + q_2^2 - q_1 q_2}\mathbf{b}_1 + \frac{q_2 - 2q_1}{q_1^2 + q_2^2 - q_1 q_2}\mathbf{b}_2\right]. \tag{B.12}$$

Comparing with Eqs. (B.8) and (B.8), we see that to leading order

$$\mathcal{A}_{v,j}(\mathbf{K}+\mathbf{q}) = -\nabla_j \arg\left[d^{\mathrm{TB}}_{cv,1}(\mathbf{k})\right]\big|_{\mathbf{k}=\mathbf{K}+\mathbf{q}}, \tag{B.13}$$

which means the divergence of the valence band Berry connections arises from a phase singularity at the K points. Further, this phase singularity is clearly just the negative of the TDM phase, and Eq. (3.9) shows that the gradient of the TDM exactly cancels the singular Berry connection near the K point. This suggests the possibility of using $\arg\left[d^{\mathrm{TB}}_{cv,1}(\mathbf{k})\right]$ as a gauge function to remove the singular behaviour from the valence band. We note that similar behaviour is observed for $d^{\mathrm{TB}}_{cv,2}$, but we do not demonstrate this explicitly.

B.2 Generalized derivatives

In order to calculate the generalized derivative of the Rabi frequency, we need expressions for partial derivatives of the dipole components. For the first component of the dipole, we have

$$\begin{aligned}
\mathrm{Re}\left[\partial_1 d^{\mathrm{TB}}_{cv,1}\right] =& -\frac{a^2|\gamma|}{2\varepsilon|f|}\sin 2\pi k_- \\
&+\frac{a^2|\gamma|\left(4|\gamma|^2|f|^2+\varepsilon^2\right)}{2\varepsilon^3|f|^3}\left(\cos 2\pi k_- - \cos 2\pi k_2\right) \\
&\times\left(\sin 2\pi k_1 + \sin 2\pi k_-\right) \qquad \text{(B.14)}\\
\mathrm{Im}\left[\partial_1 d^{\mathrm{TB}}_{cv,1}\right] =& -\frac{a^2|\gamma|\Delta}{2\varepsilon^2|f|}\left(\cos 2\pi k_- + 2\cos 2\pi k_1\right) \\
&-\frac{a^2|\gamma|\Delta\left(8|\gamma|^2|f|^2+\varepsilon^2\right)}{2\varepsilon^4|f|^3}\left(\sin 2\pi k_- + \sin 2\pi k_2 + 2\sin 2\pi k_1\right) \\
&\times\left(\sin 2\pi k_1 + \sin 2\pi k_-\right), \qquad \text{(B.15)}
\end{aligned}$$

and

$$\begin{aligned}
\mathrm{Re}\left[\partial_2 d^{\mathrm{TB}}_{cv,1}\right] =& \frac{a^2|\gamma|}{2\varepsilon|f|}\left(\sin 2\pi k_- + \sin 2\pi k_2\right) + \\
&\frac{a^2|\gamma|\left(4|\gamma|^2|f|^2+\varepsilon^2\right)}{2E_g^3|f|^3}\left(\cos 2\pi k_- - \cos 2\pi k_2\right)\left(\sin 2\pi k_2 - \sin 2\pi k_-\right) \qquad \text{(B.16)}\\
\mathrm{Im}\left[\partial_2 d^{\mathrm{TB}}_{cv,1}\right] =& \frac{a^2|\gamma|\Delta}{2\varepsilon^2|f|}\left(\cos 2\pi k_- - \cos 2\pi k_2\right) \\
&-\frac{a^2|\gamma|\Delta\left(8|\gamma|^2|f|^2+\varepsilon^2\right)}{2\varepsilon^4|f|^3}\left(\sin 2\pi k_- + \sin 2\pi k_2 + 2\sin 2\pi k_1\right) \\
&\times\left(\sin 2\pi k_2 - \sin 2\pi k_-\right). \qquad \text{(B.17)}
\end{aligned}$$

To obtain $\partial_2 d^{\mathrm{TB}}_{cv,2}$, one simply substitutes $k_1 \leftrightarrow k_2$ in the RHS of the expression for $\partial_1 d^{\mathrm{TB}}_{cv,1}$, while applying the same substitution to $\partial_2 d^{\mathrm{TB}}_{cv,1}$ gives the correct expression for $\partial_1 d^{\mathrm{TB}}_{cv,2}$. Having expressions for all the partial derivatives, the components of the generalized derivatives are then obtained using $\mathcal{D}_i d^{\mathrm{TB}}_{cv,j} = \left(g^{i\mu}\partial_\mu - i\mathcal{A}^{\mathrm{TB}}_{cv,i}\right) d^{\mathrm{TB}}_{cv,j}$, where the inverse metric tensor is given by Eq. (A.15).

Although the $1/|f|^3$ terms in the above expressions are divergent at the K points, the components of the generalized derivatives have finite magnitudes throughout the BZ. The dipole components $d^{\mathrm{TB}}_{cv,j}$ are discontinuous at K, and the gradient exactly cancels the divergence of $\boldsymbol{\mathcal{A}}_{cv}$ at the K points. Similarly to the analysis from the previous section, this cancellation can be demonstrated using a straightforward but tedious Taylor expansion about the K points.

B.3 Gauge smoothing

Here we develop the gauge function to remove non-smooth behaviour from the Berry connections and TDMs. For a general gauge transformation

$$|u_{m,\mathbf{k}}\rangle \to e^{-i\chi_m(\mathbf{k})}|u_{m,\mathbf{k}}\rangle, \tag{B.18}$$

the Berry connections transform as

$$\boldsymbol{\mathcal{A}}_m(\mathbf{k}) \to \boldsymbol{\mathcal{A}}_m(\mathbf{k}) + \nabla_{\mathbf{k}}\boldsymbol{\mathcal{A}}_m(\mathbf{k}), \tag{B.19}$$

while the TDM transforms as

$$\mathbf{d}_{nm}(\mathbf{k}) \to e^{i\chi_{nm}(\mathbf{k})}\mathbf{d}_{nm}(\mathbf{k}), \tag{B.20}$$

where $\chi_{nm} = \chi_n - \chi_m$. Motivated by Eq. (B.13), we transform the valence band using the gauge function

$$\chi_v(\mathbf{k}) = \arg\left[d^{\mathrm{TB}}_{cv,1}(\mathbf{k})\right] + \pi\left[\Theta(k_1) + k_1 - 1/2\right], \tag{B.21}$$

where the step function removes a discontinuity in $\arg\left[d^{\mathrm{TB}}_{cv,1}\right]$, the linear term restores periodicity broken by the step function, while the constant term fixes the global phase so that $\mathbf{d}_{cv}(-\mathbf{k}) = \mathbf{d}^*_{cv}(\mathbf{k})$. Note that the choice of linear phase term to restore periodicity is not unique; one could add an additional linear term whese slope is a multiple of 2π. This is an example of a radical gauge transformation [41] since it is not strictly periodic, but a phase difference of 2π between edges of the BZ does not break periodicity of the Berry connections or TDM. A linear phase function corresponds to a constant shift of the intraband Berry connection, which also shifts the Wannier centres. Here, the linear phase term is chosen to shift the Wannier centers to the home unit cell closest to the origin, which results in optimally smooth dipole moments.

Although the TDM and generalized derivatives transform covariantly, we require expressions for the gradient of the gauge function χ_v in order to transform the valence band Berry connections. Noting that

$$\arg\left[d^{TB}_{cv,1}\right] = \arctan\left[\frac{-(\Delta/E_g)\left(\sin 2\pi k_- + \sin 2\pi k_2 + 2\sin 2\pi k_1\right)}{\cos 2\pi k_- - \cos 2\pi k_2}\right], \tag{B.22}$$

we define

$$\begin{aligned}\alpha(\mathbf{k}) &= \cos 2\pi k_- - \cos 2\pi k_2 \\ \beta(\mathbf{k}) &= -(\Delta/E_g)\left(\sin 2\pi k_- + \sin 2\pi k_2 + 2\sin 2\pi k_1\right),\end{aligned} \tag{B.23}$$

as well as $\zeta^2 = \alpha^2 + \beta^2$, so that

$$\begin{aligned}\partial_\mu \chi_v &= \partial_\mu \arctan(\beta/\alpha) - \delta_{\mu,1}\left[\pi - \delta(k_1)\right] \\ &= \zeta^{-2}\left(\alpha\partial_\mu\beta - \beta\partial_\mu\alpha\right) - \pi\delta_{\mu,1},\end{aligned} \tag{B.24}$$

with

$$\begin{aligned}\zeta^2 = &\left(\cos 2\pi k_- - \cos 2\pi k_2\right)^2 \\ &+ \left(\frac{\Delta}{E_g}\right)^2 \left(\sin 2\pi k_- + \sin 2\pi k_2 + 2\sin 2\pi k_1\right)^2.\end{aligned} \tag{B.25}$$

We have ignored the derivative of the step function in χ_v, as it is found that

$$\lim_{k_1\to 0^+} \partial_1 \arg\left[d^{TB}_{cv,1}(\mathbf{k})\right] = \lim_{k_1\to 0^-} \partial_1 \arg\left[d^{TB}_{cv,1}(\mathbf{k})\right]. \tag{B.26}$$

The derivatives of the gauge function are thus

$$\begin{aligned}\partial_1\chi_v = &-\pi - \frac{2\pi\Delta}{E_g\zeta^2}\left(1 - \cos 2\pi k_1 - \cos 2\pi k_- + 2\cos 2\pi k_2 - \cos 2\pi k_+\right) \\ &- \frac{8\pi\gamma^2\Delta}{E_g^3\zeta^2}\left(\sin 2\pi k_- + \sin 2\pi k_2 + 2\sin 2\pi k_1\right)\left(\sin 2\pi k_1 + \sin 2\pi k_-\right) \\ &\times\left(\cos 2\pi k_- - \cos 2\pi k_2\right),\end{aligned} \tag{B.27}$$

and

$$\begin{aligned}\partial_2\chi_v = &\frac{2\pi\Delta}{E_g\zeta^2}\left[2 - 2\cos 2\pi k_1 + \cos 2\pi k_- + \cos 2\pi k_2 - \cos 2\pi k_+ - \cos 2\pi(2k_1 - k_2)\right] \\ &+ \frac{8\pi\gamma^2\Delta}{E_g^3\zeta^2}\left(\sin 2\pi k_- + \sin 2\pi k_2 + 2\sin 2\pi k_1\right)\left(\sin 2\pi k_2 - \sin 2\pi k_-\right) \\ &\times\left(\cos 2\pi k_- - \cos 2\pi k_2\right).\end{aligned} \tag{B.28}$$

Using these results, the components of the transformed valence band Berry connections are then

calculated as

$$\mathcal{A}_{v,\mu} \to \mathcal{A}_{v,\mu} + g^{\mu,1}\partial_1\chi_v + g^{\mu,2}\partial_2\chi_v. \tag{B.29}$$

Appendix C
Wannier quasi-classical approach to high harmonic generation

This appendix includes the publication [18] entititled "Wannier quasi-classical approach to high harmonic generation in semiconductors". This extends the work of Ref. [16], which developed a quasi-classical approximation for HHG in solids based on a saddle point approximation in the Bloch basis. In Wannier quasi-classical (WQC) analysis, the TDM is transformed to the Wannier basis, which allows the full TDM to be included in the saddle point equations. The HHG spectrum calculated using the WQC approximation agrees quantitatively with numerical simulations of the SBEs; a result that had been elusive for quasi-classical analysis using only the Bloch basis. The WQC calculation involves a 2D sum over lattice sites, and the convergence depends strongly on the spread of the Wannier functions. As a result, WQC is only feasible in the MLWF gauge. In Ref. [18] WQC was demonstrated for a 1D model, and implementing WQC higher dimensional systems is a potential application of the MLWF gauge fixing procedure described in Sec. 3.4.

optica

Wannier quasi-classical approach to high harmonic generation in semiconductors

A. M. Parks,[1,2] G. Ernotte,[1,3] A. Thorpe,[1] C. R. McDonald,[1] P. B. Corkum,[1] M. Taucer,[1] and T. Brabec[1]

[1]Department of Physics, University of Ottawa, Ottawa, Ontario K1N 6N5, Canada

Received 14 July 2020; revised 27 October 2020; accepted 9 November 2020 (Doc. ID 402393); published 14 December 2020

An intuitive and complete understanding of the underlying processes in high harmonic generation (HHG) in solids will enable the development and optimization of experimental techniques for attosecond measurement of dynamical and structural properties of solids. Here we introduce the Wannier quasi-classical (WQC) theory, which allows the characterization of HHG in terms of classical trajectories. The WQC approach completes the single-body picture for HHG in semiconductors, as it is in quantitative agreement with quantum calculations. The importance of WQC theory extends beyond HHG; it enables modeling of dynamic processes in solids with classical trajectories, such as for coherent control and transport processes, potentially providing better scalability and a more intuitive understanding.

https://doi.org/10.1364/OPTICA.402393

1. INTRODUCTION

High harmonic generation (HHG) in solids was first examined theoretically [1–5] and has since been demonstrated in a wide range of materials [6–19]. This has laid the foundation for the rapid advancement of attosecond science in condensed matter [20–28], for which HHG is a fundamental process. HHG in solids has also caught attention as a source for ultrashort XUV radiation [10,28] and as a tool to measure ultrafast dynamics and structural properties, such as band structure [12] and the Berry curvature [16,17]. HHG in solids is driven by interband and intraband currents [29,30]. While the interband current is more dominant in wideband materials such as semiconductors [12], HHG in narrow-band dielectrics is driven more by the intraband current [10]. This work focuses on interband HHG in wideband materials.

Although some experimental features can be reasonably well reproduced by numerical models [31–39], a thorough understanding of all the components shaping harmonic spectra is still missing. This inhibits progress in optimizing HHG as a radiation source and in further developing HHG as a diagnostic tool.

The principal mechanism of interband HHG has been clarified by generalizing the saddle-point approach for atomic HHG [40,41] to integrate the interband current derived in the Bloch basis [30,42–45]. Electron and hole are born at the same lattice site in real space by tunnel ionization and quiver in the laser field. When they recollide at some lattice site, a harmonic photon is emitted. Its energy is equal to the bandgap at the crystal momentum of the electron–hole pair at recollision. Despite its merits, the Bloch quasi-classical model falls short of accounting for the lattice structure; quantum mechanics allows recombination of electrons and holes at different lattice sites, as was clearly demonstrated in recent work [15,43,46].

Here we develop a generalized quasi-classical approach that accounts for the lattice structure; this is achieved by transforming the interband current from Bloch to Wannier basis followed by saddle-point integration. The basis change has a substantial effect. The resulting Wannier quasi-classical (WQC) model is found to be in quantitative agreement with quantum calculations. So far, quasi-classical k-space analysis has been used to qualitatively investigate strong field effects in gases and in the condensed matter phase; quantitative agreement has not yet been demonstrated. Whether quantitative agreement can be obtained in the Bloch basis remains to be seen; however, the richer physics revealed by the WQC picture indicates that this might not be the case. The more refined WQC picture arises from the fact that the transition dipole moment enters the classical action in the exponent, and therewith, the saddle-point equations. Previously, the Wannier basis has been used in the numerical analysis of HHG [46,47]; a maximally localized Wannier basis [48] also has the advantage of providing a smooth k-space gauge for calculating the transition dipole matrix elements [47]. This is of particular importance for treating noncentrosymmetric materials that exhibit complex transition dipoles [36,44,49].

In this work, WQC and quantum calculations are compared for a 1D delta function two-band model solid in the single particle approximation (noninteracting electron–hole pair); parameters are chosen such that the dipole moment and bandgap are representative for semiconductors. The quantitative agreement with quantum calculations suggests that the WQC approach completes the single-body picture for HHG in semiconductors.

2334-2536/20/121764-09 Journal © 2020 Optical Society of America

An electron and hole can ionize and recombine at different lattice sites with a probability determined by the tunneling exponent and Wannier dipole moments; birth and recombination sites are connected by classical trajectories; quantum effects are included by a quadratic expansion of the classical action about the classical trajectories. Beyond that, WQC analysis allows unprecedented insight into the real-space aspects of tunnel ionization in solids; it gives access to the tunnel ionized wave function in real space and therewith, to the birth location of the electron–hole pair. While Bloch quasi-classical analysis describes an electron–hole pair by a single trajectory, WQC analysis describes it by a swarm of weighted trajectories. The increased accuracy comes at the cost of higher computational load.

With a complete understanding of the single electron picture of HHG in two-band semiconductors, it is possible to begin looking at more complex dynamics. On a fundamental level, the WQC approach presents a novel platform from which alternative pathways can be developed for modeling noise and few electron–hole dynamics in solids; classical stochastic equations are easier to handle than quantum systems coupled to stochastic heat baths; as propagation from initial to final Wannier wave packet is done by classical trajectories, the space in between does not need to be resolved, in contrast to a full quantum approach. Thus, WQC analysis holds the promise to provide better scalability and a more intuitive understanding of quantum dynamics in semiconductors. Finally, multiband dynamics can be introduced into WQC analysis by adapting the approach developed in Ref. [18], which also showed that higher conduction bands mostly dominate higher plateaus, and to a lesser extent influence the first plateau of the harmonic spectrum.

One of the ultimate goals of HHG spectroscopy of solids is to extract structural and dynamic data from harmonic spectra. This will be very difficult without simple models. WQC analysis establishes the capacity to capture quantum dynamics in terms of classical trajectories in a reasonably quantitative fashion; this makes it suitable as a diagnostic tool for HHG spectra obtained from experiments and numerical quantum analysis.

More generally, our analysis opens an avenue for modeling quantum dynamics of wave packets by propagating classical trajectories. This is potentially relevant for a wide spectrum of applications, ranging from strong-field physics to transport phenomena [50,51] and coherent control [52,53].

2. THEORY

A. Two-Band WQC Model

Our formalism is developed for a 3D, two-band model. We first summarize the derivation of HHG in the Bloch basis [30]; it starts from the time-dependent Hamiltonian $H(t) = H_0 + \mathbf{x}\cdot\mathbf{F}(t)$; $\mathbf{F}(t)$ represents the laser field; H_0 is the unperturbed lattice Hamiltonian with Bloch eigenstates $\Phi_{m,\mathbf{k}}(\mathbf{x}) = 1/\sqrt{V}u_{m,\mathbf{k}}(\mathbf{x})\exp(i\mathbf{k}\cdot\mathbf{x})$ and with energies $E_m(\mathbf{k})$ in band m with crystal momentum $\mathbf{k}$; the band index $m = v, c$ refers to the valence and the conduction band, respectively; $u_{m,\mathbf{k}}$ is the periodic part of the Bloch function, $\langle\Phi_{m,\mathbf{k}}|\Phi_{m,\mathbf{k}}\rangle = 1$, and $\langle u_{m,\mathbf{k}}|u_{m,\mathbf{k}}\rangle = \upsilon$. Finally, $V = N\upsilon$ is the volume of the solid, with N and υ the number and volume of primitive unit cells. Hartree atomic units are used, unless otherwise noted.

In the presence of the laser field the wave function becomes time-dependent. In the length gauge it is represented as

$$\Psi(\mathbf{x}, t) = \sum_{m=v,c}\int_{\mathrm{BZ}} a_m(\mathbf{k}, t)\Phi_{m,\mathbf{k}}(\mathbf{x})d^3\mathbf{k}, \tag{1}$$

where $a_m(\mathbf{k}, t)$ are the probability amplitudes and integration is over the first Brillouin zone (BZ). As initial conditions, we choose an empty conduction band, $a_c(\mathbf{k}, t = 0) = 0$, and a filled valence band, $a_v(\mathbf{k}, t = 0) = 1/\sqrt{V_{BZ}}$, where V_{BZ} is the BZ volume. The ansatz (1) is substituted into the time-dependent Schrödinger equation, and the interband polarization and current are found to be [30]

$$\mathbf{p}_{cv}(t) = -i\int_{\mathrm{BZ}} \mathrm{d}\mathbf{k}\mathbf{d}(\mathbf{k})\int_{-\infty}^{t}\mathrm{d}t'\mathbf{F}(t')\cdot\mathbf{d}^*[\mathbf{k}(t', t)]e^{-iS(\mathbf{k},t',t)} + \mathrm{c.c.}, \tag{2a}$$

$$\tilde{\boldsymbol{j}}_{cv}(\omega) = i\omega\int_{-\infty}^{\infty}\mathrm{d}t e^{-i\omega t}\mathbf{p}_{cv}(t), \tag{2b}$$

with $S(\mathbf{k}, t', t) = \int_{t'}^{t}\varepsilon(\mathbf{k}(t'', t))\mathrm{d}t'' - i(t - t')/T_2$, T_2 the dephasing time, $\mathbf{k}(t', t) = \mathbf{k} + \mathbf{A}(t) - \mathbf{A}(t')$, with $\mathbf{A}(t)$ the vector potential satisfying $\mathbf{F} = -\partial_t\mathbf{A}$, and $\varepsilon = E_c - E_v$. Here, we have used the relation [54] $\langle\Phi_{m,\mathbf{k}}|\mathbf{x}|\Phi_{m',\mathbf{k}'}\rangle = \delta(\mathbf{k} - \mathbf{k}')[i\delta_{m,m'}\nabla_{\mathbf{k}} + \mathbf{d}_{mm'}(\mathbf{k})]$, with $\mathbf{d}_{mm'}(\mathbf{k}) = i\langle u_{m,\mathbf{k}}|\nabla_{\mathbf{k}}|u_{m,\mathbf{k}}\rangle$ the transition dipole moment. For a two-band system, we denote

$$\mathbf{d}(\mathbf{k}) = \mathbf{d}_{vc}(\mathbf{k}) = i\langle u_{v,\mathbf{k}}|\nabla_{\mathbf{k}}|u_{c,\mathbf{k}}\rangle, \tag{3}$$

and we assume a centrosymmetric system for which the diagonal elements $\mathbf{d}_{mm}(\mathbf{k})$ can be set to zero [44].

In the following, we will translate HHG, as described by the interband current of Eq. (2), from k space to real space by using Wannier functions. The Bloch and Wannier basis functions are connected by a Fourier transform according to [55]

$$u_{m,\mathbf{k}}(\mathbf{x}) = \sum_j w_m(\mathbf{x} - \mathbf{x}_j)e^{-i\mathbf{k}\cdot(\mathbf{x}-\mathbf{x}_j)}, \tag{4a}$$

$$w_m(\mathbf{x} - \mathbf{x}_j) = \frac{1}{\upsilon}\int_{\mathrm{BZ}} u_{m,\mathbf{k}}(\mathbf{x})e^{i\mathbf{k}\cdot(\mathbf{x}-\mathbf{x}_j)}\mathrm{d}\mathbf{k}. \tag{4b}$$

Here, $w_m(\mathbf{x} - \mathbf{x}_j)$ is the Wannier function of band m corresponding to the primitive unit cell at position $\mathbf{x}_j$. By virtue of Eq. (4b), the initial wave function,

$$\Psi(\mathbf{x}, 0) = \int_{\mathrm{BZ}}\mathrm{d}\mathbf{k}\Phi_{v,\mathbf{k}}(\mathbf{x})a_v(\mathbf{k}, t = 0) = w_m(\mathbf{x}), \tag{5}$$

corresponds to the Wannier function at position $\mathbf{x}_j = 0$. HHG can start from any other site $\mathbf{x}_j$. The initial Wannier function can be shifted to $\mathbf{x}_j$ by setting $a_v(\mathbf{k}, t = 0) = \exp(-i\mathbf{k}\cdot\mathbf{x}_j)$. As all lattice sites are identical, it is sufficient to investigate $\mathbf{x}_j = 0$.

In order to translate the interband current [Eq. (2)] into real space, the Bloch functions in the transition dipole moment [Eq. (3)] are replaced by the Wannier functions with the help of relation (4a). This leads to

$$\begin{aligned}\mathbf{d}(\mathbf{k}) &= \sum_{j,k}\int_{\upsilon} w_v^*(\mathbf{x} - \mathbf{x}_k)[\mathbf{x} - \mathbf{x}_j]w_c(\mathbf{x} - \mathbf{x}_j)e^{i\mathbf{k}\cdot(\mathbf{x}_j-\mathbf{x}_k)}\mathrm{d}\mathbf{x}\\ &= \sum_{j,l}\int_{\upsilon} w_v^*(\mathbf{x} - (\mathbf{x}_j + \mathbf{x}_l))[\mathbf{x} - \mathbf{x}_j]w_c(\mathbf{x} - \mathbf{x}_j)e^{-i\mathbf{k}\cdot\mathbf{x}_l}\mathrm{d}\mathbf{x}\\ &= \sum_l e^{-i\mathbf{k}\cdot\mathbf{x}_l}\int_V w_v^*(\mathbf{x} - \mathbf{x}_l)\mathbf{x}w_c(\mathbf{x})\mathrm{d}\mathbf{x} = \sum_l \mathbf{d}_l e^{-i\mathbf{k}\cdot\mathbf{x}_l},\end{aligned} \tag{6}$$

where the second line was obtained by setting $\mathbf{x}_k = \mathbf{x}_j + \mathbf{x}_l$ and by replacing summation index k with l in the first line. Also, note that performing $\sum_j$ in the second line changes the integration volume from a unit cell to the whole crystal volume. The Wannier dipole moments are equivalent to the Fourier series expansion coefficients of the Bloch dipole moment $\mathbf{d}(\mathbf{k})$. Interpreted in real space, the Wannier dipole moment $\mathbf{d}_l$ describes a transition where an electron is born l lattice cells away from the hole. Bloch and Wannier dipole moments are not unique; $\Phi_{m,\mathbf{k}} \to \Phi_{m,\mathbf{k}} \exp[i\alpha(\mathbf{k})]$ is also an eigenfunction for any real function α that is periodic in k space. Although the full equations, including the diagonal dipole elements $\mathbf{d}_{mm}$, are gauge-invariant [44,54], it is computationally advantageous to choose strongly confined Wannier basis functions [56,57] in order to keep the number of relevant lattice sites small. In the 1D examples discussed below we chose maximally localized Wannier basis functions [56] for which $\mathbf{d}_{mm} = 0$.

Inserting Eq. (6) into Eq. (2), the interband current follows as

$$\tilde{\boldsymbol{j}}_{er}(\omega) = \sum_{j,l} \left\{ \mathbf{d}_j [\mathbf{d}_l^* \cdot \mathbf{T}_{jl}(\omega)] - \mathbf{d}_j^* [\mathbf{d}_l \cdot \mathbf{T}_{jl}^*(-\omega)] \right\}$$

$$= \sum_{j,l} \left[\mathbf{P}_{jl}(\omega) - \mathbf{P}_{jl}^*(-\omega) \right], \tag{7a}$$

$$\mathbf{T}_{jl}(\omega) = \omega \int_{\mathrm{BZ}} \mathrm{d}\mathbf{k} \int_{-\infty}^{\infty} \mathrm{d}t \int_{-\infty}^{t} \mathrm{d}t' \mathbf{F}(t') e^{i\varphi(\mathbf{k},t',t,\mathbf{x}_l,\mathbf{x}_j)}. \tag{7b}$$

Here, $\varphi = -S(\mathbf{k}, t', t) - \omega t + \mathbf{k} \cdot (\mathbf{x}_l - \mathbf{x}_j) + [\mathbf{A}(t) - \mathbf{A}(t')] \cdot \mathbf{x}_l$; $\mathbf{P}_{jl}(\omega)$ represents the probability amplitude that the harmonic ω is generated by an electron–hole pair that is born with a relative distance $|\mathbf{x}_l|$ between electron and hole and later recombines with relative distance $|\mathbf{x}_j|$, and the propagator $\mathbf{T}_{jl}$ describes the evolution between $\mathbf{d}_l^*$ and $\mathbf{d}_j$.

B. Saddle-Point Integration

The integrals in Eq. (7b) are solved by saddle-point integration. The saddle-point equations,

$$\varepsilon[\mathbf{k}(t', t)] + \mathbf{F}(t') \cdot \mathbf{x}_l = 0, \tag{8a}$$

$$\varepsilon(\mathbf{k}) - \mathbf{F}(t) \cdot [\boldsymbol{\xi}(t', t) - \mathbf{x}_l] = \varepsilon(\mathbf{k}) + \mathbf{F}(t) \cdot \mathbf{x}_j = \mp\omega, \tag{8b}$$

$$\boldsymbol{\xi}(t', t) = \mathbf{x}_l - \mathbf{x}_j, \tag{8c}$$

result from $\partial\varphi/\partial\mu = 0$ with $\mu = t', t, \mathbf{k}$, respectively. The field quiver motion between times t' and t is given by the distance $\boldsymbol{\xi}(\mathbf{k}, t', t) = \int_{t'}^{t} \mathbf{v}(\mathbf{k}(t''), t))\mathrm{d}t''$, where $\mathbf{v}(\mathbf{k}) = \nabla_{\mathbf{k}}\varepsilon$ is the band velocity. Note that the classical action depends on the difference between conduction and valence band. As a result, the above quantities represent the difference between electron and hole band velocity and excursion distance. Finally, the $\mp$ in Eq. (8b) accounts for the complex conjugate term in Eq. (2b).

The set of Eq. (8) is solved for a linearly polarized laser field $\mathbf{F} = F\hat{\boldsymbol{x}}$; further, $\mathbf{A} = A\hat{\boldsymbol{x}}$ and $k_x = k$. The solutions of the saddle-point equations are denoted by $t' = t_b + i\delta$, $t = t_r$, $\mathbf{k}_s$. For $\delta \ll 1$, Eq. (8a) can be solved analytically; it determines the saddle-point momentum $\mathbf{k}_s = (k_s, k_{ys}, k_{zs}) = (A(t_b) - A(t_r), 0, 0)$, as well as

$$\delta = \sqrt{\frac{2(E_g + F(t_b)x_l)}{\beta_{xx}(0)F^2(t_b)}}, \tag{9}$$

where we have approximated the bandgap as

$$\varepsilon(\mathbf{k}) \approx E_g + \frac{1}{2}\sum_{i,j} k_i k_j \beta_{ij}(0), \tag{10}$$

with $i, j = x, y, z$; $\beta_{ij}(\mathbf{k}) = \partial^2\varepsilon/\partial k_i \partial k_j$ the inverse mass tensor; and E_g the minimum bandgap. The positive sign in Eq. (9) is chosen to obtain an exponentially decaying tunneling rate.

The two remaining saddle-point equations, (8b) and (8c), determine t_b and t_r. They have to be solved numerically for each possible birth site $\mathbf{x}_l$ and recombination site $\mathbf{x}_j$; for instance, by running through t_b and finding all $t_r(t_b)s$ that fulfill Eq. (8c). From those, the pairs $[t_b, t_r](\omega)$ are selected that produce a given harmonic ω via Eq. (8b). The physical implications of the saddle-point equations are discussed at the end of this subsection.

Next, the integrand of Eq. (7b) is evaluated at the saddle point, where the small imaginary birth time determines the tunneling exponent. Further, the phase φ is expanded to second order, which gives the multivariate Gaussian integral,

$$\int_{-\infty}^{\infty} \mathrm{d}\mathbf{q} \exp((i/2)\mathbf{q}^T\mathcal{H}\mathbf{q}) = (2\pi)^{5/2}/\sqrt{-i|\mathcal{H}|}, \tag{11}$$

where $\mathbf{q} = (t', t, \mathbf{k})$, and $\mathcal{H}$ is the Hessian $\mathcal{H}_{ij} = \partial^2\varphi/\partial_i\partial_j$ with $i, j \in \mathbf{q}$. The full expression for the determinant of the Hessian is provided in Appendix A. Putting everything together, we obtain the WQC propagator,

$$\mathbf{T}_{jl} = \sum_{[t_b,t_r](\omega,\mathbf{x}_l,\mathbf{x}_j)} \mathbf{g}(t_b + i\delta, t_r) e^{-t_x} e^{-i\chi(t_b,t_r)+i\pi/4}, \tag{12a}$$

$$t_x = \mathrm{Im}[\varphi(t_b + i\delta)] \approx \frac{\sqrt{2}[E_g + F(t_b)x_l]^{3/2}}{[\beta_{xx}(0)F^2(t_b)]^{1/2}}, \tag{12b}$$

$$\chi = \int_{t_b}^{t_r} \varepsilon(A(t_b) - A(\tau))d\tau + \omega t_r + \mathbf{k}_s \cdot \mathbf{x}_j, \tag{12c}$$

where $\mathbf{g} = \omega\mathbf{F}(t_b + i\delta)(2\pi)^{5/2}/\sqrt{|\mathcal{H}|}$ and to leading order the determinant from the Gaussian integral $|\mathcal{H}| \approx v_x(\mathbf{k}_s) f(t_b + i\delta, t, \mathbf{k}_s)$ [18]; see Appendix A. Further, it is convenient to split the phase in Eq. (12c) into $\chi = \chi_1 + \chi_2$, where $\chi_1 = \int_{t_b}^{t_r} \varepsilon[A(t_b) - A(\tau)]d\tau + \omega t_r$ contains the classical action and the harmonic frequency Fourier term. The second term is the Fourier term of the recombination dipole moment, $\chi_2 = \mathbf{k}_s \cdot \mathbf{x}_j$. The total probability amplitude,

$$\mathbf{P}_{jl} = e^{i\pi/4} \sum_{[t_b,t_r](\omega,\mathbf{x}_l,\mathbf{x}_j)} \left[\mathbf{g}(t_b + i\delta)\mathbf{d}_l^* e^{-t_x} e^{-i\chi_1(t_b,t_r)} \mathbf{d}_j e^{-i\chi_2(t_b,t_r)} \right], \tag{13}$$

is governed by the prefactor $\mathbf{g}$, the ionization amplitude $\mathbf{d}_l^* e^{-t_x}$, the quantum mechanical (QM) phase factor $e^{-i\chi_1}$ acquired along the classical trajectory, and the recombination amplitude $\mathbf{d}_j e^{-i\chi_2}$. For each possible birth site $\mathbf{x}_l$ and recombination site $\mathbf{x}_j$ in the lattice, the summation runs over all birth and recombination times t_r, t_b that satisfy the saddle-point conditions for a particular harmonic frequency ω.

The propagator [Eq. (12)], together with the saddle point [Eq. (8)], and the interband current [Eq. (7a)] represent the WQC description of HHG in semiconductors. They reveal a complete and detailed picture of the physical mechanisms driving HHG in real and reciprocal space, summarized in Figs. 1(a) and 1(b), respectively. The empty circles in Fig. 1(a) represent the centers

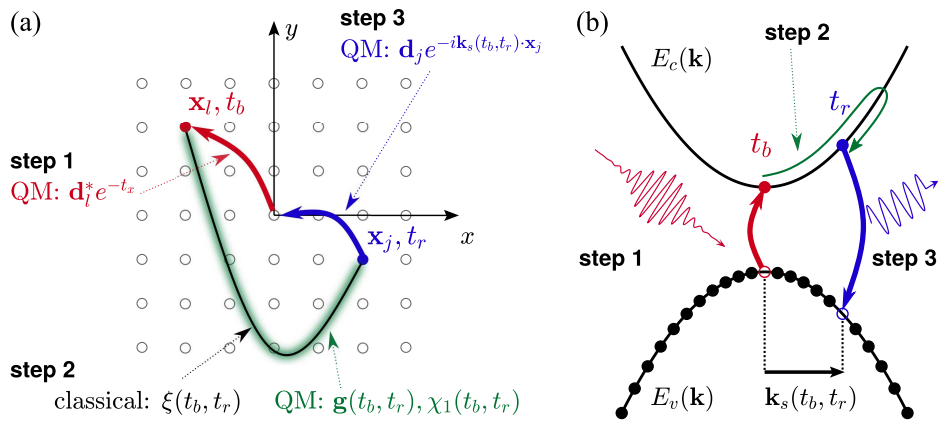

Fig. 1. Schematic of the WQC picture of interband HHG. (a) Real space picture for a model 2D lattice; empty circles denote centers of atomic unit cells at which Wannier basis functions are located. Distances shown refer to relative distance between each electron–hole pair. Classical and QM processes are indicated. The dotted arrows point to the probability amplitudes of the individual processes. In addition, the phase χ_1 picked up along the classical trajectory is indicated. HHG takes place in three steps. (1) An electron initially at the valence Wannier site $\mathbf{x}_0$ is born at $\mathbf{x}_0 + \mathbf{x}_l$, creating an electron–hole pair l lattice sites apart (red arrow), with ionization amplitude $\propto \mathbf{d}_l^* \exp[-t_x]$. (2) Then it propagates in the laser field along the classical trajectory $\boldsymbol{\xi}(t_b, t_r)$; the green shaded area indicates the quasi-classical contribution $\mathbf{g}(t_b, t_r)$ that comes from the Gaussian expansion of the propagator about the classical trajectory $\boldsymbol{\xi}$. (3) Electron and hole revisit each other and recombine j lattice sites apart with $\mathbf{d}_j$ the recombination dipole (blue arrow). (b) $\mathbf{k}$-space picture, full and empty circles in valence band indicate filled states and empty states (holes), respectively; (1) electron–hole pairs are born at the Γ point ($\mathbf{k} = 0$); (2) the laser field drives them in reciprocal space (green arrow); (3) they recombine at some different $\mathbf{k}_s$.

of the atomic unit cells $\mathbf{x}_l$, where $l = (l_x, l_y)$ in the 2D schematic. A Wannier basis function is located at each center. Initially, all Wannier sites of the valence band are filled. As all lattice sites are identical, it is sufficient to investigate $\mathbf{x}_l = 0$; see Eq. (5) above. Following the notation of our calculation, we chose indices l, j to represent birth and recombination sites, respectively. HHG proceeds in three steps:

Step 1–creation of electron–hole pair by ionization. At birth time t_b, a valence band electron localized at lattice site $\mathbf{x}_0$ transitions to the conduction band and is localized at lattice site $\mathbf{x}_0 + \mathbf{x}_l$. The tunneling probability is determined by the tunneling exponent t_x and by the Wannier dipole moment $\mathbf{d}_l^*$; see Fig. 1(a). The potential energy experienced by the created electron–hole dipole in the laser field makes the effective ionization potential $E_g + F(t_b)x_l$ birth-site-dependent; see Eqs. (8a) and (12b). In reciprocal space, the electron transitions from valence to conduction band at the Γ-point at time t_b; see Fig. 1(b). Step 1 is of a QM nature.

Step 2–electron–hole evolution in laser field. The electron–hole pair quivers in the laser field. In real space it follows the classical trajectory $\boldsymbol{\xi}(t_b, t_r)$ in Fig. 1(a) until electron and hole revisit each other and are separated by $|\mathbf{x}_j|$ at time t_r; see Eq. (8c). The propagation step is dominantly classical; of QM nature are the phase $\chi_1(t_b, t_r)$ picked up between birth and recombination time, and the quasi-classical factor $\mathbf{g}$ coming from the quadratic expansion of the classical action S about the classical trajectory. The shaded green area about the classical trajectory in Fig. 1(a) indicates the quantum correction up to the second order. In reciprocal space in Fig. 1(b), the electron–hole pair evolves from initial crystal momentum zero to saddle-point crystal momentum $\mathbf{k}_s(t_b, t_r)$, defined in Eq. (8) above.

Step 3–recombination. At time t_r, electron and hole recombine with probability amplitude $\mathbf{d}_j e^{-i\mathbf{k}_s(t_b,t_r)\cdot\mathbf{x}_j}$; see Fig. 1(a). The harmonic energy is given by the bandgap energy at $\mathbf{k}_s(t_b, t_r)$ [see Fig. 1(b)], plus the energy of the electron–hole dipole in the field $F(t_r)$; see Eq. (8b). Due to the second term, harmonics with energies somewhat larger than the maximum bandgap can be generated.

3. RESULTS

For the remainder of the paper, the WQC approach and its physical significance are explored within a 1D model system. In this case the interband current, WQC propagator, and probability amplitude reduce to scalars, namely, $\tilde{j}_{er}$, T_{jl}, and P_{jl}. Specifically, we use a 1D delta function model potential, $V(x) = \Omega \sum_{n=-\infty}^{\infty} \delta[x - (n + 1/2)a]$ with unit cell size a and barrier penetration parameter Ω. This model solid represents inversion symmetric semiconductors, for which the intraband dipole moment (Berry connection) is zero in a maximally localized Wannier basis. Details of the delta function model are given in Appendix B. For the investigated parameters, the bandgap is well approximated by the nearest neighbor dispersion $\varepsilon(k) = E_g + \Delta[1 - \cos(ka)]$, where E_g is the minimum bandgap and 2Δ represents the bandwidth. We chose $a = 7$ and considered two values $\Omega = 0.5$, 1.5 to model a weakly and tightly bound semiconductor, respectively. The corresponding bandgap parameters are $E_g = 0.141$, 0.269 and $\Delta = 0.269$, 0.17. Finally, for all runs we use a dephasing time $T_2 = T_0/2$ so that only returns within a single cycle are relevant.

In Fig. 2 the exact (QM) harmonic spectrum, as obtained from numerical integration of Eq. (2), is compared with the Wannier quasi-classical solution: Eqs. (7a), (8), (9), and (12a). For the exact approach, we use $F(t) = F_0 \sin(\omega_0 t) \exp(-(t/\tau)^2)$, where F_0 is the maximum field strength, and the pulse duration, $\tau = 40\,T_0$, is long enough to approach the continuous wave (cw) limit; ω_0 is the laser center frequency, and $T_0 = 2\pi/\omega_0$ denotes the optical

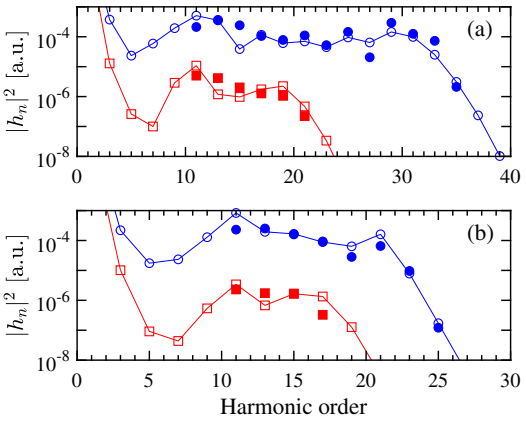

Fig. 2. Harmonic yield $|h_n|^2$ versus harmonic order n; $a = 7$, $T_2 = T_0/2$. (a)–(b) Empty blue circles with lines (exact) and filled blue circles (WQC) refer to $\Omega = 0.5$, $\omega_0 = 0.01425$ ($\lambda = 3.2$ μm), and $F_0 = 0.0025$ in (a) and $F_0 = 0.0015$ in (b); empty red squares connected by lines (exact) and filled red squares (WQC) refer to $\Omega = 1.5$, $\omega_0 = 0.0285$ ($\lambda = 1.6$ μm), and $F_0 = 0.008$ in (a) and $F_0 = 0.005$ in (b); lines are used to guide the eye.

cycle. For the highest field strength considered, an electron born at the Γ point explores only ∼60% of the BZ and does not reach the next bandgap at the edge of the BZ to transition to the second conduction band; this justifies the approximation to include only two bands. We plot the harmonic intensity $|h_n|^2 = \int_{\omega_-}^{\omega_+} d\omega |\tilde{j}_{er}(\omega)|^2$ integrated over the frequency interval $\omega_\pm = (n \pm 1/2)\omega_0$.

For the WQC calculation, we assume the cw limit, $F(t) = F_0 \sin(\omega_0 t)$, in order to facilitate interpretation of the results. Equation (12a) has been derived for finite pulses employing the Fourier transform. For a transition to the cw limit, the Fourier transform has to be replaced by a Fourier series; as a result, $\omega \to n\omega_0$, prefactor $g \to g/(2\pi T_0)$, where the $1/(2\pi)$ comes from the 1D nature of our model. The harmonic yield becomes $|h_n|^2 = |\tilde{j}_{er}(n\omega_0)|^2$ with T_{jl} given by the WQC propagator [Eq. (12a)].

In Fig. 2, the blue empty circles (exact) and blue filled circles (WQC) refer to results for the weakly bound model semiconductor, with $\Omega = 0.5$, and $\omega_0 = 0.01425$. Red empty squares (exact) and red filled squares (WQC) refer to the tightly bound semiconductor, with $\Omega = 1.5$, and $\omega_0 = 0.0285$. Plots with the same symbols in Figs. 2(a) and 2(b) correspond to the same values of Ω and ω_0, but differ in F_0.

The WQC results are only plotted above the minimum bandgap, as the quasi-classical analysis is limited to processes for which an electron is actually born in the conduction band. Below the minimum bandgap, virtual processes dominate; in this range, the intraband current can have a substantial contribution that is not shown here.

The WQC approach agrees well with the exact solution, with most data points being off by less than a factor of 2. Even the first 1–2 cutoff harmonics are described fairly well, which demonstrates that they are of quasi-classical origin. The good agreement allows us to interpret semiconductor quantum dynamics such as ionization, electron/hole transport, and HHG in terms of classical trajectories. The quantum contributions to HHG are captured

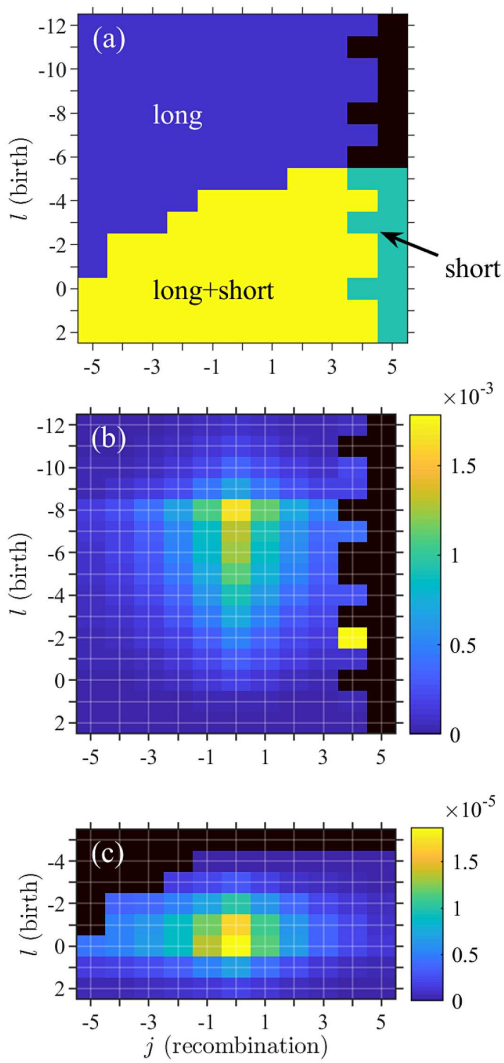

Fig. 3. Contribution of the long and short classical trajectories to the probability amplitude $|P_{jl}|$ for harmonic order $n = 15$ in a wide-band semiconductor; parameters $a = 7$, $\Omega = 0.5$, $\omega = 0.01425$, and $F_0 = 0.0025$ corresponding to filled blue circles in Fig. 2(a). (a) depicts the combinations of birth (l) and recombination (j) site indices for which each trajectory exists and contributes to P_{jl}; black regions indicate no solution. (b) shows the contribution of the long trajectory to $|P_{jl}|$, while (c) shows the contribution from the short trajectory. Note that the values of the color scale differ by 2 orders of magnitude in (b) and (c).

by the tunneling exponent t_x, by the pre-exponential factor g in Eq. (12a), and by the Wannier dipole moments in Eq. (7).

A few points disagree by a larger factor of up to 6. In particular, Fig. 2(a) shows that the WQC result for harmonic $n = 15$ exhibits larger discrepancy for the weakly bound semiconductor ($\Omega = 0.5$) compared to the more tightly bound semiconductor ($\Omega = 1.5$). The reason for this behavior is identified in Fig. 3 and will be discussed later.

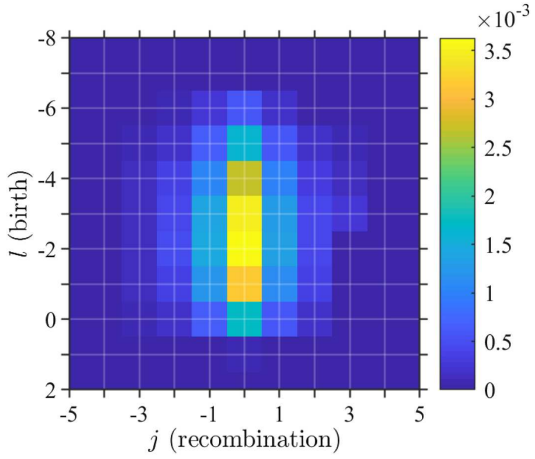

Fig. 4. Probability amplitude $|P_{jl}|$ versus birth (l) and recombination (j) site indices for harmonic order $n = 15$ in a narrowband semiconductor; parameters $a = 7$, $\Omega = 1.5$, $\omega = 0.0285$, and $F_0 = 0.008$ corresponding to filled red circles in Fig. 2(a). Here we plot the total probability amplitude $|P_{jl}|$, but note that the long trajectory is dominant; the individual contributions are similar to the behavior depicted for the wideband semiconductor in Fig. 3(b).

Numerical solution of the full saddle-point equations reveals two distinct classical trajectories that contribute to the probability amplitude P_{jl}: one long trajectory and one short. Moreover, each solution exists for only certain combinations of birth (l) and recombination (j) lattice sites. Figure 3 shows the contributions arising from the different classical trajectories for the 15th harmonic ($n = 15$) with $\Omega = 0.5$, $F_0 = 0.0025$, corresponding to the filled blue circles in Fig. 2(a). Figure 3(a) depicts the regions in the $j - l$ plane, where each trajectory contributes to $|P_{jl}(n = 15)|$. No solution exists for the dark region in the top-right, and the probability amplitude here is zero. Figures 3(b) and 3(c) show the individual contributions to the probability amplitude from the long and short trajectories, respectively. The long trajectory is dominant, as the electron–hole pair is born close to the field peak, whereas the short trajectory is born closer to the nodal point. This outweighs the effect of the short dephasing time, which favors the short trajectory. As a result, the contribution of each data point to the WQC propagator is dominantly determined by a factor $\sim g e^{-t_x}$ of a single (long) trajectory. The full probability amplitude $|P_{jl}(n = 15)|$ is essentially identical to that of Fig. 3(b).

In Fig. 4, the total probability amplitude for the 15th harmonic $|P_{jl}(n = 15)|$ is plotted as a function of birth and recombination site indices l, j for $\Omega = 1.5$, and $F_0 = 0.008$, which corresponds to the filled red squares in Fig. 2(a). For this system, the long trajectory is also dominant, and analysis of the individual contributions would reveal a picture qualitatively similar to Fig. 3.

In both Figs. 3 and 4, harmonic $n = 15$ has been selected, as the WQC result for the weakly bound semiconductor exhibits a more pronounced difference, while it agrees well for the tightly bound semiconductor. For both systems, the maximum probability is shifted towards negative birth-site indices; it is more likely for electron and hole to be born apart than at the same site. Tunnel ionization probability is determined by e^{-t_x} and by birth dipole moment d_l^*. The tunnel exponent t_x depends on the ionization potential $E_g + F(t_b)x_l$; see Eq. (12a). Thus, for the positive field, the electron–hole pair gains energy when born at increasingly negative distances, which reduces t_x. When $-x_l = E_g/F(t_b)$, t_x vanishes; in other words, the valence and conduction band levels separated by $-l$ sites align, and the electron hops from the valence to the conduction band site. The penalty to be paid is a rapidly dropping dipole moment d_l. As such, the birth-site index at which ionization is maximum is determined by a trade-off between tunnel exponent and Wannier dipole moment. The dipole elements for the parameters of Fig. 3(a) drop more slowly with increasing $|l|$ than for (b); see Appendix B. Therefore, the site of highest ionization probability is shifted more strongly towards negative l. Recombination is most probable for $j = 0$ in Figs. 3(a) and 3(b), which is consistent with previous findings [46]. The drop in probability for increasing j is due to d_j, which is why $|P_{jl}|$ extends to larger j in Fig. 3(b).

The results in Figs. 3 and 4 are displayed for birth times in the positive field cycle $0 \le t_b \le T_0/2$; the negative half-cycle would show the same picture, but mirrored about the $x-$ and $y-$ axis $(j, l \to -j, -l)$.

Recall that exact and quasi-classical results do not agree well for harmonic $n = 15$ in Fig. 2(a) ($\Omega = 0.5$). The reason is found in Fig. 3(b); disagreement is due to the point $(j, l) = (4, -2)$, which exhibits unusually high probability. We find that at this point k_s is approximately zero, and therewith $|\mathcal{H}| \approx 0$. Since $g \propto 1/\sqrt{|\mathcal{H}|}$, this leads to a large value of the prefactor g. This behavior indicates that the quadratic saddle-point expansion is no longer sufficient, and the next higher order term(s) must be included. The rules of saddle-point integration require expanding the exponent up to the first nonvanishing term. In contrast, agreement for harmonic $n = 15$ in Fig. 2(a) for $\Omega = 1.5$ is good. This is consistent with the fact that in Fig. 4, $k_s \approx 0$ does not occur in areas of high probability.

Finally, the WQC method hinges on saddle-point integration, which works well when the exponent is rapidly oscillating. This is fulfilled for wideband semiconductors with large bandwidth (Δ) and in the long wavelength limit. When transitioning to smaller Δ (dielectrics) and shorter wavelengths, saddle-point integration is expected to fail at some point. This will be subject to further research. Also, it is generally possible for transitions involving higher conduction bands to contribute to the harmonic spectrum, but this is beyond the scope of the two-band model considered here.

4. CONCLUSION

In summary, we have shown that the full single-body quantum dynamics driving HHG in wideband materials, such as semiconductors, can be quantitatively explained in terms of quasi-classical trajectory propagation. The physical insight offered by trajectory analysis will prove useful for optimization and the design of strong field and attosecond experiments and for the development of novel diagnostic applications of HHG, such as reconstruction of the dipole moment [58]. We believe that our approach presents a versatile tool for investigating open issues in strong-field solid-state physics, such as the role of noise and many-body effects in strong-field processes. Beyond that, quantitatively accurate quasi-classical analysis should be of interest for a wider range of topics in material science.

While our work is limited here to centrosymmetric materials and two-band model solids, we believe that the WQC method can contribute to understanding HHG in more complex materials. Multiband dynamics can be incorporated following the approach

outlined in Ref. [18]. Noncentrosymmetric materials exhibit an interband transition dipole phase as well as an intraband Berry phase, which lead to additional terms in the classical action. The anomalous velocity arising from the Berry phase will offset the electron–hole trajectory in the plane perpendicular to the laser polarization axis. The Bloch quasi-classical model requires the electron–hole pair to recombine at the same lattice site, thus missing important trajectories where it could recombine from nearby lattice sites.

APPENDIX A: HESSIAN

Here we provide expressions for the determinant of the Hessian $\mathcal{H}_{ij} = \partial^2\varphi/\partial_i\partial_j$ appearing in Eq. (12). Evaluation of the second derivatives yields

$$|\mathcal{H}| = \begin{vmatrix} \mathbf{F}(t')\cdot\mathbf{v}(\mathbf{k}(t',t)) & -\mathbf{F}(t)\cdot\mathbf{v}(\mathbf{k}(t',t)) & v_x(\mathbf{k}(t',t)) & v_y(\mathbf{k}(t',t)) & v_z(\mathbf{k}(t',t)) \\ +\dot{\boldsymbol{F}}(t')\cdot\mathbf{x}_l & & & & \\ -\mathbf{F}(t)\cdot\mathbf{v}(\mathbf{k}(t',t)) & \mathbf{F}(t)\cdot\mathbf{v}(\mathbf{k}) - \dot{\boldsymbol{F}}(t)\cdot\mathbf{x}_j - & -v_x(\mathbf{k}) + & -v_y(\mathbf{k}) + & -v_z(\mathbf{k}) + \\ & F_i(t)D_{ij}(t',t)F_j(t) & F_i(t)D_{ix}(t',t) & F_i(t)D_{iy}(t',t) & F_i(t)D_{iz}(t',t) \\ v_x(\mathbf{k}(t',t)) & -v_x(\mathbf{k}) + F_i(t)D_{xi}(t',t) & -D_{xx}(t',t) & -D_{xy}(t',t) & -D_{xz}(t',t) \\ v_y(\mathbf{k}(t',t)) & -v_y(\mathbf{k}) + F_i(t)D_{yi}(t',t) & -D_{yx}(t',t) & -D_{yy}(t',t) & -D_{yz}(t',t) \\ v_z(\mathbf{k}(t',t)) & -v_z(\mathbf{k}) + F_i(t)D_{zi}(t',t) & -D_{zx}(t',t) & -D_{zy}(t',t) & -D_{zz}(t',t) \end{vmatrix}, \tag{A1}$$

where the determinant is evaluated at the saddle point defined by $t' = t_b + i\delta$, $t = t_r$, $\mathbf{k} = \mathbf{k}_s$. Using linear dependence between column 2 and columns 3, 4, and 5 (see the supplement of [18]), the determinant can be simplified to

$$|\mathcal{H}| = \begin{vmatrix} \mathbf{F}(t')\cdot\mathbf{v}(\mathbf{k}(t',t)) + \dot{\boldsymbol{F}}(t')\cdot\mathbf{x}_l & 0 & v_x(\mathbf{k}(t',t)) & v_y(\mathbf{k}(t',t)) & v_z(\mathbf{k}(t',t)) \\ -\mathbf{F}(t)\cdot\mathbf{v}(\mathbf{k}(t',t)) & -\dot{\boldsymbol{F}}(t)\cdot\mathbf{x}_j & -v_x(\mathbf{k}) + & -v_y(\mathbf{k}) + & -v_z(\mathbf{k}) + \\ & & F_i(t)D_{ix}(t',t) & F_i(t)D_{iy}(t',t) & F_i(t)D_{iz}(t',t) \\ v_x(\mathbf{k}(t',t)) & -v_x(\mathbf{k}) & -D_{xx}(t',t) & -D_{xy}(t',t) & -D_{xz}(t',t) \\ v_y(\mathbf{k}(t',t)) & -v_y(\mathbf{k}) & -D_{yx}(t',t) & -D_{yy}(t',t) & -D_{yz}(t',t) \\ v_z(\mathbf{k}(t',t)) & -v_z(\mathbf{k}) & -D_{zx}(t',t) & -D_{zy}(t',t) & -D_{zz}(t',t) \end{vmatrix}. \tag{A2}$$

Here, $i, j \in \{x, y, z\}$, summation is implied when indices i or j are repeated, $D_{ij} = \int_{t'}^{t} d\tau\beta_{ij}(\mathbf{k}(t'',t))$, $\beta_{ij} = \partial_{k_i} v_j(\mathbf{k})$, and $\dot{\boldsymbol{F}}(t) = \partial_t\mathbf{F}(t)$. For completeness, $|\mathcal{H}|$ is given for a general field $\mathbf{F}(t)$; for the case treated here, set $F_y = F_z = 0$. To leading order $|\mathcal{H}| = v_x(\mathbf{k})\mathbf{f}(t',t,\mathbf{k}) + \dot{\boldsymbol{F}}(t)\cdot\mathbf{x}_l h(t',t,\mathbf{k})$, where h, $\mathbf{f}$ are minors of $|\mathcal{H}|$. For completeness, we have included time derivatives of the laser field, which are, however, small in the long wavelength limit. As a result, the leading order term is $|\mathcal{H}| = v_x(\mathbf{k})\mathbf{f}(t',t,\mathbf{k})$.

APPENDIX B: DELTA FUNCTION POTENTIAL

The WQC approach and its physical significance are explored by means of a 1D delta-function model potential, $V(x) = \Omega\sum_{n=-\infty}^{\infty}\delta[x-(n+1/2)a]$ with unit cell size a and barrier penetration parameter Ω. For the investigated parameters, the bandgap is well approximated by the nearest neighbor approximation, $\varepsilon = E_g + \Delta[1-\cos(ka)]$, where E_g is the minimum bandgap and 2Δ represents the bandwidth.

The binding energy is determined by $2E_m = K_m^2$, where $m = v, c$ and K_m is determined by

$$\cos(ka) = \cos(K_m a) + \frac{\Omega}{K_m}\sin(K_m a). \tag{B1}$$

The wave function is given by

$$\Phi_{m,k}(x) = \sqrt{\frac{1}{a}}u_{m,k}(x)\exp(ikx)$$

$$u_{m,k}(x) = A_m(k)\left[e^{i(K_m-k)x} + r_m e^{-i(K_m+k)x}\right],$$

$$A_m(k) = 1/\sqrt{1 + r_m^2 + 2r_m\sin(K_m a)/(K_m a)},$$

$$r_m(k) = \frac{\sin[(K_m-k)a/2]}{\sin[(K_m+k)a/2]}. \tag{B2}$$

From the wave function, the Bloch dipole moment is found to be

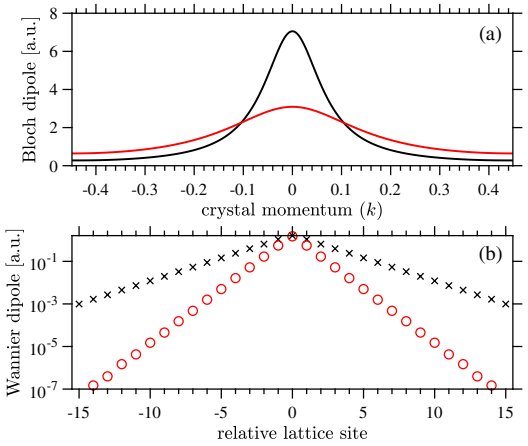

Fig. 5. (a) Bloch dipole transition elements $\mathrm{Im}[d^*(k)]$ versus k; (b) Wannier dipole transition elements d_j versus j, which represents the difference in lattice sites at which electron and hole are born. 1D model parameters, $a = 7$; $\Omega = 0.5$ (black); $\Omega = 1.5$ (red).

$$d_{cv}(k) = d^*(k) = i\frac{2A_cA_v}{E_c - E_v} \times \left\{[(K_v - k)r_c - (K_v + k)r_v]\frac{\sin[(K_v + K_c)a/2]}{(K_v + K_c)a} + [(K_v - k) - (K_v + k)r_vr_c]\frac{\sin[(K_v - K_c)a/2]}{(K_v - K_c)a}\right\}. \tag{B3}$$

We chose $a = 7$ and $\Omega = 0.5$, 1.5 to model a weakly and more tightly bound semiconductor, respectively. The corresponding bandgap parameters are $E_g = 0.141$, 0.269 and $\Delta = 0.269$, 0.17. The Bloch dipole elements $d(k)$ and Wannier dipole elements d_j are plotted in Fig. 5. As expected, d_j drops faster for the more tightly bound model. Finally, we have chosen the coordinate center at the point of inversion symmetry that corresponds with choosing a maximally localized Wannier basis [56]. For this choice, the diagonal (intraband) dipole moments are zero, and the phase of the interband dipole moment is constant.

Funding. Air Force Office of Scientific Research (FA9550-16-1-0109).

Acknowledgment. G. Ernotte was supported by the Vanier Canada Graduate Scholarship program. T. Brabec acknowledges the support of the NSERC DG and CRC programs.

Disclosures. The authors declare no conflicts of interest.

REFERENCES

1. L. Plaja and L. Roso-Franco, "High-order harmonic generation in a crystalline solid," Phys. Rev. B **45**, 8334–8341 (1992).
2. K. A. Pronin, A. D. Bandrauk, and A. A. Ovchinnikov, "Harmonic generation by a one-dimensional conductor: exact results," Phys. Rev. B **50**, 3473–3476 (1994).
3. R.-B. Liu and B.-F. Zhu, "High-order THz-sideband generation in semiconductors," AIP Conf. Proc. **893**, 1455–1456 (2007).
4. D. Golde, T. Meier, and S. W. Koch, "High harmonics generated in semiconductor nanostructures by the coupled dynamics of optical inter- and intraband excitations," Phys. Rev. B **77**, 075330 (2008).
5. J.-Y. Yan, "Theory of excitonic high-order sideband generation in semiconductors under a strong terahertz field," Phys. Rev. B **78**, 075204 (2008).
6. S. Ghimire, A. D. DiChiara, E. Sistrunk, P. Agostini, L. F. DiMauro, and D. A. Reis, "Observation of high-order harmonic generation in a bulk crystal," Nat. Phys. **7**, 138–141 (2011).
7. B. Zaks, R. B. Liu, and M. S. Sherwin, "Experimental observation of electron-hole recollisions," Nature **483**, 580–583 (2012).
8. O. Schubert, M. Hohenleutner, F. Langer, B. Urbanek, C. Lange, U. Huttner, D. Golde, T. Meier, M. Kira, S. W. Koch, and R. Huber, "Sub-cycle control of terahertz high-harmonic generation by dynamical Bloch oscillations," Nat. Photonics **8**, 119–123 (2014).
9. M. Hohenleutner, F. Langer, O. Schubert, M. Knorr, U. Huttner, S. W. Koch, M. Kira, and R. Huber, "Real-time observation of interfering crystal electrons in high-harmonic generation," Nature **523**, 572–575 (2015).
10. T. T. Luu, M. Garg, S. Y. Kruchinin, A. Moulet, M. T. Hassan, and E. Goulielmakis, "Extreme ultraviolet high-harmonic spectroscopy of solids," Nature **521**, 498–502 (2015).
11. M. Garg, M. Zhan, T. T. Luu, H. Lakhotia, T. Klostermann, A. Guggenmos, and E. Goulielmakis, "Multi-petahertz electronic metrology," Nature **538**, 359–363 (2016).
12. G. Vampa, T. J. Hammond, N. Thiré, B. E. Schmidt, F. Légaré, C. R. McDonald, T. Brabec, and P. B. Corkum, "Linking high harmonics from gases and solids," Nature **522**, 462–464 (2015).
13. G. Vampa, T. J. Hammond, N. Thiré, B. E. Schmidt, F. Légaré, C. R. McDonald, T. Brabec, D. D. Klug, and P. B. Corkum, "All-optical reconstruction of crystal band structure," Phys. Rev. Lett. **115**, 193603 (2015).
14. H. Liu, Y. Li, Y. S. You, S. Ghimire, T. F. Heinz, and D. A. Reis, "High-harmonic generation from an atomically thin semiconductor," Nat. Phys. **13**, 262–265 (2016).
15. Y. S. You, D. A. Reis, and S. Ghimire, "Anisotropic high-harmonic generation in bulk crystals," Nat. Phys. **13**, 345–349 (2017).
16. H. B. Banks, Q. Wu, D. C. Valovcin, S. Mack, A. C. Gossard, L. Pfeiffer, R.-B. Liu, and M. S. Sherwin, "Dynamical birefringence: electron-hole recollisions as probes of Berry curvature," Phys. Rev. X **7**, 041042 (2017).
17. T. T. Luu and H. J. Wörner, "Measurement of the Berry curvature of solids using high-harmonic spectroscopy," Nat. Commun. **9**, 916 (2018).
18. A. J. Uzan, G. Orenstein, Á. Jiménez-Galán, C. McDonald, R. E. F. Silva, B. D. Bruner, N. D. Klimkin, V. Blanchet, T. Arusi-Parpar, M. Krüger, A. N. Rubtsov, O. Smirnova, M. Ivanov, B. Yan, T. Brabec, and N. Dudovich, "Attosecond spectral singularities in solid-state high-harmonic generation," Nat. Photonics **14**, 183–187 (2020).
19. G. Nbadashimiye, S. Ghimire, M. Wu, D. A. Browne, K. J. Schafer, M. B. Gaarde, and D. A. Reis, "Solid-state harmonics beyond the atomic limit," Nature **534**, 520–523 (2016).
20. M. Schultze, K. Ramasesha, C. Pemmaraju, S. Sato, D. Whitmore, A. Gandman, J. S. Prell, L. J. Borja, D. Prendergast, K. Yabana, D. M. Neumark, and S. R. Leone, "Attosecond band-gap dynamics in silicon," Science **346**, 1348–1352 (2014).
21. M. Schultze, E. M. Bothschafter, A. Sommer, S. Holzner, W. Schweinberger, M. Fiess, M. Hofstetter, R. Kienberger, V. Apalkov, V. S. Yakovlev, M. I. Stockman, and F. Krausz, "Controlling dielectrics with the electric field of light," Nature **493**, 75–78 (2013).
22. S. Neppl, R. Ernstorfer, E. M. Bothschafter, A. L. Cavalieri, D. Menzel, J. V. Barth, F. Krausz, R. Kienberger, and P. Feulner, "Attosecond time-resolved photoemission from core and valence states of magnesium," Phys. Rev. Lett. **109**, 087401 (2012).
23. S. Ghimire, G. Ndabashimiye, A. D. DiChiara, E. Sistrunk, M. I. Stockman, P. Agostini, L. F. DiMauro, and D. A. Reis, "Strong-field and attosecond physics in solids," J. Phys. B **47**, 204030 (2014).
24. A. L. Cavalieri, N. Müller, T. Uphues, V. S. Yakovlev, A. Baltuška, B. Horvath, B. Schmidt, L. Blümel, R. Holzwarth, S. Hendel, M. Drescher, U. Kleineberg, P. M. Echenique, R. Kienberger, F. Krausz, and U. Heinzmann, "Attosecond spectroscopy in condensed matter," Nature **449**, 1029–1032 (2007).
25. S. Neppl, R. Ernstorfer, A. L. Cavalieri, C. Lemell, G. Wachter, E. Magerl, E. M. Bothschafter, M. Jobst, M. Hofstetter, U. Kleineberg, J. V. Barth, D. Menzel, J. Burgdörfer, P. Feulner, F. Krausz, and R. Kienberger, "Direct observation of electron propagation and dielectric screening on the atomic length scale," Nature **517**, 342–346 (2015).
26. S. Y. Kruchinin, F. Krausz, and V. S. Yakovlev, "Colloquium: strong-field phenomena in periodic systems," Rev. Mod. Phys. **90**, 021002 (2018).
27. S. Ghimire and D. A. Reis, "High-harmonic generation from solids," Nat. Phys. **15**, 10–16 (2019).
28. J. Li, J. Lu, A. Chew, S. Han, J. Li, Y. Wu, H. Wang, S. Ghimire, and Z. Chang, "Attosecond science based on high harmonic generation from gases and solids," Nat. Commun. **11**, 2748 (2020).
29. M. Kira and S. W. Koch, *Semiconductor Quantum Optics* (Cambridge University, 2011).
30. G. Vampa, C. R. McDonald, G. Orlando, D. D. Klug, P. B. Corkum, and T. Brabec, "Theoretical analysis of high-harmonic generation in solids," Phys. Rev. Lett. **113**, 073901 (2014).
31. P. G. Hawkins and M. Y. Ivanov, "Role of subcycle transition dynamics in high-order-harmonic generation in periodic structures," Phys. Rev. A **87**, 063842 (2013).
32. P. G. Hawkins, M. Y. Ivanov, and V. S. Yakovlev, "Effect of multiple conduction bands on high-harmonic emission from dielectrics," Phys. Rev. A **91**, 013405 (2015).
33. T. T. Luu and H. J. Wörner, "High-order harmonic generation in solids: a unifying approach," Phys. Rev. B **94**, 115164 (2016).
34. N. Tancogne-Dejean, O. D. Mücke, F. X. Kärtner, and A. Rubio, "Ellipticity dependence of high-harmonic generation in solids originating from coupled intraband and interband dynamics," Nat. Commun. **8**, 745 (2017).
35. M. Wu, Y. You, S. Ghimire, D. A. Reis, D. A. Browne, K. J. Schafer, and M. B. Gaarde, "Orientation dependence of temporal and spectral

properties of high-order harmonics in solids," Phys. Rev. A **96**, 063412 (2017).
36. S. Jiang, J. Chen, H. Wei, C. Yu, R. Lu, and C. D. Lin, "Role of the transition dipole amplitude and phase on the generation of odd and even high-order harmonics in crystals," Phys. Rev. Lett. **120**, 253201 (2018).
37. M. S. Mrudul, A. Pattanayak, M. Ivanov, and G. Dixit, "Direct numerical observation of real-space recollision in high-order harmonic generation from solids," Phys. Rev. A **100**, 043420 (2019).
38. L. Li, P. Lan, X. Zhu, T. Huang, Q. Zhang, M. Lein, and P. Lu, "Reciprocal-space-trajectory perspective on high-harmonic generation in solids," Phys. Rev. Lett. **122**, 193901 (2019).
39. C. Yu, S. Jiang, and R. Lu, "High order harmonic generation in solids: a review on recent numerical methods," Adv. Phys. X **4**, 1562982 (2019).
40. M. Lewenstein, P. Balcou, M. Y. Ivanov, A. L'Huillier, and P. B. Corkum, "Theory of high-harmonic generation by low-frequency laser fields," Phys. Rev. A **49**, 2117–2132 (1994).
41. L. Keldysh, "Ionization in the field of a strong electromagnetic wave," Sov. Phys. JETP **20**, 1307–1314 (1965).
42. G. Vampa, C. R. McDonald, G. Orlando, P. B. Corkum, and T. Brabec, "Semiclassical analysis of high harmonic generation in bulk crystals," Phys. Rev. B **91**, 064302 (2015).
43. L. Yue and M. B. Gaarde, "Imperfect recollisions in high-harmonic generation in solids," Phys. Rev. Lett. **124**, 153204 (2020).
44. J. Li, X. Zhang, S. Fu, Y. Feng, B. Hu, and H. Du, "Phase invariance of the semiconductor Bloch equations," Phys. Rev. A **100**, 043404 (2019).
45. A. Chacón, D. Kim, W. Zhu, S. P. Kelly, A. Dauphin, E. Pisanty, A. S. Maxwell, A. Picón, M. F. Ciappina, D. E. Kim, C. Ticknor, A. Saxena, and M. Lewenstein, "Circular dichroism in higher-order harmonic generation: heralding topological phases and transitions in Chern insulators," Phys. Rev. B **102**, 134115 (2020).
46. E. N. Osika, A. Chacón, L. Ortmann, N. Suárez, J. A. Pérez-Hernández, B. Szafran, M. F. Ciappina, F. Sols, A. S. Landsman, and M. Lewenstein, "Wannier-Bloch approach to localization in high-harmonics generation in solids," Phys. Rev. X **7**, 021017 (2017).
47. R. E. F. Silva, F. Martín, and M. Ivanov, "High harmonic generation in crystals using maximally localized Wannier functions," Phys. Rev. B **100**, 195201 (2019).
48. N. Marzari, A. A. Mostofi, J. R. Yates, I. Souza, and D. Vanderbilt, "Maximally localized Wannier functions: theory and applications," Rev. Mod. Phys. **84**, 1419–1475 (2012).
49. S. Jiang, H. Wei, J. Chen, C. Yu, R. Lu, and C. D. Lin, "Effect of transition dipole phase on high-order-harmonic generation in solid materials," Phys. Rev. A **96**, 053850 (2017).
50. S. Datta, *Electronic Transport in Mesoscopic Systems* (Cambridge University, 1997).
51. M. Ludwig, G. Aguirregabiria, F. Ritzkowsky, T. Rybka, D. C. Marinica, J. Aizpurua, A. G. Borisov, A. Leitenstorfer, and D. Brida, "Sub-femtosecond electron transport in a nanoscale gap," Nat. Phys. **16**, 341–345 (2019).
52. M. J. Stevens, R. D. R. Bhat, X. Y. Pan, H. M. van Driel, J. E. Sipe, and A. L. Smirl, "Enhanced coherent control of carrier and spin density in a zinc-blende semiconductor by cascaded second-harmonic generation," J. Appl. Phys. **97**, 093709 (2005).
53. R. A. Muniz and J. E. Sipe, "Coherent control of optical injection of spin and currents in topological insulators," Phys. Rev. B **89**, 205113 (2014).
54. E. I. Blount, "Formalisms of band theory," in *Solid State Physics* (Elsevier, 1962), Vol. **13**, pp. 305–373.
55. H. Haug and S. W. Koch, *Quantum Theory of the Optical and Electronic Properties of Semiconductors*, 5th ed. (World Scientific, 2009).
56. W. Kohn, "Analytic properties of Bloch waves and Wannier functions," Phys. Rev. **115**, 809–821 (1959).
57. A. A. Mostofi, J. R. Yates, G. Pizzi, Y. Lee, I. Souza, D. Vanderbilt, and N. Marzari, "An updated version of wannier90: a tool for obtaining maximally-localised Wannier functions," Comput. Phys. Commun. **185**, 2309–2310 (2014).
58. Y. Zhao, S.-Y. Ma, S.-C. Jiang, Y.-J. Yang, X. Zhao, and J.-G. Chen, "All-optical reconstruction of k-dependent transition dipole moment by solid harmonic spectra from ultrashort laser pulses," Opt. Express **27**, 34392–34404 (2019).

Appendix D
Circular products of dipole moments

Here we prove an interesting result concerning products of dipole moments. If we denote $\mathbf{d}(\mathbf{k})$ the matrix of dipole moments, i.e.

$$\mathbf{d}(\mathbf{k}) = \sum_{n,m} |u_{n,\mathbf{k}}\rangle\langle u_{m,\mathbf{k}}|\mathbf{d}_{nm}(\mathbf{k}) \tag{D.1}$$

with matrix elements

$$\langle u_{n,\mathbf{k}}|\mathbf{d}(\mathbf{k})|u_{m,\mathbf{k}}\rangle = \mathbf{d}_{nm}(\mathbf{k}) = (1-\delta_{nm})\langle u_{n,\mathbf{k}}|i\nabla_{\mathbf{k}}|u_{m,\mathbf{k}}\rangle, \tag{D.2}$$

then product of dipole matrix elements appearing in

$$[\mathbf{d}(\mathbf{k})^m]_{nn} \tag{D.3}$$

is gauge invariant for any $m \in \mathbb{Z}^+$. Label an arbitrary set of Bloch states $|u_{\alpha_j,\mathbf{k}}\rangle$, so that the diagonal elements of the matrix product are

$$\begin{aligned}(\mathbf{d}^m)_{nn} &= \sum_{\{\alpha\}} \mathbf{d}_{n\alpha_1}\mathbf{d}_{\alpha_1\alpha_2}...\mathbf{d}_{\alpha_{m-1}n} \\ &= \sum_{\{\alpha_m\}} \mathbf{d}_{n\alpha_1} \prod_{j=1}^{m-2} \mathbf{d}_{\alpha_j\alpha_{j+1}}\mathbf{d}_{\alpha_{m-1}n}\end{aligned} \tag{D.4}$$

where $\sum_{\{\alpha_m\}}$ indicates that we sum over the set of all indices $\alpha_1, \alpha_2, ...\alpha_{m-1}$. We want to show that the product of dipole matrix elements

$$\mathbf{T}_{n,\{\alpha_m\}} = \mathbf{d}_{n\alpha_1} \prod_{j=1}^{m-2} \mathbf{d}_{\alpha_j\alpha_{j+1}}\mathbf{d}_{\alpha_{m-1}n} \tag{D.5}$$

is gauge invariant.

Now consider gauge transformations of Bloch states

$$|u_{n,\mathbf{k}}\rangle \to |\tilde{u}_{n,\mathbf{k}}\rangle = e^{-i\chi_n}|u_{n,\mathbf{k}}\rangle \tag{D.6}$$

so that

$$\tilde{\mathbf{d}}_{nm} = e^{i\chi_{nm}}\mathbf{d}_{nm}, \tag{D.7}$$

where $\chi_{nm} = \chi_n - \chi_m$. Now, the product transforms as

$$\begin{aligned}
\tilde{\mathbf{T}}_{n,\{\alpha_m\}} &= \tilde{\mathbf{d}}_{n\alpha_1}\prod_{j=1}^{m-2}\tilde{\mathbf{d}}_{\alpha_j\alpha_{j+1}}\tilde{\mathbf{d}}_{\alpha_{m-1}n} \\
&= \mathbf{T}_{n,\{\alpha_m\}}\prod_{j=1}^{m-2} e^{i\chi_{n\alpha_1}}e^{i\chi_{\alpha_j\alpha_{j+1}}}e^{i\chi_{\alpha_{m-1}n}} \\
&= \mathbf{T}_{n,\{\alpha_m\}}e^{i\theta\{\chi_m\}},
\end{aligned} \tag{D.8}$$

and the total phase factor evaluates to

$$\begin{aligned}
\theta\{\chi_m\} &= \chi_{n\alpha_1} + \chi_{\alpha_{m-1}n} + \sum_{j=1}^{m-2}\chi_{\alpha_j\alpha_{j+1}} \\
&= (\chi_n - \chi_{\alpha_1}) + \big(\chi_{\alpha_{m-1}} - \chi_n\big) + \sum_{j=1}^{m-2}\big(\chi_{\alpha_j} - \chi_{\alpha_j+1}\big) \\
&= -\chi_{\alpha_1} + \chi_{\alpha_{m-1}} + \sum_{j=1}^{m-2}\big(\chi_{\alpha_j} - \chi_{\alpha_j+1}\big) \\
&= 0,
\end{aligned} \tag{D.9}$$

where only the first and last terms of the sum give non-vanishing contributions, but these cancel the other two terms outside the sum. We thus obtain the desired result

$$\tilde{\mathbf{T}}_{n,\{\alpha_m\}} = \mathbf{T}_{n,\{\alpha_m\}}, \tag{D.10}$$

which also implies

$$\left(\tilde{\mathbf{d}}^m\right)_{nn} = \left(\mathbf{d}^m\right)_{nn}. \tag{D.11}$$

It is important to note that all vector components of the dipole transform the same way; i.e.

$$\mathbf{e}_\mu \cdot \mathbf{d}_{nm}(\mathbf{k}) = d_{nm,\mu}(\mathbf{k}) \to e^{i\chi_{nm}(\mathbf{k})}d_{nm,\mu}(\mathbf{k}) \tag{D.12}$$

regardless of the component $\mathbf{e}_\mu$. As a corollary of the general result above, we mention that the triple product

$$d_{lm,i}d_{mn,j}d_{nl,k}$$

is also gauge invariant, regardless of the vector components i, j, k. Another special case is

$$d_{nm,i}d_{mn,j} = d_{nm,i}d^*_{nm,j},$$

which shows that the phase difference between two vector components of the dipole moment is also a gauge invariant quantity.

Appendix E
Symmetry properties of the shift vector

The shift vector corresponding to vector component $\mathbf{e}_j$ of the dipole moment is given by

$$\mathbf{R}^{(j)}_{nm}(\mathbf{k}) = \boldsymbol{\mathcal{A}}_{nm}(\mathbf{k}) - \nabla_{\mathbf{k}}\phi_{nm,j}(\mathbf{k}), \tag{E.1}$$

where $\phi_{nm,j}(\mathbf{k}) = \arg\left[\mathbf{e}_j \cdot \mathbf{d}_{nm}(\mathbf{k})\right]$. It should be emphasized that a shift vector is defined with respect to a single vector component of the dipole moment; i.e. the phases of the different dipole components lead to distinct shift vectors. In this work we consider the dipole phase parallel to the input polarization, for which we define the parallel shift vector

$$\mathbf{R}_{nm}(\mathbf{k}) = \boldsymbol{\mathcal{A}}_{nm}(\mathbf{k}) - \nabla_{\mathbf{k}}\phi_{nm}(\mathbf{k}), \tag{E.2}$$

with the phase given by

$$\phi_{nm}(\mathbf{k}) = \arg\left[\mathbf{n} \cdot \mathbf{d}_{nm}(\mathbf{k})\right], \tag{E.3}$$

for input polarization vector $\mathbf{n}$. We can also define the scalar field

$$R_{nm}(\mathbf{k}) = \mathbf{n} \cdot \mathbf{R}_{nm}(\mathbf{k}), \tag{E.4}$$

which is just the component of the shift vector parallel to the input polarization.

Using the gauge transformation relations (2.73) and (2.74) for the TDM and Berry connec-

tions, we calculate

$$\begin{aligned}
\tilde{\mathbf{R}}_{nm}(\mathbf{k}) =& \tilde{\boldsymbol{\mathcal{A}}}_{nm}(\mathbf{k}) - \nabla_{\mathbf{k}}\tilde{\phi}_{nm}(\mathbf{k}) \\
=& \tilde{\boldsymbol{\mathcal{A}}}_{nm}(\mathbf{k}) - \nabla_{\mathbf{k}} \arg\left[\mathbf{n}\cdot\tilde{\mathbf{d}}_{nm}(\mathbf{k})\right] \\
=& \tilde{\boldsymbol{\mathcal{A}}}_{nm}(\mathbf{k}) + \nabla_{\mathbf{k}}\left[\chi_n(\mathbf{k}) - \chi_m(\mathbf{k})\right] \\
& - \nabla_{\mathbf{k}} \arg\left[\mathbf{n}\cdot\mathbf{d}_{nm}(\mathbf{k})e^{i\chi_{nm}(\mathbf{k})}\right] \\
=& \tilde{\boldsymbol{\mathcal{A}}}_{nm}(\mathbf{k}) + \nabla_{\mathbf{k}}\chi_{nm}(\mathbf{k}) \\
& - \nabla_{\mathbf{k}}\left\{\arg\left[\mathbf{n}\cdot\mathbf{d}_{nm}(\mathbf{k})\right] - \chi_{nm}(\mathbf{k})\right\} \\
=& \mathbf{R}_{nm}(\mathbf{k}),
\end{aligned} \tag{E.5}$$

which confirms that the shift vector is indeed gauge invariant. Note that this result is true for any shift vector $\mathbf{R}^{(j)}_{nm}$, since all components of the dipole moment transform by the same phase under gauge transformations.

We can also examine the spatial inversion properties of the shift vector. For a time-reversal invariant system satisfying $E_m(-\mathbf{k}) = E_m(\mathbf{k})$, the $\mathbf{k}\cdot\mathbf{p}$ Eigenvalue equation for the cell-periodic functions can be used to show that $u_{m,-\mathbf{k}}(\mathbf{x})$ and $u^*_{m,\mathbf{k}}(\mathbf{x})$ are Bloch functions with the same energy eigenvalue. This leads to the inversion relation

$$u_{m,-\mathbf{k}}(\mathbf{x}) = e^{i\sigma_m(\mathbf{k})}u^*_{m,\mathbf{k}}(\mathbf{x}), \tag{E.6}$$

where $\sigma_m(\mathbf{k})$ is a gauge-dependent phase factor. From the perspective of linear algebra, the phase σ_m accounts for the fact that rotating the phase of an eigenvector of a Hermitian matrix does not affect its eigenvalue. As a consequence, the dipole matrix elements satisfy

$$\begin{aligned}
\boldsymbol{\xi}_{nm}(-\mathbf{k}) =& \langle u_{n,-\mathbf{k}}|i\nabla_{-\mathbf{k}}|u_{m,-\mathbf{k}}\rangle \\
=& -i\langle u_{n,-\mathbf{k}}|\nabla_{\mathbf{k}}|u_{m,-\mathbf{k}}\rangle \\
=& -i\int d\mathbf{x}u^*_{n,-\mathbf{k}}(\mathbf{x})\nabla_{\mathbf{k}}u_{m,-\mathbf{k}}(\mathbf{x}) \\
=& -ie^{-i\sigma_n(\mathbf{k})}\int d\mathbf{x}u_{n,\mathbf{k}}(\mathbf{x})\nabla_{\mathbf{k}}e^{i\sigma_m(\mathbf{k})}u^*_{m,\mathbf{k}}(\mathbf{x}) \\
=& -ie^{-i\sigma_{nm}(\mathbf{k})}\int d\mathbf{x}u_{n,\mathbf{k}}(\mathbf{x})\nabla_{\mathbf{k}}u^*_{m,\mathbf{k}}(\mathbf{x}) \\
& + e^{-i\sigma_{nm}(\mathbf{k})}\langle u_{m,\mathbf{k}}|u_{n,\mathbf{k}}\rangle\nabla_{\mathbf{k}}\sigma_m(\mathbf{k}) \\
=& e^{-i\sigma_{nm}(\mathbf{k})}\boldsymbol{\xi}^*_{nm}(\mathbf{k}) + \delta_{nm}\nabla_{\mathbf{k}}\sigma_m(\mathbf{k}),
\end{aligned}$$

where $\sigma_{nm} = \sigma_n - \sigma_m$. This inversion relation might seem intuitive in a particular gauge where $\sigma_n = \sigma_m = 0$; this would imply Berry connections with even parity, and $\mathbf{d}_{nm}(-\mathbf{k}) = \mathbf{d}^*_{nm}(\mathbf{k})$. However, assuming a particular gauge lacks generality, and it is preferable to work with gauge invariant quantities which have unambiguous symmetry properties. For the shift vector, we calculate

$$\begin{aligned}
\mathbf{R}_{nm}(-\mathbf{k}) =& \boldsymbol{\mathcal{A}}_{nm}(-\mathbf{k}) - \nabla_{-\mathbf{k}} \arg\left[\mathbf{n}\cdot\mathbf{d}_{nm}(-\mathbf{k})\right] \\
=& \boldsymbol{\mathcal{A}}_{nm}(-\mathbf{k}) + \nabla_{\mathbf{k}}\left[\sigma_n(\mathbf{k}) - \sigma_m(\mathbf{k})\right] \\
&+ \nabla_{\mathbf{k}} \arg\left[\mathbf{n}\cdot\mathbf{d}_{nm}(\mathbf{k}) e^{-i\sigma_{nm}(\mathbf{k})}\right] \\
=& \boldsymbol{\mathcal{A}}_{nm}(-\mathbf{k}) + \nabla_{\mathbf{k}}\sigma_{nm}(\mathbf{k}) \\
&+ \nabla_{\mathbf{k}}\left\{\arg\left[\mathbf{n}\cdot\mathbf{d}_{nm}(\mathbf{k})\right] - \sigma_{nm}(\mathbf{k})\right\} \\
=& \mathbf{R}_{nm}(\mathbf{k}),
\end{aligned} \tag{E.7}$$

where we observe that the gauge-dependent phases cancel. We thus conclude that the gauge invariant shift vector has even k-space inversion symmetry, which is equivalent to the even inversion symmetry of the band energies.

It is also interesting to consider the special case of an inversion symmetric crystal, for which the lattice potential obeys $V(-\mathbf{x}) = V(\mathbf{x})$. In this case, the $k\cdot p$ Eigenvalue equation leads to the relation

$$u_{m,-\mathbf{k}}(\mathbf{x}) = e^{i\bar{\sigma}_m(\mathbf{k})} u_{m,\mathbf{k}}(-\mathbf{x}). \tag{E.8}$$

Note that σ_m and $\bar{\sigma}_m$ result from different inversion symmetries and are generally distinct. We emphasize that the inversion relation (E.6) is general for any TR invariant crystal, while an inversion symmetric system satisfies the additional relation (E.8). For the dipole matrix elements, we have

$$\begin{aligned}
\boldsymbol{\xi}_{nm}(-\mathbf{k}) &= i\int d\mathbf{x} u^*_{n,-\mathbf{k}}(\mathbf{x}) \nabla_{-\mathbf{k}} u_{m,-\mathbf{k}}(\mathbf{x}) \\
&= -ie^{-i\bar{\sigma}_n(\mathbf{k})} \int d\mathbf{x} u^*_{n,\mathbf{k}}(-\mathbf{x}) \nabla_{\mathbf{k}} e^{i\bar{\sigma}_m(\mathbf{k})} u_{m,\mathbf{k}}(-\mathbf{x}) \\
&= -ie^{-i\bar{\sigma}_n(\mathbf{k})} \int d\mathbf{x} u^*_{n,\mathbf{k}}(\mathbf{x}) \nabla_{\mathbf{k}} e^{i\bar{\sigma}_m(\mathbf{k})} u_{m,\mathbf{k}}(\mathbf{x})
\end{aligned} \tag{E.9}$$

where we have changed the integration variable $\mathbf{x} \to -\mathbf{x}$, and we note that the sign change from

$-d\mathbf{x}$ is canceled by the exchange of integration limits over the unit cell. We thus have

$$\begin{aligned}\boldsymbol{\xi}_{nm}(-\mathbf{k}) =& - ie^{-i\bar{\sigma}_{nm}(\mathbf{k})}\int d\mathbf{x} u^*_{n,\mathbf{k}}(\mathbf{x})\nabla_{\mathbf{k}} u_{m,\mathbf{k}}(\mathbf{x}) \\ &+ e^{-i\bar{\sigma}_{nm}(\mathbf{k})}\langle u_{m,\mathbf{k}}|u_{n,\mathbf{k}}\rangle\nabla_{\mathbf{k}}\sigma_m(\mathbf{k}) \\ =& - e^{-i\bar{\sigma}_{nm}(\mathbf{k})}\boldsymbol{\xi}_{nm}(\mathbf{k}) + \delta_{nm}\nabla_{\mathbf{k}}\bar{\sigma}_m(\mathbf{k}),\end{aligned} \tag{E.10}$$

which shows that $\mathbf{d}_{nm}(-\mathbf{k})$ and $\mathbf{d}_{nm}(\mathbf{k})$ differ by a gauge dependent phase. Further, $\boldsymbol{\mathcal{A}}_m(-\mathbf{k}) = -\boldsymbol{\mathcal{A}}_m(\mathbf{k}) + \nabla_{\mathbf{k}}\bar{\sigma}_m(\mathbf{k})$, which means the Berry connection is purely gauge-dependent since it vanishes if $\nabla_{\mathbf{k}}\bar{\sigma}_m = \nabla_{\mathbf{k}}\sigma_m = 0$. In other words, the Berry connection in an inversion-symmetric system has no gauge invariant component, and we can safely conclude that the Berry curvature must vanish as a result. Finally, the shift vector in an inversion symmetric system must satisfy

$$\begin{aligned}\mathbf{R}_{nm}(-\mathbf{k}) =& \boldsymbol{\mathcal{A}}_{nm}(-\mathbf{k}) - \nabla_{-\mathbf{k}}\arg\left[\mathbf{n}\cdot\mathbf{d}_{nm}(-\mathbf{k})\right] \\ =& - \boldsymbol{\mathcal{A}}_{nm}(\mathbf{k}) + \nabla_{\mathbf{k}}\bar{\sigma}_{nm}(\mathbf{k}) \\ &+ \nabla_{\mathbf{k}}\arg\left[\mathbf{n}\cdot\mathbf{d}_{nm}(\mathbf{k})e^{i\pi}e^{-i\bar{\sigma}_{nm}(\mathbf{k})}\right] \\ =& - \mathbf{R}_{nm}(-\mathbf{k}),\end{aligned} \tag{E.11}$$

which implies odd inversion symmetry. Clearly, the shift vector must vanish in an inversion symmetric system, since a non-trivial function cannot possess both even and odd parity. This shows unambiguously that the dipole phase and Berry connections do not contribute to the dynamics in an inversion symmetric system. This conclusion is consistent with previous findings [27, 28, 48], but the present analysis using the shift vector has the advantage of being gauge-independent; i.e. no assumptions regarding gauge-dependent phases are required.

Appendix F
Saddle point equations for the strong field approximation

In this appendix we derive the SFA saddle point equations for the component of the interband current parallel to the applied field. The spectrum of the parallel current is

$$\mathbf{n}\cdot\mathbf{j}_{\rm er}(\omega) = -\omega\int_0^{t_0} dt e^{-i\omega t}\int d\mathbf{K}|d_j(\mathbf{K}_t)|\int_{-\infty}^{t} dt' F(t')|\bar{\Omega}(\mathbf{K}_{t'})|e^{i\mathcal{S}(\mathbf{K},t',t)} + \text{c.c.}, \tag{F.1}$$

where $\mathbf{n}$ is the polarization vector, and

$$\mathcal{S}(\mathbf{K},t',t) = \int_{t'}^{t} d\tau\left[\varepsilon(\mathbf{K}_\tau) + \mathbf{F}(\tau)\cdot\mathbf{R}_{cv}(\mathbf{K}_\tau)\right] \tag{F.2}$$

is the gauge invariant action. The gradient of the action is

$$\begin{aligned}\nabla_{\mathbf{K}}\mathcal{S} &= \nabla_{\mathbf{K}}\int_{t'}^{t} d\tau\left[\varepsilon(\mathbf{K}_\tau) + \mathbf{F}(\tau)\cdot\mathbf{R}_{cv}(\mathbf{K}_\tau)\right]\\ &= \int_{t'}^{t} d\tau\left\{\nabla_{\mathbf{K}}\varepsilon(\mathbf{K}_\tau) + \mathbf{F}(\tau)\times\left[\nabla_{\mathbf{K}}\times\mathbf{R}_{cv}(\mathbf{K}_\tau)\right] + \left[\mathbf{F}(\tau)\cdot\nabla_{\mathbf{K}}\right]\mathbf{R}_{cv}(\mathbf{K}_\tau)\right\},\end{aligned} \tag{F.3}$$

where we have used the fact that $\mathbf{F}$ is independent of $\mathbf{K}$. Further, since the curl of a gradient is zero, we have

$$\nabla_{\mathbf{k}}\times\mathbf{R}_{cv}(\mathbf{k}) = \boldsymbol{\Omega}_c(\mathbf{k}) - \boldsymbol{\Omega}_v(\mathbf{k}) \equiv \boldsymbol{\Omega}(\mathbf{k}), \tag{F.4}$$

where $\boldsymbol{\Omega}_m(\mathbf{k}) = \nabla_{\mathbf{k}}\times\boldsymbol{\mathcal{A}}_m(\mathbf{k})$ is the Berry curvature. Define the total interband velocity $\mathbf{v}_t(\mathbf{k}) = \nabla_{\mathbf{k}}\varepsilon(\mathbf{k}) + \mathbf{F}(t)\times\boldsymbol{\Omega}(\mathbf{k})$, where the second term is known as the anomalous velocity. The gradient of the action is then

$$\begin{aligned}\nabla_{\mathbf{K}}\mathcal{S} &= \int_{t'}^{t} d\tau\left[\mathbf{v}_\tau(\mathbf{K}_\tau) - \partial_\tau\mathbf{R}_{cv}(\mathbf{K}_\tau)\right]\\ &= \Delta\mathbf{x}(\mathbf{K},t',t) - \mathbf{R}_{cv}(\mathbf{K}_t) + \mathbf{R}_{cv}(\mathbf{K}_{t'}),\end{aligned} \tag{F.5}$$

where $\Delta\mathbf{x}(\mathbf{K}, t', t)$ is the electron-hole separation due to quiver motion between birth and recombination. The saddle points equations are thus

$$\nabla_{\mathbf{K}}\mathcal{S} = \Delta\mathbf{x}(\mathbf{K}, t', t) - \mathbf{R}_{cv}(\mathbf{K}_t) + \mathbf{R}_{cv}(\mathbf{K}_{t'}) = 0 \tag{F.6a}$$

$$-\partial_{t'}\mathcal{S} = \varepsilon(\mathbf{K}_{t'}) + \mathbf{F}(t') \cdot \mathbf{R}_{cv}(\mathbf{K}_{t'}) = 0 \tag{F.6b}$$

$$\partial_t\mathcal{S} = \varepsilon(\mathbf{K}_t) + \mathbf{F}(t) \cdot \mathbf{R}_{cv}(\mathbf{K}_t) = \omega, \tag{F.6c}$$

which are clearly gauge invariant. Eqs. (F.6) are consistent with Ref. [35], although we encounter an additional term due to the anomalous velocity since our analysis is multi-dimensional.

We label the saddle point momentum $\bar{\mathbf{K}}$ and consider electron hole pairs born at time t', which later recombine at $t = t_r$ to emit a harmonic photon. The real part of Eq. (F.6b) equation with $t' = t_b + i\delta$ gives

$$\bar{\mathbf{K}} = -\mathbf{A}(t_b). \tag{F.7}$$

Evaluating Eq. (F.6a) at the saddle point, we have

$$\begin{aligned} 0 &= \int_{t_b}^{t_r} d\tau \mathbf{v}_\tau(\bar{\mathbf{K}}_\tau) - \mathbf{R}_{cv}(\bar{\mathbf{K}}_{t_r}) + \mathbf{R}_{cv}(\bar{\mathbf{K}}_{t_b}) \\ &= \int_{t_b}^{t_r} d\tau \mathbf{v}_\tau \left[\bar{\mathbf{K}} + \mathbf{A}(\tau)\right] - \mathbf{R}_{cv}\left[\bar{\mathbf{K}} + \mathbf{A}(t_r)\right] + \mathbf{R}_{cv}\left[\bar{\mathbf{K}} + \mathbf{A}(t_b)\right] \\ &= \int_{t_b}^{t_r} d\tau \mathbf{v}_\tau \left[\mathbf{A}(\tau) - \mathbf{A}(t_b)\right] - \mathbf{R}_{cv}\left[\mathbf{A}(t_r) - \mathbf{A}(t_b)\right] + \mathbf{R}_{cv}(0), \end{aligned} \tag{F.8}$$

which we use to find combinations of t_b and t_r during an optical cycle. We can then identify trajectories contributing to each harmonic using Eq. (F.6c)

$$\varepsilon\left[\mathbf{A}(t_r) - \mathbf{A}(t_b)\right] + \mathbf{F}(t_r) \cdot \mathbf{R}_{cv}\left[\mathbf{A}(t_r) - \mathbf{A}(t_b)\right] = \omega(t_b; t_r). \tag{F.9}$$